

Michele Gaudreault

**JSASS 13th INTERNATIONAL SESSIONS
in
37th AIRCRAFT SYMPOSIUM**

October 13-15, 1999

**Ota-ku Sangyo Plaza
Tokyo, Japan**

**DISTRIBUTION STATEMENT A
Approved for Public Release
Distribution Unlimited**

**The Japan Society for Aeronautical and Space Sciences
(JSASS)**

DTIC QUALITY INSPECTED 4

19991117 058

REPORT DOCUMENTATION PAGE			Form Approved OMB No. 0704-0188	
Public reporting burden for this collection of information is estimated to average 1 hour per response, including the time for reviewing instructions, searching existing data sources, gathering and maintaining the data needed, and completing and reviewing the collection of information. Send comments regarding this burden estimate or any other aspect of this collection of information, including suggestions for reducing this burden, to Washington Headquarters Services, Directorate for Information Operations and Reports, 1215 Jefferson Davis Highway, Suite 1204, Arlington, VA 22202-4302, and to the Office of Management and Budget, Paperwork Reduction Project (0704-0188), Washington, DC 20503.				
1. AGENCY USE ONLY (Leave blank)	2. REPORT DATE 9 Nov 99	3. REPORT TYPE AND DATES COVERED Proceedings, 13-15 Oct 99		
4. TITLE AND SUBTITLE Proceedings of JSASS 13th International Sessions in 37th Aircraft Symposium, Creative Flight - Growth and Evolution to the Future Generations - Aeronautics for the Twenty-First Century		5. FUNDING NUMBERS F6256299M9122		
6. AUTHOR(S) The Japan Society for Aeronautical and Space Sciences (JSASS), Chairperson Dr. Norihiro Goto, Professor of Aeromautics and Astronautics, Kyushu University, Fukuoka, Japan				
7. PERFORMING ORGANIZATION NAME(S) AND ADDRESS(ES) The Japan Society for Aeronautical and Space Sciences (JSASS)		8. PERFORMING ORGANIZATION REPORT NUMBER N/A		
9. SPONSORING/MONITORING AGENCY NAME(S) AND ADDRESS(ES) AOARD UNIT 45002 APO AP 96337-5002		10. SPONSORING/MONITORING AGENCY REPORT NUMBER CSP-98-07		
11. SUPPLEMENTARY NOTES				
12a. DISTRIBUTION AVAILABILITY STATEMENT Approved for public release; distribution is unlimited.		12b. DISTRIBUTION CODE A		
13. ABSTRACT (Maximum 200 words) Sampling of the 10 Sessions included the following: "A New Optimal Guidance Law for Short-range Homing Missiles" "Effective Filtering of Target Glint" "Design of a Flight Control System for Propulsion Controlled Aircraft" "Nonlinear Optimal in Helicopter Flight Control" "Flow Control Method Using Unsteady Sensitivity Analysis" "Simulation of A Flexible Aircraft Dynamics" "BVI Noise Predictions Using Euler/FW-H Method" "Suppression of Supersonic Jet Noise by Free Rotating Vane-Type Tab" "An Accelerated Co-Evolutionary Algorithm Using Neural Networks" "A Study of the Swimming Path of the Penguin"				
14. SUBJECT TERMS Optimal Planar Evasive Maneuvers, Pilot-Induced Oscillations, Role of Aeroelasticity			15. NUMBER OF PAGES 179	
			16. PRICE CODE	
17. SECURITY CLASSIFICATION OF REPORT UNCLASSIFIED	18. SECURITY CLASSIFICATION OF THIS PAGE UNCLASSIFIED	19. SECURITY CLASSIFICATION OF ABSTRACT UNCLASSIFIED	20. LIMITATION OF ABSTRACT UL	

Proceedings of
JSASS 13th INTERNATIONAL SESSIONS
in 37th AIRCRAFT SYMPOSIUM

Creative Flight – Growth and Evolution to the Future Generations
- Aeronautics for the Twenty-First Century -

October 13-15, 1999

Ota-ku Sangyo Plaza
Tokyo, Japan

The Japan Society for Aeronautical and Space Sciences
(JSASS)

Copyright © by
the Japan Society for Aeronautical and Space Sciences (JSASS)

Chairperson
Dr. Norihiro Goto
Professor of Aeronautics and Astronautics
Kyushu University
Fukuoka, 812-8581, JAPAN

Organizing Committee

Kenji Hamamoto	Fuji Heavy Industry
Tadashige Ikeda	Nagoya University
Noboru Kobiki	Kawasaki Heavy Industry
Naoki Matayoshi	National Aerospace Laboratory
Hideto Motohashi	Mitsubishi Heavy Industry
Seiya Ueno	Yokohama National University

Acknowledgement

The organizing committee of the 13th International Sessions in the 37th Aircraft Symposium wishes to thank the following for their contribution to the success of this conference:

"United States Air Force Asian Office of Aerospace Research and Development (AOARD)".

Table of Contents

Plenary Session

Assessment of Aeronautical Science for the 21st Century

J. J. S. Shang	571
----------------------	-----

Session 1 Guidance and Control 1

1E1: A New Optimal Guidance Law for Short-range Homing Missiles

C.-S. Lin, L.-P. Tsao, and H.-C. Chang	575
--	-----

1E2: Real-Time Missile Trajectory Optimization Using Parameter Optimization

J. Ahn, T. Lee, and Y. Kim	579
----------------------------------	-----

1E3: A Study to Obtain a Realistic Game Solution in an Aircombat Game

F. Imado and J. Shinar	583
------------------------------	-----

Session 2 Guidance and Control 2

1E4: Optimal Planar Evasive Maneuvers against Proportionally Guided Ground-to-Air Missiles

I. Rhee, E.-J. Song, and M.-J. Tahk	587
---	-----

1E5: Effective Filtering of Target Glint

T.-L. Song and D.-G. Lee	593
--------------------------------	-----

1E6: Maneuvering Target Tracking Using Input Estimation with Multiple Model

S.-J. Shin and T.-L. Song	597
---------------------------------	-----

Special Lecture 1

1E7: Pilot-Induced Oscillations (PIO) : Causes and Corrections

B. S. Liebst	601
--------------------	-----

Session 3 Guidance and Control 3

1E8: Robust Control Design for Structured System Uncertainties in Flight Control System Design

A. Legowo, H. Okubo, E. Muramatsu, and H. Tokutake,	609
---	-----

1E9: Design of a Flight Control System for Propulsion Controlled Aircraft

Y. Ochi and K. Kanai	613
----------------------------	-----

1E10: Multivariable Flight Control Design Using Co-Evolutionary Algorithm

K.-M. Koo, H.-S. Chi, and M.-J. Tahk	617
--	-----

Session 4 Guidance and Control 4

1E11: Nonlinear Optimal in Helicopter Flight Control

A. An and Y. Wang	621
-------------------------	-----

1E12: Design Method of an Autonomous Helicopter Flight Controller by a Neural Network

H. Nakanishi, A. Satoh, and K. Inoue	625
--	-----

1E13: A Study of the Flight Safety under IMC

Y. Kumamoto, H. Fujimoto, T. Amano, and K. Kobayashi,	629
---	-----

1E14: A Natural Way to Implement WADGPS in East Asia: Decentralized WADGPS

C. Kee and C.-S. Pyung	633
------------------------------	-----

Session 5 Computational Fluid Mechanics 1

2E1: Inverse Design of Thick Supercritical Airfoils

T. E. Pambagjo, K. Nakahashi, and S. Obayashi	639
---	-----

2E2: Unsteady Supersonic Cavity Flow Simulations Using Navier-Stokes Equations and k-omega SST Turbulence Model

J. Zhang and E. Morishita	643
---------------------------------	-----

2E3: A Study on Shock Wave/Boundary Layer Interaction Phenomena with Chemically Nonequilibrium

A. Matsumoto and S. Aso	647
-------------------------------	-----

2E4: Flow Control Method Using Unsteady Sensitivity Analysis

H.-J. Kim, C. Kim, and O.-H. Rho	651
--	-----

Special Lecture 2

2E5: A CFD Procedure for Aerospace Applications

R. W. MacCormack	655
------------------------	-----

Session 6 Fluid Mechanics and Structure 1

2E6: Estimation of Tilt Rotor Dynamics and Aerodynamics in Low Speed Forward Flight	
K. Itoh and T. Nagashima	659
2E7: Simulation of A Flexible Aircraft Dynamics	
H. R. Kheirandish and J. Nakamichi	665
2E8: Structural Fatigue Life Extension and Damage Tolerance Using Hole Cold Expansion Technology	
L. Reid	669
2E9: SAAB Aerospace: An Overview of Full Scale Testing Programs	
G. R. Woelffer	673

Special Lecture 3

2E10: The Role of Aeroelasticity in Recent German and European Aircraft Research and Development	
H. Hoenlinger, F. Kissling, and R. Voss	675

Session 7 Fluid Mechanics and Structure 2

3E1: On the Dynamic Stability of a Completely Free Stiff-Edged Cylindrical Shell Subjected to Follower Force	
S.-H. Park and J.-H. Kim	685
3E2: Parametric Instability of a Viscoelastic Composite Beam under a Periodic Force	
T.-W. Kim and J.-H. Kim	689
3E3: BVI Noise Predictions using Euler/FW-H Method	
A. Ochi, E. Shima, T. Aoyama, and S. Saito	693

Session 8 Aerodynamics

3E4: A Study on Aerodynamic Characteristics Improvement of Modified Arrow Wing of Next-Generation SST due to Lateral Blowing	
M. Kamishita, S. Aso, K. Karashima, and K. Sato	697
3E5: On Reynolds and Mach Number Effects at Two-Dimensional Wind Tunnel Testing	
B. Rasuo	701
3E6: Suppression of Supersonic Jet Noise by Free Rotating Vane-Type Tab	
K. Ibrahim and Y. Nakamura	705

Session 9 Guidance and Control 5

3E7: Adaptive and Robust Control of Wing Flutter	
T. Degaki and S. Suzuki	709
3E8: Parameter Identification of Spin-Stabilized Projectiles by Using Modified Newton-Raphson Minimization Technique	
Z.-S. Kuo and H.-Y. Huang	713
3E9: An Accelerated Co-Evolutionary Algorithm Using Neural Networks	
J.-H. Kim, C.-S. Park and M.-J. Tahk	717
3E10: Application and Testing of a SQP Code to Some Trajectory Optimization Problems	
M. Tava and S. Suzuki	721

Session 10 Guidance and Control 6

3E11: Co-Evolutionary Methods for Trajectory Optimization of Space Launch Vehicles	
H.-W. Woo, W.-R. Roh, Y. Kim, and M.-J. Tahk	725
3E12: Hypervelocity Trajectories of Ballistic Entry By Using Improved Matched Asymptotic Expansions	
Z.-S. Kuo and Y.-L. Yang	729
3E13: An Integrated Method for Shape and Flight Trajectory Optimization of Spaceplane	
T. Tsuchiya and S. Suzuki	733
3E14: Orbital Maneuvering of Reusable Launch Vehicle through Tether	
K. D. Kumar and Y. Miyazawa	737
3E15: A Study of the Swimming Path of the Penguin	
M. Harada, S. Ito, N. Arai, and Y. Naito	741

Assessment of Aeronautical Science for the 21st Century

J.S. Shang *

Center of Excellence for Computing Simulation
U.S. Air Force Research Laboratory
Wright-Patterson Air Force Base, OH 45433-7912

1 Abstract

An assessment of scientific issues for aircraft technology has been accomplished. By addressing the limitations of aircraft performance, the critical and basic topics for improvement have been identified as turbulence, aerodynamic bifurcation, and vortex interaction. Specific areas of future emphasis are also highlighted.

2 Introduction

The U.S. National Research Council performed an invaluable study of the aeronautical technology requirement for the future (1). In the analysis, the technological challenge to aeronautics has been meticulously articulated. Seven key aerodynamics technological needs were also identified as in the following; Low speed and high lift for subsonic configurations, Subsonic aircraft propulsion/airframe integration, Aerodynamic cruise performance, Low speed and high lift for supersonic configurations, Supersonic aircraft propulsion/airframe integration, Aerodynamics of rotorcraft, and Simulation capability. It is immediately obvious that these needs are complex, interdisciplinary, and most can only be addressed through modeling and simulation.

A meaningful assessment of the required aeronautical technologies may best be achieved by breaking down the technology into its genus in science (2). Then one can conduct analysis for its progress to become an interdisciplinary technology. For an example, the most critical concern of propulsion/airframe integration is the surge and rotating stall of axial flow compressors which is frequently attributed to inlet distortion (3,4). In fact, this observed flowfield is affected by turbulence, transition, and flow separation, but is only manifested by the vortex generated from the inlet. The ability to eliminate this performance limiting phenomenon must be derived from our basic knowledge of aerodynamics. Therefore, it is logical to focus on the scientific issue for an accurate assessment of aeronautical technology.

Turbulence, bifurcation, and vortex interactions are present in nearly all practical aeronautical applications. All these fluid dynamic phenomena are nonlinear and have a strong element of time dependency associated with them. Therefore, they remain as the unresolved and least

understood areas in fluid dynamics. It is well-known, that the vortex breakdown over the wing may result from the interaction of a streamwise vortex generated by a strake or a leading edge extension (LEX) and an adverse axial pressure gradient. The net effect leads to loss of lift toward the trailing edge of the wing resulting in a pitch-up motion, and finally induces severe aircraft buffeting. The prospect of using simulation techniques via either a ground facility or computer to duplicate the aircraft in flight is rather daunting. Nevertheless, attempts will be made to assess the current status in simulation technologies and to identify the need for future improvements.

3 Turbulence

There is little doubt that turbulence is the most difficult subject in fluid dynamics, and is also unfortunately the most common form of fluid motion (5). Direct numerical simulation (DNS) of transition and turbulence has been demonstrated recently (6). The key point brought out for the first time is that indeed the turbulent phenomenon can be recovered from the time-dependent Navier-Stokes equations. Equally important, these DNS results now can achieve a spatial resolution comparable to that of the micro-instrument in experimental simulations (5). The complementary activities in turbulence research among the two simulation techniques is now truly possible.

Application of DNS to engineering needs is impractical for now; therefore, the development of alternatives such as the large-scale eddy simulation (LES) and turbulence modeling becomes necessary. The LES is built on the premise that small-scale turbulence is nearly isotropic and has universal characteristics that may be successfully modeled. The most recent large-scale simulations are based on the dynamic subgrid-scale models of Germano et al (7). This LES approach is able to describe the laminar wall layer and the backscatter of turbulent energy correctly. Although the original model has been extended to compressible transition flow (8), LES is still not cost effective for engineering applications.

For the aforementioned reasons, a better phenomenological turbulence model is repeatedly identified as the pacing item for CFD (9,10). These engineering tools (11) are crucial for applications but always have a limited range of validity. These phenomenological turbulence models fared poorly in predicting flow separation,

Senior Scientist and Leader

turbulence amplification through shock waves, and vortex interactions (2,5). Flow phenomena such as these are complex, but experimental efforts can be designed to isolate dominant effects. In fact, the decay and growth of turbulent kinetic energy and shear stress have been measured within a three-dimensional turbulent boundary layer when interacting with a longitudinal vortex (12). Experimental data of these types will provide a solid point of reference before the quantification of turbulence modeling can begin.

Finally, complex turbulent flowfield measurements should be encouraged which is the only exception to the axiom of returning to basics. The cornerstone of the phenomenological turbulence model is built on the process of calibration. The less the user needs to extrapolate the range of validity the more likely the model will be used. Therefore, preparation of the turbulence model for a class of particular applications in aircraft aerodynamic performance will be much more productive than stopping short with only classic and simple benchmarks.

4 Aerodynamic Bifurcation

The bifurcation of a dynamic system is best described to be a transition between different dynamic states; it always involves the change of at least one controlling parameter in the junction of stability boundaries (13). Thus bifurcation has its roots in the stability of both temporal and spatial flowfield structure. Aerodynamic bifurcation becomes a concern to flight because sudden changes in dynamic characteristics of the flowfield around an aircraft induces drastic responses from the flying vehicle. The nonlinear phenomenon is almost a common occurrence at the outer performance limits of aircraft which frequently coincide with the stability boundaries of aircraft motion (14).

Bifurcations encountered in flight include flow separation, compressor surge and rotating stall, static and dynamic stall of a wing, vortex breakdown, aileron buzz, wing rock, buffeting, flutter, as well as laminar-turbulent transition. The most difficult issue in bifurcation research lies in the identification of the control parameters, the tedious search for the critical point, and finally the determination of the subcritical or the supercritical behavior (13).

Vortex breakdown has attracted an enormous amount of research attention (2). A favorable comparison between data and computations was obtained for the laminar transient vortex breakdown over a delta wing at high incidence by a pitch-and-hold motion (15). It would be a singular accomplishment in aerodynamic research, should the same level of understanding be extended to turbulent flows.

Experimental data on compressor surge and rotat-

ing stall seem to indicate that the bifurcation has a clearly defined limit in the pressure rise characteristic of a compressor (4,16). The research on initial emergence and the ensuing growth of the stall cells of short length scale appears to be most promising (4).

Buffet, buffeting, and flutter result from the selective response of structural modes excited by the pressure fluctuations. Mabey (14) has carefully defined the difference among these bifurcations. Since the aircraft structure acts as a selective filter for the excited frequency spectra, the scaling issue in testing is even more demanding. Data measurement accuracy for dynamic simulation also needs substantial improvement. Simulation of these phenomena requires a sustained effort to nurture the highly complex interdisciplinary endeavor.

The laminar-turbulent transition process is the most important bifurcation phenomenon in fluid mechanics. The difficulty of its simulation arises from the fact that the initial disturbances from the environment are nearly indiscernible. Depending on the nature and spectrum of the disturbance environment, the perturbations will selectively and linearly amplify the normal modes of a receptive shear flow. The process is completed by the ensuing nonlinear wave interaction (17). In experimental simulation, disturbances from the test environment that meet the criterion of receptivity are numerous, but the mechanisms through which these disturbances enter and excite the shear layer are still not completely understood. On the concerns of flight vehicle and environmental factors to transition, one must echo Reshotko's articulation for needed research on surface roughness, particulate effect, and flight testing. Additional insight regarding flight experiments for transition is deferred to works of Reshotko (17).

5 Vortex Interactions

Vortex interactions span the entire range of aircraft operation. At the microscopic scale, vortices and their random interactions with the large scale motion constitute turbulence. In macroscopic dimensions, the interaction of vortices generated from a hybrid wing contributes significantly to lift capability and it may also enhance or degrade the resistance of aircraft to departure in rapid maneuvers. The impingement by wake vortices has been known to create hazards to trailing aircraft in take-off and landing operations. Since the vortex is "a finite volume of rotational fluid bounded by irrotational fluid or solid wall" (18), steep gradients around the kinematic structure always exist. The numerical resolution requirement for a vorticity dominant flow field is very stringent, and for three-dimensional computation is often beyond current computational capability (2). A formulation based on vorticity dynamic equations in the Lagrangian frame may be very promising.

In aircraft applications, the vortex interaction with solid surfaces overshadows other forms of interference (18,19). This is particularly evident when the vortical impingement has produced catastrophic structural failure via either the fatigue process or the over-stressed condition at a dynamic loading (20). At present, there is no sufficient data to provide either an unambiguous characterization of vortex breakdown induced empennage buffet or the compressor blade row environment for high cycle fatigue analysis. The need of experimental investigation on the vortex-solid-surface interacting phenomenon is urgent; this knowledge will be invaluable to focus future research in aerodynamics.

6 Experimental Simulation Technologies

For flight vehicles, the two most frequently used tools for design and analysis are experimental and computational simulation of aerodynamic performance. The validity of experimental simulation technology in aeronautics is built on the principle of dynamic similarity. The concept of similitude can reduce the degrees of freedom of the studied phenomena through the similarity rule. However, if the flowfields under study are strongly influenced by fine scale turbulence and laminar-turbulent transition, the accuracy of simulations to flow physics will be uncertain (2,14). In dynamic testing for the buffeting and flutter envelopes, the duplication of modes and natural frequencies of two structures will pose a formidable challenge, if possible (14). The most valuable experimental data for understanding the flow physics are detailed flowfield structure measurements. These data should be obtained by either micro- or non-intrusive techniques.

In spite of past successes in product development, experimental or computational simulation technology alone still cannot meet the accuracy requirements for aircraft design. From now on, an even more efficient design process is demanded to fit a shrinking research and development environment, and also to create future opportunity for science. In order to meet this challenge, we need to improve the design process. A more efficient design process needs better tools and fewer iterative cycles by integrating the required engineering at the onset. However, integrating the pertaining air vehicle technologies requires continuous investment to meet realizable expectation. A way to achieve the objective is to focus scientific resources into areas crucial to aeronautical technology (1).

Instead of addressing the database development for engineering needs, the requirement will be highlighted on the issues of the unresolved or the least understood areas in aerodynamics. In order to retain the widest range of impact to engineering applications, research in aerodynamics needs to return to the basics.

7 Interdisciplinary Computational Simulation

In a short span of the last decade, the predictive capability for aerodynamic performance by CFD has progressed from components of air vehicles to entire configurations (2). Despite these successes, there is clear evidence that aircraft designers still do not have the confidence to use CFD as the primary tool. Part of the reason is that the aircraft design process is iterative, starting from conceptual generation, preliminary development, and finally to the detailed design (21). At each stage, the accuracy requirement is progressively more demanding. The overall performance of the aircraft is also an interdisciplinary endeavor. Currently, the coupled computational capability of aerodynamics, flight dynamics, structural mechanics, and chemical kinetics is extremely limited. Finally, the two most critical shortfalls in CFD, the description of turbulence and the low numerical processing rate, have reduced most CFD simulations only to steady state asymptotes.

The first issue in simulating high speed flows is the description of turbulence. The Kolmogorov scales of turbulent motion are unresolvable using the existing numerical procedures on state-of-the-art distributed memory multicomputers. At flight conditions, the number of mesh points and the data processing rate for an aircraft simulation determined by directly solving the Navier-Stokes equations are more than a quadrillion and hundreds of teraflops respectively. In practical applications, engineering judgment and approximations become unavoidable (2,5,8). In general, LES is expected to be more reliable in reproducing the flow structures of shear layer, separated and vortical flows than the turbulent models of the Reynolds-averaged Navier-Stokes equations. A fertile research area for LES resides in wall-layer modeling.

Numerical accuracy and efficiency is closely interlocked in any aircraft performance simulation. Any realistic aircraft simulation requires not only to integrate multiple scientific disciplines but also to accommodate complex configurations. Recent progress in high performance, scalable parallel computing and compact-differencing based algorithms have offered some excellent opportunities to develop an interdisciplinary computing simulation capability (22,23). The spectral-like numerical algorithm (24), in principle, can reduce the grid-point density need of three-dimensional simulations by a thousand-fold. Scalable massively parallel computing has also demonstrated the ability to reduce the calendar time of a simulation by two orders of magnitude and permitted problem sizes unattainable just a few years ago. The outlook is promising, at least, the simulation technique can be applied to evaluate the engineering feasibility for risk reduction. The challenge in science issues alone warrants a redoubled effort, the impact to aeronautical technology

is just too enormous to ignore.

8 Concluding Remarks

The current aerodynamic simulation technology is still unable to meet all the challenges of advanced air vehicle design.

In order to accelerate the maturation of simulation techniques for aircraft design and analysis, available resource should be concentrated on selected topics basic to aerodynamics. Only basic knowledge can attain the widest range of applications.

The areas of future emphasis which impact air vehicle design are identified as turbulent, aerodynamic bifurcation, and vortex interaction.

9 Acknowledgment

The author is grateful for the stimulating discussions from members of the Center. The sponsorship of the present effort by USAF Office of Scientific Research is deeply appreciated.

10 References

1. Covert, E.E., Chairman of Aeronautics and Space Engineering Board, Aeronautical Technologies for the Twenty-First Century, National Research Council, National Academy Press, Washington, D.C., 1992.
2. Shang, J.S., Assessment of Technology for Aircraft Technology, *J. of Aircraft*, Vol 32, 1995, pp. 611-617.
3. Greitzer, E.M., Review - Axial Compressor Stall Phenomena, *J Fluid Engineering*, Vol 102, June 1980, pp. 134-151.
4. Day, I.J., Active Suppression of Rotating Stall and Surge in Axial Compressors, *J Turbomachinery*, Trans ASME, Vol 115, 1993, pp. 40-47.
5. Bradshaw, P., Turbulence: The Chief Outstanding Difficulty of Our Subject, Exp. in Fluid, Vol. 16, Feb. 1994, pp. 203-216
6. Kim, J. and Moin, P., Application of a Fractional-Step Method to Incompressible Navier-Stokes Equations, *J. Comp. Physics*, Vol 59, No 2, 1985.
7. Germano, M., Piomelli, U., Moin, P., and Cabot, W.H., A Dynamic Subgrid-Scale Eddy Viscosity Model, *Physics of Fluid A*, Vol 3, 1991, pp. 1760-1765.
8. Lesieur, M. and Metais, O., New Trends in Large-Eddy Simulations of Turbulence, *Annu. Rev. Fluid Mech.*, Vol 28, 1996, pp. 45-82.
9. Chapman, D.R., Mark, H., and Pirtle, M.W., Computers vs Wind Tunnels in Aerodynamic Flow Simulations, *Astronautics and Aeronautics*, Vol 13, 1975, pp. 22-30 and 35.
10. Shang, J.S., An Assessment of Numerical Solutions of the Compressible Navier-Stokes Equations, *J. of Aircraft*, Vol 25, 1985, pp. 353-370.
11. Wilcox, D.C., Comparison of Two-Equation Turbulence Models for Boundary Layers with Pressure Gradient, *AIAA J. Vol 31 No 8*, Aug. 1993, pp. 1414-1421.
12. Shabaka, I.M.M.A., Metha, R.D., Bradshaw, P., Longitudinal Vortices Imbedded in Turbulent Boundary Layers, Part 1, Single Vortex, *J. Fluid Mech*, Vol 155, 1985, pp. 37-57.
13. Seydel, R., From Equilibrium to Chaos: Practical Bifurcation and Stability Analysis, Elsevier Science Publishing Co., New York, 1988, pp. 1-17.
14. Mabey, D.G., Physical Phenomena Associated with Unsteady Transonic Flows, *Progress In Astronautics and Aeronautics*, Vol 120, AIAA, 1989, pp. 1-55.
15. Visbal, M.R., Onset of Vortex Breakdown Above a Pitching Delta Wing, *AIAA J. Volume 32*, 1994, pp. 1568-1575.
16. Garnier, V.H., Epstein, A.H., and Greitzer, E.M., Rotating Waves as a Stall Inception Indication in Axial Compressors, *ASME J. Turbomachinery*, Vol 113, 1991, pp. 290-302.
17. Reshotko, E., Boundary Layer Instability, Transition and Control, *AIAA Paper 94-0001*, Jan. 1994
18. Saffman, P.G. and Baker, G.R., Vortex Interactions, *Ann. Rev. Fluid Mech.*, Vol 11, 1979, pp. 65-122.
19. Doligaski, T.L., Smith, C.R., and Walker, J.D.A., Vortex Interactions with Walls, *Ann Rev., Fluid Mech.*, Vol 26, 1994, pp. 573-616.
20. Gordnier, R.E. and Visbal, M.R., Numerical Simulation of the Impingement of a Streamwise Vortex on a Plate, *Int. J. of CFD*, Vol 12, 1999, pp. 49-66.
21. Labrujere, Th.E. and Slooff, J.W., Computational Methods for the Aerodynamic Design of Aircraft Components, *Annu. Rev. Fluid Mech.*, Vol 25, 1993, pp.183-214.
22. Shang, J.S., An Outlook of CEM Multidisciplinary Applications, *AIAA Preprint 99-0336*, 37th AIAA Aerospace Science Meeting, Reno NV, January 11-14, 1999
23. Gaitonde, D.V., Development of a Solver for 3-D Non-ideal Magnetogasdynamics, *AIAA Preprint 99-3610*, 30th Plasmadynamics and Laser Conference, Norfolk VA, 28 June - 1 July, 1999.
24. Lele, K., Compact Difference Schemes with Spectral-like Resolution. *J. Comp. Physics*, Vol 103, 1992, pp. 16-42.

Ching-Show Lin* Lu-Ping Tsao** Hui-Chen Chang***

*Department of System Engineering, Chung Cheng Institute of Technology Tahsi, Taoyuan, 33509, Taiwan, R.O.C.

*** Department of Electronics Engineering, Ta-Hwa Institute of Technology Chung-Lin, Hsin-Chu, 30740, Taiwan, R.O.C.

Key Words: homing missiles, optimal guidance, proportional navigation law

ABSTRACT

Using the exact nonlinear equations of motion in the plane, a new optimal guidance law (OPG) for short-range homing missiles, based on minimizing the interception time, is presented. It is assumed that a precise knowledge of the target's motion is available to the missile. Unlike the conventional optimal guidance approach where the commanded lateral acceleration of the missile is considered the control variable, the study directly exploits the flight-path angle as the control one to derive analytically the optimal missile trajectory for intercepting the target. Numerical simulation is used to evaluate the performance of the proposed guidance law and to make a comparison with that of the true proportional navigation (TPN) and augmented proportional navigation law (APN). It is verified that the performance of the proposed guidance law, in terms of the interception time and miss distance has a superiority over that of the two schemes. The APN necessitates the least control energy expenditure among the three schemes.

1. INTRODUCTION

Over the past four decades, the proportional navigation law (PN) has been widely employed in the air-to-air missile guidance design for its simplicity and ease of implementation. It is known that the proportional navigation law gives better performance against a nonmaneuvering target. However, dealing with the highly maneuverable targets, the performance of the PN degrades sharply. Hence, there are increasing demands for the development of new guidance laws to replace the PN.

The optimal control theory, based on linearizing the relative equations of motion, was used to derive the guidance laws that better treat the maneuvering targets[1-4]. Many of them take the target maneuver into account to cope with the highly maneuverable targets and also demonstrate the advantage. However, the optimal guidance laws are only valid for small line of sight angles.

An optimal solution to the guidance problem for a maneuvering target, using the exact nonlinear equations of motion, was derived by Guelman and Shinar[5]. The work assumed a perfect knowledge of the target behavior, and minimized a performance index that is a linear combination of the interception time and control energy cost. We recall the performance index as

$$J = t_c + k \int_0^{t_c} u^2 dt$$

where k is the weighting factor and u is the lateral acceleration command of the missile. The choice of k value depends on the different engagement conditions. In general, for short ranges,

where time is paramount. $k \rightarrow 0$ for longer ranges, when maximum energy should be saved, a large k can be chosen. In the time optimal problem (that is, $k \rightarrow 0$), the lateral acceleration command derived by Guelman and Shinar is infinity. Assuming the capability of the lateral acceleration is limited, they found without any mathematical proof that the missile employed the strategy of a hard turn followed by a straight-line path to attack the target. In addition, the direction of the hard turn must be determined by the final angular values of the engagement. Unfortunately, the turn direction is not clear in advance. Hence, they defined the sign of the control as a positive direction in order to solve the optimal guidance problem. However, the definition limited the scope of the guidance law application.

In order to handle the time optimal guidance problem, the study directly exploits the flight-path angle, instead of the lateral acceleration, as the control variable to formulate the problem. The capture criterion is to minimize the interception time duration for a given miss distance. The optimal trajectory intercepting the evasive target with minimum time is solved in a closed form. The approach, as far as the authors can determine, has not been considered in the open literature before.

The rest of the paper is organized as follows. In Section II, the optimal guidance control problem is formulated in the exact nonlinear relative equations of motion. The optimization problem is then solved in Section III. The implementation of the resulting optimal guidance scheme is analyzed in Section IV. In Section V, the results of the simulation study conducted to evaluate the OPG performance and a comparison with the performance of the TPN and APN schemes are presented. Discussions based on the simulation results are also included. Finally, the conclusions are drawn in Section VI.

2. PROBLEM FORMULATION

In order to formulate the guidance problem, we shall make the following assumptions:

1. The missile-target engagement is two-dimensional motion.
2. The missile and target are considered as constant-velocity mass points.
3. The time lag in the missile guidance system is neglected.
4. A complete knowledge of the target's motion is available to the missile.

Consider a two-dimensional engagement geometry as shown in Fig. 1. Therefore, the engagement model can be represented by the following differential equations:

$$\dot{\theta} = [V_M \sin(\theta - \gamma_M) - V_T \sin(\theta - \gamma_T)] / r, \quad \theta(0) = \theta_0 \quad (1)$$

$$\dot{r} = -V_M \cos(\theta - \gamma_M) + V_T \cos(\theta - \gamma_T), \quad r(0) = r_0 \quad (2)$$

where r is relative range, θ is the line of sight angle, γ_M is

*Ph.D. Candidate, Dep. Of System Engineering

** Associate Professor, Dep. Of System Engineering

*** Instructor, Dep. Of Electronics Engineering

the flight-path angle of the missile, and V_T and V_M are the velocities of the missile and target, respectively. And, the flight-path angle of the target $\gamma_T = \gamma_T(t)$ is a given continuous function of time. The optimal guidance problem which needs to be solved is to find the optimal missile trajectory $\gamma_M(t)$ such that the capture condition defined by

$$r(t_f) \leq R \quad (3)$$

is assured while the performance index J

$$J = t_f = \int_0^{t_f} 1 dt \quad (4)$$

is minimized, which means that the total time for the interception is minimized because the interception time is regarded as a prime factor for the homing missile against a near target.

3. OPTIMAL GUIDANCE CONTROL SOLUTION

The nonlinear optimization problem proposed above can be solved analytically by applying the maximum principle [6]. Let us now write the Hamiltonian H for the problem.

$$H = 1 + \lambda_r [-V_M \cos(\theta - \gamma_M) + V_T \cos(\theta - \gamma_T)] + \lambda_\theta [V_M \sin(\theta - \gamma_M) + V_T \sin(\theta - \gamma_T)] / r \quad (5)$$

The governing equations of the adjoint variables can be derived via the following relations.

$$\dot{\lambda}_r = \lambda_\theta [V_M \sin(\theta - \gamma_M) - V_T \sin(\theta - \gamma_T)] / r^2 = \lambda_\theta \dot{\theta} / r, \quad \lambda_r(t_f) \text{ free} \quad (6)$$

$$\begin{aligned} \dot{\lambda}_\theta &= -\lambda_\theta [V_M \cos(\theta - \gamma_M) - V_T \cos(\theta - \gamma_T)] / r \\ &- \lambda_r [V_M \sin(\theta - \gamma_M) - V_T \sin(\theta - \gamma_T)] = -\lambda_r \dot{\theta} + \lambda_\theta \dot{r} / r \\ \lambda_\theta(t_f) &= 0 \end{aligned} \quad (7)$$

By solving Eqs.(6) and Eqs.(7) of differential equations in terms of r and θ , we get

$$\lambda_r = c_1 \sin(\theta + c_2) \quad (8)$$

$$\lambda_\theta = c_1 r \cos(\theta + c_2) \quad (9)$$

where c_1 and c_2 are constants of integration. Eqs. (9) has to satisfy the boundary condition at $t = t_f$, thus we get

$$c_2 = \pi/2 - \theta_f + \pi \quad (10)$$

Due to the fact that we are dealing with a free end time problem, thus the Hamiltonian satisfies

$$H_f = 0 \quad (11)$$

After some calculation, we obtain

$$c_1 = \pm 1 / r_f \quad (12)$$

Taking c_1 is positive and substituting Eqs.(12) and (10) into Eqs.(8) and (9), we get

$$\lambda_r = \cos(\theta_f - \theta) / r_f \quad (13)$$

$$\lambda_\theta = r \sin(\theta_f - \theta) / r_f \quad (14)$$

where

$$\dot{r}_f = -V_M \cos(\theta_f - \gamma_{Mf}) + V_T \cos(\theta_f - \gamma_{Tf}) \quad (15)$$

The control function $\partial H / \partial \gamma_M = 0$ gives

$$\gamma_M = \theta + \tan^{-1}(\lambda_\theta / r \lambda_r) \quad (16)$$

Substituting Eqs.(13) and (14) into Eqs. (16), we derive the surprising result as

$$\gamma_M = \theta_f \quad (17)$$

The resulting control law means that the missile heading is steered into the final line of sight of the missile and target. However, because of the presence of the heading error defined the difference between the current missile heading and the final line of sight, the missile must make a hard turn at the initial phase of the engagement and then go straight to hit the target. The fact also verifies Guleman's study on the time optimal guidance problem.

4. CONTROL LAW APPLICATION

For implementation of the resulting control law obtained in the previous section, we have to find the exact value of θ_f . This requires the solution of the entire system of Eqs.(1) and (2) when the control law is applied by Eqs.(17). However, it is too difficult to derive the exact value of θ_f by solving the nonlinear differential equations. Fortunately, the final engagement geometry throws a new light on this problem. From the final engagement geometry at $t = t_f$ as shown in Fig 1., we have

$$V_{Mf} = [(X_T - X_{M(t_f)})^2 + (Y_T - Y_{M(t_f)})^2]^{1/2} - R \quad (18)$$

$$\theta_f = \tan^{-1}(Y_T - Y_{Mf} / X_T - X_{Mf}) \quad (19)$$

In order to compute the value of θ_f , we have to obtain the positions of the missile and target at $t = t_f$, respectively. Firstly, the equations of the missile's motion is expressed by

$$\dot{X}_M = V_M \cos \gamma_M \quad (20)$$

$$\dot{Y}_M = V_M \sin \gamma_M \quad (21)$$

Using Eqs.(17) into Eqs.(20) and (21) and integrating both equations from $t = 0$, $X_M(0) = 0$, and $Y_M(0) = 0$ to $t = t_f$, $X_M(t_f) = X_{Mf}$, and $Y_M(t_f) = Y_{Mf}$, we obtain

$$X_{Mf} = t_f V_M \cos \theta_f \quad (22)$$

$$Y_{Mf} = t_f V_M \sin \theta_f \quad (23)$$

Secondly, since it is assumed that the target's motion γ_T is known as a function of time, thus we can get the position of the target at $t = t_f$ as

$$X_T = X_0 + \int_0^{t_f} V_T \cos \gamma_T dt \quad (24)$$

$$Y_T = Y_0 + \int_0^{t_f} V_T \sin \gamma_T dt \quad (25)$$

By using Eqs.(22), (23), (24) and (25) into Eqs.(18) and Eqs.(19), the values of θ_f and t_f can be solved. Now, we start to calculate the value of t_f . It is clear to see that Eqs.(18) is a nonlinear equation. The nonlinear nature means that it cannot be solved explicitly and a numerical method must be applied. Arranging Eqs.(18) in the form

$$t_f = \{[(X_T - X_{M(t_f)})^2 + (Y_T - Y_{M(t_f)})^2]^{1/2} / V_M - R / V_M\} = f(t_f) \quad (26)$$

and applying the quadratically convergent Newton-Raphson method [7], yield the approximate value of t_f . Then, by substituting t_f into Eqs. (19), the exact value of θ_f is determined. And, since the flight-path angle command of the missile is given, the required acceleration command for the missile is also derived. As a result, the optimal control law can be carried out without any difficulty.

5. SIMULATION RESULTS

1. Simulation conditions

A highly difficult engagement scenario is chosen to evaluate the performance of the OPG. Besides, a comparison of the performance is also made with the true proportional guidance law (TPN) and augmented proportional guidance law (APN) where

$$u_{TPN} = -N \ddot{r} \dot{\theta} \quad (28)$$

$$u_{APN} = -N \ddot{r} \dot{\theta} + \frac{N}{2} a_T \quad (29)$$

and navigation constant N is set 3 here. And, we assume that the lateral acceleration limit of the missile is 30G

($G = 9.81 \text{ m/sec}^2$) and the final relative range R of the OPG is set 10^{-2} in this simulation study. In the engagement scenario, the missile has a constant velocity of 600m/s, and is fired in the direction 50 degree away from the reference line. The target executes a 9G maneuver in the initial direction 120 degree away from the reference line with a constant velocity of 400m/s. The initial relative range is 3 km.

2. Simulation results

Simulation results for the three guidance laws are listed in Table 1. The missile-target trajectory of the engagement is shown in Fig. 2. The time histories of the missile lateral acceleration are shown in Fig. 3.

The simulation results show that the OPG gives best performance in terms of the miss distance and interception time among the three schemes. And, the APN requires far less energy cost than the other two schemes. The energy cost is defined by integrating the square of the lateral acceleration command with respect to time.

3. Discussions

There is no surprise that the TPN has a performance inferior to those of the OPG and APN guidance laws. Since the rate of the line of sight is smaller at far range, the TPN drives the missile heading slightly towards the collision course at the beginning of the engagement and then saturates at the final phase of the engagement. Fig.3 demonstrates the fact. This is because the TPN responds to the change rate of line of sight only, and is unaware of the existence of target maneuver. Hence, it induces large miss distances. This also indicates that the TPN can not intercept the target with highly evasive maneuver. In contrast, the APN, with an extra term to account for target maneuver, enables the missile to maneuver in a more efficient manner. At the early phase of the engagement, the APN commands the missile heading quickly towards the collision course and then the missile lateral acceleration command is decreasing until the hit. Accordingly, it yields less miss distances, interception time and control energy expenditure than the TPN. On the other hand, the missile guided by the OPG makes a hard turn with full energy toward the collision course at the early phase of the engagement and then goes straight until the impact. As a result, coping with the highly maneuverable target, the OPG yields the least interception time and miss distance among the three schemes. In addition, the simulation results also verifies Guelman's study on the time optimal problem.

6. CONCLUSION

The problem of finding a nonlinear optimal guidance law for the missile to capture a maneuvering target, while minimizing the interception time, has been solved successfully

in a closed form. Different from the conventional approach which the lateral acceleration is used as the control variable, we directly employs the flight-path angle as the control one. The proposed optimal guidance law is to steer the missile heading into the final line of sight of the missile and target, which can be obtained by using the final engagement geometry. The performance of the OPG is evaluated and compared with the TPN and APN by a highly difficult engagement scenario. Simulation results show that the proposed optimal guidance law achieves the best performance in terms of the miss distance and interception time among the three missile guidance laws. And, the APN requires the least energy cost among the three missile guidance laws.

In order to implement the OPG, the future trajectory of the target must be known in advance; however, it is impossible to do that in a realistic environment. Hence, the realization of the OPG has to be carried out step by step, based on the real time estimation of the target's current state and acceleration and the prediction of its future trajectory.

REFERENCES

- [1] Cottrell, R. G., "Optimal Intercept Guidance for Short Range Tactical Missile," *AIAA Journal*, Vol. 9, 1971, pp. 1414-1415.
- [2] Kreindler, E., "Optimality of Proportional Navigation," *AIAA Journal*, Vol.11, 1973, pp. 878-880.
- [3] Asher, R. B., and Matuszewski, J. P., "Optimal Guidance with Maneuvering Targets," *Journal Spacecraft*, Vol.11, No 3, 1973, pp. 204-206.
- [4] Nazarov, G. J., "An Optimal Terminal Guidance Law," *IEEE Transaction on Automatic Control*, AC-21, No. 1, 1976, pp.407-408.
- [5] Guelman, M., and Shinar, J., "Optimal guidance law in the plane," *Journal of Guidance, Control, and Dynamics*, Vol. 7, No. 4, 1984, pp. 471-476
- [6] Bryson, A. E., Jr., and Ho, Y., *Applied Optimal Control*, Hemisphere, Washington, DC, 1975.
- [7] Powell, M. J. D., "Minimization of functions of several variables" *Numerical Analysis*, an Introduction, 1966

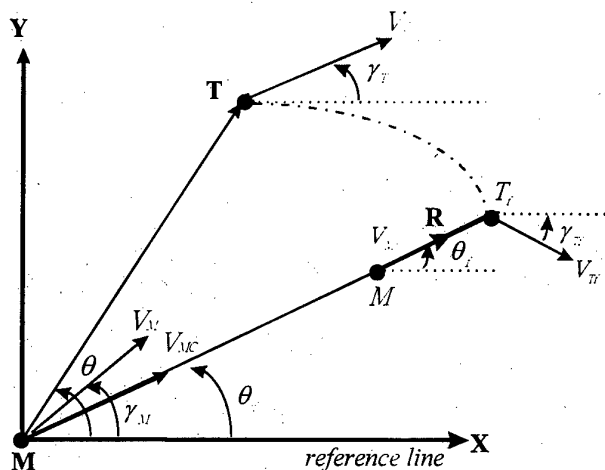


Fig 1. Geometry of interception

Table 1. Simulation results

scenario	item	TPN	APN	OPG
1	interception time	3.70sec	3.62sec	3.52sec
	miss distance	60.61m	0.08m	0.02m
	energy cost	160890	88803	95796
	(m^2/sec^3)			

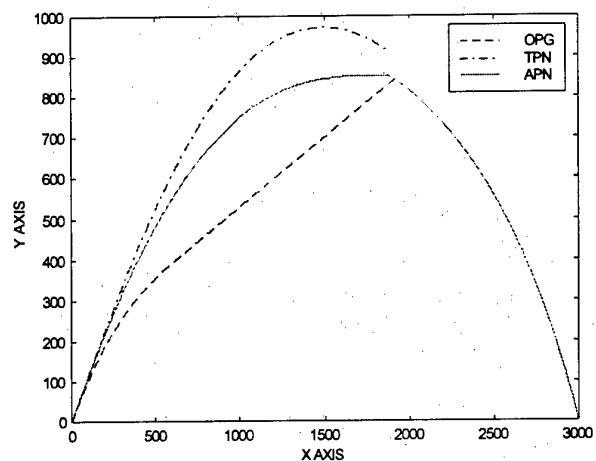


Fig.2 Missile and target trajectories

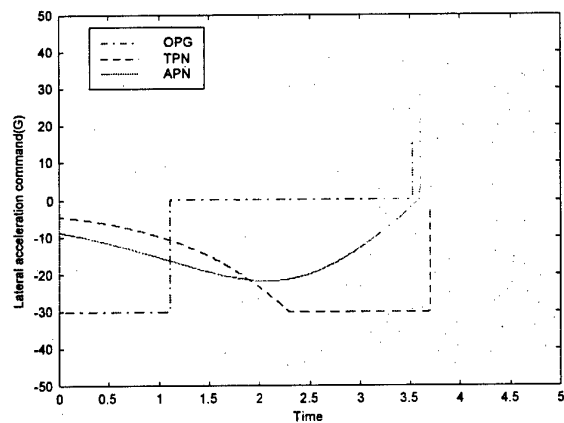


Fig.3 Time histories of missile lateral acceleration

REAL-TIME MISSILE TRAJECTORY OPTIMIZATION USING PARAMETER OPTIMIZATION

Jaemyung Ahn,* Taeyoung Lee,* and Youdan Kim†

Department of Aerospace Engineering
Seoul National University, Seoul 151-742, Korea

Key Words: Guidance and Control, Flight Dynamics

ABSTRACT

Missile trajectory optimization is performed to obtain the optimal intercept trajectories against a descending target. The missile is assumed to be a point mass moving in three dimensional space, and thrust, gravity and aerodynamic forces are assumed to dominate the forces acting on it. Burnout velocity is considered as the performance index, inequality constraints on the control variables are considered, and inequality constraints on the dynamic pressure multiplied by the angle of attack is also considered to guarantee structural safety. The direct method is used to solve this problem, and only the control variables are parameterized. When the pre-computed optimal input is implemented, the missile may deviate from the pre-computed optimal trajectory due to external disturbances as well as internal uncertainties. To compensate for these effects, a real time trajectory optimization algorithm is proposed.

1. Introduction

The purpose of trajectory optimization is to obtain the optimal control histories and the state histories that minimize the specified performance index subject to the dynamic equations while satisfying several equality and inequality type constraint equations. The missile intercept problem can be formulated as a trajectory optimization problem searching for an optimal input for a specific objective function and constraints. There are many different approaches for solving this problem, and the direct method is one of the most widely used methods for solving the trajectory optimization problem.[1-4] In the direct method, control and/or state histories are parameterized, and the trajectory optimization problem is converted into the parameter optimization problem. This method is popular since it is relatively easy to guess the initial control/state trajectories, and the method has good convergence properties. When the pre-computed optimal input is implemented in a real situation, the missile may deviate from the pre-computed optimal trajectory due to external disturbances as well as internal uncertainties. Therefore, a real-time algorithm is required to compensate for this error to perform the intercept mission effectively. This is a 'real-time trajectory optimization process' and also requires a fast computation algorithm for real-time execution.

In this paper, a trajectory optimization problem for intercepting a descending target is formulated and solved by using the parameter optimization method. Burn-out velocity of the missile is considered as the objective function, and several constraints are also considered to guarantee structural safety. A real-time algorithm to compensate the trajectory deviation during real flight is also proposed, and is verified by numerical simulation.

2. Problem Formulation

The mission of a missile is to intercept a non-maneuvered descending target.[5] The launch geometry of the intercept problem is shown in Fig. 1. To obtain the equations of motion, it is assumed that the intercept missile is modeled as a point mass moving in a three dimensional space that contains the center of a spherical, rotating Earth with an inverse-square gravitational field. The obtained equations of motion of the missile are [6]

$$\frac{dr}{dt} = V \sin \gamma \quad (1)$$

$$\frac{d\theta}{dt} = \frac{V \cos \gamma \cos \psi}{r \cos \phi} \quad (2)$$

$$\frac{d\phi}{dt} = \frac{V \cos \gamma \sin \psi}{r} \quad (3)$$

$$\frac{dV}{dt} = \frac{1}{m} F_T - g \sin \gamma + \omega^2 r \cos \phi (\sin \gamma \cos \phi - \cos \gamma \sin \psi \sin \phi) \quad (4)$$

$$V \frac{d\gamma}{dt} = \frac{1}{m} F_N \cos \sigma - g \cos \gamma + \frac{V^2}{r} \cos \gamma + 2\omega V \cos \psi \cos \phi + \omega^2 r \cos \phi (\cos \gamma \cos \phi + \sin \gamma \sin \psi \sin \phi) \quad (5)$$

$$V \frac{d\psi}{dt} = \frac{1}{m} \frac{F_N \sin \sigma}{\cos \gamma} - \frac{V^2}{r} \cos \gamma \cos \psi \tan \phi + 2\omega V (\tan \gamma \sin \psi \cos \phi - \sin \phi) - \frac{\omega^2 r}{\cos \gamma} \cos \psi \sin \phi \cos \phi \quad (6)$$

where F_T and F_N denotes the tangential force and normal force to the missile velocity, respectively, and can be expressed as

$$F_T = T \cos \alpha - D \quad (7)$$

$$F_N = T \sin \alpha + L \quad (8)$$

* Graduate Student, Department of Aerospace Engineering

† Associate Professor, Department of Aerospace Engineering

with thrust T , drag force D and lift L . [6] Note that the dynamic equations of the missile are composed of 6 state variables and two input variables as follows:

$$x^T = [r \ \theta \ \phi \ V \ \gamma \ \psi] \quad (9)$$

$$u^T = [\alpha \ \sigma] \quad (10)$$

Fig. 2 shows the coordinate system used in this paper.

The mission of the missile is to intercept the descending target, and the burn-out velocity is taken as the performance index as follows:

$$J = \frac{c}{V(t_{BO})} \quad (11)$$

where $V(t_{BO})$ is burn-out velocity, and c is a positive constant. To intercept the target, the following boundary condition is imposed at the final time.

$$\|x_M(t_f) - x_T(t_f)\| = 0 \quad (12)$$

where $x_M(t_f)$ and $x_T(t_f)$ denote the missile and target positions at final time t_f , respectively.

Inequality constraints are imposed on the input angles as

$$-5^\circ < \alpha < 5^\circ \quad (13)$$

$$-90^\circ < \sigma < 90^\circ \quad (14)$$

and the following inequality constraint is also considered to avoid structural destruction due to lateral loading.

$$\max \left\{ \left| \frac{1}{2} \rho(\tau) V(\tau)^2 \alpha(\tau) \right| \right\} < Q_0, \quad 0 < \tau < t_f \quad (15)$$

where Q_0 is a positive constant determined to guarantee structural safety.

To solve the problem stated above, the parameter optimization technique is used. Input variables are parameterized, and state variables are obtained by direct integration of the equations of motion. The initial heading angle and final time are also included in the parameter vector. In this study, the SQP (Sequential Quadratic Programming) Algorithm is chosen to solve the parameter optimization problem. [7-9]

3. Numerical Example

The aerodynamic data of the intercept missile were obtained from Ref. [10]. The initial state values of the intercept missile are: $r_0 = 6370$ km, $\phi_0 = 36.4^\circ$, $\theta_0 = 127.3^\circ$, $V_0 = 27$ m/sec, and $\gamma_0 = 90^\circ$. The vehicle is assumed to have the following characteristics

Initial mass = 907.2 kg

Diameter(D) = 0.41 m

Reference Area(S_{ref}) = 0.132 m²

Length = 5.3 m

Specific Impulse(I_{sp}) = 270 sec

Mass Flow Rate(\dot{m}) = $\begin{cases} 27.06 \text{ Kg/s}, & 0 \leq t \leq 10 \\ 9.02 \text{ Kg/s}, & 10 \leq t \leq 57 \\ 0 \text{ Kg/s}, & t > 57 \end{cases}$

The descending target is assumed to be a 1000 Kg point mass without maneuvering, and the reference area of the

target is assumed to be 0.2827 m². The initial values of short range targets are as follows: height $h_T(0) = 87$ km, velocity $V_T(0) = 1123$ m/s, and flight path angle $\gamma_T(0) = -12.1$ deg. The initial values of long range targets are as follows: height $h_T(0) = 222$ km, velocity $V_T(0) = 2194$ m/s, and flight path angle $\gamma_T(0) = -30.0$ deg. Sample target trajectories are shown in Fig. 3. Q_0 in the inequality constraint is set as 8000 Pa-rad. The total number of parameters is 26: 12 for the angle of attack, 12 for the bank angle, 1 for the initial heading angle, and 1 for the final time. The i -th angle of attack (bank angle) parameter represents the angle of attack value (bank angle) at time t_{i-1} . The control values $\alpha(t)$ and $\sigma(t)$ are expressed by interpolating these values. Time t_i s, where the input parameters are located, are defined as follows:

$$t_0 = 0, \quad t_1 = 7, \quad t_{k+1} = t_k + 5, \quad (k = 1, 2, \dots, 11)$$

Tolerance for convergence is set as 1 m. Fig. 4 and Fig. 5 show one of the numerical results of the short range case, and Table 1 summarizes the performances of numerical examples.

4. Real-time Trajectory Optimization

In this section, an algorithm is proposed to correct trajectory deviation errors during flight by a real-time process. When missile states are measured after a specific interval from launching, the states become different from the pre-computed values because of external disturbances and uncertainties. To perform the intercept mission successfully, the control input should be modified during the flight. If the control input is corrected by using the optimization process with the measured states, then the modified control input may not be applied to the missile due to the computational burden. To avoid this difficulty, the proposed algorithm divides the phases into computation and implementation. At the current phase, the optimal input computed at the previous phase is used, while the optimization is performed to compute the next phase's control input. The missile states at the beginning of the next phase are predicted by using the measurement data at the current phase, and the predicted values are used as the initial values in the optimization process. Fig. 6 shows the overview of the real-time algorithm, and the method of real-time trajectory optimization algorithm is summarized as follows:

[Step 1] Solve optimal trajectory problem to obtain $u(t)$. $t_0 \leq t \leq t_{BO}$.

[Step 2] After launching, measure real states $x(t_1)$ at time t_1 , and predict the states $\hat{x}(t_2)$ using $x(t_1)$.

[Step 3] During $t_1 \leq t \leq t_2$, using $\hat{x}(t_2)$ as the initial value, solve optimal trajectory problem to obtain the corrected input $u(t)$. $t_2 \leq t \leq t_{BO}$.

[Step 4] Computed $u(t)$ is used for $[t_2, t_3]$. Measure the real states $x(t_2)$ at time t_2 , and during $t_2 \leq t \leq t_3$ solve optimal trajectory problem to obtain $t_3 \leq t \leq t_{BO}$.

[Step 5] Repeat Step 4.

For the real-time optimization algorithm stated above, the partition of time interval should be determined previously. The time points t_1, t_2, \dots, t_n 's are defined as the points where the parameters are located. The interval for the first step calculation is $[t_1, t_2]$, and the input calculated in this interval is used in $[t_2, t_3]$. Successively, the k -th step calculation is performed in $[t_k, t_{k+1}]$, and the calculated input is used in $[t_{k+1}, t_{k+2}]$.

To reduce the computation time, the objective function and the inequality constraints are not considered, and only the intercept condition (missile and target position at the final time) is considered as the equality constraint. Compared with the initially optimized result, this method does not deteriorate burn-out velocity to a significant degree. The initial input of each step was selected using the previous step input. To guarantee the continuity of the input, the first parameter is fixed and the other parameters are used for optimization. Fig. 7 shows the initial input selection of each step.

For the realization of the proposed algorithm, the computation time used for each step must be shorter than the time interval. Therefore, the 'maximum iteration number (i_{\max})' is introduced, and the optimization process is stopped if the iteration is executed more than i_{\max} times, even though the position error at the final time is larger than the error tolerance. The maximum iteration number is determined by the following equation.

$$(N_\alpha + N_\sigma - 1 - 2k) \times (t_{BO} - t_{k+1}) \times i_{\max}^k = \text{Constant}$$

Then, the maximum iteration number of each step is as follows: $i_{\max}^1=4, i_{\max}^2=5, i_{\max}^3=7, i_{\max}^4=9, i_{\max}^5=13, i_{\max}^6=19, i_{\max}^7=33, i_{\max}^8=68, \text{ and } i_{\max}^9=228$.

Real-time algorithm simulation was executed for a short-range target. For environmental error, 10% random noise was added to the drag force. We used the CFSQP solver[11] and IBM Pentium 266MHz computer for simulation. Table 2 summarizes the real-time simulation results. Error before real-time calculation (3rd column) could be reduced much (4th column) by the proposed algorithm. For the first five steps, iteration was stopped because of the iteration number limit even though the position error after calculation (4th column) was larger than 1 m. However, after the 5th step, the iteration was terminated by position error convergence. According to this table, the maximum elapsed time among steps is 7.41 sec. For real application, it should be shorter than the step interval (5 sec). However, faster CPUs will be able to execute this process within the time interval. Fig. 8 shows corrected inputs by the real-time algorithm.

(Table 1) Trajectory Optimization Performances

Case		t_f (sec)	Miss Dist. (m)	$V(t_{BO})$ (m/sec)	max $ Q\alpha $ (Pa-rad)
Short Range	1	58.31	0.89	3142.5	8000
	2	66.49	0.68	3141.2	8000
Long Range	1	80.81	0.32	3134.8	7130
	2	80.34	0.38	3132.0	8000

5. Concluding Remarks

Missile trajectory optimization is performed for the missile intercept problem. Burn-out velocity is taken as the performance index, and several inequality constraints are considered. The parameter optimization technique, a kind of the direct method, is used to solve the optimization problem, and only the control variables are parameterized. A real-time algorithm is also proposed to compensate for the trajectory deviation resulting from the external disturbances. The proposed method is verified by numerical simulation.

References

- [1] Lawden, D.R., "Rocket Trajectory Optimization: 1950-1963," *Journal of Guidance, Control, and Dynamics*, Vol.14, No.4 pp.705-711, 1991.
- [2] Kulakow, L.J., and Stancil, R.T., "Rocket Boost Trajectories for Maximum Burnout Velocity," *ARS Journal*, Vol.30, No.7, pp.612-618, 1960.
- [3] Dougherty, J.J., and Speyer, J.L., "Near-Optimal Guidance Law for Ballistic Missile Interception," *Journal of Guidance, Control, and Dynamics*, Vol.20, No.2, pp.355-361, 1997.
- [4] Hermann, A.L., and Conway, B.A., "Direct Optimization Using Collocation Based on High-Order Gauss-Lobatto Quadrature Rules," *Journal of Guidance, Control, and Dynamics*, Vol.19, No.3, pp.592-599, 1996.
- [5] Hough, M.E., "Optimal Guidance and Nonlinear Estimation for Interception of Decelerating Targets," *Journal of Guidance, Control, and Dynamics*, Vol.18, No.2, pp.316-324, 1995.
- [6] Vihn, N.X., *Optimal Trajectories in Atmospheric Flight*, Elsevier, New York, NY, 1981.
- [7] Polak, E., *Optimization Algorithms and Consistent Approximations*, Springer-Verlag, New York, NY, 1997.
- [8] Fletcher, R., *Practical Methods of Optimization*, John Wiley and Sons, New York, NY, 1987.
- [9] Bryson, Jr., A.E., and Ho, Y.-C., *Applied Optimal Control*, A Halsted Press Book, John Wiley & Sons, 1975.
- [10] Engineering Science Data Item Number 77021, "Properties of A Standard Atmosphere," Engineering Science Data Unit, 1977.
- [11] Lawrence, C., Zhou, J.L., and Tits, A.L., *User's Guide for CFSQP Version 2.5*, University of Maryland, 1997.

(Table 2) Result of Real-time Simulation

Step	Interval (sec)	Error ¹ (m)	Error ² (m)	Comp. Time (s)	No. of iteration
1	12-17	57.5	26.4	7.41	4*
2	17-22	104.5	24.6	6.59	5*
3	22-27	72.4	40.4	6.92	7*
4	27-32	56.8	32.3	7.41	9*
5	32-37	42.9	16.3	7.25	13*
6	37-42	30.5	0.17	6.54	15
7	42-47	15.6	0.91	5.99	25
8	47-52	8.14	0.41	3.74	27
9	52-57	5.19	0.25	2.26	31

1) and 2): Before¹⁾ and after²⁾ real-time optimization

* iterated i_{\max} times

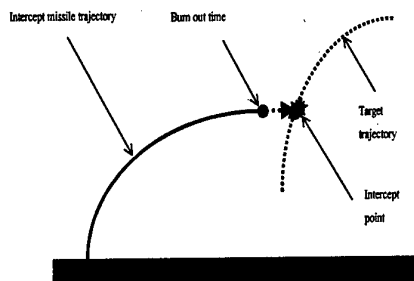


[Fig. 1] Missile intercept scenario

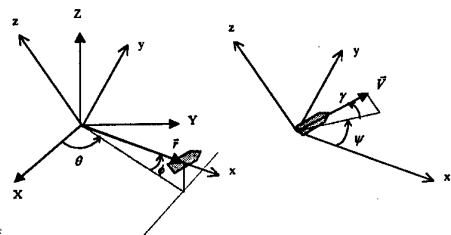


[Fig. 2] Definition of coordinate system

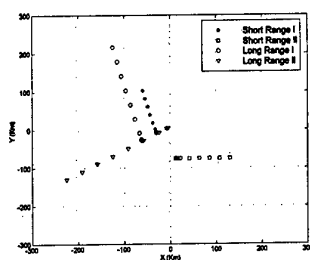


[Fig. 3] Target Trajectories

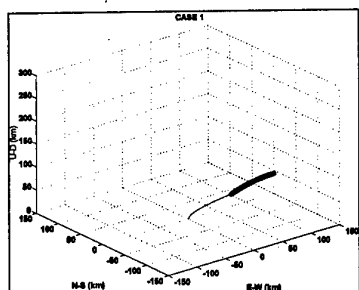


[Fig. 4] Missile trajectory: Short range case I

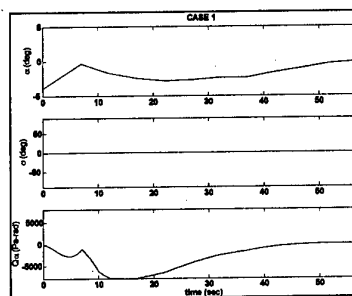


[Fig. 5] Inputs / $Q\alpha$, Short range case I

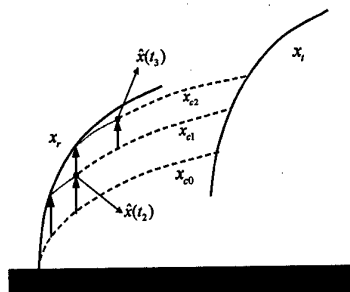


[Fig. 6] Overview of Real-time Algorithm

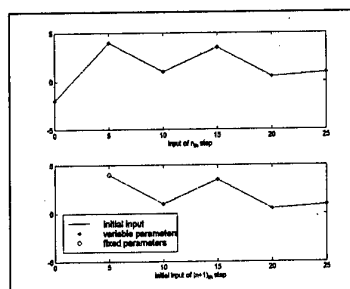


[Fig. 7] Initial input of each step

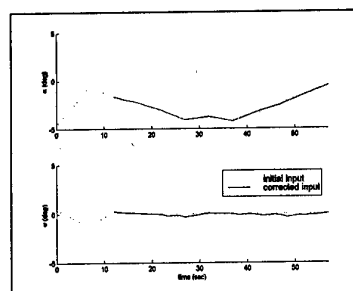


[Fig. 8] Corrected Inputs

A STUDY TO OBTAIN A REALISTIC GAME SOLUTION IN AN AIRCOMBAT GAME

Fumiaki Imado* and Josef Shinar**

* Shinshu University, 500 Wakasato Nagano, Nagano 380-0922 JAPAN

** Israel Institute of Technology, Haifa 32000 ISRAEL

Key Words: Optimal Control, Differential Games, Aircraft

ABSTRACT

A method to obtain a game solution in a practical complex problem is proposed, and an example in an aircombat game is presented. The principle of the method is, at first to obtain a feedback form suboptimal solution for both players. Next, by solving the one-sided optimal control problems for both players, and by improving the feedback form solution, we can get the approximate saddle point solution. An application for a minimum time pursuit-evasion air-combat game is presented, and the accuracy achieved by the method is shown to be very good.

1. BACKGROUND

Many aerospace tasks belong to the class of pursuit-evasion problems and can be addressed either in an optimal control or in a zero-sum differential game formulation. The advantage of the differential game formulation is that it is robust with respect to the disturbances created by an adversary controlling agent. Because of the inherently complex nonlinear mathematical models used for representing aerospace problems, no closed form solutions are available and iterative numerical methods have to be used.

* Professor, Dept. of Mechanical Systems Engineering

** Professor, Faculty of Aerospace Engineering

Such methods solve, for each set of initial conditions, a nonlinear two-point boundary-value problem of high dimensions and yield the control functions in a feedback representation. There exist several algorithms that solve successfully the optimal control version of such problems, requiring the minimization (or maximization) of a cost function, denoted by J . The solution of a zero sum differential game, that requires the simultaneous minimization and maximization of the same cost function, i.e. a simultaneous mini-max convergence, is much more difficult. For this reason many scientists refrain to address problems in a game formulation.

2. MATHEMATICAL MODEL

Figure 1 shows the pursuit-evasion geometry of two aircraft, where "P" and "E" denote a pursuer and an evader, respectively. R is the relative distance, V_p and V_e are velocities of the pursuer and evader, and ϕ_p and ϕ_e shows their directions, and ψ shows the evader's direction. System equations are given as follows,

$$\dot{R} = -V_p \cos(\phi_p - \psi) + V_e \cos(\phi_e - \psi) \quad (1)$$

$$\dot{\psi} = [-V_p \sin(\phi_p - \psi) + V_e \sin(\phi_e - \psi)] / R \quad (2)$$

$$\dot{V}_p = [-\xi_p(T_{mp}) - D_{0p} - n_p^2 D_{lp}] / m_p \quad (3)$$

$$\dot{V}_e = [-\xi_e(T_{me}) - D_{0e} - n_e^2 D_{le}] / m_e \quad (4)$$

$$\dot{\phi}_p = g(n_p^2 - 1)^{1/2} / V_p \quad (5)$$

$$\dot{\phi}_e = g(n_e^2 - 1)^{1/2} / V_e \quad (6)$$

Where Tm is the maximum available thrust, D_0 is the zero-lift drag, D_I is the induced drag, m is the aircraft mass, and n is the normal load factor. The following relations exist between drag and lift coefficients,

$$D = \frac{1}{2} \rho v^2 s [C_{D0} + k(C_L - C_{L0})^2] \quad (7)$$

$$L = \frac{1}{2} \rho v^2 s (C_L - C_{L0})^2 \quad (8)$$

$$D = D_0 + n^2 D_I \quad (9)$$

$$D_0 = \frac{1}{2} \rho v^2 s C_{D0} \quad (10)$$

$$D_L = 2k(mg)^2 / (\rho v^2 s) \quad (11)$$

The control variables are the thrust T and lift coefficient C_L . The stopping condition is when the range between the pursuer and the evader becomes equal to the capture range R_c .

$$\Omega \equiv R - R_c \quad (12)$$

The performance index of the game is the time of capture.

$$J = t_f \quad (13)$$

A feedback form of the approximation of the optimal control for both players are expressed as follows.¹⁾

$$\xi_i = 1, \quad \varsigma_i = (\dot{\phi}_s)_i \left(\frac{2V_i}{V_i' - V_i} \right)^{1/2} \sin\left(\frac{\phi - \phi_i}{2}\right) \quad (14)$$

Where ς is the optimal required turning rate, related to the aerodynamic load factor n by

$$\varsigma = \frac{g}{V} (n^2 - 1)^{1/2} \quad (15)$$

$\dot{\phi}_s$ is the sustained turning rate with full thrust,

$$\dot{\phi}_s = \frac{g}{V} \left(\frac{J_m - D_0 - D_I}{D_I} \right)^{1/2} \quad (16)$$

and V' is the reference speed obtained from the reduced-order game solution.

Originally the value of V' is assumed to be the aircraft maximum speed.

3. IMPLEMENTATION

Table 1 shows initial conditions employed. Both aircraft are YF16,

however the C_{D0} of the evader is intentionally increased than the actual one. The computation is performed through the following process.

a) Simulations are conducted by employing suboptimal law (eq.14) for both players, for several parameters of V_i' . The histories of C_L 's; C_{LP} and C_{Le} are stored, and the interception time t_f is registered.

b) Solve the minimum time optimal control of the pursuer, while the evader employs the suboptimal law (eq. 14). The solution is obtained by steepest ascent method²⁾, and the time history of C_{LP} obtained in step a) is employed as the nominal control. The solutions are obtained for several value of the evader's V_r ; V_{re} , and the interception times are registered.

c) Solve the maximum time optimal control of the evader, while the pursuer employs the suboptimal law (eq.14) in the same way as step b). The time history of C_{Le} obtained in step a) is employed as the nominal control, and the interception times for several value of the pursuer's V_r ; V_{rp} are registered.

Let us denote the performance indices in step a); $J(u^*, v^*)$, Step b); $J(u^0, v^*)$ and step c); $J(u^*, v^0)$, where superfixes "*" and "0" mean suboptimal and optimal, respectively. It is clear that the following relation exists,

$$J(u^0, v^*) < J(u^*, v^*) < J(u^*, v^0) \quad (17)$$

If the difference between $J(u^0, v^*)$ and $J(u^*, v^0)$ is small enough, then, we can consider $J(u^*, v^*)$ as the approximate solution of this mini-max problem.

4. RESULTS

As mentioned in section 2, the cost function of the game is the final time. In Fig.2, the thin and bold lines show $J(u^*, v^*)$ and $J(u^0, v^*)$ respectively, for several values of V_e' . In Fig.3, the thin

and bold lines show $J(u^*, v^*)$ and $J(u^*, v^0)$ respectively, for several values of V_p . These $J(u^*, v^*)$ and $J(u^*, v^0)$ are shown together in Fig.4. The optimal values of these are 52.9475sec and 53.0450sec, yielding $\Delta J = 0.0975$ sec; which is less than 0.2% of the interception time. The corresponding $J(u^*, v^*)$, obtained by simulation, turned out to be 52.9614sec, which is within the expected range. Figures 5 through 7 show some variable's histories corresponding to $J(u^*, v^*)$, where the solid lines and dotted lines show those of the pursuer and evader, respectively. Figure 5 shows velocity histories, Fig.6 shows control histories, and Fig.7 shows the trajectories of the pursuer and the evader.

5.CONCLUSIONS

The above given results demonstrate the feasibility to solve with a satisfactory

accuracy pursuit-evasion game of interest by using the above outlined method. However, the accuracy that can be achieved in this way depends strongly on the validity of the functional form selected for the approximate strategies.

ACKNOWLEDGEMENT

This study is conducted with financial assistance from JSPS (Japan Society for the Promotion of Science), and authors greatly appreciate to their favor.

REFERENCES

- 1) J. Shinar, "Evaluation of Suboptimal Pursuit-evasion Game Strategies for Air Combat Analysis", Journal of Guidance, Controls, and Dynamics, Vol.8, No.1, pp.9-15, 1985.
- 2) A.E. Bryson Jr., and W.F. Denham, "A Steepest Ascent Method for Solving Optimum Programing Problems", Journal of Applied Mechanics", Vol.29, No.6, pp.247-257, 1962

Table 1. Initial condition

R	3000m
ϕ	1.0472
V_p	240 m/s
V_e	260 m/s
ϕ_p	0
ϕ_e	0
R_c	2500 m

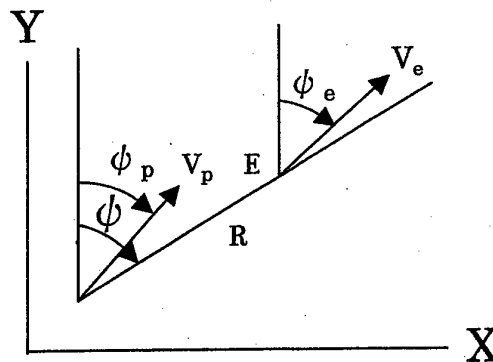


Fig.1 Horizontal interception geometry

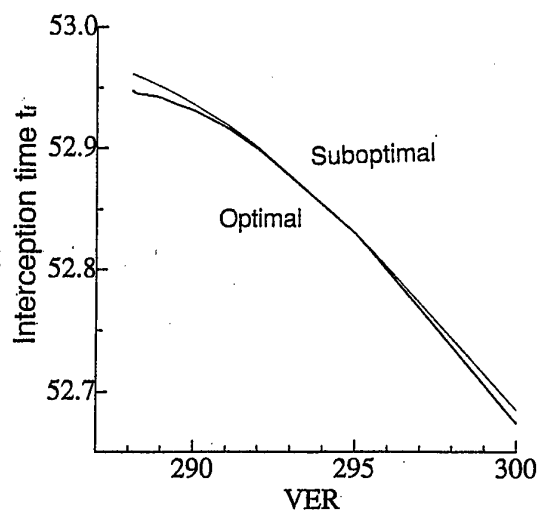


Fig.2 Pursuer's suboptimal and optimal controls

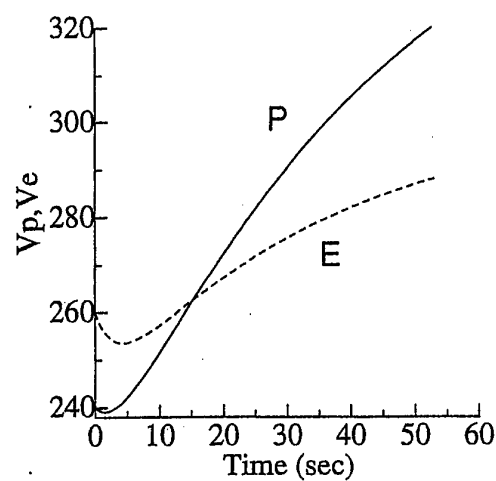


Fig.5 Velocity histories

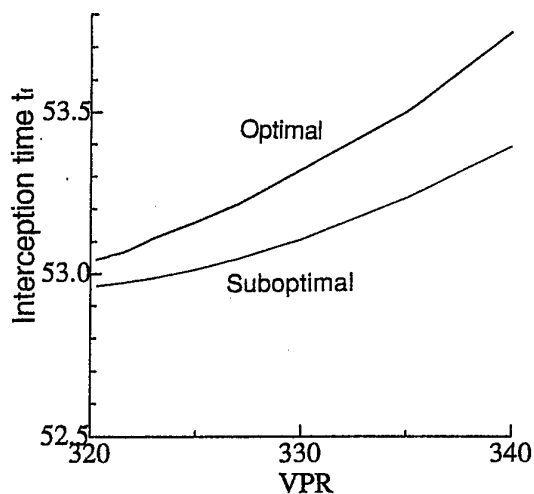


Fig.3 Evader's suboptimal and optimal controls

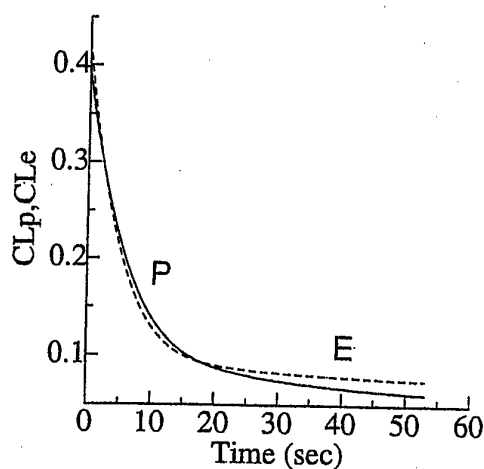


Fig.6 Control histories

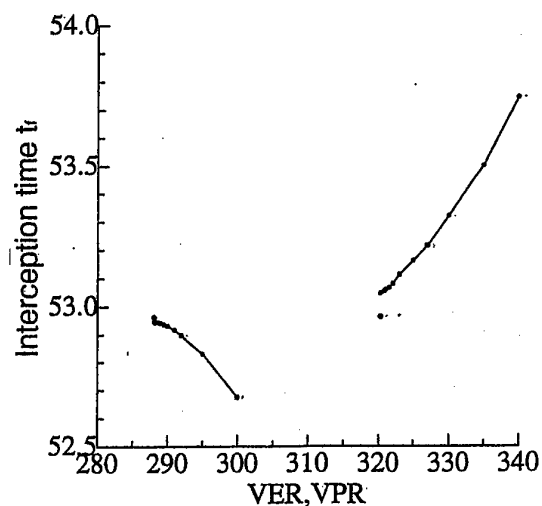


Fig.4 Optimal controls of the pursuer and evader

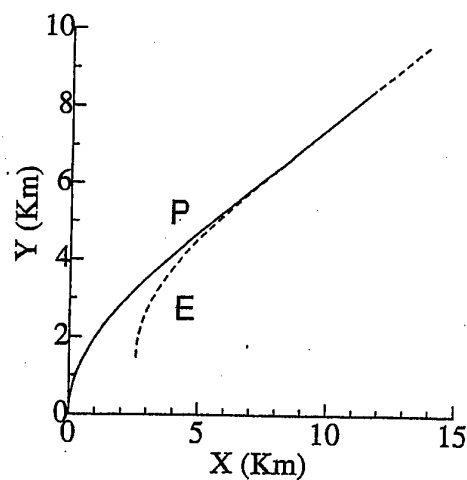


Fig.7 Trajectories

Optimal Planar Evasive Maneuvers against Proportionally Guided Ground-to-Air Missiles

Ihnseok Rhee*

Korea University of Technology and Education
307 Gajeon-Ri, Byungchun-myoun, Chunan, Choongnam, Korea 330-860
email : rhee@kut.ac.kr

Eun-Jung Song[†] and Min-Jae Tahk[‡]

Korea Advanced Institute of Science and Technology
373-1 Kusung-Dong Yousung-Ku Taejeon, Korea 305-701
email: ejsong@fdcl.kaist.ac.kr, mjtahk@fdcl.kaist.ac.kr

Key Words: Optimal Evasion, Proportional Navigation, Ground-to-Air Missile, Neural Network

ABSTRACT

An optimal evasion problem against the proportional navigation ground-to-air missiles in 2-dimensional vertical plane has been considered. For a ground-to-air missile, dynamic pressure is so low during initial phase after launch that the angle of attack of missile could be very large. Maximum angle of attack of ground-to-air missile has been considered in the generation of lateral acceleration command to keep the angle of attack within the operation range. Realistic models for both aircraft and missile have been used in the optimal evasion problem. Pull-up maneuvers have been shown to be optimal evasive maneuvers of target aircraft flying at low altitude against a missile fired at an aircraft heading toward missile while push-over maneuver against a missile fired to chase aircraft tail. A neural network has been trained on the optimal evasive maneuvers generated off-line to implement real-time evasion policy.

1 Introduction

Nonlinear differential game approach could be used to obtain optimal evasive aircraft maneuvers against missiles [1]. In differential game, a missile tries to minimize miss distance while an aircraft maximizes miss distance. The resulting aircraft maneuver is optimal against all missile maneuvers. However, missile and aircraft models are usually simplified to solve nonlinear differential game problems. By fixing the missile guidance strategy, the missile evasion problem becomes a one-sided optimal control problem. Since an optimal control problem generally is less complicated than a differential game, more realistic models for both mis-

sile and aircraft could be used for the missile evasion problem. Ref. [2] investigates evasive maneuvers by assuming linearized kinematics with constant speeds. Because of drag force, speeds of missile and aircraft are no longer constant in real world. Ref. [3] and [4] take account of drag force including induced drag term in missile and aircraft model.

Unlike previous works that considered an air-to-air missile, we study optimal evasive maneuvers against a PNG ground-to-air missile. Since ground-to-air missiles move from ground to the altitude of aircraft and air density have an effect on missile and aircraft performance, the altitude variation should be considered in missile and aircraft models. Hence, an aircraft evasion problem in the vertical plane is analyzed in this paper. Another characteristic of a ground-to-air missile is that it starts with zero initial speed. Therefore the maneuverability of the ground-air-missile is degraded by low dynamic pressure of the missile in initial phase. The missile model used here takes account into the maneuverability degradation in initial phase. The optimal evasion problem is discretized to construct a parameter optimization problem. A neural network is trained on optimal trajectory derived numerically to implement real-time suboptimal evasion policy.

2 System Models

Figure 1 shows the relative geometry between the missile and the target aircraft. The origin of XZ axis locates on the missile launcher. The subscripts m and t are used to denote the missile and the target aircraft, respectively.

By assuming that the target aircraft maneuvers with maximum thrust during evasion, the point-mass aircraft model is described by following equations:

$$\dot{V}_t = (T_t \cos \alpha_t - D_t)/m_t - g \sin \gamma_t \quad (1a)$$

$$\dot{\gamma}_t = (T_t \sin \alpha_t + L_t)/m_t V_t - g \cos \gamma_t / V_t \quad (1b)$$

$$\dot{x}_t = V_t \cos \gamma_t \quad (1c)$$

*Associate Professor, Department of Mechanical Engineering, Korea University of Technology and Education

[†]Graduate student, Dept. of Aerospace Engineering, Korea Advanced Institute of Science and Technology

[‡]Associate Professor, Dept. of Aerospace Engineering, Korea Advanced Institute of Science and Technology

$$\dot{h}_t = V_t \sin \gamma_t \quad (1d)$$

$$\dot{m}_t = -T_t/cg \quad (1e)$$

where g is the gravitational acceleration, V_t , γ_t , x_t , h_t and m_t denote the velocity, flight path angle, ground distance, altitude and mass of aircraft, respectively. The specific fuel consumption, $1/cg$, is assumed to be constant and the maximum thrust, T_t , is specified as a function of altitude and Mach number. The aerodynamic forces, lift L_t and drag D_t , can be represented by [5]

$$\begin{aligned} L_t &= \bar{q}_t S_t C_L = \bar{q}_t S_t C_{L_0} \alpha_t \\ D_t &= \bar{q}_t S_t C_D = \bar{q}_t S_t (C_{D_0} \alpha_t + \eta C_{L_0} \alpha_t^2) \end{aligned}$$

where \bar{q}_t and S_t denote the dynamic pressure and wing area of the aircraft, respectively. The aerodynamic coefficients of aircraft C_{L_0} , C_{D_0} and η are given as functions of Mach number. The angle of attack, α_t , is the control variable and is limited so that the aircraft may not stall. The load factor also should be limited within the maximum value :

$$|\alpha_t| \leq \alpha_{max} \quad (2)$$

$$|L_t/m_t g| \leq n_{max} \quad (3)$$

where α_{max} is the maximum angle of attack of the aircraft and n_{max} is the maximum load factor. Since the lift is produced by α_t , equation (3) also constrain the range of the angle of attack.

In a ground-to-air missile model adopted, missile launcher and autopilot system are taken into account. The point mass model of a ground-to-air missile is described by

$$\dot{V}_m = (T_m - D_m)/m_m - g \sin \gamma_m \quad (4a)$$

$$\dot{\gamma}_m = \begin{cases} 0 & : \text{on launcher} \\ -(a_m + g \cos \gamma_m)/V_m & : \text{otherwise} \end{cases} \quad (4b)$$

$$\dot{x}_m = V_m \cos \gamma_m \quad (4c)$$

$$\dot{h}_m = V_m \sin \gamma_m \quad (4d)$$

$$\dot{a}_m = \begin{cases} 0 & : 0 \leq t \leq t_s \\ (a_c - a_m)/\tau_m & : t > t_s \end{cases} \quad (4e)$$

where V_m , γ_m , x_m , h_m , m_m and T_m denote the velocity, flight path angle, ground distance, altitude, mass and thrust of missile respectively. The missile autopilot described by equation (4e) is modeled as a first order lag system. a_m , a_c and τ_m denote the lateral acceleration, lateral acceleration command and autopilot time constant of missile. Just after launch, the dynamic pressure of missile is so low that it is difficult to control the missile with aerodynamic force. Therefore missile guidance is started t_s after launch. The thrust and mass are given by

$$\begin{aligned} T_m(t) &= T_{max}, \quad m_m(t) = -\bar{c}t + m_{m_0} & : 0 \leq t \leq t_b \\ T_m(t) &= 0, \quad m_m(t) = -\bar{c}t_b + m_{m_0} & : t > t_b \end{aligned}$$

where t_b and m_{m_0} denote the propellant burnout time and the initial mass respectively and it is assumed that

the thrust T_{max} and the rate of mass change \bar{c} are constant while the propellant is burning.

Aerodynamic forces acting on missile are usually measured with respect to the body axis instead of the stability axis. Figure 2 shows the body and the stability axes of missile. $X_b Z_b$ is the body axis and $X_s Z_s$ is the stability axis. X and Z represent the body axis components of the aerodynamic force. For a small angle of attack, the drag D_m and the lift L_m can be represented as

$$D_m = -Z \sin \alpha_m - X \cos \alpha_m \approx -Z \alpha_m - X \quad (5)$$

$$L_m = -Z \cos \alpha_m + X \sin \alpha_m \approx -Z + X \alpha_m \quad (6)$$

where α_m is the angle of attack of missile. Since $C_{L_0} = C_{Z_0} = 0$ for a symmetric missile, from equations (5) and (6) the aerodynamic coefficients of missile with respect to the stability axis can be obtained by

$$C_D = -C_X - C_{Z_0} \alpha_m^2 \quad (7)$$

$$C_{L_0} = -C_{Z_0} + C_X \quad (8)$$

Since the lateral acceleration is produced by the lift

$$a_m = L_m/m_m = \bar{q}_m S_m C_{L_0} \alpha_m / m_m \quad (9)$$

where \bar{q}_m and S_m are the dynamic pressure and the reference area of the missile respectively. From equations (5) and (7), the drag force of the missile is described by a function of the lateral acceleration :

$$D_m = \bar{q}_m S_m C_D = k_1 + k_2 a_m^2 \quad (10)$$

where

$$k_1 = -\bar{q}_m S_m C_X, \quad k_2 = \frac{-m_m^2 C_{Z_0}}{\bar{q}_m S_m C_{L_0}^2}$$

Since a ground-to-air missile does not have enough dynamic pressure at initial phase to produce sufficient lateral acceleration, it can be observed from equation (9) that even small acceleration command to missile autopilot could make the angle of attack very large at the initial phase of engagement. Hence, the acceleration command should be applied for the missile not to stall as well as not to exceed the maximum acceleration. Let \bar{a}_{max} be

$$\bar{a}_{max} = \min(a_{max}, \bar{q}_m S_m C_{L_0} \alpha_{m_{max}} / m_m)$$

where a_{max} and $\alpha_{m_{max}}$ are the maximum acceleration and the maximum angle of attack of the missile, respectively. The lateral acceleration command for the proportional navigation guidance(PNG) missile is given by

$$a_c = \begin{cases} N \sigma V_m - g \cos \gamma_m & : |a_c| \leq \bar{a}_{max} \\ \bar{a}_{max} \text{sign}(a_c) & : |a_c| > \bar{a}_{max} \end{cases} \quad (11)$$

where N is the navigation constant and σ is the line-of-sight angle. The missile velocity is used to generate the

guidance command as in [6]. The rate of line-of-sight is given as

$$\dot{\sigma} = (\Delta h \Delta \dot{x} - \Delta \dot{h} \Delta x) / r^2 \quad (12)$$

where $\Delta x = x_t - x_m$, $\Delta h = h_t - h_m$ and $r^2 = \Delta x^2 + \Delta h^2$.

3 Optimal Evasive Maneuver

The objective of evasive maneuver is to maximize the relative distance $r(t_f)$ at the time of closest approach t_f . Hence, the missile evasion problem can be stated as follows.

Find the aircraft control history $\alpha_i(t)$ such that

$$\max_{\alpha_i} r^2(t_f) \quad (13)$$

subject to aircraft and missile state equations (1), (4), (5), (11) and (12), and control variable inequality constraint equations (2) and (3). Equation (13) is a terminal time free optimization problem. The evasive maneuver ends when the missile comes closest to the aircraft, that is, the relative distance vector \vec{r} is normal to the relative velocity vector $\dot{\vec{r}}$. Therefore, the terminal time t_f is determined from following terminal condition.

$$\begin{aligned} \vec{r} \cdot \dot{\vec{r}} \Big|_{t=t_f} &= \frac{1}{2} \frac{d}{dt} (r^2) \Big|_{t=t_f} \\ &= \frac{1}{2} (\Delta x \Delta \dot{x} + \Delta h \Delta \dot{h}) \Big|_{t=t_f} = 0 \end{aligned} \quad (14)$$

Above terminal condition also holds for the case that the relative distance or the relative velocity is zero.

A constraint optimal control problem is converted to a finite dimensional nonlinear program by discretizing state and control variables. The numerical solver used here is DIRCOL package[7] where discretization is done based on Hermite-Simpson collocation method[8][9][10]. The resulting nonlinear program is solved by sequential quadratic programming (SQP)[11].

4 Suboptimal Evasive Maneuver Using Neural Networks

The great potential of feedforward artificial neural networks has long been recognized in pattern recognition, identification, estimation, and control of dynamical system [12]. Most of the application of feedforward networks are based on their approximating abilities. If it consists of two layers and they have sufficient numbers of neurons, it can approximate any arbitrary function between input and output [13]. This basic result means that a network should be able, at least in principle, to learn any nonlinear mapping.

Based on this fact, it was proposed to train a neural network on optimal trajectories derived numerically [14]. The network learns to associate a current state vector with a proper control signal.

$$u^*(t) = u(\vec{x}(t)) \quad (15)$$

While many numerical techniques exist to compute open-loop optimal controls, the computation time is too long for real-time implementation and the design of optimal feedback controller is often not feasible. Numerically obtained optimal trajectories contain information on how the state variables have an effect on the control signal. A neural network then extracts this information from off-line generated trajectories and uses them in a feedback scheme to generate a suboptimal policy.

In this study, the optimal evasive maneuver is assumed to be a function of the relative position and relative velocity :

$$\alpha_i^* = \alpha_i(\vec{r}, \dot{\vec{r}}) \quad (16)$$

Then the training patterns, each of which is a combination of $x_m - x_t$, $h_m - h_t$, $v_m \cos \gamma_m - v_t \cos \gamma_t$, $v_m \sin \gamma_m - v_t \sin \gamma_t$, and α_i , are obtained by sampling several optimal trajectories in time. The neural network accepts $x_m - x_t$, $h_m - h_t$, $v_m \cos \gamma_m - v_t \cos \gamma_t$, $v_m \sin \gamma_m - v_t \sin \gamma_t$, as input variables and is trained to output the value of α_i specified by the training set. Using the error backpropagation algorithm with Levenberg-Marquardt learning rule, the neural network controller is trained (see Figure 3).

Then the trained weights and biases contain information from which near-optimal trajectories can be generated in a feedback fashion. Since the training data is composed of optimal trajectories for various scenarios, the target can adapt to changes, both in missile states and its own trajectory. The structure of the neural network is determined as 2 hidden layers, and there are 6 and 4 units in each layer. Sigmoidal functions are used in activation functions of hidden layers and a linear function in the output layer. Figure 4 shows the implementation details of the new evasive maneuver described above. The missile and target information input to the neural-network block, which outputs the near-optimal evasive maneuver.

5 Numerical Examples

Time interval of the missile avoidance problem consists of four phases in general. The first phase is from the initial time to the time when the missile departs from the launcher, the second phase is from the end of the first phase to the guidance start time t_s , the third phase is from t_s to the propellant burnout time t_b and the fourth phase is from t_b to t_f . The first phase is divided into 2 equal intervals, the second into 2 equal intervals, the third into 9 equal intervals and fourth phase into 4 equal intervals for the discretization of the

continuous time optimal control problem. By the way, the missile-target engagement sometimes ends before the propellant burns out and hence the third phase described above ends at t_f . In that case, the final third phase is divided into 15 equal intervals.

The F-4C fighter aircraft considered in [5] is used as a target aircraft. The aerodynamic data are given as a function of Mach number in tabular form and the maximum thrust data are given as a function of Mach number and altitude in tabular form. For optimization, both data are represented by continuous curve. The aerodynamic data are interpolated by cubic spline. The maximum thrust data at each altitude shown in table are first fitted by a fourth order polynomial which is a function of Mach number. The maximum thrust at an altitude is obtained by interpolating linearly the data calculated from the polynomial representation of the maximum thrust. The maximum angle of attack and the maximum load factor are assumed to be 15 deg and 7g, respectively. The fighter aircraft is assumed to weigh 15870Kgf and fly in level with 280m/sec from right to left in Figure 1 initially.

The aerodynamic coefficients and parameters of the ground-to-air missile considered here are shown in Figure 5 and Table 1. The aerodynamic coefficient C_X consists of C_{X_0} and C_{X_b} :

$$C_X = \begin{cases} C_{X_0} & : \text{ before burnout} \\ C_{X_0} + C_{X_b} & : \text{ after burnout} \end{cases}$$

The standard atmosphere model [15] is used to compute the density and the speed of sound at a given altitude. It is assumed that the missile is fired at sea level along the initial line-of-sight to the target aircraft.

Evasive maneuvers are studied on various initial positions of target aircraft. Figure 6 illustrates the optimal evasive maneuvers of target flying at 1000m altitude, i.e, $h_t(0) = 1000\text{m}$. For the cases $x_t(0) = 0\text{m}$ and $x_t(0) = 1000\text{m}$ the engagement ends before propellant burns out. Pull-up maneuvers are shown to be optimal against a missile fired at aircraft heading toward missile. However, push-over maneuvers with which the target turns toward missile are optimal against a missile fired to chase aircraft tail. Similar maneuvers are observed as optimal maneuvers for $h_t(0) = 1500\text{m}$ and 1800m.

Table 2 shows miss distances by the optimal evasive maneuvers. Symbol 'o' in figure 7 denotes miss distance shown in Table 2. In initial phase of engagement, the dynamic pressure of the missile is so low that the acceleration produced by missile control surface is very limited. It can be observed from figure 7 that the degradation of the missile maneuverability in initial phase makes the evasive maneuver of the target very effective for a close initial relative distance between the missile and the target. As the initial ground distance is getting farther, the miss distance reduces dramatically.

A neural network described in section 4 is trained on the optimal evasive maneuvers obtained above. Lines

in figure 7 denote the miss distances generated by the target aircraft maneuvered by the neural network controller. Figure 7 shows that the neural network controller produces near-optimal evasive maneuver.

6 Conclusions

In this paper, we considered optimal evasive maneuvers in 2-dimensional vertical plane against a proportionally guided ground-to-air missile. For a ground-to-air missile, dynamic pressure is so low during initial phase after launch that missile control surface could not produce enough lateral acceleration. This characteristic of a ground-to-air missile was embedded in the missile model by limiting the acceleration command to the missile autopilot in order that the missile may not stall. It was shown that the degradation of missile maneuverability in initial phase makes the miss distance very large for the target very close to the missile at initial time. For the aircraft flying at low altitude, pull-up maneuvers were shown to be optimal evasive maneuvers of target aircraft flying at low altitude against a missile fired at an aircraft heading toward missile while push-over maneuver against a missile fired to chase aircraft tail.

A neural network was trained on the optimal evasive maneuvers generated off-line. It was shown that the resulting neural network controller produced near-optimal evasive maneuver.

Acknowledgments

This work was supported by Agency for Defense and Development(ADD) and Automatic Control Research Center(ACRC) at Seoul Nation University. Authors thank to Professor von Stryk for allowing us to use DIRCOL.

References

- [1] Guelman, M., Shinar, J. and Green, A., "Qualitative Study of a Planar Pursuit Evasion Game in the Atmosphere", *Journal of Guidance, Control and Dynamics*, Vol. 13, No. 6, 1990, pp. 1136-1142.
- [2] Ben-Asher, J. and Cliff, E. M., "Optimal Evasion Against a Proportionally Guided Pursuer," *Journal of Guidance, Control and Dynamics*, Vol. 12, No. 4, 1989, pp. 598-601.
- [3] Imado, F. and Miwa, S., "Fighter Evasive Maneuvers Against Proportional Navigation Missile," *Journal of Aircraft*, Vol. 23, No. 11, 1986, pp. 825-830.
- [4] Ong, S. Y. and Pierson, B. L., "Optimal Planar Evasive Aircraft Maneuvers Against Proportional Navigation Missiles," *Journal of Guidance, Con-*

tol and Dynamics, Vol. 19, No. 6, 1996, pp. 1210-1215.

- [5] Bryson, A. E. Jr., Desai, M. N., and Hoffman, W. C., "Energy-State Approximation in Performance Optimization of Supersonic Aircraft," *Journal of Aircraft*, Vol. 6, No. 6, 1969, pp. 481-488.
- [6] Blacklock, J. H., *Automatic Control of Aircraft and Missiles*, 2nd Ed. John Wiley & Sons Inc., 1991.
- [7] von Stryk, O., *User's Guide for DIRCOL ver. 1.2*, Technische Univ. Munchen, Aug., 1997.
- [8] von Stryk, O., "Numerical Solution of Optimal Control Problems by Direct Collocation", in *Optimal Control - Calculus of Variations, Optimal Control Theory and Numerical Methods*, International Series of Numerical Mathematics III, pp. 129-143.
- [9] Hargraves, C. R. and Paris, S. W., "Direct Trajectory Optimization Using Nonlinear Programming and Collocation," *Journal of Guidance and Control*, Vol. 10, No. 4, 1987, pp. 338-342.
- [10] Enright, P. J. and Conway, B. A., "Discrete Approximation to Optimal Trajectories Using Direct Transcription and Nonlinear Programming," *Journal of Guidance, Control and Dynamics*, Vol. 15, No. 4, 1992, pp. 994-1002.
- [11] Gill, P. E., Murray, W., Saunders, M. A. and Wright, M. H., *User's Guide for NPSOL (Version 4.0)*, Report SOL 86-2, Department of Operations Research, Stanford University, 1986.
- [12] Haykin, S., *Neural Networks, A Comprehensive Foundation*, 2nd Edition, Prentice-Hall, New Jersey, 1999.
- [13] Hornik, K., Stinchcombe, M., and White, H., "Multilayer feedforward networks are universal approximators," *Neural Networks*, Vol. 2, pp 359-366, 1990.
- [14] Song, E. J., Lee, H., and Tahk, M. J., "On-line suboptimal midcourse guidance using neural networks," *Proc. of the 35th SICE Annual Conference*, Tottori Univ., Japan, pp 1313-1318, 1996.
- [15] Houghton, E. L. and Brock, A. E., *Aerodynamics for Engineering Students*, 2nd Edition, Edward Arnold Ltd., 1970.

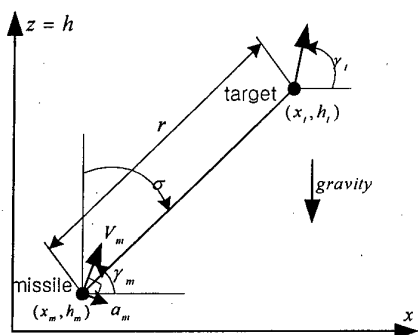


Figure 1: Relative geometry

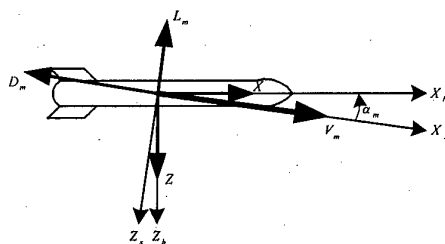


Figure 2: Axes of missile

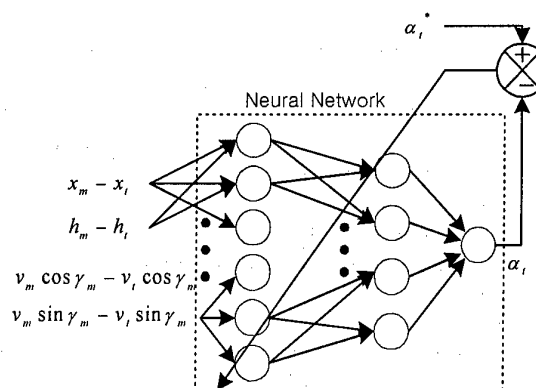


Figure 3: Training of neural network controller

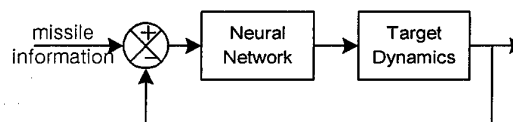


Figure 4: Guidance loop using neural network

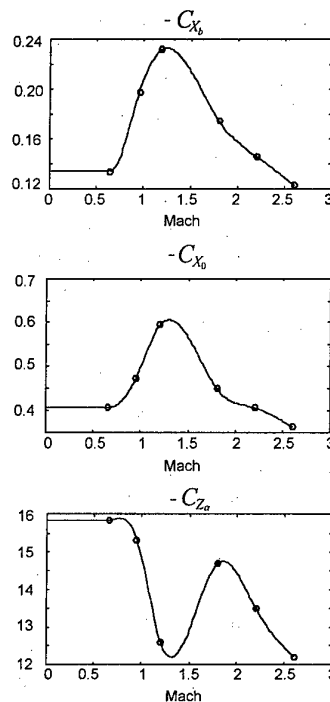
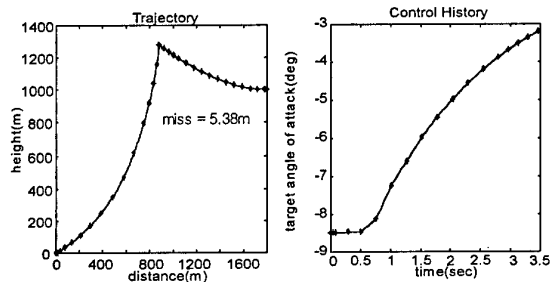
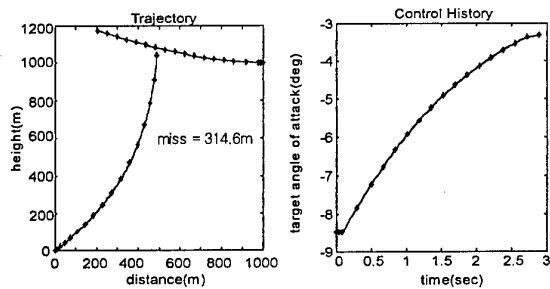


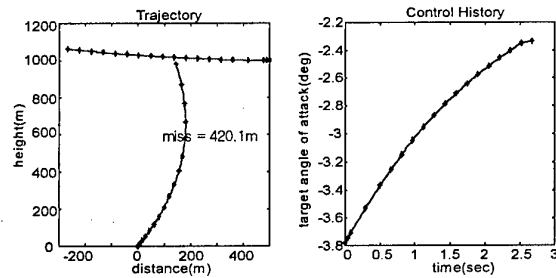
Figure 5: Aerodynamic coefficients of missile



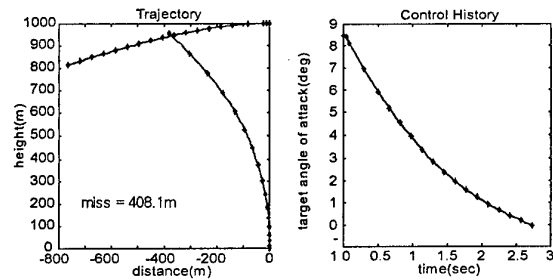
(a) $x_i(0)=1800\text{m}$



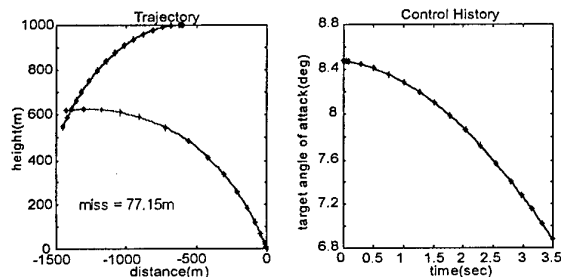
(b) $x_i(0)=1000\text{m}$



(c) $x_i(0)=500\text{m}$



(d) $x_i(0)=0\text{m}$



(e) $x_i(0)=-600\text{m}$

Figure 6: Evasive maneuvers

$m_{m0} = 77.4\text{Kg}$	$N = 4$
$\bar{c} = 9.5\text{Kg/sec}$	$\tau_m = 0.1\text{sec}$
$T_{max} = 22174\text{N}$	$a_{max} = 40g$
$t_b = 2.8\text{sec}$	$t_s = 0.5\text{sec}$
$\alpha_{m_{max}} = 20\text{deg}$	$S_t = 0.1296\text{m}^2$
launcher length = 1m	

Table 1: Missile parameters

$h_i(0) = 1000\text{m}$		$h_i(0) = 1500\text{m}$		$h_i(0) = 1800\text{m}$	
$x_i(0)$ (m)	miss (m)	$x_i(0)$ (m)	miss (m)	$x_i(0)$ (m)	miss (m)
-678	1.39				
-670	9.44				
-650	29.29				
-600	77.15	-445	2.49	-30	2.62
-500	164.30	-400	28.00	-20	5.28
0	408.10	0	184.70	0	10.42
500	420.10	500	229.50	500	66.79
1000	314.60	1000	156.10	800	44.65
1500	137.70	1200	101.20	900	29.23
1600	95.78	1400	34.75	1000	10.11
1700	51.63	1490	1.25	1020	5.86
1800	5.38			1040	1.48

Table 2: Miss distances

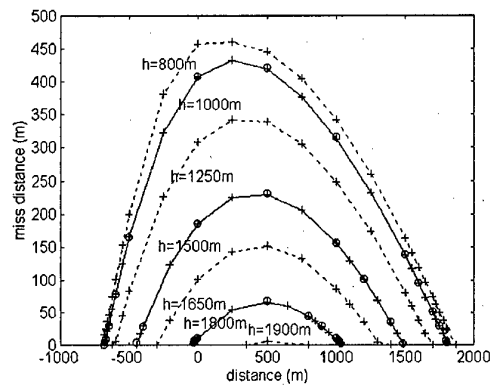


Figure 7: Miss distances

Effective Filtering of Target Glint

Taek Lyul Song*, and Dong Gwan Lee**

Hanyang University

Dept. of Control and Instrumentation Engineering

Sa 1 Dong 1271, Ansan, Kyunggido, 425-791, Korea

Key Words: Guidance and Control, Glint Filtering

ABSTRACT

In this paper, an effective filter structure is suggested for filtering of target glint in active homing engagements of a ship to ship missile. The proposed filter has decoupled range and angle channels so that it has a sound mathematical basis as well as computational efficiency as applied to the IMM algorithm. The proposed algorithm in conjunction with an impact angle control law is tested by a series of simulation runs and it is shown to have superior performance compared with the other filter structures.

I. INTRODUCTION

It is known that when tracking large targets at short ranges, tracking accuracy may be affected severely without proper filtering of target glint in active radar homing engagements. Glint noise is generated by changes in the target aspect angle relative to the radar beam, and it produces target angle fluctuations due to the random wandering of the center of the radar reflecting beam which degrade tracking accuracy.

Mathematical modeling of glint noise has been studied by several researchers. Among them, [1] suggests that glint noise is non-Gaussian and it is the mixture of two normal distributions, each with zero-mean and fixed variance. The occurrence probabilities of two normal noises are different. Glint noise as the mixture of a Gaussian noise and heavy-tailed Laplacian outliers is proposed in [2] and a minimum variance filter using the Masreliez's algorithm is used for the non-Gaussian glint noise. Nonlinear radar measurement equations are linearized to represent the measurements as the sum of Gaussian state variables and glint noises. The interacting multiple model (IMM) algorithm [4] with two extended Kalman filters (EKF) is proposed for glint noise filtering in [3]. The first EKF is matched to the mode of Gaussian measurement noise and the second EKF is matched to the mode of Laplacian measurement noise. Linear system dynamics are established in Cartesian coordinates where the measurements are nonlinear functions of state variables. Besides using the EKF, [3] uses pseudomeasurements obtained by converting the original nonlinear spherical measurements into linear measurements [5]. The pseudomeasurements used in the mode probability update of the IMM algorithm are corrupted by biased and correlated state dependent noises. The state dependent noises have

statistical characteristics different from the original measurement noises. Therefore, it is not justified in [3] to use the assumptions in the mode probability calculation that the state dependent noises are uncorrelated and independent of Gaussian prior, and that the nature of the state dependent noises is not changed by the conversion.

II. SYSTEM DESCRIPTIONS

A. Glint Model

From the empirical approach, [1] shows that the glint noise is non-Gaussian and heavy-tailed, and that the glint can be modeled as the mixture of a Gaussian noise with moderate variance and a Gaussian noise with large variance. It is proposed in [2] that the heavy-tailed behavior of the glint noise is more suitably modeled as the mixture of a Gaussian noise with high occurrence probability and a Laplacian noise with low occurrence probability. The probability density function of the glint noise can be written as

$$f(v) = (1 - \varepsilon)f_g(v) + \varepsilon f_l(v) \quad (1)$$

where ε is the occurrence probability of the Laplacian noise and the subscripts of the function f , g and l stand for Gaussian and Laplacian, respectively, i.e.,

$$\begin{pmatrix} f_g(v) \\ f_l(v) \end{pmatrix} = \begin{pmatrix} \frac{1}{\sqrt{2\pi}\sigma_g} \exp\left(-\frac{v^2}{2\sigma_g^2}\right) \\ \frac{1}{2\eta} \exp\left(-\frac{|v|}{\eta}\right) \end{pmatrix} \quad (2)$$

Laplacian parameter η is related to the Laplacian noise variance sigma as $2\eta^2 = \sigma_l^2$. The IMM algorithm using two EKFs is proposed in [3] to filter the glint noise with the above characteristics.

B. Proposed Filter Structure

A modified version of the channel-decoupled filter of [6] is used in the IMM algorithm. The state variables defined in the polar coordinates are separated into range and angle channel variables. The missile-target engagement configuration is depicted in Fig. 1 where the target is tracked continuously by

* Associate Professor

** Graduate student

an active seeker on board the missile.

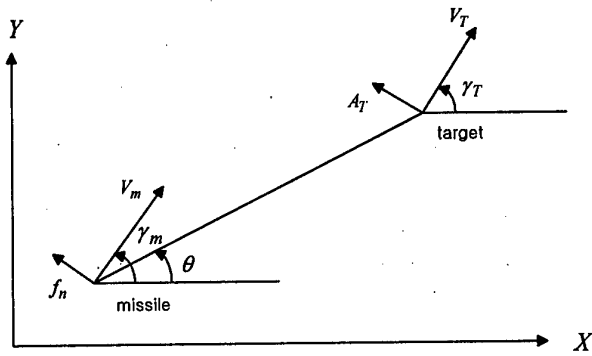


Fig. 1 Missile-target engagement configuration

In Fig. 1, r denotes the missile-to-target relative range and θ denotes the missile-to-target line-of-sight (LOS) angle formed by the seeker.

The state vector of the range channel x_r under the assumption of a zero-lag autopilot is composed of r , \dot{r} , and A_{T_r} , target acceleration in the relative range direction. The continuous dynamics employing the Singer model [8] for target acceleration are represented as

$$\dot{x}_r = \begin{pmatrix} 0 & 1 & 0 \\ \theta^2 & 0 & 1 \\ 0 & 0 & -\frac{1}{\tau} \end{pmatrix} x_r + \begin{pmatrix} 0 \\ -1 \\ 0 \end{pmatrix} A_{m_r} + \begin{pmatrix} 0 \\ 0 \\ \frac{1}{\tau} \end{pmatrix} \omega_r \quad (3)$$

where A_{m_r} is missile acceleration in the relative range direction and ω_r is a white Gaussian process noise with zero-mean and power spectral density of $2\tau\sigma_{A_r}^2$. Note that $\sigma_{A_r}^2$ is the assumed variance of the target acceleration and τ is the correlation time-constant of target maneuver. Similarly, the angle channel dynamics can be described by

$$\dot{x}_\theta = \begin{pmatrix} 0 & 1 & 0 \\ 0 & -\frac{2\dot{r}}{r} & \frac{1}{r} \\ 0 & 0 & -\frac{1}{\tau} \end{pmatrix} x_\theta + \begin{pmatrix} 0 \\ -\frac{1}{r} \\ 0 \end{pmatrix} A_{m_\theta} + \begin{pmatrix} 0 \\ 0 \\ \frac{1}{\tau} \end{pmatrix} \omega_\theta \quad (4)$$

where $x_\theta = (\theta, \dot{\theta}, A_{T_\theta})^T$, A_{m_θ} and A_{T_θ} represent missile and target accelerations perpendicular to the relative range direction respectively, and ω_θ is a white Gaussian noise with zero-mean and power spectral density of $2\tau\sigma_{A_\theta}^2$.

The measurements from the active seeker are noise-corrupted relative range and angle information such as

$$z_r = H x_r + v_r \quad (5)$$

and

$$z_\theta = H x_\theta + v_\theta \quad (6)$$

where $H = (1, 0, 0)$ and v_r and v_θ are independent measurement noises and each noise can be modeled as the

mixture of a Gaussian noise and Laplacian noise satisfying the probability density function of (1).

For glint noise filtering, the IMM algorithm [4] is applied to each channel so that each channel requires two filters based on two modes of operation: one with a Gaussian measurement noise (M^1) and the other with a Laplacian measurement noise (M^2). The Kalman filter based on M^2 is considered to be a minimum mean square error (MMSE) estimator rather than a minimum variance estimator since the estimates are not conditional means [9].

Probability of M^j , $j=1, 2$ at $t=k$ can be obtained from the Bayesian formula [4, 9] as

$$\Pr(M_k^j | Z_k) = \frac{f(z_k | M_{k-1}^j, Z_{k-1}) \sum_{i=1}^2 \pi_{ji} \Pr(M_{k-1}^i | Z_{k-1})}{\sum_{j=1}^2 f(z_k | M_{k-1}^j, Z_{k-1}) \sum_{i=1}^2 \pi_{ji} \Pr(M_{k-1}^i | Z_{k-1})} \quad (7)$$

where π_{ji} is the transition probability from M^i at $t=k-1$ to M^j at $t=k$. With the above definition, the mode transition probability matrix composed of π_{ji} 's becomes the transpose of the mode transition probability matrix defined in [3]. The probability density functions of the measurements z_r of (5) and z_θ of (6) conditioned on M^1 and the prior observations $Z_{k-1} = \{z_1, z_2, \dots, z_{k-1}\}$ needed in the mode probability update step can be obtained as

$$\begin{pmatrix} f(z_r | M^1, Z_r) \\ f(z_\theta | M^1, Z_\theta) \end{pmatrix} = \begin{pmatrix} N(z_r; H \bar{x}_r^{(1)}, H \bar{P}_r^{(1)} H^T + \sigma_{r_s}^2) \\ N(z_\theta; H \bar{x}_\theta^{(1)}, H \bar{P}_\theta^{(1)} H^T + \sigma_{\theta_s}^2) \end{pmatrix} \quad (8)$$

where the subscript k and $k-1$ indicating the time step are omitted, and $\sigma_{r_s}^2, \sigma_{\theta_s}^2$ are variances of the measurement noises v_r and v_θ under the assumption of M^1 , respectively. Note that $\bar{x}^{(1)}$ and $H \bar{P}^{(1)} H^T$ for the range and the angle channels represent mean and variance of the Gaussian prior under M^1 . The convolution of the Gaussian prior and the Laplacian measurement noise is required to obtain the probability density functions of the measurements z_r and z_θ based on M^2 . After some work, one obtains for both z_r and z_θ ,

$$f(z | M^2, Z) = \frac{1}{2\eta} e^{\frac{\sigma^2}{2\eta^2}} \left[e^{-\frac{z-\bar{x}_1}{\eta}} G\left(-\frac{z-\bar{x}_1-\frac{\sigma^2}{\eta}}{\sigma}\right) + e^{\frac{z-\bar{x}_1}{\eta}} G\left(-\frac{z-\bar{x}_1+\frac{\sigma^2}{\eta}}{\sigma}\right) \right] \quad (9)$$

where \bar{x}_1 and σ^2 are defined as $H \bar{x}^{(2)}$ and $H \bar{P}^{(2)} H^T$ representing mean and variance of the Gaussian prior calculated under M^2 . The standard normal distribution function G in (9) can be obtained from

$$G(\alpha) = \int_{-\infty}^{\alpha} \frac{1}{\sqrt{2\pi}} \exp\left(-\frac{x^2}{2}\right) dx \quad (10)$$

The above result can be used for the both range and angle channels with proper parameters.

C. EKF Approach

If linear system dynamics and nonlinear measurement equations are used to formulate target tracking as [3], an EKF could be a practical candidate used to estimate the target states. Unlike the friendly target tracking example of [3] where the target accelerations are assumed to be known to the tracker, active homing engagements treated in this paper do not allow this situation. The six-element state vector x under the assumption of a zero-lag autopilot is composed of missile-to-target relative position, relative velocity, and target acceleration vectors in Cartesian coordinates. The continuous system dynamics including the Singer model for target accelerations are represented by

$$\dot{x} = A x + B A_m + G \omega \quad (11)$$

$$A = \begin{pmatrix} 0 & I_2 & 0 \\ 0 & 0 & I_2 \\ 0 & 0 & -\frac{1}{\tau} I_2 \end{pmatrix}, \quad B = \begin{pmatrix} 0 \\ -I_2 \\ 0 \end{pmatrix}, \quad G = \begin{pmatrix} 0 \\ 0 \\ \frac{1}{\tau} I_2 \end{pmatrix}$$

where $x = (X, Y, \dot{X}, \dot{Y}, A_{Tx}, A_{Ty})^T$, $A_m = (A_{mx}, A_{my})^T$ and the process noise $\omega = (\omega_X, \omega_Y)^T$ is a white Gaussian noise vector with zero-mean and power spectral density of $2\sigma_{A_r}^2 I_2$.

Nonlinear measurements from the active seeker are represented as

$$\begin{pmatrix} z_r \\ z_\theta \end{pmatrix} = \begin{pmatrix} \sqrt{X^2 + Y^2} + v_r \\ \tan^{-1} \frac{Y}{X} + v_\theta \end{pmatrix} \quad (12)$$

where v_r and v_θ are independent measurement noises and each noise can be modeled as the mixture of a Gaussian noise and a Laplacian noise as (1). Detailed explanation of the EKF as applied to the IMM algorithm is omitted for brevity.

III. SIMULATION RESULTS

A series of Monte Carlo simulation runs is carried out to analyze performance of glint noise filtering in radar homing engagements of a ship to ship missile. Performance of the IMM algorithm using the proposed filter structure is compared with those of the IMM algorithm using the EKFs and single channel-decoupled filters based on M^1 and M^2 .

The missile dynamics used in this planar engagement study is expressed by

$$\begin{pmatrix} \dot{V}_m \\ \dot{X}_m \\ \dot{Y}_m \\ \dot{\gamma}_m \end{pmatrix} = \begin{pmatrix} -\lambda V_m \\ V_m \cos \gamma_m \\ V_m \sin \gamma_m \\ f_n / V_m \end{pmatrix} \quad (13)$$

where V_m , X_m , Y_m , γ_m and f_n represent missile speed, X -position, Y -position, flight path angle and lateral acceleration respectively as depicted in Fig. 1. The simulation scenario

used in this study is the same as [1] and is omitted for brevity.

Initial probabilities for M^1 and M^2 for the IMM algorithm are 0.8 and 0.2, respectively while the mode transition probability matrix satisfies

$$\pi_{ij} = \begin{bmatrix} 0.8 & 0.8 \\ 0.2 & 0.2 \end{bmatrix} \quad (14)$$

The variances of the Gaussian measurement noises are $\sigma_r^2 = (5m)^2$ and $\sigma_\theta^2 = (0.0025 \text{ rad})^2$, respectively while the variances of the Laplacian noises are calculated from

$$\sigma_{r_l} = C \sigma_{r_g}, \quad \sigma_{\theta_l} = C \sigma_{\theta_g} \quad (15)$$

where C is chosen among $\{\sqrt{10}, 6.7, 10\}$ depending on the scenario. The occurrence probability of the glint noise ε is 0.2.

Figs. 2 shows the combined estimates of the target X -position and calculated from the both algorithms, and the proposed filter structure shows better performance. In this case $C = 6.7$ is used for the glint noise variances. The combined estimates of the target X -acceleration in Fig. 3 indicate that the proposed filter has superior performance in estimating target acceleration. Similar results can be seen from the estimates of the Y -axis target state variables. Table I is a summary of 25 runs of Monte Carlo simulation carried out to evaluate the performance of the impact-angle-controlled missile at the final engagement phase. The IMM algorithm with the channel-decoupled filter structure, a single filter matched to the Gaussian measurement noises, a single filter matched to the Laplacian noises, and the IMM algorithm with the EKF structure are employed for target state estimation. It can be seen that the IMM algorithms give superior guidance performance in miss distance and impact angle at the final engagement phase over the single filters in the presence of target glint. The IMM algorithms show similar performance for different glint noise variances while the single filters show deteriorated performance in both miss distance and impact angle as the glint noise variance increases. Comparing the two IMM algorithms, the IMM algorithm with the proposed filter structure shows better performance in estimating the target state variables whereas it shows similar guidance performance at the final phase. However, the proposed filter requires less memories and computational burden in the filtering algorithm as shown in the previous section. Moreover, the mode probability update step of the IMM algorithm is much simpler due to the decoupled range and angle channels indicating that the proposed algorithm shows excellent performance and computational efficiency.

IV. CONCLUSIONS

The results of this study indicate that the IMM algorithms give superior guidance performance over the single filters at the final engagement phase. The IMM algorithm using the proposed filter structure shows superior performance compared with the IMM algorithm using the EKFs.

Table I.

Results of simulation at the final phase

Filter structure glint noise variance		IMM (proposed)	IMM (EKF)	Single filter with σ_g^2	Single filter with σ_t^2
$\sigma_t = \sqrt{10}\sigma_g$	Miss distance	3.142557	3.301063	3.269154	3.419639
	Impact angle	44.48786	46.60895	44.60991	44.08031
$\sigma_t = 6.7\sigma_g$	Miss distance	2.853402	3.164966	4.98823	4.309562
	Impact angle	44.51585	46.57057	44.03856	41.90776
$\sigma_t = 10\sigma_g$	Miss distance	3.112393	3.1279	8.753103	5.557068
	Impact angle	44.56748	46.67002	42.32366	40.53528

Moreover, the proposed filter structure is more efficient in computational procedures of the filtering algorithm and of the mode probability update step of the IMM algorithm due to the decoupled range and angle channels. It is also shown that the proposed filter has a firm and sound mathematical basis for the mode probability update step of the IMM algorithm whereas the EKF needs excessive assumptions lacking justification.

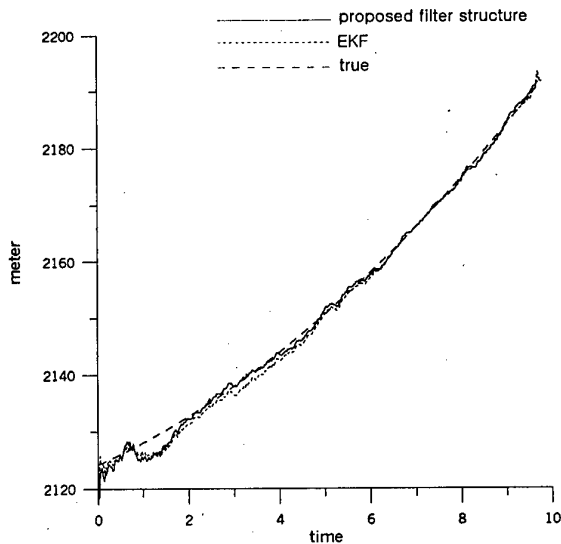


Fig. 2 True and estimated target X-position

References

- [1] Hewer, G. A., Martin, R. D., and Zeh, J. "Robust preprocessing for Kalman filtering of glint noises," IEEE Transactions on Aerospace and Electronic Systems, Vol. 23, No. 1 (Jan. 1987), 120-128.
- [2] Wu, W., "Target tracking with glint noise" IEEE Transactions on Aerospace and Electronic Systems, Vol. 29, No. 1 (Jan. 1993), 174-185.
- [3] Daeipour, E., and Bar-Shalom, Y., "An interacting multiple model approach for target tracking with glint noise," IEEE Transactions on Aerospace and Electronic Systems, Vol. 31, No. 2 (Apr. 1994), 706-715.
- [4] Blom, H. and Bar-Shalom, Y., "The interacting multiple model algorithm for systems with Markovian switching coefficients," IEEE Transactions on Automatic Control, Vol. 33, No. 8, (Aug. 1988), 780-783.
- [5] Lerro, D., and Bar-Shalom, Y., "Tracking with debiased consistent converted measurements versus EKF," IEEE Transactions on Aerospace and Electronic Systems, Vol. 29, No. 3 (Jul. 1993), 1015-1022.
- [6] Pearson, J. B., and Stear, E. B., "Kalman filter applications in airborne radar tracking," IEEE Transactions on Aerospace and Electronic Systems, Vol. 10, No. 3 (May 1974), 319-329.
- [7] Song, T. L., Shin, S. J., and Cho, H., "Impact angle control for planar engagements," Proceedings of the second ASCC, Jul. 1997, Seoul, III-23-III-26, also to appear in IEEE Transactions on Aerospace and Electronic Systems, Vol. 35, No. 4 (Oct. 1999).
- [8] Singer, R. A., "Estimating optimal tracking filter performance for manned maneuvering targets," IEEE Transactions on Aerospace and Electronic Systems, Vol. 6, No. 4 (Jul. 1970), 473-483.
- [9] Jazwinski, A. H., Stochastic Processes and Filtering Theory, Academic Press, New York and London, 1970.

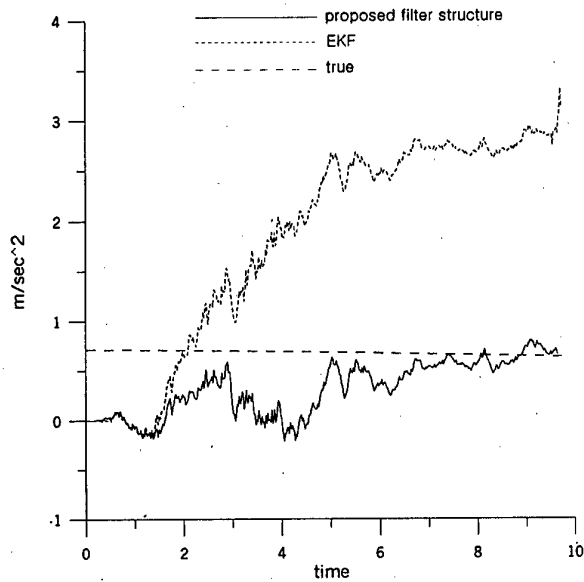


Fig. 3 True and estimated target X-acceleration

Maneuvering Target Tracking Using Input Estimation with Multiple Model

Sang Jin Shin *, and Taek Lyul Song **

Hanyang University

Dept. of Control and Instrumentation Engineering

Sa Dong 1271, Ansan, Kyunggi-do, 425-791, Korea

Keyword: Guidance and Control

Abstract

To increase the performance of maneuvering target tracking, IE/MM algorithm is suggested in this paper. Modeling the unexpected target maneuver as hypothesized multiple models and incorporating test statistics to detect the maneuver onset time into design of an adaptive input estimator produce an estimation scheme that greatly reduces the large tracking errors commonly induced by an unexpected target maneuver.

1. Introduction

Accurate tracking of target states is very important in modern missile guidance systems and tactical weapons, so that maneuvering target tracking has been an issue for a long time. Many researchers have studied to get the best maneuvering target modeling, since estimation of target states requires appropriate modeling for unknown target dynamics. In [1], target acceleration is assumed as a first order semi-Markov process called the Singer model. In [2], Magill proposes a bank of N parallel Kalman filters which utilize different target maneuver models. This multiple modeling technique has evolved to the Interacting Multiple Model (IMM) algorithm [3], in which the change of the system dynamics is modeled as a Markovian parameter having a transition probability.

Input estimation is another estimation technique which detects whether there exists target maneuver, and if exists, directly estimates the magnitude of the target maneuver. Therefore, in tracking with an input estimation algorithm, it is important to find out the maneuver onset time when the target initiated maneuver though it may be impossible to find out the exact time. Bogler proposes an input estimation algorithm to derive a recursive least square solution based on multiple-model filtering to calculate the input magnitude in [4]. In addition, a hypothesis test to detect the maneuver onset time is proposed to enhance the estimation performance. However, if the estimated maneuver onset time is far from the true one, the algorithm employing a finite window length produces large tracking errors. This motivates the proposed input estimation algorithm of this paper for obtaining the consistent tracking performance even in such a case. The proposed algorithm estimates target states with a noninteracting multiple model approach called the multiple model adaptive estimation (MMAE) method [8,9] that utilizes a bank of Kalman filters based on switching maneuver models. The maneuver detection and estimation performance is evaluated using computer simulations.

* Graduate student

** Associate Professor

2. Input Estimation with Multiple Model

In this section, an efficient filter algorithm is established based on the multiple model estimation with two independent mode sets. One mode set is related to the magnitude of target acceleration as is used in the MMAE algorithm [8], the other set is related to the starting time of the maneuver as is used in the input estimation algorithm of [4]. Computational complexity of the MMAE algorithm to estimate the target acceleration is greatly reduced by introducing a recursion rule for the relation between the output of the i th hypothesized filter and that of a nominal filter assuming no unknown maneuver. The maneuver onset time is detected by evaluating the test statistics developed from a modified version of the generalized likelihood ratio (GLR) test for finding the most likely onset time within a finite window length. The test statistic is a function of the assumed onset time and it utilizes the combined state estimates developed under the assumption that the target maneuver starts at the assumed onset time. The average delay of the proposed detection scheme is also obtained by a numerical analysis.

2.1 Efficient Computation of the MMAE

In the MMAE algorithm, it is assumed that the system obeys one of a finite number of possible maneuver-related modes or hypotheses. Each filter of a bank of N Kalman filters utilizes a different mode of target acceleration, and each filter operates on the same measurement sequence. Fig. 1 illustrates a schematic diagram of the MMAE.

Consider the one dimensional range tracking problem in which the state variables are composed of position and velocity of a target. Discrete-time system dynamics with sampling interval Δt are described as

$$x_{k+1} = Ax_k + w_k, \quad E[w_k w_j] = \begin{cases} Q_k, & k = j \\ 0, & k \neq j \end{cases} \quad (1)$$

where A is the state transition matrix, and w_k is a process noise vector. If the target initiates the maneuver with a constant acceleration u_k , then the target dynamics are changed to

$$x_{k+1} = Ax_k + Bu_k + w_k \quad (2)$$

The measurement z_k is related to the state vector x_k by

$$z_k = Hx_k + v_k, \quad E[v_k v_j] = \begin{cases} R_k, & k = j \\ 0, & k \neq j \end{cases} \quad (3)$$

The propagation step of the i th Kalman filter based on the i th mode \tilde{H}^i implying that the magnitude of target acceleration is u^i satisfies

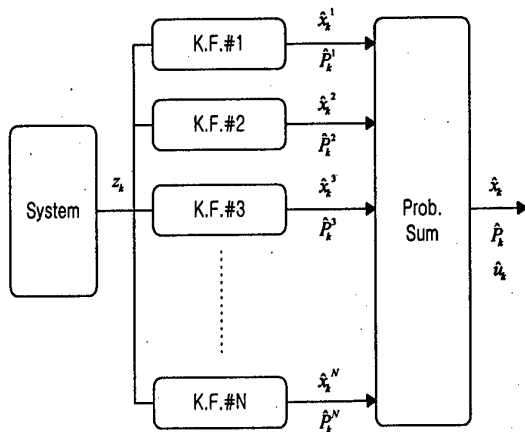


Fig. 1. Schematic diagram of the MMAE.

$$\bar{x}_{k+1}^i = A\hat{x}_k^i + Bu^i \quad (4)$$

$$\bar{P}_{k+1}^i = A\hat{P}_k^i A^T + Q_k \quad (5)$$

where \bar{x}_{k+1}^i and \bar{P}_{k+1}^i are the predicted estimate and the predicted covariance, respectively and where \hat{x}_k^i and \hat{P}_k^i are the updated estimate and the updated covariance.

The measurement update step of the i th Kalman filter requires

$$\hat{x}_k^i = \bar{x}_k^i + K_k^i (z_k - H\bar{x}_k^i) \quad (6)$$

$$K_k^i = \bar{P}_k^i H^T (H\bar{P}_k^i H^T + R_k)^{-1} \quad (7)$$

$$\hat{P}_k^i = (I - K_k^i H) \bar{P}_k^i \quad (8)$$

In order to estimate the target state, the total probability theorem [5] can be used to combine the estimated values, \hat{x}_{k+1}^i 's, $i=1,2,\dots,N$ from the Kalman filter bank. Then the combined target state estimate is expressed as

$$\hat{x}_{k+1} = \sum_{i=1}^N \hat{x}_{k+1}^i \text{Prob}(\tilde{H}_{k+1}^i | Z_{k+1}), \quad (9)$$

where $\text{Prob}(\tilde{H}_{k+1}^i | Z_{k+1})$ is probability mass function based on the hypothesis \tilde{H}^i , Z_{k+1} is the previous observations $\{z_1, z_2, \dots, z_k, z_{k+1}\}$. $\text{Prob}(\tilde{H}_{k+1}^i | Z_{k+1})$ is obtained from the Bayesian formula [5] as

$$\text{Prob}(\tilde{H}_{k+1}^i | Z_{k+1}) = \frac{p(z_{k+1} | \tilde{H}_{k+1}^i, Z_k) \sum_{j=1}^N \text{Prob}(i|j) \text{Prob}(\tilde{H}_k^j | Z_k)}{\sum_{m=1}^N p(z_{k+1} | \tilde{H}_{k+1}^m, Z_k) \sum_{n=1}^N \text{Prob}(m|n) \text{Prob}(\tilde{H}_k^n | Z_k)}, \quad (10)$$

where $\text{Prob}(i|j)$ is the transition probability [8,9] from the mode \tilde{H}^j at $t=k$ to the mode \tilde{H}^i at $t=k+1$. The combined error covariance for \hat{x}_{k+1} is obtained as

$$\hat{P}_{k+1} = \sum_{i=1}^N (\hat{P}_{k+1}^i + \hat{x}_{k+1}^i \hat{x}_{k+1}^{i^T}) \text{Prob}(\tilde{H}_{k+1}^i | Z_{k+1}) - \hat{x}_{k+1} \hat{x}_{k+1}^T. \quad (11)$$

When the measurement z_k is available, the residuals $v_k^1, v_k^2, \dots, v_k^N$ are generated as shown in (6), and used to calculate the probabilities of $\tilde{H}_k^1, \tilde{H}_k^2, \dots, \tilde{H}_k^N$ via (10).

Since all the filters of Fig. 1 use the same measurement at every sampling instant, and the process noise representing the model uncertainty is thought to be identical in all N filters,

the gains of N filters are identical. With this in mind, the filtering algorithm for the i th Kalman filter can be simplified by utilizing the nominal filter algorithm. The measurement update step of the nominal Kalman filter satisfies

$$\hat{x}_k^n = \bar{x}_k^n + K_k^n (z_k - H\bar{x}_k^n) \quad (12)$$

$$K_k^n = \bar{P}_k^n H^T (H\bar{P}_k^n H^T + R_k)^{-1} \quad (13)$$

$$\hat{P}_k^n = (I - K_k^n H) \bar{P}_k^n, \quad (14)$$

whereas the propagation step consists of

$$\bar{x}_{k+1}^n = A\hat{x}_k^n \quad (15)$$

$$\bar{P}_{k+1}^n = A\hat{P}_k^n A^T + Q_k. \quad (16)$$

Let \bar{e}_k^i denote the difference between \bar{x}_k^i and \bar{x}_k^n , then

$$\bar{e}_{k+1}^i = A(I - K_k^n H) \bar{e}_k^i + Bu^i, \quad (17)$$

where $K_k^i = K_k^n$, and $\bar{e}_0^i = 0, i=1,2,\dots,N$. For a recursive algorithm, U_0^{k+1} and V_0^{k+1} are introduced as

$$U_0^{k+1} = AU_0^{k+1} + B, \quad V_0^0 = 0 \quad (18)$$

$$V_0^{k+1} = (I - K_{k+1}^n H)U_0^{k+1}, \quad (19)$$

then the state estimates of the i th filter can be obtained from

$$\bar{x}_k^i = \bar{x}_k^n + U_0^k u^i \quad (20)$$

$$\hat{x}_k^i = \hat{x}_k^n + V_0^k u^i. \quad (21)$$

Substituting the result of (21) into (9), we can obtain the combined estimates as well as the combined covariance of \hat{x}_k as

$$\hat{P}_k = \hat{P}_{k+1}^n + \sum_{i=1}^N \hat{x}_k^i \hat{x}_k^{i^T} \text{Prob}(\tilde{H}_k^i | Z_k) - \hat{x}_k \hat{x}_k^T. \quad (22)$$

The estimated acceleration and its covariance are obtained by using the total probability theorem as

$$\hat{u}_k = \sum_{i=1}^N u^i \text{Prob}(\tilde{H}_k^i | Z_k) \quad (23)$$

$$\hat{P}_{u_k} = \sum_{i=1}^N u^i u^{i^T} \text{Prob}(\tilde{H}_k^i | Z_k) - \hat{u}_k \hat{u}_k^T.$$

With the above algorithm, the amount of computation is reduced drastically since the estimates of every hypothesized filter can be calculated from the nominal filter so that the filtering steps of N filters are replaced by (18)~(21).

2.2 Maneuver Detection

So far, we have developed a computationally efficient multiple model algorithm to estimate the target acceleration under the assumption that the maneuver onset time is known. The algorithm is applied to determine the maneuver onset time by imposing the hypothesis on the possible maneuver events in a finite window length. A modified version of the generalized likelihood ratio test of [6] is established for detecting the onset time. By varying the assumed maneuver time consecutively within the window length, score functions called the test statistics are evaluated with the residuals calculated from the combined estimates of the MMAE algorithm. The maximum value of the test statistics is required to exceed the threshold determined from a predetermined PFA before maneuver is declared and corrected by the estimates of the MMAE algorithm.

After the target maneuver u at $t=k_m$, the residual of

the nominal filter at $t = k$ becomes

$$v_k = HU_k^T u + \tilde{v}_k, \quad (24)$$

where \tilde{v}_k is zero-mean white noise sequence. In order to find the maneuver onset time, a modified version of the GLR test is used with the hypotheses imposed on the maneuver instants. Let θ denote the hypothesized maneuver onset time varying within the window length, the score statistic to be maximized can be written as

$$\frac{\max_{k-L+1 \leq \theta \leq k} p(v|\theta, Z_k)}{p(v|\tilde{H}^0, Z_k)}, \quad (25)$$

where L is the window length, $p(v|\theta, Z_k) = \sum_{i=1}^N p(v|\tilde{H}^i, \theta, Z_k) \text{Prob}(\tilde{H}^i|\theta, Z_k)$, and the estimates of IE/MM proposed in the previous section are used instead of the least squares estimates used in [4] and [6]. By using the monotonic character of the natural logarithm function, (25) becomes

$$J(\theta) = -\frac{1}{2} \sum_{k=\theta}^l (v_k - HU_k^T E[u_i|Z_i, \theta])^T S_k^{-1} (v_k - HU_k^T E[u_i|Z_i, \theta])^T + \frac{1}{2} \sum_{k=\theta}^l v_k^T S_k^{-1} v_k, \quad (26)$$

where $S_k = H\tilde{P}_k H^T + R_k$, and $E[u_i|Z_i, \theta]$ is the estimate of target acceleration at $t=l$ assuming that the target initiated the maneuver at $t=\theta$. To find the threshold satisfying the predetermined PFA with the index of (26) is statistically equivalent to find the threshold γ for $\Delta J(\theta)$ expressed as

$$\Delta J(\theta) = \sum_{k=\theta}^l \frac{HU_k^T E[u_i|Z_i, \theta]}{S_k} v_k. \quad (27)$$

As the statistical property of $\Delta J(\theta)$ is Gaussian, we can obtain threshold γ from a normalized form of $\Delta J(\theta)$, denoted here as $\Delta \bar{J}(\theta)$, by using the error function [7] with a proper PFA . After some mathematical arrangements, we obtain a criterion for maneuver detection with the test statistic as

$$\max_{k-L+1 \leq \theta \leq k} \Delta \bar{J}(\theta) > \gamma, \quad (28)$$

$$\text{where } \Delta \bar{J}(\theta) = \frac{n(\theta)}{d(\theta)}, \quad d(\theta) = \sqrt{\sum_{k=\theta}^l (HU_k^T)^2 / S_k},$$

$$n(\theta) = \sum_{k=\theta}^l (HU_k^T / S_k) v_k, \quad PFA = \int_{\gamma}^{\infty} N(0,1) d\tau.$$

From (28), we know not only the existence of target maneuver but also the maneuver onset time.

2.3 Average Delay and Window Length

To obtain a proper window length, we need to look up how much time it takes to detect target maneuver - delay time or average delay [10].

Recall that the test statistic $\Delta J(\theta)$ in equation (27) is Gaussian with zero-mean under the hypothesis \tilde{H}^0 . If there exists target maneuver at $t = k_m$, mean and variance of test statistic $\Delta J(\theta)$ become

$$m_{k_m+l} = E[\Delta J] = \sum_{k=k_m}^{k_m+l} \frac{(HU_k^T)^2}{S_k} u \quad (29)$$

$$\sigma_{k_m+l} = \sqrt{\sum_{k=k_m}^{k_m+l} \frac{(HU_k^T)^2}{S_k}},$$

where k_m is target maneuver onset time. Let p_{k_m+l} denote the detection probability of target maneuver at $k = k_m + l$, then p_{k_m+l} satisfies

$$p_{k_m+l} = \left(\prod_{i=1}^{l-1} (1 - p_{d_{k_m+i}}) \right) p_{d_{k_m+l}}, \quad (30)$$

$$p_{d_{k_m+l}} = \int_{\gamma_{k_m+l}}^{\infty} N(m_{k_m+l}, \sigma_{k_m+l}^2) d\tau,$$

where γ_{k_m+l} is related with PFA ,

$$PFA = \int_{\gamma_{k_m+l}}^{\infty} N(0, \sigma_{k_m+l}^2) d\tau. \quad (31)$$

After the calculation of p_{k_m+l} , $l=1,2,\dots$, we can obtain the average delay N_d and delay time t_d such as

$$\text{Average delay: } N_d = \lim_{l \rightarrow \infty} \sum_{i=1}^l i \cdot p_{k_m+i} \quad (32)$$

$$\text{Delay time: } t_d = N_d \cdot \Delta t. \quad (33)$$

Because of highly nonlinear terms in calculating the average delay, a numerical analysis is recommended. In Fig. 2, the average delay is depicted. Measurement and process noise variances used in the numerical analysis are $Q=2^2$, $R=8^2$, respectively, and $PFA=0.0001$ is used to set up the threshold γ , and sampling frequency is 20 Hz. From Fig. 2, we can establish the relations between the window length and the target acceleration.

3. Simulation Results

The proposed algorithm is applied to a one-dimensional tracking problem to verify the performance through a series of simulation runs. Initially the target with velocity 200m/sec is located at 2100m apart from the tracker. Measurement and process noise variances used in the simulation study are the same as the one in the previous section. $PFA=0.0001$ is used. The window length L with an assumption that target maneuver would be smaller than $0.5g$ ($g=9.8m/sec^2$) is selected as 40 from Fig. 2 which depicts the average delay expected in the proposed algorithm. The hypotheses of maneuver magnitude are dispersed from $-4g$ to $4g$ with $1g$ interval. If the target executes a constant $2g$ maneuver at $t=10sec$, Figs. 3 and 4 show the estimates of target acceleration evaluated from the proposed algorithm, Bogler's method [4] and a single filter of which states are composed of position, velocity and acceleration with the Singer model [1]. Input estimation methods such as IE/MM and Bogler's method have superior tracking performance over the single filter. However, as shown in Fig. 4, if estimated maneuver onset time is far from true maneuver onset time, the tracking performance of the Bogler's input estimation becomes degraded. However, even in this case the IE/MM algorithm compared with

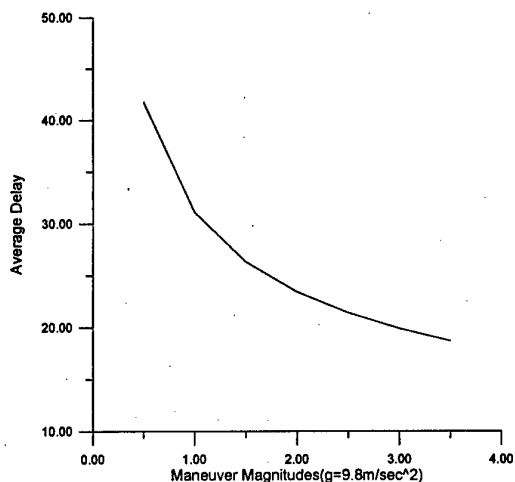


Fig. 2. Average delay versus target maneuver magnitudes

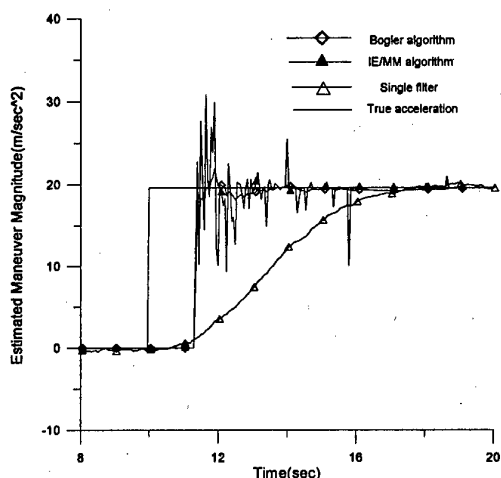


Fig. 3. Estimated target accelerations(1)

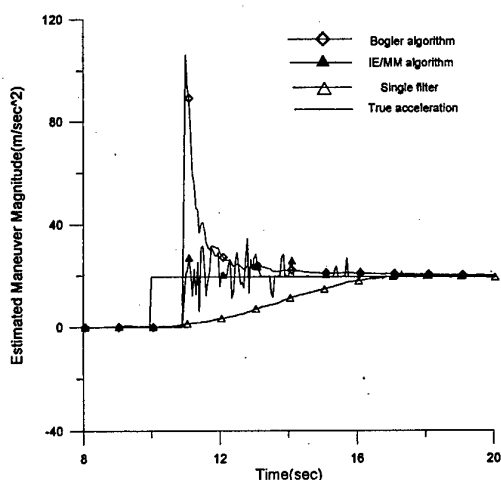


Fig. 4. Estimated target accelerations(2)

Bogler' method is less sensitive in the transient phase, and produces reliable estimates.

4. Conclusions

This paper proposes an input estimation(IE) algorithm based on multiple model adaptive estimation(MMAE). A major difference between the proposed algorithm and the IE algorithm suggested by Bogler lies on the fact that this method utilizes N Kalman filters based on switching maneuver models to estimate target accelerations while Bogler's IE uses the least squares error(LSE) estimates. A method using a nominal Kalman filter is suggested to simplify the state estimation algorithm of the existing MMAE as it is applied to the target acceleration estimation problem. Similar to the Bogler's algorithm, the proposed algorithm consists of a test statistic with a finite window length derived from the generalized probability ratio test suggested by Wilks. The resulting test statistic is a Gaussian-sum type rather than the chi-square distributed form of Bogler's. Average time delay of maneuver detection in the proposed test statistic is analyzed to determine the window length. Simulation studies indicate that the proposed algorithm always produces reliable estimates of target accelerations as well as target maneuver onset time while the Bogler's IE produces large errors when the estimated maneuver onset time is far from the true one such that there is not enough accumulated information, in particular. Ways to shorten computation time for the proposed algorithm are for future studies.

REFERENCES

1. Singer, R. A., "Estimating optimal tracing filter performance for man maneuvering target," IEEE Transactions on Aerospace and Electronic Systems, AES-6, 4, pp 473-483, Jul., 1970.
2. Magill D. T., "Optimal adaptive estimation of sampled stochastic process," IEEE Transactions on Automatic Control, AC-10, pp 434-439, Apr.
3. Blom, H. A.P., and Bar-Shalom, Y., "The interacting multiple model algorithm for systems with Markovian switching coefficients," IEEE Transactions on Automatic Control, AC-33, pp 780-783, Aug., 1988.
4. Bogler, P. L., "Tracking a maneuvering target using input estimation," IEEE Transactions on Aerospace and Electronic Systems, AES-23, 3, pp 298-310, May., 1987.
5. Papoulis, A., "Probability, random variables, and stochastic process," McGraw-Hill, 1991
6. Willsky, A. S. and Jones, H. L., "A generalized Likelihood ratio approach to the detection and estimation of jumps in linear systems," IEEE Transactions on Automatic Control, AC-21, pp 108-112, Feb., 1976.
7. Greenberg, M. D., "Foundations of Applied Mathematics," Prentice-Hall, 1978
8. Moose, R. L., Sistanizadeh, M. K., and Skagfjord, G., "Adaptive estimation for a system with unknown measurement bias," IEEE Transactions on Aerospace and Electronic Systems, AES-22, 6, pp 732-739, Nov., 1986.
9. Maybeck, P. S., and Halon, P. D., "Performance enhancement of multiple model adaptive estimator," IEEE Transactions on Aerospace and Electronic Systems, AES-31, 4, pp 1240-1254, Oct., 1995.
10. Wang, T. C., Varshney, P. K., "A tracking algorithm for maneuvering targets," IEEE Transactions on Aerospace and Electronic Systems, AES-29, 3, pp 910-924, Jul., 1993.

PILOT-INDUCED OSCILLATIONS (PIO): CAUSES AND CORRECTIONS

Brad S. Liebst*

Air Force Institute of Technology
Wright-Patterson AFB, Ohio 45433-7765
USA

Key Words: Handling Qualities, Stability and Control

ABSTRACT

It has been suggested that pilot-induced oscillations (PIO) be classified into three categories: 1) Linear pilot-vehicle system oscillations, 2) Quasi-linear pilot-vehicle system oscillations with actuator rate and/or position saturation, and 3) Nonlinear pilot-vehicle system oscillations with transitions. For most modern recorded PIOs (e.g., YF-22) the PIO records show that actuator rate limiting occurred and therefore are of the Quasi-linear Type 2. This paper demonstrates through simulations the root causes of the Type 2 PIO and then shows how a newly developed nonlinear rate limiter pre-filter (RLPF) and a software rate limit (SWRL) filter are useful in preventing the Type 2 PIO. Lastly motion base simulator and flight test results show that the RLPF/SWRL filter is successful in preventing departure and/or PIO.

1. INTRODUCTION

PIOs have been noted in airplanes since the Wright Brothers. Sometimes these events have led to loss of aircraft, or worse, life. PIOs are often sudden or unexpected. PIOs often occur during high gain events requiring tight control by the pilot; such as landing, air refueling, and target tracking. Predicting PIO is difficult due to the adaptive nature of the pilot. With the advent of highly augmented digital fly-by-wire aircraft, the potential for PIO has increased. There are a variety of reasons (both linear and nonlinear) that cause PIOs. One of the more common factors in PIOs is the presence of actuator rate limiting. The purpose of this study was to develop nonlinear pre-filters that reduce the effects of actuator rate limiting on longitudinal PIO and/or departure.

2. PIO CAUSES

A recent study has suggested that PIOs be classified into three categories: 1) Linear pilot-vehicle system oscillations, 2) Quasi-linear pilot-vehicle system oscillations with actuator rate and/or position saturation, and 3) Nonlinear pilot-vehicle system oscillations with transitions [1].

In Type 1 PIOs the causal factors can be explained by linear theory; the most common factors being excessively high stick gain and excessive lag in the system. The assorted sources of lag include: actuators, digital system time delays, mechanical control and feel systems, and pilot lag. Type 1 PIO is responsible for many older aircraft PIO. A prime

example is the maiden flight of the YF-16 where a PIO occurred and after which significant stick gain reductions were made.

Type 3 PIOs fundamentally depend upon nonlinear transitions in either the pilot or the effective aircraft dynamics. This most commonly occurs whenever the aircraft's flight control system switches modes resulting in a significant change in the vehicle dynamics triggering a PIO response from the pilot. An example of this is the YF-22 accident. The aircraft at low altitude with the afterburners on, immediately after retracting the landing gear, had significantly higher stick gains than intended due to the fact that during the flight test this mode was an unanticipated flight configuration. As is common in PIO accidents, the pilot afterward stated that he did not know he was in a PIO and thought that the oscillations were caused by a system failure of some kind. Figure 1 shows the YF-22 accident time histories for the pilot pitch stick command and the pitch control surface deflection.[1] What is interesting to note is that while the original trigger for the PIO was the mode switching, the PIO actually develops as a Type 2 PIO which is reflected in the sawtooth pattern of rate limiting by the pitch control surface.

The focus of this study was on the Type 2 PIO because almost all modern recorded severe PIOs have shown rate limiting. These include the Space Shuttle, YF-22, C-17, and JAS-39 Gripen. Most large aircraft control surface actuators are hydraulically driven. Of course because of size and weight constraints the hydraulic pumps have a limit to how fast they can drive the actuators. In the F-16, for example, the elevator rate limit is ± 60 deg/sec. Rate limiting has been identified with PIO for two primary reasons. First, it introduces additional phase lag, or delay, between the commanded (dec) and actual (de) control surface actuator position. As is the case in most control systems, this additional phase lag tends to de-stabilize the closed-loop system. The second reason rate limiting has been identified in PIO is the effective reduction in gain. The pilot sees this as a reduction in control effectiveness, so he may compensate with larger inputs making the problem worse. These two rate limiting concepts are shown in figure 2. Figure 2 is the response of a rate limited actuator depicted in figure 4 with the actuator rate saturation set at ± 10 deg/sec and the actuator displacement saturation set at ± 35 deg. The features of rate limiting are clearly: 1) a sawtooth output pattern, 2) the peaks of the sawtooth are phase delayed behind the peaks of the input sine wave, and 3) the peak amplitude of the sawtooth is reduced compared to the input sine wave. It should be noted that Type 2 PIO is considered quasi-linear because the nonlinearity introduces a dominant lag resulting in basically a Type 1 PIO.

* Professor and Head, Dept. of Aeronautics & Astronautics
Email: Bradley.Liebst@afit.af.mil

Table 1 – Aircraft Configurations

Case	Bare Airframe Poles	Kq	K α	A/C Poles With Stability Augmentation	Target Amplitude
A	$-.017 \pm j .074$ $-2.20 \pm j 2.22$	0	0	$-.017 \pm j .074$ $-2.20 \pm j 2.22$	50
B	$-.016 \pm j .079$ $-1.42 \pm j 1.86$.14	.21	as above	50
C	$-.009 \pm j .097$ $-.86 \pm j .084$.24	.51	as above	20
D	$-.017 \pm j .033$ 1.07, -1.67	.34	.61	as above	20

One might ask why older aircraft PIOs were of the Type 1 PIO and more recent aircraft PIOs are of the Type 2. The reason is that many modern aircraft are designed with automatic feedback control stabilizing a marginally stable (or even unstable) bare airframe. This design concept goes by many names, one of the more common being relaxed static stability (RSS). RSS is a two edged sword. On the one hand it enables reductions in tail size which reduces weight and enhances low-observability, but on the other hand the feedback control required to stabilize the system takes up a significant portion of the available rate and position capacity of the control surfaces leaving little for the pilot which exacerbates the PIO tendency. This concept is easily demonstrated with simulation.

Consider a SIMULINK model of the longitudinal dynamics of an aircraft shown in figure 3. The model consists of: bare airframe dynamics, actuator dynamics including displacement and rate saturation (see figure 4), stability augmentation consisting of angle of attack (α) and pitch rate (q) feedback, and a pilot model in which the pilot closes an outer pitch attitude (θ) loop while attempting to track a target which is a square pulse input. The pilot is modeled as a gain and a pure delay. While this is a very simple model for a pilot it will be adequate to demonstrate Type 2 PIO. Regardless of pilot model chosen, it is still a model and cannot define a human being in all circumstances at all times and is therefore a limitation. The interested reader is referred to reference 2 for a detailed examination of mathematical pilot models. Four different aircraft configurations were examined with progressively increasing amounts of stability augmentation. Case A is an aircraft which has no stability augmentation and whose bare airframe has level 1 handling qualities. This is confirmed in figure 5 which shows that Case A short period dynamics are clearly in the center of the "Good" handling qualities region of the figure which was taken from reference 3. For purposes of the remaining discussion the "Good" region of figure 5 will be considered as level 1 handling qualities, the "Acceptable" region as level 2 handling qualities and the combined "Poor" and "Unacceptable" regions as level 3 handling qualities. Case B is an aircraft whose bare airframe has only level 2 (nearly level 1) but with a small amount of stability augmentation is moved to the exact same pole locations of that of Case A and hence the pilot sees a level 1 aircraft. Case C again presents the pilot with the same level 1 dynamics as Case A but does so with increased feedback gains and the bare airframe while stable has degraded to level 3 handling qualities. Case D is an aircraft whose bare airframe is unstable and requires significant stability augmentation to bring it to the level 1 dynamics of Case A. Table 1 lists the aircraft poles with and without stability

augmentation, the feedback gains, and the amplitude of the target pulse in degrees for the simulations presented in figures 6-9. In all the simulations presented in figures 6-9: the target pulse width was fixed at 0.5 secs, the pilot gain was fixed at 0.17, the pilot delay was fixed at 0.25 seconds, the pilot stick and actuator displacement saturations were fixed at ± 35 degrees, the actuator rate saturation was fixed at ± 60 deg/sec. Since all four cases present the pilot with the same level 1

dynamics (assuming no saturations) all four give nearly identical good results when a small amplitude target pulse of 5 degrees is applied and no significant displacement or rate saturations have occurred. However, for large target amplitudes saturations will occur. Of course, in systems involving a displacement saturation nonlinearity in the forward loop, when the saturation occurs the closed loop system effectively becomes open loop. In our example here open loop would correspond to the bare airframe dynamics which in Cases B and C are significantly different than that of the closed loop system and in Case D drastically different in that it goes from level 1 highly stable dynamics to highly unstable dynamics. This fact along with the fact that rate limiting will add delay and amplitude attenuation even if the displacement limits aren't reached are recipes for potential PIOs.

Let's examine figure 1 again to discuss how Type 2 PIOs quite typically develop. The PIO begins as a small to medium amplitude pilot stick command without displacement saturation but with rate limiting. Then within two or three stick cycles the pilot develops into a bang-bang type input cycling between the stick displacement limits. While in the bang-bang mode the fact that rate limiting is of less importance does not detract from the fact that the PIO onset was clearly triggered by rate limiting.

Let's now turn to the simulation results in figures 6-9 to see if our math model correctly reproduces the measured behavior of figure 1. The Case A results provided in figure 6 show that as expected if the bare airframe is level 1 and no stability augmentation is required that the pilot doesn't PIO and the response is similar to the small amplitude response. Case B results are provided in figure 7. We see that for Case B the pilot still provides good control with no PIO, however, the response is somewhat worse in terms of track error because of the fact that the bare airframe dynamics are degraded compared to that of Case A. As an aside since the equations of motion are nonlinear when saturations are included it is possible to drive Cases A and B unstable given a large (but unrealistic) enough target pulse. Case C results are provided in figure 8. We see that the pilot develops into the full blown PIO in the same manner as measured in the flight of figure 1. That is a few cycles of progressively larger rate limited pilot inputs followed by a stage in which the pilot is providing full authority stick in a bang-bang limit cycle. Case D of figure 9 shows what happens when the bare airframe is highly unstable after the rate limiting has been instigated by the pilot. In this case the pilot does not transition into a bang-bang limit cycle but rather the aircraft completely departs. This situation described in Case D has been measured in flight and will be further discussed in Section 3 below. [4] It is clear in Cases C and D that much of the capacity of the actuator is taken up by the feedback

control. This can be verified in figures 8 and 9 by comparing the pilot stick command (dp) with the command being sent to the actuator (dec) (which would be the sum of the pilot and the feedback) where it is evident that those two signals are substantially different.

The key to Type 2 PIO prevention appears to be in making sure the onset is never triggered by significantly reducing or eliminating the amount of phase delay and amplitude attenuation introduced by the actuator becoming rate limited. A proposed method to accomplish this is discussed in the next Section.

3. PIO CORRECTIONS

One obvious solution to rate limit driven PIO is to raise the rate limit of the actuator. This is easily demonstrated with our simulation model where all four cases remained stable when the actuator rate saturation was raised to 200 deg/sec. But, raising the actuator rate limit requires bigger and heavier actuators which means a reduction in weight available for payload and hence a reduction in performance. Another obvious solution is to design the bare airframe to have level 1 handling qualities so that only small amounts of feedback are required decreasing the probability that the actuators will saturate. The down side to this fix is that the benefits of RSS are lost. The solution discussed in the remainder of this Section is to develop a controller that reduces or eliminates the added phase delay and amplitude attenuation introduced by the actuator rate limiting.

Even though amplitude attenuation is unavoidable, previous analyses have shown that installing a nonlinear pre-filter before the actuator in an attempt to keep the actuator output closer in phase to the commanded input produced desirable results. [5, 6, 7] If an input signal to an actuator is filtered by taking its derivative, limiting the rate, and then integrating, the output will reverse in phase with the commanded input. However, this process can result in a bias that must be removed. This logic is shown in figure 10. Typical bias development caused by the filter described in figure 10 is shown in figure 11. Various schemes have been tested by previous researchers with little success for bias removal. [4] In addition, when digital differencing is used to accomplish differentiation, noise entering the pre-filter may frequently cause improper logic switching. Again, all previous research in this area was unsuccessful in handling noise. [4] The nonlinear rate limiter pre-filter (RLPF) presented here improves on previous concepts in two ways: 1) removes bias quickly at the rate limit by incorporating a reset integrator, and 2) noise filtering is incorporated for the switching decision. The RLPF switches between the commanded input and the rate limited input, instead of continuously filtering the input. The RLPF attempts to send the commanded input through cleanly whenever possible. In order, to reverse closely in phase, the RLPF looks at not only the first derivative, but also the second derivative to determine if the command is reversing. Although filtering high frequency noise prevents improper switching, the switching decision is delayed due to the noise filter lag. This is counter-productive, but is unavoidable, and is recovered somewhat by using the second derivative information. The RLPF logic is shown in figure 12. In addition to the RLPF another software rate limit filter (SWRL) placed directly after the RLPF in the pilot command path as additional saturation protection. The software rate limit is set below the

actuator rate limit allowing the feedbacks to achieve a greater percentage of the actuator capacity.

Reference 4 gives a detailed report on the test results of the proposed filter for SIMULINK models, tests in the Large Amplitude Multimode Aerospace Simulator (LAMARS), and flight tests in the NF-16D Variable Stability In-flight Simulator Test Aircraft (VISTA) by a USAF Test Pilot School test team. Because space is limited here only one of the over 30 test configurations flown on the LAMARS simulator and only one of the over 30 test configurations flown on the VISTA will be presented. The interested reader is encouraged to examine reference 4 for the remaining SIMULINK, LAMARS, and VISTA results. All configurations were flown by USAF Test Pilot School students, each with over 1300 hours of cockpit time. Steps were always taken to assure the pilots were blind to the configurations flown. For both the LAMARS and VISTA results to be discussed next the aircraft flight tested were similar to that of case D presented in Section 2. For the LAMARS tests, the bare airframe dynamics were unstable with short period poles at $-1.34, 2.27$; and the short period poles with stability augmentation move to $-3.52 \pm j4.81$. Figure 13 shows the results of a LAMARS flight in which the RLPF only is incorporated. The results show that when the RLPF is added to the pilot command path it prevents him from departing. In part b of figure 13 we see the classic sawtooth rate saturation Type 2 PIO without the RLPF in place and in part c we see that the RLPF does an excellent job of reversing in phase with the pilot resulting in the prevention of the PIO. Figure 13 was for an actuator rate limit of 60 deg/sec, however, rate limits as low as 30 deg/sec were tested with RLPF preventing PIO in all cases. Figure 14 shows the results of a VISTA flight in which the RLPF and SWRL are incorporated. For the VISTA tests, the bare airframe dynamics were unstable with short period poles at $-1.34, 2.27$; and the short period poles with stability augmentation move to $-3.25 \pm j3.31$. For the flight configuration shown the pilots always PIO'd or departed without the filters and PIO and/or departure was always prevented with the filter. Again it can be seen in figure 14 that the filters command in-phase reversals and bias removal as designed resulting in PIO prevention. In all of the LAMARS testing and in all but a few of the VISTA tests the RLPF/SWRL filter was able to prevent departure and/or PIO in configurations that were susceptible to departure and/or PIO without the filter.

4. CONCLUSIONS

Three categories of PIO were discussed: 1) Linear pilot-vehicle system oscillations, 2) Quasi-linear pilot-vehicle system oscillations with actuator rate and/or position saturation, and 3) Nonlinear pilot-vehicle system oscillations with transitions. With the advent of highly augmented RSS aircraft, the potential for PIO has increased due to the increased demand placed upon the actuator to accommodate the stability augmentation. This is evident in the fact that most modern recorded PIOs show that actuator rate limiting occurred and therefore are of the Quasi-linear Type 2. To prevent Type 2 PIO a nonlinear rate limiter pre-filter (RLPF) and a software rate limit (SWRL) filter were developed to protect aircraft from closed loop instability caused by excess phase lag induced by actuator rate limiting. The filters provide nonlinear logic that reverses closely in phase with an

input which in turn reduces the phase lag induced by actuator rate limiting and thereby preventing the onset of a PIO. The proposed method improves on previous designs in two ways: 1) effectively removes bias provided the rate limit is not set extremely low, and 2) handles noise effectively. Computer simulation, motion based piloted simulation, and flight tests in the VISTA NF-16D incorporating the RLPF/SWRL filter were accomplished. The RLPF/SWRL filter was able to prevent departure and/or PIO in the vast majority of flight configurations that were susceptible to departure and/or PIO without the filter.

REFERENCES

1. Klyde, D., McRuer, D., and Myers, T., Unified Pilot-Induced Oscillation Theory, Volume I: PIO Analysis With Linear and Nonlinear Effective Vehicle Characteristics, Including Rate Limiting, Flight Dynamics Directorate, Wright-Patterson AFB, WL-TR-96-3028, December 1995.
2. McRuer, D., Clement, W., Thompson, P., and Magdaleno, R., Minimum Flying Qualities, Volume II: Pilot Modeling For Flying Qualities Applications, Flight Dynamics Laboratory, Wright-Patterson AFB, WRDC-TR-89-3125, January 1990.
3. O'Hara, F., "Handling Criteria", Journal of The Royal Aeronautical Society, vol. 71, no. 676, pp. 271-291, 1967.
4. Chapa, Michael, A Nonlinear Pre-Filter To Prevent Departure and/or Pilot-Induced Oscillations (PIO) Due To Actuator Rate Limiting, MS Thesis, AFIT/GAE/ENY/99M-01. Graduate School of Engineering, Air Force Institute of Technology (AU), Wright-Patterson AFB OH, March 1999.
5. A'Harrah, R., "An Alternate Control Scheme For Alleviating Aircraft-Pilot Coupling," Proceedings of the AIAA Guidance and Control Conference, Scottsdale AZ, 1-3 August 1994.
6. Deppe, P., Chalk, C., and Shafer, M., Flight Evaluation of An Aircraft With Side and Centerstick Controllers an Rate-Limited Ailerons, Final Report No. 8091-2, Advanced Technology Center, Calspan Corporation, Buffalo NY, April 1994.
7. Koper, J., An Approach For Compensating Actuator Rate Saturation, Interim Report No. NADC-87120-60, Air Vehicle and Crew Systems Technology Department, Naval Air Development Center, Warminster PA, August 1987.

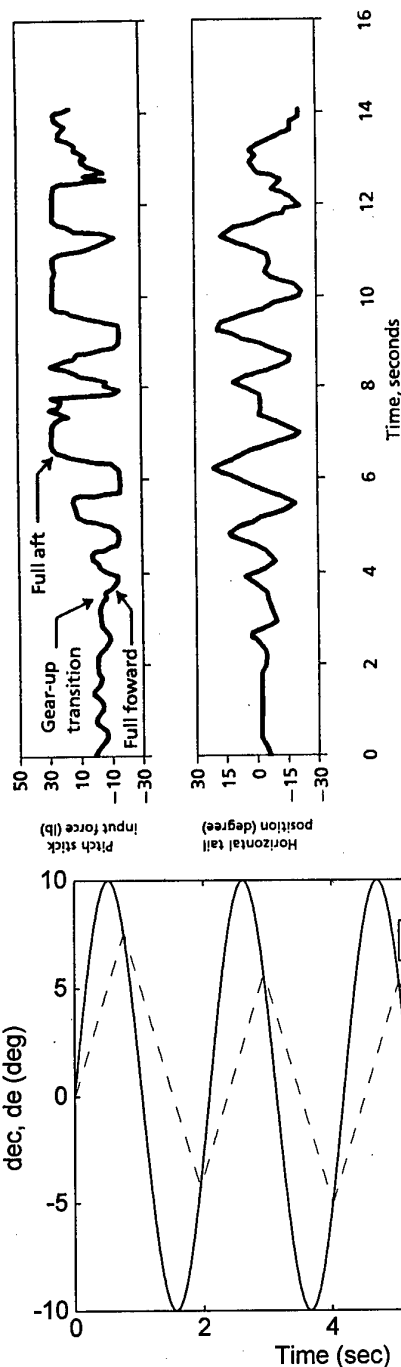


Figure 1 - YF-22A Accident Time History.

Figure 2 - Example Time History of Rate Limiting.

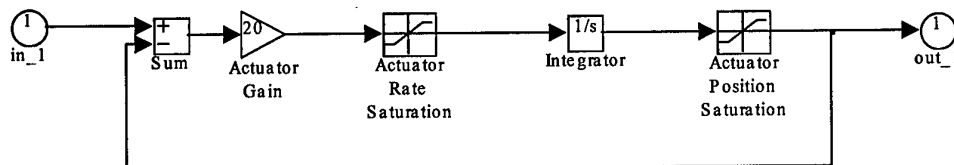


Figure 4 - Simulink Model of Actuator.

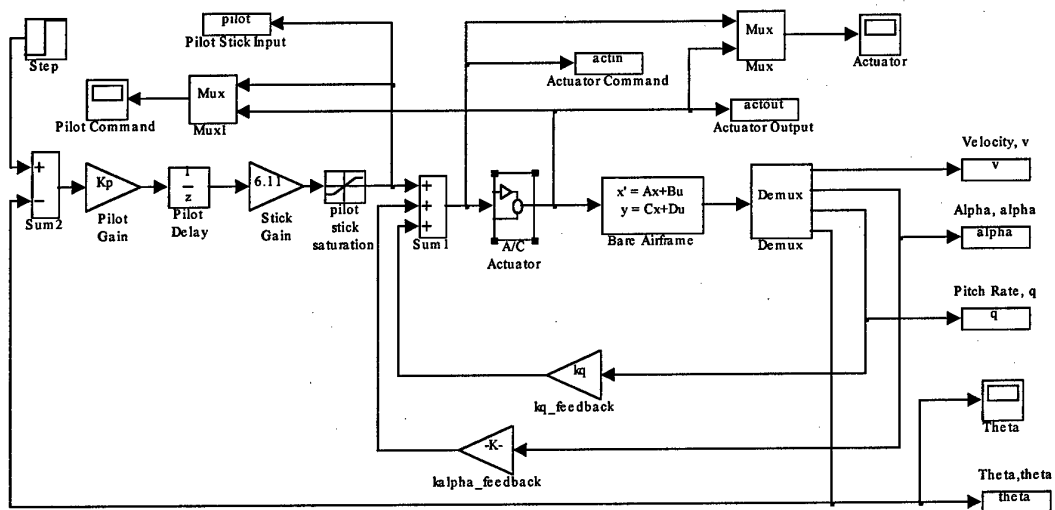


Figure 3 – Simulink A/C-Pilot Model to Demonstrate Type 2 PIO.

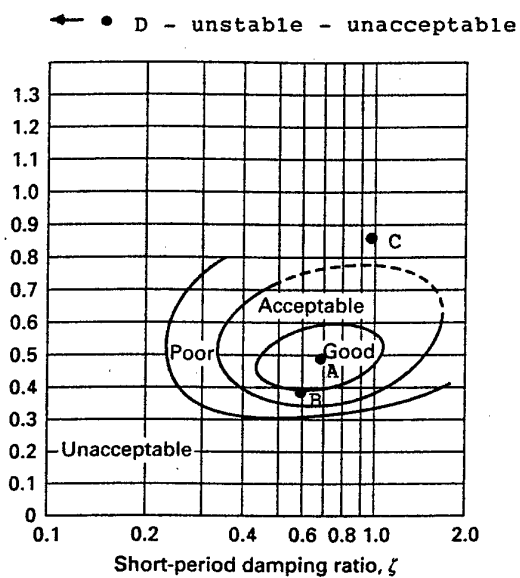


Figure 5 – Short Period Handling Qualities.

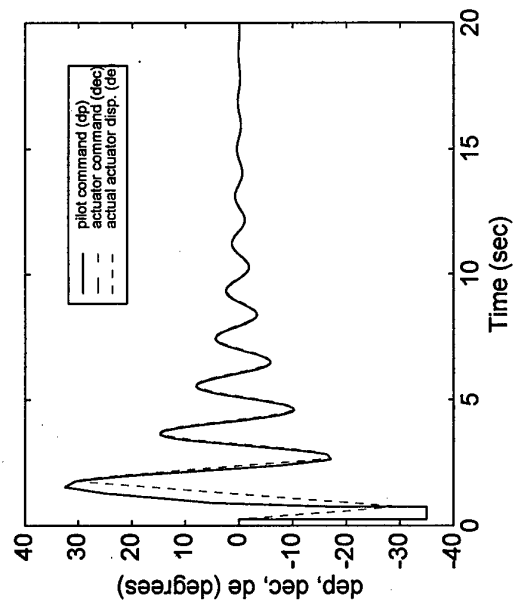


Figure 6 – Case A Simulation Results.

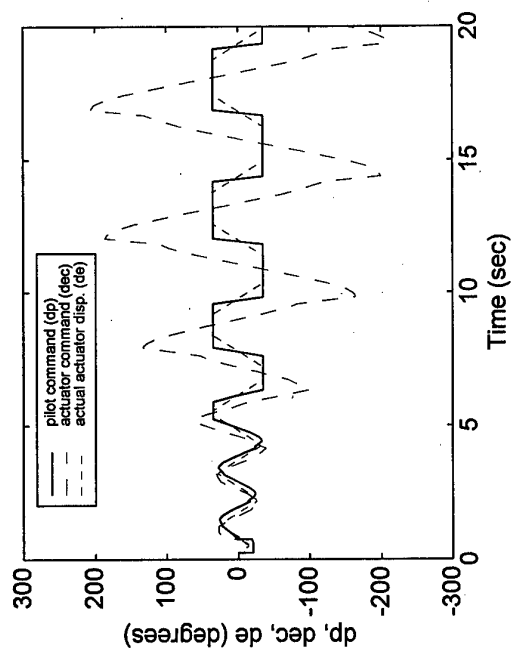


Figure 8 – Case C Simulation Results.

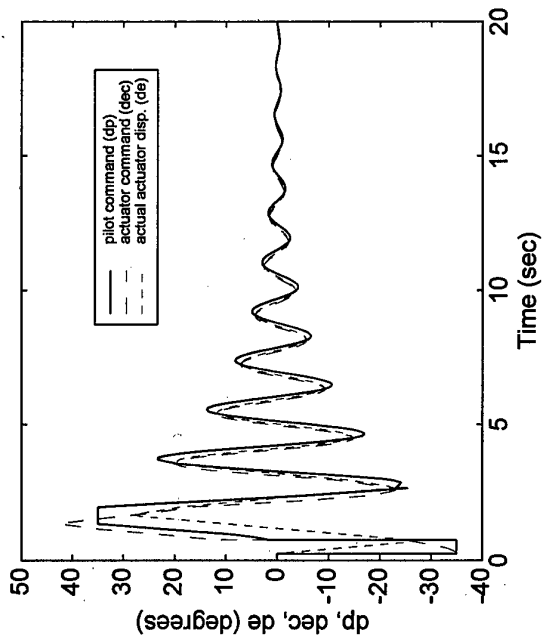


Figure 7 – Case B Simulation Results.

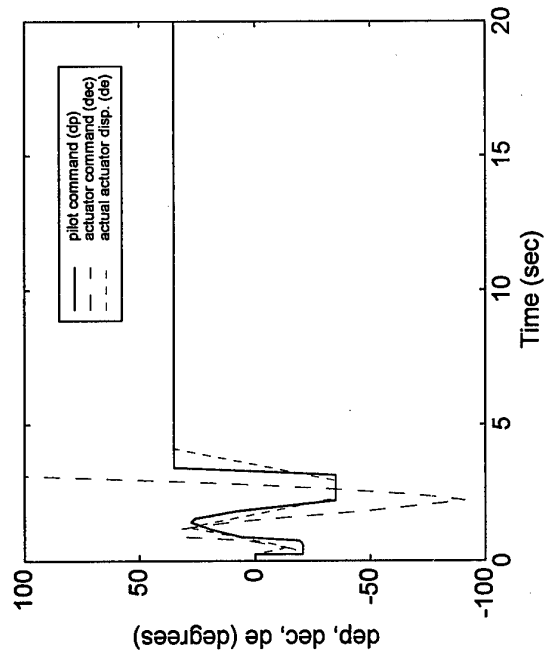


Figure 9 – Case D Simulation Results.

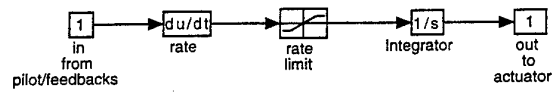


Figure 10 – Simple Filter Logic.

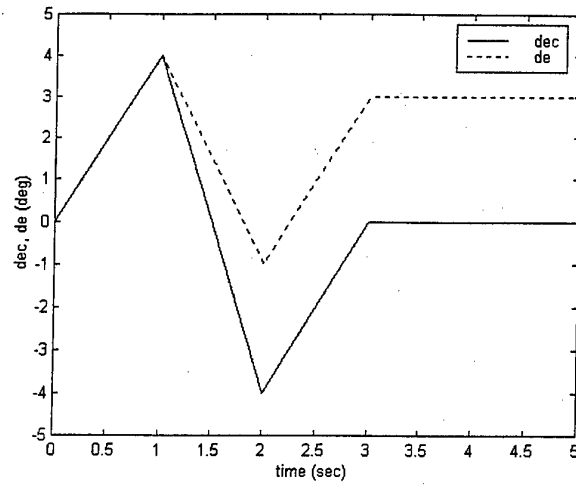


Figure 11 – Example Bias Development.

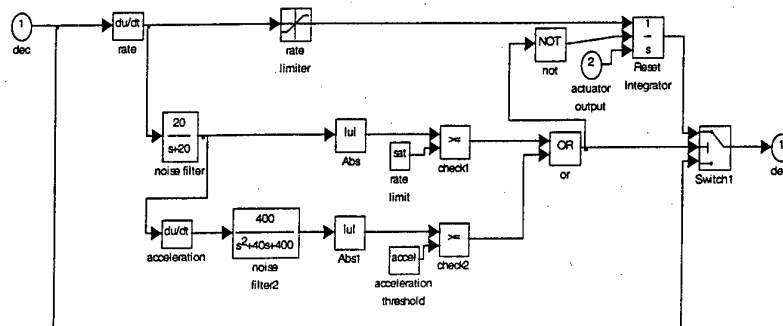


Figure 12 – Rate Limiter Pre-Filter (RLPF).

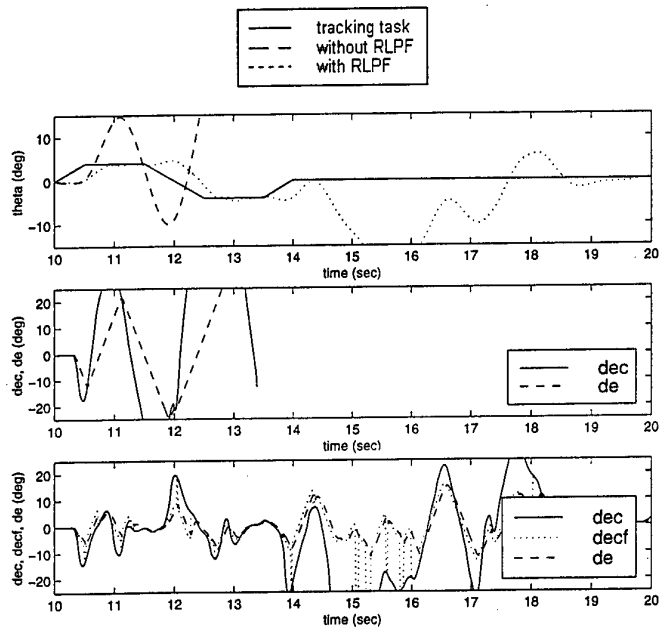


Figure 13 – LAMARS Test Results.

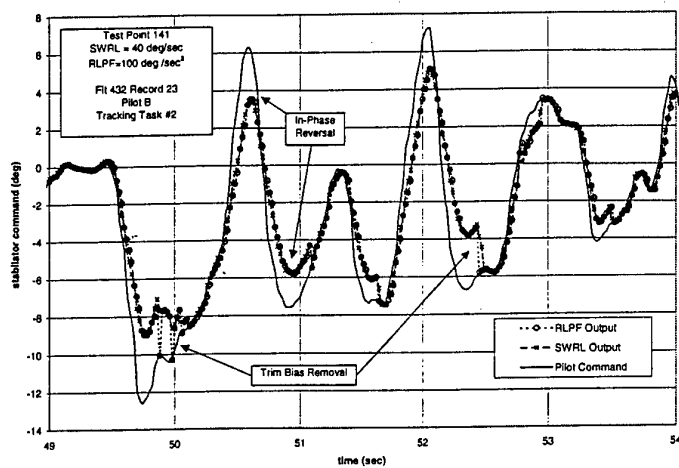


Figure 14 – VISTA Test Results.

ROBUST CONTROL DESIGN FOR STRUCTURED SYSTEM UNCERTAINTIES IN FLIGHT CONTROL SYSTEM DESIGN

Ari Legowo*, Hiroshi Okubo**, Eiichi Muramatsu***, Hiroshi Tokutake****

Osaka Prefecture University, Gakuen-cho 1-1, Sakai, Osaka, 599-8531 Japan

Key Words: Flight Dynamics, Stability and Control, Guidance and Control

ABSTRACT

In this paper, inaccurate elements of the system dynamics matrix are considered as uncertainties factor for robust control design problems. This factor will be modeled as a structured matrix so that its elements represent the model perturbations associated with system's state variables. The closed-loop system is designed as a robust control system, where dynamic response of the closed-loop system will be still in its convergence although it gets perturbations as uncertainties factor of the system dynamics matrix.

This paper uses pole assignment or eigenstructure assignment approach for the design of robust control. The feedback gain is computed by using a solution of Sylvester equation, where the optimum of criterion index is used to estimate the maximum tolerance of uncertainties values such that the characteristic of closed-loop system remains in the design criterion area.

The proposed method is applied to design of flight control system of the N250 aircraft for longitudinal dynamics.

1. INTRODUCTION

To represent the motion of aircraft when controlled by flight control system and to design the automatics control systems, equation of aircraft motions is derived as a linear differential equation, called linear state space equation. In the derivation process many assumptions and linear modeling are taken i.e. the aircraft is considered as a rigid body, hits small disturbances, and there is no cross effect between longitudinal and or lateral/directional when the series of state variables are formed. It may cause differences in dynamic responses between the real flight (which has a nonlinear model) and the linear model. Although the differences are quiet small, they can influence the dynamics and performance, and can degrade the

stability of aircraft extremely.

In this paper, inaccuracies in linear model are modeled as structured uncertainties of state matrix of nominal system. Then in order to build a robust system the maximum tolerance values of structured uncertainties are determined.

An aircraft's dynamics model on longitudinal modes is explained firstly, and then in next chapter, the robust control model is derived by the solution of Sylvester equation and the optimum solution such that the closed loop system has a maximum tolerance of uncertainties factors is determined. The robust control design is used to determine the maximum tolerance of uncertainties of the dynamic matrix for the N250 aircraft flight control system on longitudinal dynamic. The characteristics values of the robust system are dedicated to *Military Flying Quality Specifications*.

2. AIRCRAFT'S EQUATION OF MOTION ON LONGITUDINAL MODE

Linear dynamics model of aircraft's longitudinal modes is derived from the equilibrium of kinematics and forces equations, where some assumptions and a linearization for expanding the derivatives by Taylor series are taken [2]. The simplified linear system model of aircraft longitudinal dynamics is as follows

$$\dot{x} = Ax + Bu \quad (1)$$

Where $x = [\Delta u \ w \ q \ \Delta \theta]^T$ is state variable and $u = [\delta_E]$ is input control and $A \in \mathbb{R}^{4 \times 4}$ is state matrix:

$$A = \begin{bmatrix} x_u & x_w & 0 & -g \cos \theta \\ z_u^* & z_w^* & z_q^* & -g_1 \sin \theta \\ m_u^* & m_w^* & m_q^* & -g_2 \sin \theta \\ 0 & 0 & 1 & 0 \end{bmatrix} \quad (2)$$

and $B \in \mathbb{R}^{4 \times 1}$ is input matrix:

* Graduate Student

** Professor, Department of Aerospace engineering

*** Lecture, Assistant Prof. Department of Aerospace engineering

**** Research Associate, Department of Aerospace engineering

$$B = \begin{bmatrix} x_{\delta_E} \\ z_{\delta_E} \\ m_{\delta_E} \\ 0 \end{bmatrix} \quad (3)$$

This equation represents a nominal linear system.

3. ROBUST CONTROL DESIGN

To analyze the relation between nominal system and desired system, Sylvester equation (also called Lyapunov equation) is presented as follows [4]

Sylvester equation:

Given (A, B) controllable and (G, A_d) observable and if desired eigenvalues $\lambda(A_d) = \Lambda_d$ are distinct, then $\exists S \in \mathbb{R}^{n \times n}$ (non singular) such that

$$AS - SA_d = -BG \quad (4)$$

In this control system problem, it is assumed that closed loop system has state feedback model. So, the control law and closed loop system can be written as follows

$$u = Fx \quad (5)$$

$$\dot{x} = (A + BF)x \quad (6)$$

From equation (4), the characteristic values of closed loop system and desired system have a relationship as bellow

$$\lambda(A + BGS^{-1}) = \lambda(A_d) \quad (7)$$

In order to make the characteristic of closed loop system and desired system are same, closed-loop state matrix should be

$$A_c = A + BGS^{-1} \quad (8)$$

Where the feedback gain of the closed loop system (6) is given as

$$F = GS^{-1} \quad (9)$$

In this paper robust control system is modeled by a system that has state matrix as combination between its nominal system and inaccuracies tolerance so called structured uncertainties (ΔA) .

Therefore, the state matrix of uncertainties system is

$$A_u = A + \Delta A \quad (10)$$

And the structured uncertainties is defined as:

$$\Delta A = \sum_{i=1}^r \epsilon_i E_i \quad (11)$$

where E_i is instrumental matrix, a square matrix with elements '1' or '0', and ϵ_i is magnitude of matrix E_i .

Then to analyze how the structured uncertainties ΔA can

influence performance of desired system, we assume that uncertainties of desired system also has term like in equation (8). Using the Sylvester equation for system with structured uncertainties in equation (10)

$$\left(A + \sum_{i=1}^r \epsilon_i E_i \right) S - S(A_d + \Delta A_d) = -BG \quad (12)$$

where ΔA_d is structured uncertainties of desired system due to ΔA . Then, to eliminate appropriate variables using equation (2) results

$$\Delta A_d = \sum_{i=1}^r \epsilon_i S^{-1} E_i S \quad (13)$$

Taking the norm-2 of both sides of equation above and using triangular inequality

$$\sum_{i=1}^r \epsilon_i^2 \geq \frac{\|\Delta A_d\|_2^2}{\sum_{i=1}^r \|S^{-1} E_i S\|_2^2} \quad (14)$$

From equation above, we can define a performance index (cost function) such that the robust control design will result an optimum design.

The aim of this designing is to evaluate the maximum magnitude of structured uncertainties value ϵ_i when tolerance of desired performance $\|\Delta A_d\|_2$ is given. Thus, we introduce the performance index of robust control problem as follows

$$J = \max_G \sum_{i=1}^r \epsilon_i^2 \quad \text{or} \quad (15)$$

$$J = \min_G \sum_{i=1}^r \|S^{-1} E_i S\|_2^2$$

If we take norm-2 value as a maximum singular value, then performance index above becomes

$$J = \min_G \sum_{i=1}^r \bar{\sigma}_i^2(S^{-1} E_i S) \quad (16)$$

Let define J_c as follows

$$J_c = \sum_{i=1}^r \bar{\sigma}_i^2(S^{-1} E_i S) \quad (17)$$

To approach the minimum value of J we should find G such that derivative of J_c due to G is equal or close to zero.

In order to find this derivative analytically equation (17) is partitioned by its matrix decomposition and after some

algebraic tricks have been taken this derivative becomes

$$\frac{\partial J_C}{\partial G} = 2B^T Y^T \quad (18)$$

where Y is solution of Sylvester equation:

$$A_d Y - Y A = -J_z \quad (19)$$

and matrix J_z is represented as follows:

$$J_z = \sum_{i=1}^4 \bar{u}_i (S^{-1} E_i S) [v_i u_i^T S^{-1} E_i - S^{-1} E_i S v_i u_i^T S^{-1}] \quad (20)$$

where u_i, v_i are decomposition matrix of matrix $S^{-1} E_i S$.

Finally, we use a numerical algorithm iteratively to find G such that equation (18) is close to zero, and second derivative of J_C due to G is positive. [4]

4. APPLICATION TO N250 AIRCRAFT

The proposed method is applied to find the maximum tolerance of uncertainties of longitudinal dynamics of N250 aircraft. The N250 is commuter aircraft for 50-70 passengers powered by two turboprop engines, and it has been built by Indonesian Aircraft Industries.

The nominal system of longitudinal dynamic at trim condition of 160 Knots airspeed, 10000 Feet altitude and 0 degree flaps setting (cruise condition) has a state matrix and input matrix as follows:

$$A = \begin{bmatrix} -0.0248 & 0.0894 & 0 & -9.7222 \\ -0.5963 & -0.8057 & 79.5544 & -1.2243 \\ 0.0005 & -0.0342 & -1.3713 & 0.0041 \\ 0 & 0 & 1 & 0 \end{bmatrix} \quad (21)$$

$$B = \begin{bmatrix} 0.0063 \\ -0.1478 \\ -0.0756 \\ 0 \end{bmatrix}$$

In longitudinal dynamics, there are two modes to be considered:

- (i) phugoid mode
- (ii) short period mode

For the reason that short period mode has 'strong' stable characteristics and phugoid mode has 'almost' unstable characteristics, only in phugoid mode the robustness of longitudinal dynamic system is analyzed.

In phugoid mode, parameters q and α are constant, thus only u and $\Delta\theta$ have dynamic motions. The nonlinear equations

of $\Delta\theta$ has been formed as follows [2]:

$$\begin{aligned} \Delta\dot{\theta} &= q \cos \phi - r \sin \phi \\ \dot{\phi} &= p + q(\sin \phi + r \cos \phi) \tan \theta \end{aligned} \quad (22)$$

For small ϕ equation (22) can be approximated by a linear model:

$$\Delta\dot{\theta} = c_1 q + c_2 \theta \quad (22)$$

There is a difference between the model above and the model in nominal linear system (19) that takes $c_1 = 1$ and $c_2 = 0$. From this reality, we can build an instrumental matrix as follows:

$$E = \begin{bmatrix} 0 & 0 & 0 & 0 \\ 0 & 0 & 0 & 0 \\ 0 & 0 & 0 & 0 \\ 0 & 0 & 1 & 1 \end{bmatrix} \quad (24)$$

To generate the desired system *Military Flying Qualities Specifications* for longitudinal dynamic responses are needed as a design criterion. From this regulation, we can choose a proper requirement as follows [3]:

- (i) For short period mode, damping ratio (ζ) equals to 0.7 and natural frequency (ω_n) equals to 2 rad/s.
- (ii) For phugoid mode, damping ratio (ζ) equals to 0.09 and natural frequency (ω_n) equals to 0.2 rad/s.

According to the design criterion above, the desired system can be built to have characteristic values shown in Table 1.

From characteristic values of desired system we can define a boundary of stability i.e. choose the real part of phugoid's characteristic values, thus

$$\|\Delta A_d\|_2 = 0.018$$

The proposed algorithm has been applied to find the optimal G iteratively. After 23 iterations the performance index is decreased as, (see Fig. 1)

$$J = 1.2314$$

The feedback gain is obtained as

$$F = [0.0381 \quad -0.0652 \quad 8.5210 \quad 1.7135]$$

Table 1 Characteristic values of desired system

short period	phugoid
-1.4000 + 1.4283 i	-0.0180 + 0.1992 i
-1.4000 - 1.4283 i	-0.0180 - 0.1992 i

Using equation (12) the maximum tolerance is given as

$$\epsilon = 0.0162$$

Figure 2 displays deviations of the characteristic values of closed-loop system due to the structured uncertainty ($0 \sim \epsilon$, with increment of 0.1ϵ).

5. CONCLUSIONS

The proposed method using a simple algorithm to find the minimum performance index can determine successfully the maximum tolerance of structured uncertainties of robust system. Result of a numerical example shows that the system with uncertainties factor remains in stable area.

Nomenclature

A	: state matrix of nominal system
B	: input matrix
A_u	: state matrix of uncertainties system
A_d	: state matrix of desired system
A_c	: state matrix of closed loop system
E_i	: instrumental matrix
ϵ_i	: magnitude of matrix E_i
ΔA_d	: uncertainties of desired system
$\bar{\sigma}(A)$: largest singular value of matrix A
$\lambda(A)$: characteristic value of matrix A
α	: angle of attack
θ	: angular angle in pitch
ϕ	: angular angle in roll
q	: angular velocity in pitch
r	: angular velocity in yaw
ζ	: damping ratio
ω_n	: natural frequency

REFERENCE

1. Lean, Donald Mc. "Automatic Flight Control Systems," Prentice-Hall Intern., 1990.
2. Etkin, B. and Duff Reid, L. "Dynamics of Flight," John Wiley, 1996.
3. Stevens, B.L. and Lewis, F.L. "Aircraft Control and Simulation," John-Wiley, 1992.
4. Legowo, A. "Robust Control Design with Structured Uncertainties," M.S. Thesis, Bandung Institute of Technology, 1993.
5. Zhou, K. and Khargonekar, PP. "Stability Robustness Bounds for Linear State Space Models with Structured Uncertainty," IEEE Trans. Automat. Contr., Vol. AC-32, pp 621-623, 1987.
6. Juang, Y.T. "Robust Stability and Robust Pole Assignment of Linear System with Structured Uncertainty," IEEE Trans. Automat. Contr., Vol. 36, pp 635-637, 1991.

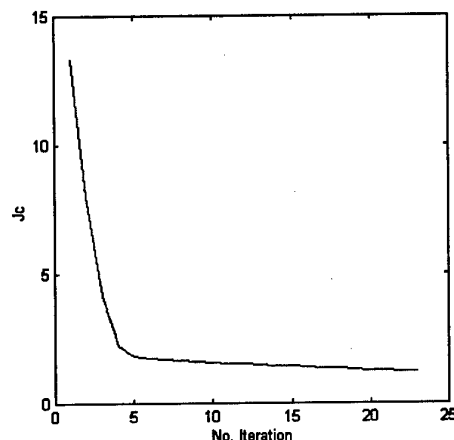


Fig 1 Performance index versus number of iteration

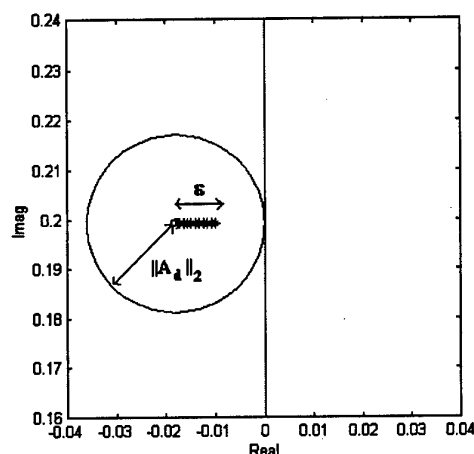


Fig 2 Characteristic values of closed loop system with uncertainties (phugoid mode)

DESIGN OF A FLIGHT CONTROL SYSTEM FOR PROPULSION CONTROLLED AIRCRAFT

Yoshimasa Ochi* and Kimio Kanai**

National Defense Academy

1-10-20 Hashirimizu, Yokosuka 239-8686, Japan

Key Words: Guidance and Control, ACT, Flight Control, Propulsion Controlled Aircraft, Safety

ABSTRACT

This paper describes a design method of a flight control system for propulsion controlled aircraft, which are controlled using thrust only. Particularly, design of a flight control system for ILS-coupled approach and landing is considered, because it is one of the most critical phases in flight control. The H-infinity state feedback control is applied to the design to synthesize the guidance and control system at a time, unlike the classical control that synthesizes it separately, closing the feedback loops one by one. Thereby the design procedure becomes straightforward and the entire control system can be optimal. The effectiveness of the flight control system is illustrated through computer simulation using a linear model of the Boeing 747 in a gust disturbance environment.

1. INTRODUCTION

Propulsion controlled aircraft (PCA) are controlled using thrust only. Such a situation can occur, when the whole hydraulic systems completely fail as in the accidents of the Boeing 747 of Japan Airlines in 1985 and the DC-10 of United Airlines in 1989. As the accidents show, it is difficult for human pilots to control the aircraft using thrust only, especially in approach and landing. Those accidents motivated NASA Dryden Flight Research Center (DFRC) to challenge the problem of automatic control of PCA. They designed flight control systems for PCA and successfully conducted simulations and flight tests on the F-15 fighter and the MD-11 jet transport.^{1,2} NASA Ames Research Center also conducted piloted simulation tests on the Boeing 747-400 jet transport.³

Although the details of the controller design in those researches are not revealed, the control systems are designed basically based on the classical control and gain adjustment. Most autopilots currently used are designed by the classical

control. However, the approach synthesizes a feedback control system by one-by-one loop closure, so that it takes time to design and besides it is difficult to optimize the whole control system. The optimization is important for aircraft with small control power such as PCA.

In our study the state-space method is applied to design of the control system for ILS (instrument landing system)-coupled approach and landing; that is, the H-infinity state feedback control is employed. Since the approach and landing is one of the most critical phases in flight, automatic control is particularly necessary for precise control of PCA. Usually the ILS-coupled approach and landing system consists of a guidance system and a flight control system. However, using the state-space design method, the guidance and control systems can be designed as a single control system at a time. The effectiveness of the control system is illustrated through computer simulation using longitudinal and lateral-directional linear models of the Boeing 747 jet transport in an approach configuration. It will be shown the gust disturbances affect the performance of the control system.

2. GLIDE SLOPE AND FLARE CONTROLS

2.1 Geometry of the glide slope problem

In the longitudinal control for the ILS-coupled approach the aircraft is guided to the runway by tracking the beam emitted from the glide slope transmitter located near the end of the runway. Figure 1 shows the geometry of the glide slope centerline (GSC) and the aircraft.⁴

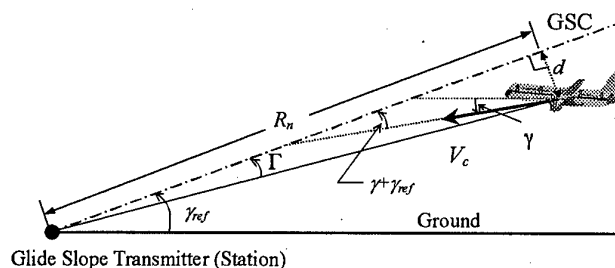


Fig. 1 Geometry of the glide slope problem

* Associate Professor, Department of Aerospace Engineering

** Professor, Department of Aerospace Engineering

The aircraft is guided so that the tracking error angle Γ becomes zero. From Fig. 1, Γ is approximately expressed as

$$\Gamma = \int_0^t V_c (\gamma + \gamma_{ref}) d\tau / R_n \quad (1)$$

where the variables are defined in Fig. 1.

2.2 Controller Design

Since all the states of aircraft motion are often measurable, we apply the H_∞ state-feedback control to the glide-slope-tracking problem. The aircraft and engine dynamics are described by the following linear time-invariant state equation with the output equation:

$$\dot{x}_p = A_p x_p + B_p u_p \quad (2)$$

$$y_p = C_p x_p + D_p u_p \quad (3)$$

where the state variables are $x_p = [u \ w \ q \ \theta \ \delta_{th}]^T$ and control variable is $u_p = \delta_{thc}$; u is forward speed(m/s), w downward speed(m/s), q pitch rate(rad/s), θ pitch angle(rad), δ_{th} engine thrust (N), and δ_{thc} thrust command. It is assumed that the engine dynamics is represented by a first-order delay system. Defining y_p as $y_p = [u \ -\gamma]^T = [u \ -\theta + \alpha]^T$, C_p and D_p are given as

$$C_p = \begin{bmatrix} 1 & 0 & 0 & 0 & 0 \\ 0 & 1/U_0 & 0 & -1 & 0 \end{bmatrix}, \quad D_p = \begin{bmatrix} 0 \\ 0 \end{bmatrix}$$

where U_0 is the nominal trim air speed and $\alpha = w/U_0$.

Figure 2 shows a block diagram of the glide slope control system for the generalized plant that includes weighting functions. The criterion outputs are the speed error z_1 , multiplied by $\alpha_1/(T_1 s + 1)$, the integrated tracking error z_2 , and the weighted collective thrust command z_3 . The external inputs are the reference speed u_{ref} , the reference flight path angle γ_{ref} , and the reference tracking angle Γ_{ref} . The feedback control gain matrices K_1 and K_2 are determined so that the infinity norm of the closed-loop transfer function from the external inputs to the criterion outputs can be small. Note that the geometric relation, Eq. (1) is embedded in Fig. 2 and that the output of the integrator is a state of the controller. For details of the design, the reader is referred to Ref. 5.

In flare control, the sink rate as well as the forward speed must be decreased to make a safe landing. Hence the sink rate dh/dt is controlled to follow the reference model given by

$$\dot{h}_{ref} = -\frac{1}{\tau} h \quad (4)$$

where h is the altitude and τ is a time constant given appropriately. The control system that achieves the control objective is designed in the same way as the glide slope control system. Figure 3 shows a block diagram of the flare control system for the generalized plant.

3. LATERAL-DIRECTIONAL CONTROL

3.1 Geometry of the lateral-directional guidance

Lateral-directional guidance to the runway is performed by capturing the beam from the Omni or localizer. Figure 4 shows the geometry of the lateral beam guidance.⁴ The control objective is to guide the aircraft to the centerline of the beam and make the heading angle Ψ agree with the reference angle Ψ_{ref} . In the same way as Γ , the angle λ between the beam centerline and the line drawn from the station to the aircraft is given as

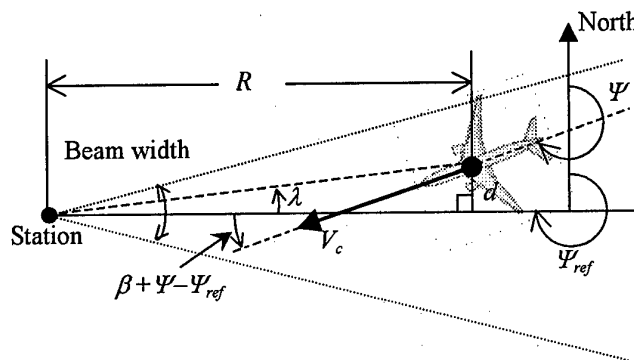


Fig. 4 Geometry of lateral beam guidance

$$\lambda = \frac{1}{R} \int_0^t V_c (\beta + \Psi - \Psi_{ref}) d\tau \quad (5)$$

3.2 Controller Design

The aircraft dynamics are described by the linear lateral-directional equations of motion. The state variables are $x_p = [\beta \ p \ r \ \phi \ \Psi \ \Delta\delta_{th}]^T$, where β is sideslip angle (rad), p roll rate (rad/s), r yaw rate (rad/s), and ϕ roll angle (rad/s). The control input is the differential thrust between the left and right engines $u_p = \Delta\delta_{thc}$. The control system is structured in the same way as the glide slope control.

without $\frac{1}{Ts+1}$ blocks

4. SIMULATION

The flight condition is that the altitude is the sea level and the airspeed is 84.7 m/s (278 ft/s). The engine dynamics is modeled as a first order delay system with a time constant of 1.5 s. Assuming that the trim thrust is 50% of the maximum cruise thrust at the flight condition, the available thrust is given by $|\delta_{thc}| \leq 2.5 \times 10^5$ N. In lateral-directional control, we assume that the

left and right engines produce the thrust $(\delta_h + \Delta\delta_h)/2$ and $(\delta_h - \Delta\delta_h)/2$, respectively. The derivatives with respect to the differential thrust are estimated from the thrust derivatives of the longitudinal model. In the simulation nonlinearities of kinematic and geometric relations in the guidance systems are taken into account. Γ and λ are computed using actual aircraft location instead of using Eqs. (1) and (5).

The simulation is conducted in a wind disturbance environment. The stochastic wind models in Ref. 6 are used. The forward gust, vertical gust, side gust, and roll gust are considered. The root-mean-square value of the translational gusts is 0.701m/s and that of the roll gust is 0.0129rad/s.

The glide slope control is engaged at the initial time when the aircraft in level flight captures the GSC at a horizontal distance of 18520m from the station and an altitude of 971m. Figure 5 shows the flight path in the vertical plane. The dotted lines indicate beam bounds of $\pm 0.5\text{deg}$ from the GSC. The aircraft is guided to the GSC without going out of the beam capture zone.

Figure 6 shows the flight path in flare control. The time history of the sink rate is shown in Fig. 7. The flare control takes over the glide slope control when the aircraft descends to 75m above ground level. By the flare control the aircraft pitches up, while decreasing the flight path angle and the airspeed. Thus, a moderate sink rate at the touchdown of 1.3m/s is achieved.

In the lateral-directional control, the aircraft captures the guidance beam at a distance of 22520m from the localizer in the runway direction and an offset of 912m to the right of the runway ($\lambda=2.3\text{deg}$). Figure 8 shows the flight path in the horizontal plane. The dotted lines indicate beam bounds of $\pm 2.5\text{deg}$. Although the flight path a little oscillates near the runway, it is within the runway, hence the aircraft touches down on the runway. The time histories of the state variables are shown in Fig. 9. As seen from these figures, the aircraft makes an 'S-turn' to line up the runway. The time histories of the thrust commands are shown in

Fig. 10, which indicates that the control is carried out using the thrust within the limits.

5. CONCLUSIONS

As the simulation results show, the flight path and state variables fluctuate due the disturbances. The fluctuation affects the control performance, especially when the aircraft approaches the station, because the loop gain increases near the station and it destabilizes the control system. For this reason, the flare control is engaged at a higher altitude than in the case of no disturbances. Besides, the sink rate at touchdown varies with the disturbances and the initial altitude of the flare control. In order to make the control system robust against the disturbances and the altitude, the uncertainties must be explicitly taken into account in the design.

REFERENCES

1. Burcham Jr. F. W., "Landing safely when flight controls fail," *AIAA Aerospace America*, October, 1997, pp. 20-23.
2. Burken J. J. and Burcham Jr. F. W., "Flight Test Results of Propulsion-Only Emergency Control System on MD 11 Airplane," *AIAA J. of Guidance, Control, and Dynamics*, Vol. 20, 1997, pp. 980-987.
3. Bull, J., et al. "Piloted Simulation Tests of Propulsion Control as Backup to Loss of Primary Flight Controls for a B747-400 Jet Transport," NASA TM-112191, April, 1997.
4. Blakelock, J. H., *Automatic Control of Aircraft and Missiles*, 2nd Ed., John Wiley & Sons, Inc., 1991.
5. Y. Ochi and K. Kanai, "Automatic Approach and Landing for Propulsion Controlled Aircraft by H_∞ Control," *IEEE Conference on Control Applications*, August 1999 (to appear).
6. Bryson, A. E., *Control of Spacecraft and Aircraft*, Princeton Univ. Press, 1994.

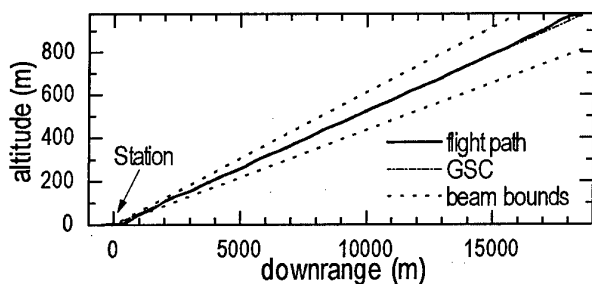


Fig. 5 Flight path in the vertical plane

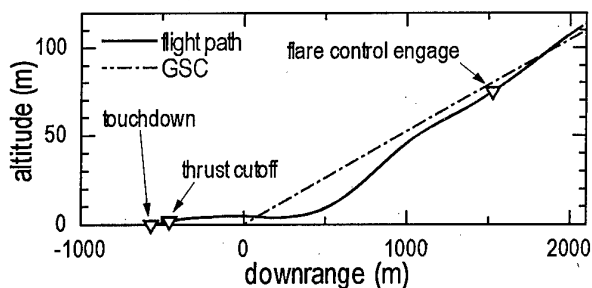


Fig. 6 Flight path in flare control

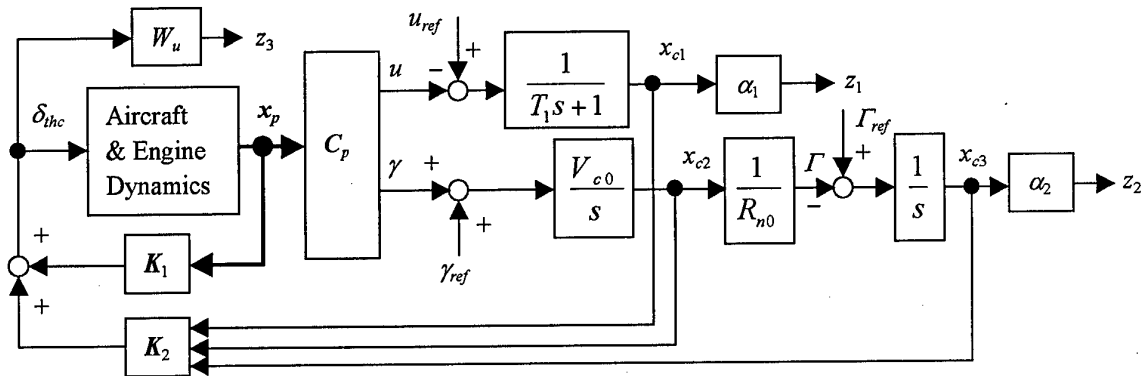


Fig. 2 Glide slope control system

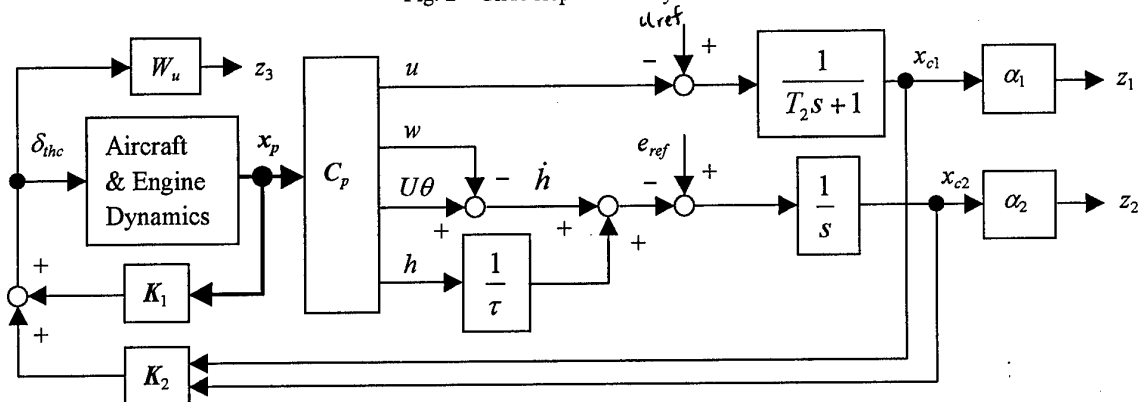


Fig. 3 Flare control system

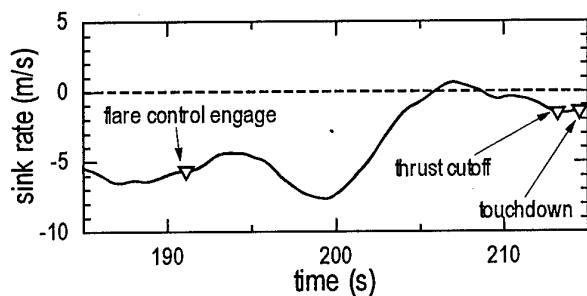


Fig. 7 Time history of sink rate in flare control

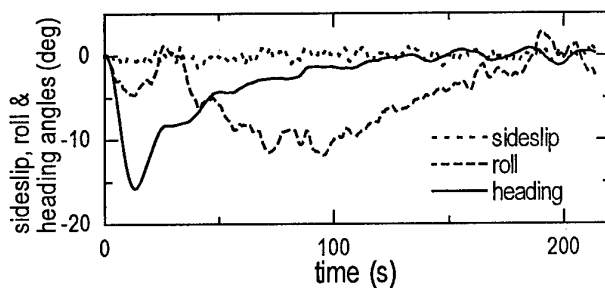


Fig. 9 Time histories of sideslip, roll and heading angles

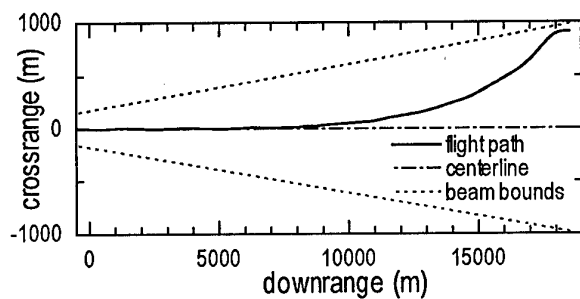


Fig. 8 Flight path in the horizontal plane

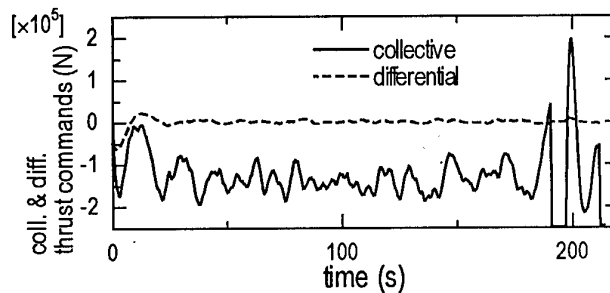


Fig. 10 Time histories of thrust commands

Multivariable Flight Control Design Using Co-Evolutionary Algorithm

Kuen-Mo Koo*, Hyo-Seon Chi* and Min-Jea Tahk**

Department of Aerospace Engineering,
Korea Advanced Institute of Science and Technology(KAIST)
373-1 Kusong-dong, Yusong-gu, Taejeon, 305-701, Korea

Key Words: flight control, constrained optimization, co-evolution

ABSTRACT

This paper presents a practical design method on multivariable feedback control problems. The method is primarily based on the co-evolution approach developed for solving saddle-point problems. In this paper, the proposed method is applied to the multivariable flight control design of a drone aircraft and for the sake of the comparison, the design result of mixed H_2/H_∞ design with pole assignment which is based on the LMI approach is also presented.

1. INTRODUCTION

A number of methods have been proposed to solve multivariable control problems. The familiar methods for the multivariable control designs are perhaps LQG/LTR and H_∞ design methods which are state feedback/observer control system[1][2]. Since they only involve solving two Riccati equations, their control design procedures are relatively simple and by using a frequency-domain loop shaping procedure, they can address some important stability robustness specifications. However, these design methods mostly depend on the frequency-domain aspects and they can not consider the various design requirements such as time domain specifications simultaneously.

It is noted that H_2 and H_∞ synthesis can be expressed in terms of linear matrix inequalities(LMIs) and they can be solved efficiently by convex optimization algorithms[3]. For the multivariable control design, the LMI approach is so attractive that it can address multi-objective design problems such as mixed H_2/H_∞ synthesis with regional pole placement. By placing closed loop poles into a suitable LMI regions, the time-domain specifications can also be considered. But in some cases, assigning the regions of closed-loop poles for time-domain specifications can be ineffective and their designs are also iterative to obtain a desirable result.

In this paper, we introduces a more practical control design method to consider the various design requirements directly and simultaneously. In this method, the controller design problem is posed as a parameter optimization problem subjected to inequality constraints and it is solved by using a co-evolution algorithm recently developed to solve saddle-point problems[4][5]. This method also utilizes the augmented Lagrangian approach to reformulate a constrained optimization problem as a saddle-point problem and to convexify nonconvex parameter optimization problems. The main ad-

vantage of this method is its applicability to a broad spectrum of the controller design problems since it can address the various design requirements directly by selecting the cost and the constraints freely to meet them. Also, since the method is primarily based on the conventional evolutionary algorithms in its evolution process, either derivatives or initial guesses are not required as in the nonlinear programming techniques. For convenience, the method is referred to as a Co-Evolutionary Augmented Lagrangian Method(CEALM).

This paper introduces the CEALM briefly in section 2. In section 3, a lateral/directional flight control design is performed by using this method and, for the sake of comparison, the mixed H_2/H_∞ synthesis with pole displacement. In section 4, concluding remarks are given.

2. CO-EVOLUTIONARY AUGMENTED LAGRANGIAN METHOD(CEALM)

In this section, a co-evolutionary algorithm for solving constrained optimization problem is briefly described. Detail description for this algorithm is given at [5].

Consider a general inequality-constraint parameter optimization problem of the form.

$$\min_{x \in \Omega} f(x) \quad (1)$$

subject to

$$g_k(x) \leq 0 \quad k = 1, \dots, m \quad (2)$$

where Ω is the set of all $x \in R^n$ with $x^l \leq x_i \leq x^u$, $i = 1, \dots, n$.

For this primal problem, we have the following Lagrangian dual problem.

$$\max_{\lambda} L(\lambda) \quad \text{subject to} \quad \lambda_k \geq 0 \quad (3)$$

where λ denotes a $m \times 1$ Lagrangian multiplier. Then, if we define (x^*, λ^*) as the optimum of the Lagrangian which satisfies the Kuhn-Tucker necessary conditions, it is known that $L(x^*, \lambda^*)$ is a saddle point representing a minimum with respect to x and a maximum with respect to λ [6].

$$\min_x L(x, \lambda^*) = \max_{\lambda} L(x^*, \lambda) = L(x^*, \lambda^*) \quad (4)$$

for any $x \in \Omega$ and $\lambda_k \geq 0$, $k = 1, \dots, m$.

However, if the primal problem is nonconvex over Ω , the minimum of the Lagrangian doesn't provide the true minimum of the primal problem. To avoid this difficulty, we use the augmented Lagrangian function(ALF) which

* Graduate Student, Department of Aerospace Engineering

** Associate Professor, Department of Aerospace Engineering

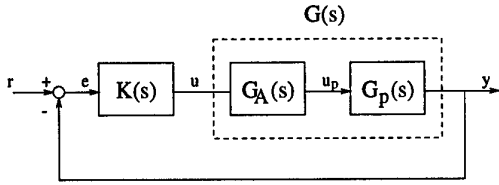


Fig. 1. LQG control structure

can convexify the primal problem with quadratic penalty terms.

$$L_A(x, \lambda, \rho) = f(x) + \sum_{k=1}^m p_k(x, \lambda_k, \rho) \quad (5)$$

where the penalty term p_k is given as

$$p_k(x, \lambda_k, \rho) = \begin{cases} \lambda_k g_k(x) + \rho g_k^2(x) & \text{if } g_k(x) \geq -\frac{\lambda_k}{2\rho} \\ -\frac{\lambda_k^2}{4\rho} & \text{if } g_k(x) < -\frac{\lambda_k}{2\rho} \end{cases} \quad (6)$$

It is known that the minimum of the ALF provides the solution to the original primal problem for some finite value of the penalty parameter ρ , and the optimum parameter x^* becomes an unconstrained minimum of $L_A(x, \lambda^*)$ if λ^* is given. In practice, λ^* is not known in advance, but obtained by means of iterative scheme beginning with an arbitrary λ . Using this concept, the saddle point of the ALF can be obtained by using the co-evolutionary algorithm proposed in Ref. [4]-[5]. In this algorithm, the saddle point problem is viewed as a static zero-sum game[7] between two players X and Y , where X and Y represent the parameter vector x and the multiplier λ , respectively. The fitness of an option of each player is determined according to the security strategy of the player.

3. FLIGHT CONTROL DESIGN EXAMPLE

A. DESIGN PLANT MODEL

Consider a problem of designing a lateral/directional flight control system for a drone aircraft[8]. The linearized plant model is given by

$$\dot{x}_p(t) = A_p x_p(t) + B_p u_p(t) \quad (7)$$

$$y_p(t) = C_p x_p(t) \quad (8)$$

This model consists of six states, two control inputs and outputs. The plant states are sideslip angle, roll rate, yaw rate, roll angle, elevon and rudder surface deflections. The control inputs δ_{e_c} and δ_{r_c} consist of elevon and rudder servo command. Sideslip angle and roll angle are defined as outputs. The open-loop eigenvalues associated with roll subsidence, spiral and dutch roll mode are -3.0771 , 0.0075 and $0.0801 \pm 0.726i$, respectively. It is noted that the original plant have lightly-damped unstable spiral and dutch roll poles in the RHP.

B. CLEAM DESIGN

In designing the controller using the CEALM, any controller structures can be used. Here, the LQG structure, which is the full state feedback/observer system, is

used for the purpose of illustrating the design method and for the comparison with mixed H_2/H_∞ synthesis. A LQG control structure is shown in Fig.1 and the open loop transfer function matrix of the compensated system, $G(s)K(s)$, are defined as

$$G(s) = C(sI - A)^{-1}B = G_p(s)I/s \quad (9)$$

$$K(s) = K_c(sI - A + BK_c + K_f C)^{-1}K_f \quad (10)$$

where K_f and K_c denote 8×2 filter gain matrix and 2×8 controller gain matrix.

Then, the design objective is to obtain the gain parameters of K_f and K_c in order that the closed-loop system may satisfy 1) nominal stability, 2) frequency-domain performance and stability robustness requirements, 4) time-domain performance requirements such as overshoot, settling time, zero steady-state error and control input magnitude restrictions. Specifically, the design is performed to allow the aircraft to track a 30 deg step roll angle command without steady-state sideslip.

To apply the CEALM, we must select the cost and the constraints that properly represent the design requirements. For the primal-dual formulation, the cost, $f(x)$, is chosen to minimize the settling times and the time integrated norm of the response errors.

$$f = w_f [t_{s\beta} + t_{s\phi}] + \int_{t_0}^{t_f} [|\beta| + t|\phi - \phi_{com}|] dt \quad (11)$$

The settling time is weighted by $w_f = 10$ in the sense of normalization while the roll angle error is weighted by time to penalize steady-state roll angle error. The value of t_0 is chosen as 2 sec, which is the desired settling time.

Additionally, the constraints, $g_i(x)$, to be met are selected as follows by considering the design requirements:

$$g_1 = c_1 \cdot \text{Max}(\text{Re}[\lambda_i]) \leq 0$$

$$g_2 = 60 \text{ (dB)} - \sigma_{\min}|G(j\omega_1)K(j\omega_1)| \leq 0$$

$$g_3 = 20 \text{ (dB)} - \sigma_{\min}|G(j\omega_2)K(j\omega_2)| \leq 0$$

$$g_4, g_5 = \text{Max}(|\delta_e| & |\delta_r|) - 20 \text{ (deg)} \leq 0$$

$$g_6 = \text{Max}(|\beta|) - 4.5 \text{ (deg)} \leq 0$$

$$g_7 = \text{Max}(\phi) - 1.15\phi_{com} \leq 0$$

Here, λ_i denotes the closed-loop poles of the compensated system and ω_1 and ω_2 are 0.001 and 0.1 rad/s, respectively. g_1 is the nominal stability constraint with a large weighting factor $c_1 = 10^6$ since it should be satisfied at first. g_2 and g_3 indicate the low-frequency performance constraints as shown graphically in Fig.4 with shaded regions. But, high-frequency constraints are not included since they are easily satisfied due to the high frequency fast roll-off. For the time-domain constraints,

Table 1 Parameter values for CEALM

No. of minimizing variable (X)	32
No. of maximizing variable (Y)	7
No. of parent population (μ)	10
No. of offspring population (λ)	50
No. of matching	50
No. of maximum generation	6000

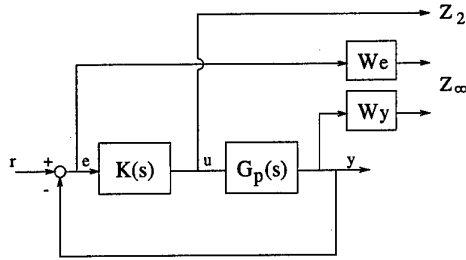


Fig. 2. Mixed H_2/H_∞ control structure

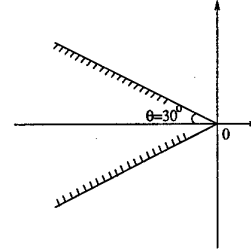


Fig. 3. LMI region

the control input magnitude and the roll response overshoot are limited within ± 20 deg and 15 %, respectively. Sideslip transient response is also restricted within ± 4.5 deg.

For the above constraints and cost function, the augmented Lagrangian, a function of the gain parameters and Lagrangian multiplier can be established with the penalty parameter $\rho=1000$. Now the co-evolutionary algorithm is applied by defining the minimizing parameter X as the gain parameters of K_f and K_c , and the maximizing vector Y as the Lagrangian multipliers. The search space of X is restricted to ± 5 for K_f and ± 500 for K_c . After generating the parent population and offspring population, a conventional evolution strategy is used for recombination, mutation, and selection with (μ, λ) -selection method described in [9]. Parameter values for numerical calculation are shown in Table 1.

C. MIXED H_2/H_∞ DESIGN

In this section, the mixed H_2/H_∞ design method is applied to the same problem to compare the result. Since H_∞ control design is mainly concerned with the frequency domain performance and does not guarantee the time-domain transient behaviors, it is necessary to include both specifications and solve a mixed H_2/H_∞ with pole assignment using LMI approach.

Fig.2 shows the mixed H_2/H_∞ control structure. In this design, the output z_∞ is consists of the weighted error e and weighted output response y to compromise low and high frequency-domain specifications. The selected weights are as follows:

$$W_e = \frac{0.35s + 0.7}{(s + 0.0001)(s/1000 + 1)} I_{2 \times 2} \quad (12)$$

$$W_y = \frac{986s + 4805}{s + 14823} I_{2 \times 2} \quad (13)$$

The output z_2 is considered as the control input to be regulated. To improve the transient behavior, we add a pole-assignment constraint such that the closed-loop poles should be located in the LMI region shown in Fig. 3. Then, the mixed H_2/H_∞ control may be described as to find a controller $K(s)$ which minimizes $\|T_2\|_2$ subjected to $\|T_\infty\|_\infty < \gamma$ and the pole placement constraint.

D. RESULTS AND COMPARISONS

For the CEALM, several runs are performed with randomly chosen initial populations. The evolution of 4000

iterations produces consistent results satisfying all the constraints. The best fitness value is obtained with $f = 116.5606$ and the gain matrices are obtained as

$$K_f = \begin{bmatrix} -3.849 & 1.294 \\ 1.120 & -0.156 \\ 2.932 & 4.869 \\ 5.000 & -4.870 \\ -4.577 & -4.596 \\ -4.796 & 4.569 \\ -5.000 & 4.970 \\ 4.129 & -1.992 \end{bmatrix} \quad K_c = \begin{bmatrix} 364.961 & -470.001 \\ 86.203 & -10.859 \\ 458.811 & 372.513 \\ -84.908 & 426.571 \\ -363.833 & 268.858 \\ -5.453 & -100.125 \\ 499.846 & -33.912 \\ 416.377 & 358.541 \end{bmatrix}^T$$

For the above gain matrices, the resulting singular values of $G(s)K(s)$ and output time responses are shown in Figs.4 and 5, respectively. Fig.6 illustrates the required control surface deflections.

As can be seen from these figures, the results of the CEALM satisfy all of the design requirements with reasonable singular values and output time responses. The singular values exhibit an integral action decreasing with a slope of -20 dB/dec in the low-frequency region along the boundary of the performance requirements. The result shows that the maximum sideslip response is 2.85 deg and the roll response overshoot is 15%. The settling times of the roll angle and sideslip response are 1.92 and 2.41 sec, respectively. Also, it is evident that the control surface deflections and its rates are acceptable.

The mixed H_2/H_∞ design is performed with the previously selected weighting functions using LMI control toolbox of MATLAB[10], for which γ is selected as 1 by a trade-off concerning the requirements. The optimal H_2 performance is obtained as 8.18. The results of the mixed H_2/H_∞ design are also shown in Figs. 4 and 5. As shown in these figures, the mixed H_2/H_∞ design produces the similar results with the CEALM, especially in the frequency-domain singular values. But the time-domain results show that it gives larger roll angle overshoot and sideslip than does the CEALM. Furthermore, Fig. 6 shows that it also requires larger control surface deflections and rates. For the mixed H_2/H_∞ design, the difficulties may arise in some cases because it can not assign the time-domain specifications directly rather than giving the regions of the closed loop poles and minimizing the control input. On the other hand, for the CEALM, the design requirements can be stated in both frequency- and time-domain directly and simultaneously by including them in the cost and constraints of the ALF, and hence, it has a much more degrees of freedom in designing the gain parameters to satisfy the various design requirements.

4. CONCLUSION

In this paper, multivariable flight control design using the co-evolutionary algorithm is introduced and described with a design example. The design problem is reformulated as an unconstrained saddle-point problem by introducing the augmented Lagrangian function and solved by the co-evolutionary algorithm. The design example shows that the CEALM can address not only frequency-domain design requirements but also time-domain ones directly and simultaneously by including them into the cost and the constraints, and is widely applicable for the multivariable control design problems.

ACKNOWLEDGMENT

This work was supported by Korea Science Foundation under Contract 96-0200-04-01-3.

REFERENCES

- [1] Doyle, J. C. and Stein, G., "Multivariable Feedback Design: Concepts for a Classical/Modern Synthesis," *IEEE Transactions on Automatic Control*, Vol. AC-26, No.1, 1981, pp. 4-16.
- [2] Doyle, J., Glover, K., Khargonekar, P. and Francis, B., "State Space Solutions to Standard H_2 and H_∞ Control Problems," *IEEE Transactions on Automatic Control*, Vol. 34, No. 8, 1989, pp. 831-848.
- [3] Boyd, S., Ghaoui, L. E., Feron, E. and Balakrishnan, V., *Linear Matrix Inequalities in System and Control Theory*, SIAM Publication, 1994.
- [4] Park, C. S. and Tahk, M. J., "A coevolutionary minimax solver and its application to autopilot design," *Proceedings of JSASS Aircraft Symposium*, Tokyo, 1997.
- [5] Tahk, M. J., "Co-evolution for Engineering Optimization Problems: Minimax Design and Constrained Optimization," *Proceedings of JSASS Aircraft Symposium*, Yokosuka, 1998, pp. 679-685.
- [6] Vanderplaats, G. N., *Numerical Optimization Techniques for Engineering Design*, McGraw-Hill, 1984.
- [7] Basar, T., Serali, G. J. and Shetty, C. M., *Dynamic Noncooperative Game Theory*, Academic Press, 1982.
- [8] Ridgely, D. B., Banda, S. S., McQuade, T. E. and Lynch, P. J., "Linear-Quadratic-Gaussian with Loop-Transfer-Recovery Methodology for an Unmanned Aircraft," *Journal of Guidance, Control and Dynamics*, Vol.10, No.1, 1987, pp. 82-89.
- [9] Bäck, T., *Evolutionary Algorithms in Theory and Practice*, Oxford University Press, 1966.
- [10] Gahinet P., Nemirovski A., Laub A. and Chilali M., "The LMI Control Toolbox," *Proceedings of the 33rd Conference on Decision and Control*, 1994, pp. 2038-2041.

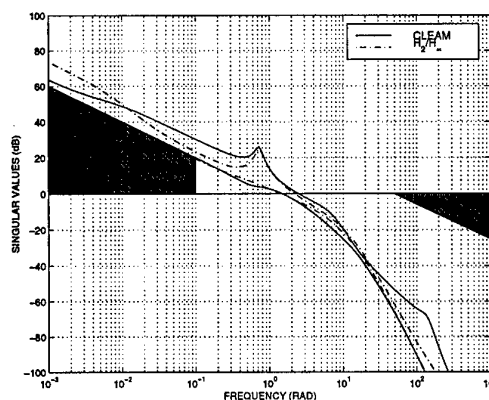


Fig. 4. Singular values of $G(s)K(s)$

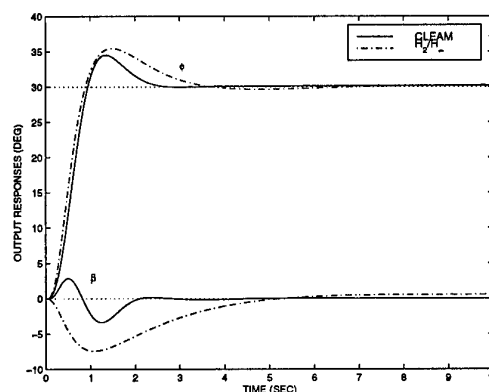


Fig. 5. Output time responses

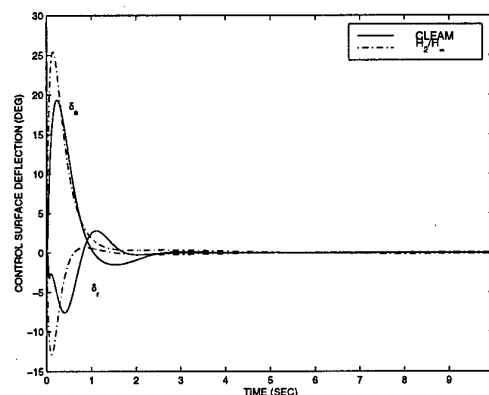


Fig. 6. Control surface deflections

Nonlinear Optimal in Helicopter Flight Control

Andrew An* Youfu Wang**

Beijing University of Aeronautics and Astronautics
No.37 Xueyuan Road, Beijing, 100083, P.R.China

Key Words: **Flight Dynamics Guidance and Control Helicopters**

ABSTRACT

A nonlinear optimal method, which based upon the geometry theory, has been presented in the paper. The method utilizes the concept of infinite hierarchical optimal control and the vector fields theory on manifold to simplified the solution processing in control law design.

It has been shown that the control law satisfied the system of first order, quasi-linear, partial differential equations. It could be obtained that highly precision in helicopter flight control. The method could avoid solving the Riccati equation, which is very complicated in solution processing. The significant of the paper method is to looking for a global solution in convex function.

1 Introduction

Many progresses have been made by geometry nonlinear control in some fields. There have been more and more applications in engineering. The reason is based upon both research forward and much nonlinear precision control problem need to be solved. A lot of analysis and simulation have been done such as in reference [1]-[3]. As one of the application,

we have presented the nonlinear optimal hierarchy method for helicopter positioning control in Reference [4]. In this paper, we'll present another example in control system tracing a moving target. The general describing as following.

To the nonlinear control system,

$$\dot{x}/dt = F(x) + g(x)u$$

$$y = h(x)$$

Assume satisfy the square condition, the system Hamilton equation can be written in following equation:

$$H = \sum pF$$

In which, p is the cooperator. Also we have proved the equations in ref.[4] that the nonlinear hierarchy optimal control expression as following:

$$u = -\sum k y^{(i)} - L[v - \nabla W g/2]$$

$$dv/dt = -2R^{-1}g(x)^T Q[z(t)-h(x)]$$

in which, that R and Q are weighting operator, W is the Lyapunov function. z is the

* Engineer of Beijing University of Aeronautics & Astronautics

** Professor of Beijing University of Aeronautics & Astronautics

traced signal, i is the character number.

2 Return to target maneuver

Computer has simulated the example helicopter Return to Target maneuver. The maneuver processing has been presented here.

A rather complex indication of the maneuverability of a helicopter is the return to target maneuver. In this maneuver, the helicopter passes over a spot (target) in forward flight and then tries to turn to the same spot in the shortest possible time. The most critical ground rule is that the whole maneuver must be done at constant altitude. This simulates a nap-of-the-earth maneuver in which the target might be hostile and capable of destroying the helicopter if given the opportunity. Shorter times could be achieved if the maneuver were done with a zoom and dive.

The optimum return-to-target maneuver at constant altitude consists of a combined deceleration and banked turn until the flight path is pointed back at the target followed by a level flight acceleration. A discussion of the maneuver in ref.[5] pointed out that the deceleration could be increased by sideswiping to increase the parasite drag, but that flight tests using this technique revealed the danger of the pilot becoming disoriented and losing the target. For this reason, calculations should be done assuming a zero sideslip turn during the banked deceleration phrase.

3 The Helicopter Model

The helicopter model as following:

$$dU/dt = F_x/m + VR - WQ - g \sin \theta$$

$$dV/dt = F_y/m + WP - UR - g \sin \phi \cos \theta$$

$$dW/dt = F_z/m + UQ - VP - g \cos \phi \cos \theta$$

$$I_x dP/dt = L - (I_z - I_y)RQ$$

$$I_y dQ/dt = M - (I_x - I_z)PR$$

$$I_z dR/dt = N - (I_y - I_x)PQ$$

and motion equations in general.

The target we choose moving objects at velocity 1 m/sec constant along a straight line.

The graphics of the simulation results show in the appendix.

4 Conclusion

The simulation results are smooth and exact in the helicopter motion. It is characteristics of the control law. Because the control signal are solved in first order differential equation, so the algorithm is not need to solve the Riccati equation.

More simulation shows that shorter response time can be obtained.

The method also can be applied whether the target moving or stopped.

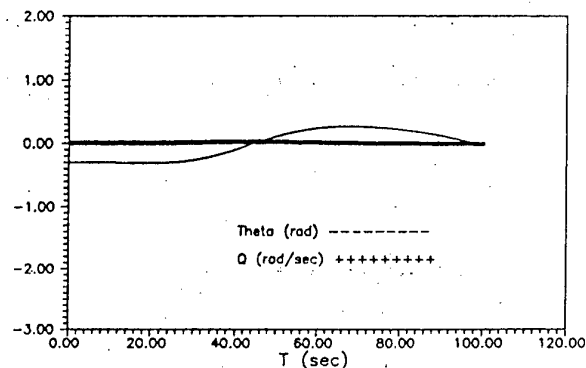
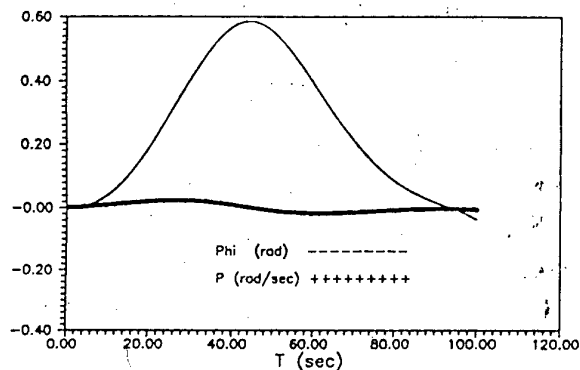
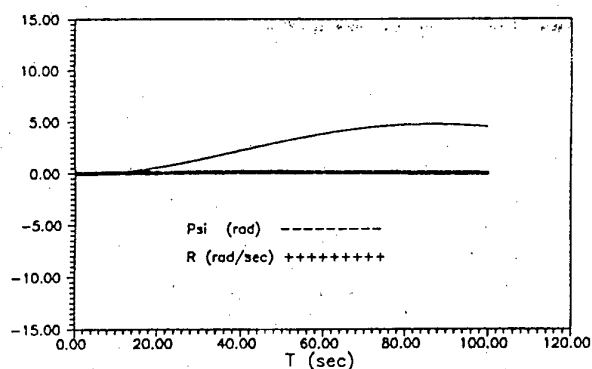
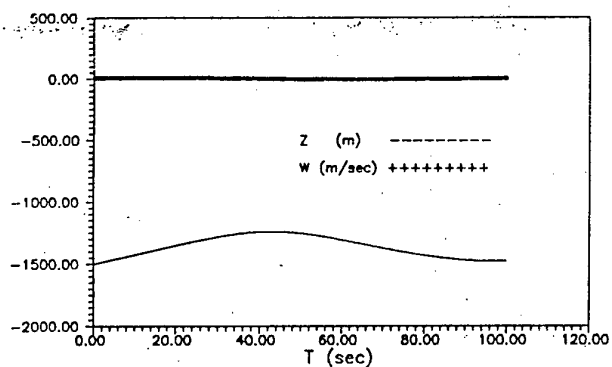
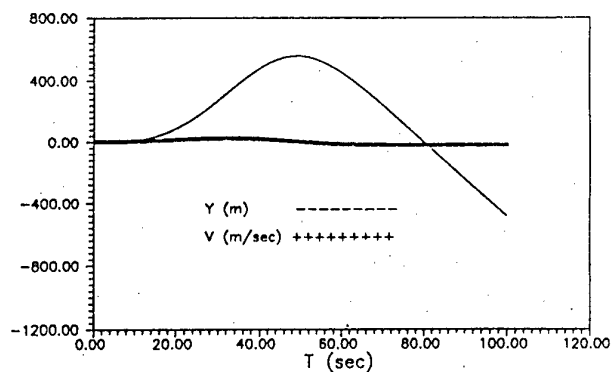
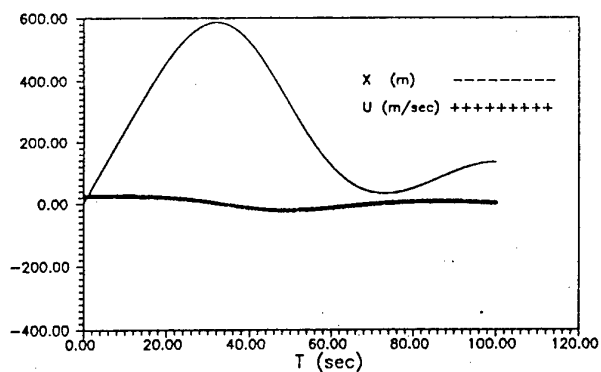
References

1. Hauser, J., Sastry S. and Meyer G., "On the Design of Nonlinear Controllers for Flight Control System". Proceeding of the AIAA Guidance, Navigation and Control Conference, AIAA, Washington DC, Aug. 1989.
2. M. Fliess, "On a possible connection between volterra series and nonlinear optimal control". Proc. Conf. In Science and System, 1983.
3. Andrew An, "Some subjects of nonlinear control and their application in flight control". Doctoral dissertation of the Beijing University of Aeronautics and Astronautics, 1993.11

4. Andrew An etc, "Geometry nonlinear optimal feedback tracing in helicopter positioning control", ICAS, USA, 1994

5. Jenney and Decker, "Maneuverability Criteria for Weapons Helicopters", AHS 20th Forum, 1964

Appendix



Design Method of an Autonomous Helicopter Flight Controller by a Neural Network

Hiroaki NAKANISHI *, Akira SATO † and Koichi INOUE ‡

Email: nakanishi@vib.kuaero.kyoto-u.ac.jp

Key Words: Guidance and Control, Stability and Control, Helicopter

Abstract

This paper describes an approach for designing an autonomous flight control system of an unmanned helicopter by use of a neural network. Because only a nonlinear flight simulator in which information about the dynamics of the helicopter is not available, can be used in designing controller, an efficient method to design a controller is not found so that trial-and-error is inevitable in conventional design methods. Therefore we use a neural network and train it to be a controller without the knowledge about the dynamics of the helicopter. But conventional training algorithm based on gradients needs an exact model of the plant because the Jacobian of the plant is necessary. To overcome this difficulty to train a neural network, we propose to use Powell's conjugate direction algorithm for training, and any information about the dynamics of the helicopter is not necessary to design controllers. Numerical simulations show the effectiveness of our method.

1 Introduction

Classical methods are often used in designing an autonomous flight controller of an unmanned helicopter, so that linear controllers are usually used. But the dynamics of the helicopter is highly nonlinear, so the controller cannot use the capacity enough. Nonlinear controllers of the helicopter are investigated in [1], and it is based on feedback linearization technique. But it is assumed that the dynamics of the helicopter is fully known. In conventional methods, the exact dynamics must be known so that exact aerodynamic coefficients are necessary to design controllers. But it is hard to obtain exact aerodynamic coefficients. In many cases, parameters of the plant are very important, so that they are hardly opened to the public.

One of attractive ability of neural networks is that they can approximate complex nonlinear functions[2,



Figure 1. YAMAHA RMAX

3], and the neural network becomes a desirable function by training. The most famous training algorithm is the Error Back-Propagation algorithm, which is based on the gradient method. Many researchers used the ability of neural networks to design control systems[4, 5]. There are two approaches to design controllers by use of a neural network. One is to use the neural network as adaptive controller (on-line training approach), and the other is designing a controller by training a neural network (off-line training approach). In [6], on-line training is investigated, but off-line training is still needed to design an approximated controller by a neural network and a known mathematical model is necessary in the off-line training. Most methods to design controllers by off-line training a neural network are based on the gradient method, so that calculating exact gradient is necessary, that is, the Jacobian of the system is needed to calculate it. Therefore the exact mathematical model of the plant is needed to train by conventional methods.

In this paper, a design method of autonomous flight controllers of the unmanned helicopter, YAMAHA RMAX shown in Figure 1, is investigated. Aerodynamic coefficients are not public and the mathematical model of RMAX cannot be obtained, but a flight simulator of RMAX is offered by YAMAHA Motor CO.,

*Research Associate, Department of Aeronautics and Astronautics, Graduate School of Engineering, Kyoto University

†YAMAHA Motor CO., LTD.

‡Professor, Department of Aeronautics and Astronautics, Graduate School of Engineering, Kyoto University

LTD.. The flight simulator is developed for checking controllers before flight experiments, and any information about the dynamics of RMAX is masked. In conventional methods, there is no way except for trial-and-error, to design controllers using only the flight simulator. But trial-and-error needs great efforts and costs time. To overcome these difficulty, we use a neural network to design flight controllers, and propose to use the Powell's conjugate direction algorithm[7] for training the neural network, so that any information about the dynamics of the helicopter is not necessary to train controllers. Our method is easily to be built into the flight simulator to design an autonomous flight controller automatically. In this paper, two typical controller, nonlinear feedback controller and gain scheduling controller, are treated, and the effectiveness of our method is shown by some numerical simulations.

2 Neural Network and Training Algorithm

A neural network can emulate any continuous function to any desired accuracy[3] so that many researchers attempt to apply the neural network to control engineering. Figure 2 shows the structure of a multi-layered neural network, and three layered neural networks are used in this paper. Among training algorithms, the Back-Propagation is the most famous. In the Back-Propagation algorithm, the desired response, which is called the teacher signal, is necessary, and the gradient toward the desirable response is calculated. Because the gradient is necessary in training a neural network, an exact mathematical model of the plant is necessary. It is hard to obtain the exact mathematical model of the plant, and some important parameters of the plant are often not open to public. Especially, aerodynamic coefficients and other parameters of the unmanned helicopter, YAMAHA RMAX, are not public, so that training methods based on gradients are not available.

We had proposed a training method based on Powell's conjugate direction algorithm[8], which can be applied to problems which include not-differentiable functions. In the Powell's conjugate direction algorithm, conjugate directions of the cost function are computed without calculating its derivatives, and we can compute minimum or maximum of the cost function. The basic algorithm is as following. The function to be minimized is $f(x)$ and x is a vector of R^n , and s_1, s_2, \dots, s_n are linearly independent directions of R^n .

1. Determine x_0 as start point.
2. For $i = 1, 2, \dots, n$, calculate λ_i so that $f(x_{i-1} + \lambda_i s_i)$ is a minimum, and define $x_i = x_{i-1} + \lambda_i s_i$.
3. Find the integer $m(1 \leq m \leq n)$, so that

$\{f(x_{m-1}) - f(x_m)\}$ is a maximum, and define $\Delta = \{f(x_{m-1}) - f(x_m)\}$.

4. Calculate $f_3 = f(2x_n - x_0)$, and define $f_1 = f(x_0)$ and $f_2 = f(x_1)$.
5. If either $f_3 \geq f_1$ or $2(f_1 - 2f_2 + f_3) \cdot (f_1 - f_2 - \Delta)^2 \geq (f_1 - f_2)^2$, use old directions s_1, s_2, \dots, s_n for the next iteration and use x_n for the next x_0 , otherwise
6. defining $s = x_n - x_0$, calculate λ so that $f(x_n + \lambda s)$ is a minimum, use $x_1, s_2, \dots, s_{m-1}, s, s_{m+1}, \dots, s_n$ as new directions and use $x_n + \lambda s$ as the starting point for the next iteration.
7. Repeat from 2.

Details of the algorithm are shown in [7], and the method to design an optimal control system by use of neural network is shown in [8]. In this method, only I/O data is required to design controllers and the Jacobian of the plant is not necessary, so that it can be applied to if I/O data can be available. Therefore, the training method can be used to design an autonomous flight controller even if information about the dynamics are masked. If the state of the helicopter is available in a flight simulator, our training algorithm is easily built into it so that a flight controller is automatically designed by the neural network.

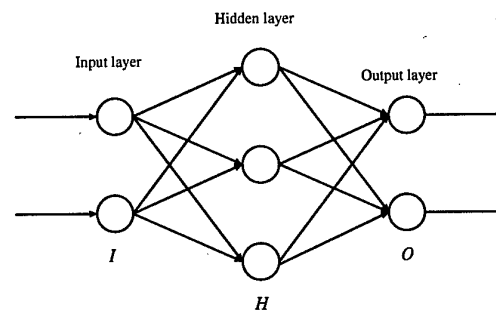


Figure 2. Multilayered Neural Network

3 Designing Autonomous Flight Controller

In this section, the flight simulator which is offered from YAMAHA Motor CO., LTD. is explained briefly. Figure 3 shows an outlook of the simulator, and it is developed on Microsoft Windows system, and is a 6-DOF simulator including nonlinear effects. In the program of the simulator, any value which describes the state of the helicopter is public and available, but the dynamics is not. Because it is developed for the final

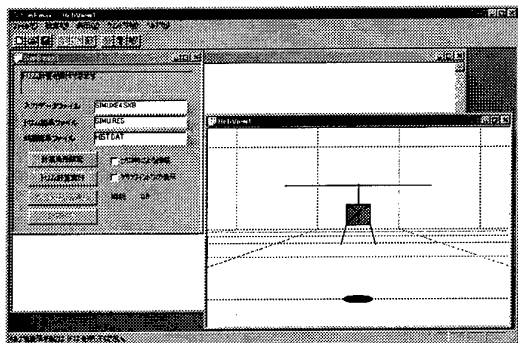


Figure 3. Console window of the flight simulator

the developing controller before on-board testing, not for designing controllers, the purpose of the simulator is achievable without information about the dynamics of the helicopter. But the knowledge is required in designing controllers, and sophisticated controllers cannot be designed efficiently without it. If a simulator in which the dynamics is not open to public is only available and any other information cannot be used, then only trial-and-error by use of the simulator seems to be the solution to design controllers. But trial-and-error costs much time and computations, it may be hard to carry out and is not very efficient. Therefore an efficient method to design controllers in which any information except for the state of the helicopter is not used is desired. The method explained in the previous section is suitable for this purpose, and it enables to design sophisticated controllers even if important parameters are masked in designing. In this paper, it is assumed that the simulator can emulate the real helicopter RMAX perfectly.

4 Simulations

In this paper, positioning control of the helicopter is considered. Two typical controllers are trained by neural networks. For simplification, there are some control surfaces (elevator, aileron, rudder and collective) but each controller is designed independently. In our simulations, controllers of rudder and collective are fixed, and PID controllers which are originally built in are used. Therefore only the movement of the helicopter in a horizontal plane is considered and controlled by neural networks. $[x, y, z]$ denotes the helicopter position in the local ground frame, x, y axes points forward and right respectively.

4.1 Nonlinear Feedback Controller

In this simulation, a neural network acts as a nonlinear feedback controller and outputs the control sig-

nal. The block diagram is shown in Figure 4. At first, the controller of aileron is also a fixed PID controller and x-positioning controller is trained by a neural network. The network has 7 hidden units, and inputs of the neural network are positioning error $d - x$, velocity v_x , pitch angle θ , and pitch rate q . The output of the neural network is the signal to the elevator. In training, the performance index described as

$$J = \sum_{t=0}^T (x(t) - d(t))^2 + v_x^2(t) + 10\theta^2(t) + 10^3 q^2(t) \quad (1)$$

is used and it is minimized by the training. The position controlled by the neural network is shown in Figure 5. In this simulation, the desired position d is switched stepwise at $t = 0.5 (d = 3)$ and $t = 30 (d = 0)$, and the figure shows that the neural network can learn to be a x-positioning controller properly.

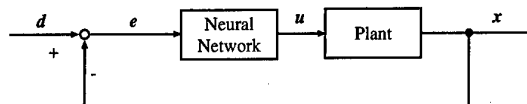


Figure 4. Nonlinear feedback controller

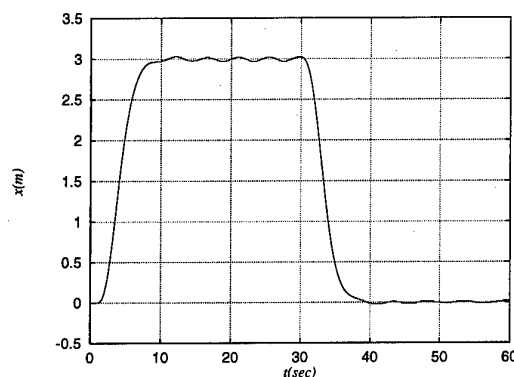


Figure 5. Step response (x)

4.2 Gain Scheduling Controller

Gain scheduling is very powerful method, but it is not easy to design. Our method is easily applied to design gain scheduling controller, and the block diagram is shown in Figure 6. In this simulation, y-positioning controller is designed to training a neural network. Positioning error $d - y$, velocity v_y , roll angle ϕ and roll rate p are inputs to the network, and it outputs gains of the controller, and the controller outputs the control signal to aileron. In training the network, other controllers are fixed, the performance index described as

(2) is minimized by training. Figure 7 shows the step response.

$$J = \sum_{t=0}^T 10(y(t) - d(t))^2 + v_y^2(t) + \phi^2(t) + p^2(t) \quad (2)$$

Moreover, Figure 8 shows the flight path controlled by x and y positioning controllers which are trained grain scheduling controllers, and the desired flight path is described as

$$\begin{bmatrix} x \\ y \end{bmatrix} = \begin{bmatrix} 2 \cos(3\sigma) \cos(\sigma) - 2 \\ 2 \cos(3\sigma) \sin(\sigma) \end{bmatrix} \quad \sigma \in [0 : 2\pi] \quad (3)$$

From Figure 8, it is shown that controllers using neural networks have good performance.

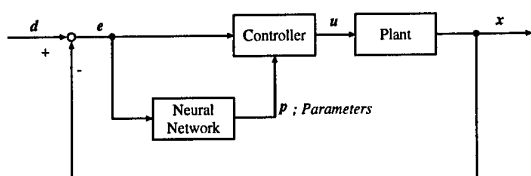


Figure 6. Gain scheduling controller

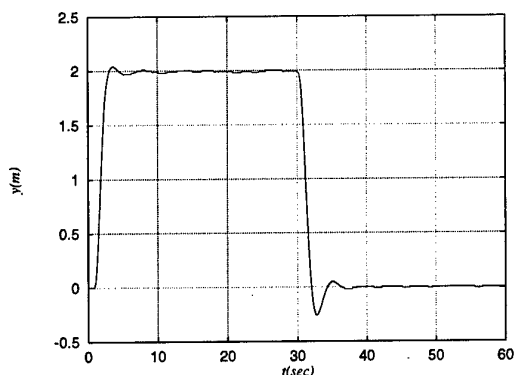


Figure 7. Step response (y)

5 Conclusions

In this paper, a method to design autonomous flight controllers by use of a neural network is proposed. Although any information about the dynamics of the helicopter is not available, controllers can be designed efficiently by the method. Our design method is easily built in simulators of any other plants, so that effective controllers can be designed without being open to public. Simulation results shown in this paper are still not enough, but it is expected that flight controllers of the autonomous helicopter will much improved by our method.

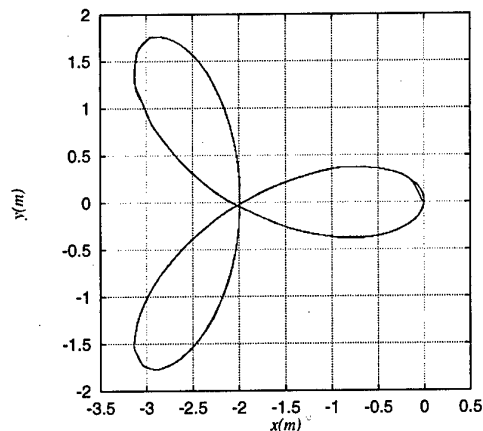


Figure 8. Flight path controlled by neural networks

References

- [1] M.W. Heiges, P.K. Menon and D.P. Schrage. Synthesis of a Helicopter Full Authority Controller. In *Proceedings of the AIAA Guidance, Navigation and Control Conference*, pages 207-213. AIAA, 1989.
- [2] D.E. Rumelhart, G.E. Hilton, and R.J. Williams. *Parallel Distributed Processing*. MIT Press, 1986.
- [3] K. Funahashi. On the Approximate Realization of Continuous Mappings by Neural Networks. *Neural Networks*, 2(3):183-192, 1989.
- [4] K.S. Narendra. Gradient Methods for the Optimization of Dynamical Systems Containing Neural Networks. *IEEE Trans. Neural Networks*, 2(4):252-262, 1991.
- [5] K.S. Narendra and K. Parthasarathy. Identification and Control of Dynamical Systems Using Neural Networks. *IEEE Tran. Neural Networks*, 1(1):252-262, 1990.
- [6] B.S. Kim and A.J. Calise. Nonlinear Flight Control Using Neural Networks. *Journal of Guidance, Control and Dynamics*, 20(1):26-33, 1997.
- [7] M.J.D. Powell. An Efficient Method for Finding the Minimum of a Function of Several Variables Without Calculating Derivatives. *Computer Journal*, 7:155-162, 1964.
- [8] H. Nakanishi, T. Kohda and K. Inoue. A Design Method of Optimal Control System by Use of Neural Network. In *Proceedings of the 1997 International Conference on Neural Networks*, pages 871-875. IEEE, 1997.

A Study of the Flight Safety under IMC

Yuichi Kumamoto*, Hajime Fujimoto*, Takaki Amano**, Keiji Kobayashi***

Advanced Technology Institute of Commuter helicopter LTD.
Kakamigahara City, Gifu-Pref. 504-8710 Japan

Key Words: Flight Simulator, Helicopters, Guidance and Control

ABSTRACT

Recently, accidents of small aircraft, especially that of helicopters, have been increased in Japan. The various reasons for that are supported. One of the most attractive and most important causes is an operation in bad weather (poor visibility). The cause can be divided into two cases, one is the loss of communications and his/her position during the unexpected rapid weather change, and the other one is the excessive workloads by the loss of visual cue (ex. Vertigo).

Under the above circumstances, the drastic improvement of the helicopter operations safety in bad weather has been researched and developed from 1994 to 2000 by ATIC (Advanced Technology Institute of Commuter helicopter Ltd.). Our goals are;

1. To improve the ability of instrument flight of helicopters.
2. To improve the ability of the IFR operations based on the future navigation systems with the Global Positioning System (GPS).

After introducing the outline of whole "Flight Safety study", this paper mainly describes the Automatic Flight Control System with DGPS helicopter precision terminal procedures to enable near zero-zero approaches to a hovering at heliports, including the recent result of flight simulation.

1. INTRODUCTION

1.1 Technical problem for helicopter IFR operation

Recently, safety and dispatch reliability of the helicopter are taken seriously, the operation by the instrument flight is required in order to realize safety and reliability in which the helicopter is equivalent to the fixed wing aircraft. However, there is a CNS problem in present helicopter IFR system and especially, the technical problem have been left for the safe operation in bad weather.

1. It is difficult to operate IFR using the ATC from the ground in low altitude because communication and radar system does not work at this region.
2. Present IFR systems and standards are for

fixed wing aircraft, so they're not suitable for the IFR operation of the helicopter.

3. The IFR operation to a low altitude at the heliport is very difficult in present IFR system.

From such circumstances, the accidents also occur frequently because of sudden weather change in VFR operation (14 times for 12 years from 1985). Not only foregoing problem but also other problems such as noise and low dispatch reliability have been left in technical problem to be solved.

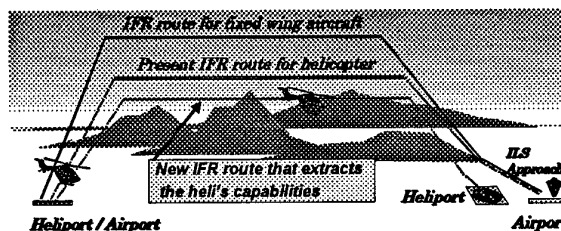


Fig. 1 Present helicopter IFR operation

1.2 Outline of ATIC

The Advanced Technology Institute of Commuter helicopter (ATIC) was established in March 1994 with investments from the Japan Key Technology Center (organization of the Ministry of International Trade and Industry and the Ministry of Posts and Telecommunications) to address these technical aspects of helicopter flight.

There are two research themes in the ATIC - noise reduction and flight safety improvement. ATIC Research Dept. No. 1 is undertaking research into external noise-reducing technology, while research into helicopter flight safety technology is being conducted by ATIC Research Dept. No. 2.

For flight safety, many researches have been executed and future air navigation system (FANS) using the GPS has been constructed in the world. The helicopter IFR operation using infrastructures such as GPS system has been also considered in Japan and it will be operated in early 21st centuries.

For the above circumstances, the ATIC research Dept. No.2 has studied the helicopter which can

* Guidance Research Engineer

** System Research Engineer

*** Control Research Engineer

ensure safety and operation reliability under IMC by dividing the goal into two of "simplification of the navigation" and "simplification of the flight". In this paper, we describe mainly the simplification of the navigation.

We have studied the following technologies to reduce the pilot workload.

1. technology which accurately navigates the fixed flight path from the takeoff to the landing by manual operation and automatic operation.
2. technology that the pilot can intuitively recognize that the operation is rightly carried out.
3. technology which can display information effectively for pilot.

Research progress of the ATIC research Dept. No.2 is shown at table 1. The concept study was carried out in 1994, and the flight simulations were performed 8 times from 1995 to 1998. The ground test was carried out from 1998 to 1999 using hardware and software that will be actually used in flight test.

Table 1 ATIC schedule

94	95	96	97	98	99	2000
Concept Study	Design and Development			Ground Test	Flight Test	

We briefly introduce the flight verification system, then describe the development of flight management system for civil helicopters, which reduce the pilot workload, including the results of the evaluations obtained using the latest flight simulations.



Fig. 2 The Flight Experiment Helicopter

2.DESIGN OF THE APPROACH PROFILE

It is necessary to develop IFR operation ability by

utilizing capabilities of the helicopter in order to improve the flight safety and dispatch reliability under IMC, and there are some problems to be solved for the IFR operation in approach and landing. These elements are concretely required.

1. It shouldn't interfere with the operation of fixed wing commercial aircraft around the airport, and it should be operated simultaneously.
2. The operation in the pinnacle heliport should be enabled.
3. Noise problem in the building roof operation in urban area or heliport operation should be overcome.

In this study, the course which combined a steep angle profile of 12 degrees considering low noise with the TA vertical take-off and landing approach profile was designed (Fig. 3).

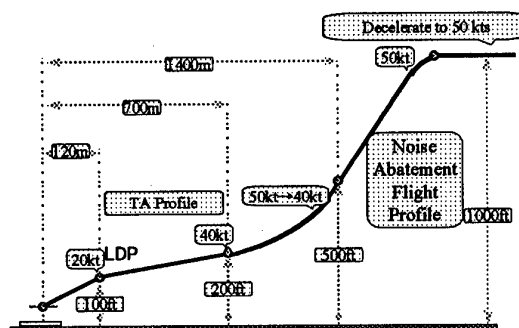


Fig. 3 Approach Profile

By flying at 50kt and -1000fpm, the region that is easy to generate slap noise is avoided under low-noise profile approach. The transition segment for connecting with the conventional TA profile is set after the low-noise profile end, and the speed is decelerated from 50kt to 40kt, and the height is also descended from 500ft to 200ft. It is similar to the TA profile after the transition segment end. This profile has been confirmed that it is available for the practical use by using actual helicopter (BK117).

Fig. 4 shows the comparison the above-mentioned flight path with the course in the ILS approach used in the conventional helicopter IFR operation. We see from fig. 4 that it is not necessary to operate in low altitude for long time if we use the new course, then it's possible to solve the noise problem very easily. And, it is also possible to prevent the interference of the fixed wing aircraft because the conventional ILS approach course can be avoided by flying this course. In addition, it is also possible to land on heliport and building roof in urban area where ILS has not been provided.

LDP-landing decision point

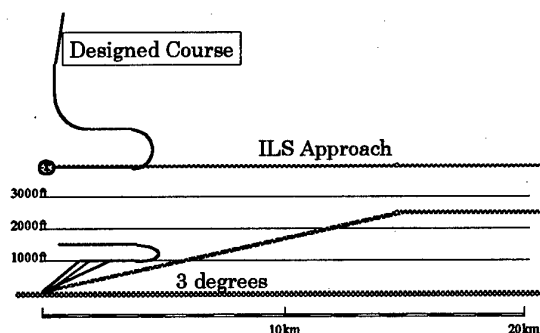


Fig. 4 Comparison with New App. and ILS

3. DESIGN REQUIREMENT

The design requirement of the guidance function for automatic flight is shown in table 2. These values are designed, as the error for automatic flights, without including the error of GPS and the accuracy of hardware. The flight path for the automatic flight is divided into three of en-route, approach and hovering. And requirements for height error, lateral deviation, speed error are set for each segment. En-route is defined as the segment from SID to STAR and approach as the segment to the hovering after the STAR.

Table 2 The Design Requirements For Automatic Flight

	En-route	Approach	Hovering
Herr[ft]	± 30.0	± 30.0	± 5.0
Dev[ft]	± 50.0	± 50.0	± 20.0
Verr[kt]	± 10.0	± 10.0	—

4. RESULTS OF FLIGHT SIMULATION

A simulated cockpit for the simulation was prepared and used in this study connected to a dome-type flight simulator of Kawasaki Heavy Industries, Ltd. (KHI).

Our primary evaluation results thus far are described below, based on the latest simulation. The wind conditions were checked around the Gifu Air Base used by flight test carried out from the middle in 1999, we set wind direction 315°, steady wind of 20kt and gust.

The automatic flights were carried out from en-route to hovering in AEO (All Engine Operative) and BLD (Balked LanDing) /CLD (Continued LanDing) in OEI (One Engine Inoperative). By performing sufficient flight simulations prior to a flight demonstration, satisfactory performance, reliability, and safety can be established before starting the flight tests.

4.1 Results of the evaluation on en-route

Fig. 5 shows the time histories of the velocity error on en-route. We see from the graph (a) of fig. 5 that velocity error was within ± 3 knots in no wind condition. It is satisfied with the design requirement for

automatic flight that we established. On the other hand, the graph (b) of the velocity error in wind condition is not smoother than the result of the above. It is considered that it is based on the effect of the gust. There is a part that exceeds the design requirement in wind condition. But the design requirement has been established under no wind condition and the helicopter is controllable in this case, of course there is no tendency to diverge by gust.

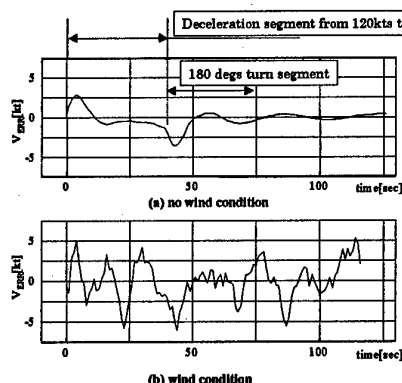


Fig. 5 V error (En-route)

Fig. 6 shows the graph of the deviation and height error on en-route. The frame in bold line in the graph shows the design requirement of the automatic flight set in ATIC.

In case of there being no wind, there is a part in which the height error deviates from the design requirement a little. It is occurred in the leg that decelerates from 120kt to 80kt. This cause is because the rate-of-climb arises in order to do the pitch-up in the deceleration. And, it is equal on the height error in case of the no wind condition and wind condition. On lateral deviation, there is a part that deviates from the design requirement. It is occurred near the changeover from the turning descent leg to the level straight-line leg.

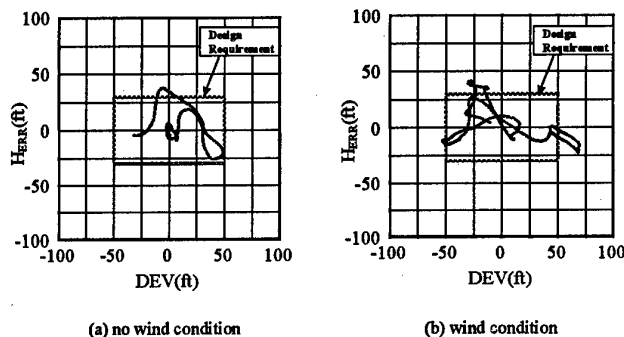


Fig. 6 Results of Evaluation (En-route)

4.2 Results of the evaluation on approach

Fig. 7 shows the time histories of the velocity error on approach. We see from the graph (a) of fig. 7 that the velocity error was within ± 3 knots in no wind condition and it was satisfied with the designed requirement. Attitudes of the helicopter were changed so frequently by deceleration and descent that the velocity error fluctuated frequently in comparison with the case of en-route. The graph (b) of fig. 7 shows the velocity error in the case of wind condition. We see from the graph (b) of fig. 7 that the motion of the velocity error calmed down from about 120 seconds. The wind condition causes this result. At the beginning of the evaluation, though the helicopter was under the influence of gust because airspeed was used for reference speed, reference speed was changed to the ground speed by height of helicopter (about 500 ft), then the helicopter was out of influence of gust. It is clear that the velocity error was satisfied with the design requirement because it was within ± 5 knots in both cases.

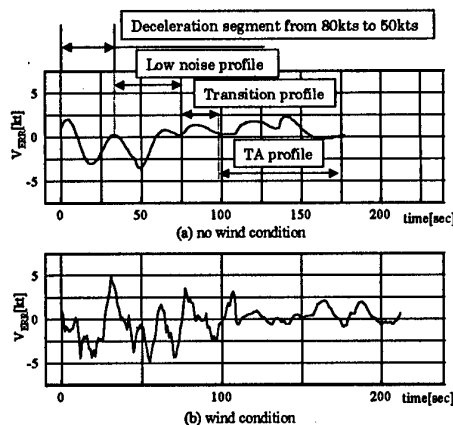


Fig. 7 V error (Approach)

Fig. 8 shows the graph of the deviation and height error on approach. We can see from fig. 8 that both deviation and height error were satisfied with the design requirements. The accuracy on the approach is better than that on en-route, because by using the gain scheduling by the airspeed, it becomes higher gain as lower speed.

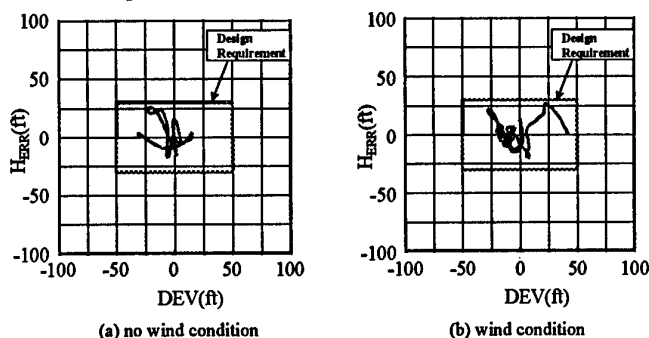


Fig.8 Results of Evaluation (Approach)

5. CONCLUSIONS

In this paper, the development of a flight management system especially automatic flight for civil helicopters being undertaken by ATIC to reduce pilot workloads has been described. The design requirements are established, considering the operation of civil helicopters, designed a guidance function based on those requirements, and evaluated the results of our design through flight simulations. The following results were obtained:

1. We designed the approach profile that could solve both of "noise problems at heliport or building roof in urban area" and "interference with the fixed wing aircraft operation in the airport" and we examined the profile for automatic flight.
2. The guidance function in the engine failure was examined. And two logic of go around mode and continued landing mode were established.
3. Then, we confirmed through the flight simulation that the guidance function was satisfied with our design requirements.

The results of override function were omitted by circumstances of the space this time,

4. We also examined the override function by flight simulation, and we confirmed that the function was very useful to the automatic flight.

We established the automatic flight, the flight simulation test for FD flight will be carried out at least 3 times in future, and pursue to establish the logic for FD flight.

The flight test is also started from September 1999, and about 100 flights have been scheduled including the evaluation of the automatic flight and FD flight.

REFERENCES

1. Y.Kumamoto, H.Fujimoto, M.Takasaki, K.Kobayashi, A Study of the Guidance function for Commuter Helicopter of the 36th Aircraft symposium Oct. 1998.
2. Y.Kumamoto, H.Fujimoto, T.Amano, K.Kobayashi, A Study of the Flight Safety under IMC of the 25th European Rotorcraft Forum Sep. 1999.

A Natural Way to Implement WADGPS in East Asia: Decentralized WADGPS

Changdon Kee* and Chul-Soo Pyong**

*Department of Aerospace Engineering, Seoul National University
Seoul, Korea, 151-742*

Key Words: GPS, GNSS, SBAS, WAAS, WADGPS

ABSTRACT

With the advent of the globalization era, interest has been growing in the operation of Global Navigation Satellite System (GNSS). Three systems are currently under development; the WAAS in the United States, the EGNOS in Europe, and the MSAS in Japan. In particular, the WAAS is being developed by the FAA and the Phase 1 WAAS is now scheduled for September 2000. Japan will use its own satellites (MTSAT-1 and MTSAT-2) as an interface to the civil user community. International Civil Aviation Organization (ICAO) has named this generic WAAS-type system a Satellite-Based Augmentation System (SBAS). The SBAS will be a supplementary navigation aid for all phases of flight down to category I precision approach. While reducing cost and complexity, it will eventually be a primary means of navigation for en-route travel and non-precision approaches air navigation.

Considering the above situations, it is imperative that we establish Wide Area Differential GPS (WADGPS) covering East Asia to complete the aforementioned GNSS. The GNSS then allows international aviation users to fly worldwide with a single avionics system. Indeed, it is urgent to discuss the Asian WADGPS Network Construction Plan with all the Asian countries concerned. Under these imminent circumstances, this paper proposes a totally new, "revolutionary" Asian version of WADGPS, which has decentralized parallel processing capabilities. As a result, each Asian country will gain the advantages of control from decentralized WADGPS that breaks from existing architecture.

* Assistant Professor, Department of Aerospace Engineering

** Graduate Student, Department of Aerospace Engineering

1. INTRODUCTION

WADGPS is based on station-network, which usually comprises Wide-area Reference Stations (WRSs) and Wide-area Master Station (WMS). Multiple WRSs observe all GPS satellites in view and collect GPS signals received from all of them. The WRSs send their raw measurement data to central processing site referred to as WMS. The WMS processes the raw data to generate WADGPS vector corrections; satellite ephemeris & clock correction and ionospheric correction [1]. Taken together, the estimated WADGPS corrections are transmitted to users via geosynchronous satellite. Using the broadcast corrections, users calculate their positions with a desired accuracy. In short, a standard WADGPS basically turns to centralized architecture, in which all the raw measurements observed at local sensors, namely WRSs, are converged into one central processor, WMS to yield a vector of WADGPS corrections and its covariance matrix. While producing the optimal estimate, this framework may experience an overwhelming concentration of raw measurements and a high computational load of central processor. In fact, the WMS has such predominant power over the whole network that the sovereignty of WMS will be a critical issue among interested parties.

Yet, a standard centralized WADGPS hardly seems to be a natural solution for the East Asian region. In an attempt to ultimately achieve the real-time implementation of WADGPS in East Asia, international collaboration among the interested Asian countries is essential. But the region's countries are of a deep-rooted heterogeneity with respect to historical and political background. We still find a significant level of international tensions between democracy and communism. It is related to our and many of our neighbors' questions as to whether a nation with WMS's sovereignty can be trusted as a security partner.

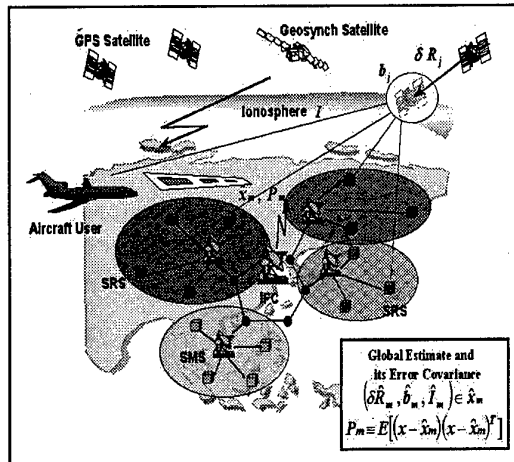
On the grounds of an excessive concentration of raw measurements and a lack of mutual confidence, each country might hesitate to participate in Asian WADGPS Network Construction Campaign. Some subtle matters could undermine the goals of Asian WADGPS Network Construction.

To mitigate these impediments, this paper develops a totally new, "revolutionary" WADGPS version with decentralized parallel processing capabilities. Decentralized hierarchical architecture would provide augmentation to overcome the structural deficiencies of existing architecture and would also solve the control issue of the network by distributing an exorbitant mission of central processor into several local processors and guaranteeing operational independence within a homogeneous local area. Therefore it could more easily induce "constructive engagement" in the Asian WADGPS project and eventually promote the feasibility of this project.

2. DECENTRALIZED WADGPS ARCHITECTURE

The WADGPS network could be regarded as a kind of large-scale multisensor system, which basically includes scores of widely dispersed sensors and a few data processors. This paper suggests a more neutral formulation for "extended interoperability", which is also applicable to the interoperation and integration of distributed SBASs [2]. This formulation allocates an inordinate mission of central processor into several local processors and places the autonomy of their operation on each homogeneous local area. Each local processor at each step generates its associated error covariance as well as its own estimate, based solely on its own available local information. Meanwhile, global fusion filter is newly introduced in a higher level of the hierarchy. All such decentralized structures assume some amount of local processing at local processors, the results of which are communicated to a global fusion filter further up in the hierarchy. The global fusion filter then combines all the local estimates and their corresponding error covariances to generate the global estimate and error covariance. The concept of decentralized WADGPS is depicted in Figure 1.

First of all, in the next section, we design fundamental infrastructure of WADGPS network in the conceptual view.



3. INFRASTRUCTURE

The following subsections describe the detailed function of fundamental infrastructure in the proposed "Decentralized WADGPS."

3.1 Sub-area Master Station (Local Processor)

The primary function of local processor is to take the atmospherically corrected pseudoranges and the ionospheric measurements from local sensors, to compute its associated error covariance as well as local estimate, and to transmit those local correction information to global fusion filter further up in the hierarchy. Another major function of master station is to monitor the integrity of the signal. Figure 2 shows a schematic diagram of local processor.

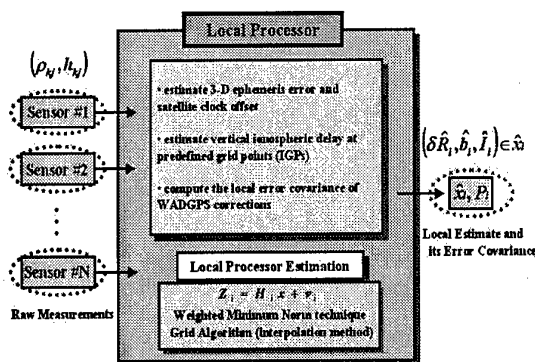


Fig. 2. Schematic Diagram of Local Processor

As suggested by this figure, each master station is dedicated to an individual subsystem. It is also in direct contact with sub-area tracking sites. Each local processor

plays a crucial role as "prefilter" in compressing the local sensor data and reducing the fusion filter processing rate. The independent operation of prefilter allows such a concurrent or parallel processing at the local nodes that it can achieve substantial gains in computation speed.

3.2 Information Fusion Center (Global Fusion Filter)

The primary function of global fusion filter is to combine the information from the separate local processors, to generate the global estimate and error covariance, and to broadcast those global correction information to geosynchronous satellite through GEO Uplink System (GUS). Figure 3 shows a schematic diagram of global fusion filter.

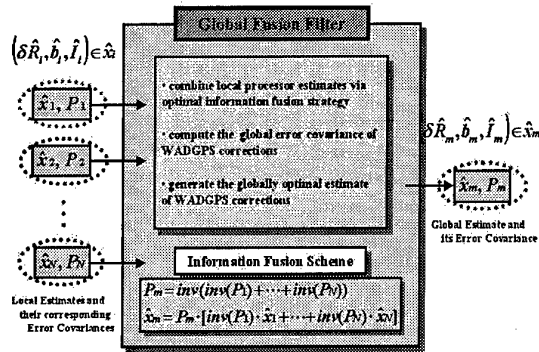


Fig. 3. Schematic Diagram of Global Fusion Filter

On the other hand, the information fusion center (IFC) has much more restrictive power than current wide-area master station (WMS). The IFC is very limited in responsibility to collect a high level of distributed information and then to construct its optimal combination through information sharing approach. It only provides complementary and cooperative data while retaining specific levels of independence. Realistically, this paper recommends that each subsystem have its own IFC for an autonomous operation.

Vector Correction Fusion

Dr. Carlson already developed the federated Kalman filter (FKF) amenable to a parallel processing environment in 1990 [3]. The information sharing approach implemented by the FKF can be summarized by the following additive equation.

$$P_m = [P_1^{-1} + P_2^{-1} + \dots + P_N^{-1}]^{-1} \quad (1)$$

$$\hat{x}_m = P_m [P_1^{-1} \hat{x}_1 + P_2^{-1} \hat{x}_2 + \dots + P_N^{-1} \hat{x}_N] \quad (2)$$

where P_i^{-1} ($i = 1, \dots, N$) and \hat{x}_i ($i = 1, \dots, N$)

are local information matrices and local estimates, respectively.

In the structure of the above fusion filter, a globally optimal estimate and its error covariance are only obtained by the optimal combination of those local processor solutions. This conclusion suggests that the IFC can achieve global optimality by sharing only a minimum amount of high level information.

Satellite ephemeris & clock corrections are generated at each local nodes through single-point least square solution. Thus they are typical vector corrections with error covariance in matrix form. Note that there exist cross-correlations between all the GPS satellites observable at each local subsystem. At the core of fusion process, it is an indispensable procedure to search for the combination of GPS satellites commonly observable at two or more separate subsystems.

Ionospheric correction fusion of neighboring networks can be conducted in a similar way. The IFC equivalently applies a scalar version of information sharing approach to all the IGP's commonly predefined at two or more separate subsystems.

4. WADGPS SIMULATIONS

In this research, we conducted the conceptual design of the Asian WADGPS network and evaluated the performance of the overall system. Coverage area is set to be the region between $5^\circ \sim 55^\circ$ N and $100^\circ \sim 150^\circ$ E as shown in Figure 4. A total of 28 tracking sites were selected as reference station candidates of the Asian WADGPS network. Here we devise two specific alternatives for the East Asian region. A full range of performance analysis for each case is discussed and synthesized.

< Alternative I >

First of all, we divide the whole East Asian region into 4 separate sub-areas. One is Korea & Japan in Sub-Area #1, another Russia in Sub-Area #2, a third China & Mongolian in Sub-Area #3, and the fourth is the South East Asian countries in Sub-Area #4 -- for example, Taiwan, Philippines, Thailand, Vietnam, Cambodia, Singapore, Brunei, and so forth. The profile of each independent subsystem is depicted in Figure 4. We call this decomposition style "alternative I" in this paper. For the relative performance comparison, the station location of "alternative I" is set to be exactly the same as that of "alternative II".

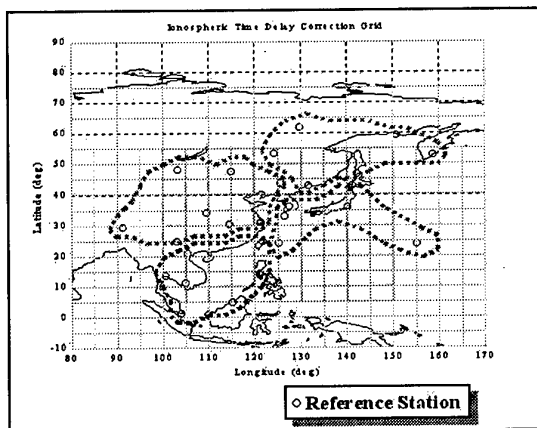


Fig. 4. Coverage Area & Decomposition of the Asian WADGPS Network (Alternative I)

Centralized vs. Decentralized

To begin with, on alternative I proposal, we performed simulations of the current centralized WADGPS and proposed decentralized WADGPS algorithms for 24 hours. Figure 5 & 6 show the contour plots of vertical positioning RMS error for centralized WADGPS and decentralized WADGPS, respectively. According to the figures, it can be revealed that the performance of centralized WADGPS is somewhat better than that of decentralized WADGPS. The former guarantees the optimality of vector correction, while the latter produces estimates that are globally optimal, or conservatively suboptimal. Therefore, the proposed decentralized architecture results in the degradation of WADGPS accuracy to some extent. However, the result of decentralized architecture is also acceptable with a sufficient accuracy.

Isolation vs. Exchange/Fusion

If a national emergency occurs in the East Asian region, each independent subsystem may stop transmitting high level information into IFC due to national security. The IFC may sometimes get out of order unexpectedly. Even in such cases, however, each local performance is still available. For such data isolation mode, the contour plot of vertical positioning RMS error is depicted in Figure 7.

Comparing data isolation mode with data exchange/fusion mode given in Figure 6, we can find that the degradation of positioning accuracy occurs conspicuously in the boundaries of the individual subsystems. Through the complementary and cooperative data processing, the overall system performance gets to exceed the union of the individual subsystem performances.

< Alternative II >

Secondly, in a more elaborate manner, we partition the whole East Asian region into 8 separate subsystems. It is called "alternative II" in this paper.

Alternative I vs. II

We also performed simulations of the alternative II formation for 24 hours. As clearly mentioned before, alternative II is practically decomposed on the basis of independent nation. Considering political circumstances and international relationships in East Asia, it seems more realistic than aforementioned alternative I. But a detailed decomposition leads inevitably to far more complicated fusion process.

Figure 8 & 9 show the simulation results of alternative II for data exchange/fusion mode and data isolation mode respectively. From the Figure 6 & 8, we can find that alternative I & II provide a virtually equal quality of navigation service throughout the whole coverage area. It is evident that the new fusion filter design has much more powerful capacity than we thought before trials.

As clearly exposed in Figure 9, there are severe coverage deficiencies at each of the individual subsystem boundaries. By sharing only a high level of distributed information with each other, individual subsystems can overcome the deterioration on the borders and expand their service area into the entire East Asian region. The direct reason of this compensation is that the increased visibility of satellites and the intersections of ionospheric sub-grids lessen a degree of uncertainties in local vector corrections and thus enable the IFC to compute more accurate estimates with the assistance of external information.

Table 1 summarizes the positioning performance of several different configurations over the whole coverage area.

Table 1. Performance Comparison of Some Different Configurations (vertical error, rms value)

Type	Up (m)	Type	Up (m)
Stand-alone	63.75	Centralized	2.01
Fusion (I)	2.62	Isolation (I)	3.19
Fusion (II)	2.62	Isolation (II)	5.13

5. CONCLUSIONS

In this study, we tried to suggest a substantial alternative to implement WADGPS in East Asia. A solution of natural way is so called "Decentralized WADGPS." It is a more neutral framework including the considerations of

political environment and international relationships. The full operational capability of the proposed Asian WADGPS network will drastically increase the safety of flight for all users by providing three-dimensional guidance for all non-precision and precision landings at virtually all qualified airports within the coverage area.

After all, in an attempt to successfully install the Asian WADGPS network, it is prerequisite to consolidate the international collaboration based on mutual benefit. Interdependence is a higher value than independence. Our challenge is to apply the principles of creative cooperation toward a synergistic effect of the Asian WADGPS project. Joint Research & Development (R&D) among the interested Asian countries will be the first step of a thorny way to final real-time WADGPS operation.

REFERENCES

- [1] Kee, C. and D.H. Shin, "Wide Area Differential GPS (WADGPS) in East Asia," *Proceedings of JSASS 11th International Sessions in 35th Aircraft Symposium*, Tokyo, Japan, October, 1997, pp.609-613.
- [2] Dai, D., T. Walter, P. Enge, and J.D. Powell, "Interoperation of Distributed SBAS: Theory, Experience and Future Perspective," *Proceedings of the ION GPS-98*, Nashville, Tennessee (USA), September, 1998, pp.1355-1364.
- [3] Carlson, N.A., "Federated Square Root Filter for Decentralized Parallel Processes," *IEEE transactions on Aerospace and Electronic Systems*, Vol.26, No.3, May, 1990, pp.517-525.
- [4] Kee, C. and C.S. Pyong, "A Solution of a Natural Way to Implement WADGPS in East Asia: Decentralized WADGPS," *Proceedings of the ION GPS-99*, Nashville, Tennessee (USA), September, 1999. (Final manuscript was submitted and accepted.)

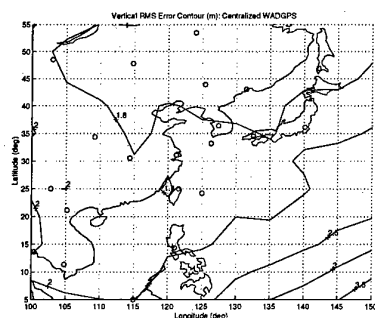


Fig. 5. Centralized WADGPS

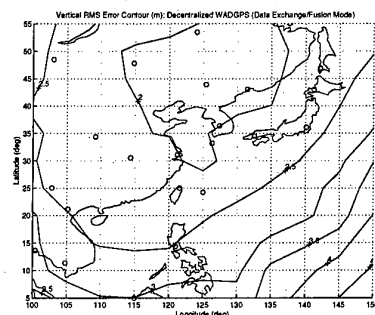


Fig. 6. Decentralized WADGPS: Alternative I or Data Exchange/Fusion Mode

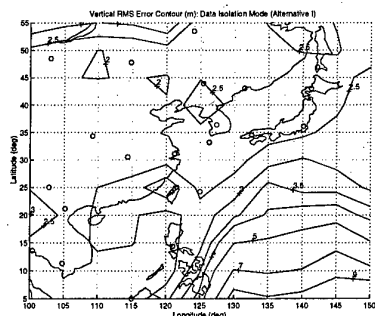


Fig. 7. Data Isolation Mode: Alternative I

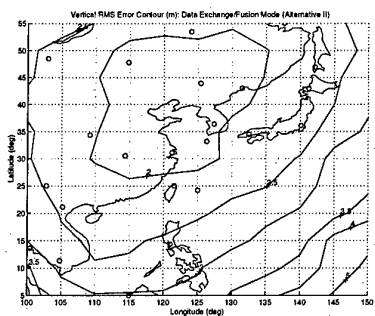


Fig. 8. Data Exchange/Fusion Mode: Alternative II

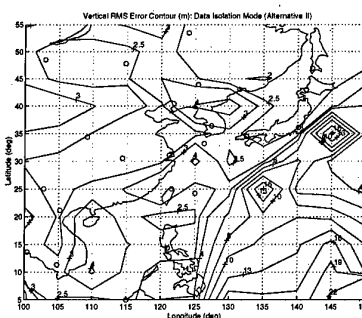


Fig. 9. Data Isolation Mode: Alternative II

INVERSE DESIGN OF THICK SUPERCRITICAL AIRFOIL

Tjoetjoe Eko Pambagio*,

Kazuhiro Nakahashi**,

Shigeru Obayashi***

Tohoku University, Sendai 980-8579-01, Japan

Key word : Wings and Airfoil Sections

ABSTRACT

In this paper, a study on designing a thick supercritical airfoil by utilizing the Takanashi's inverse design method is discussed. One of the problems to design a thick supercritical airfoil by Takanashi's method is that an oscillation of the geometry may occur during the iteration process. To reduce the oscillation, an airfoil parameterization method is utilized as the smoothing procedure. A guideline to determine the target pressure distribution to realize the thick airfoil is also discussed.

Nomenclatures

C_L	= lift coefficient
C_D	= drag coefficient
C_p	= pressure coefficient
c	= airfoil chord length
M	= Mach number
M_∞	= freestream Mach number
\hat{t}	= estimated maximum thickness ratio
t	= maximum airfoil thickness
x, z	= Cartesian coordinate in the chordwise and normal direction taking from the origin at the leading edge
Δz	= geometry correction in z direction

Introduction

The current trend in the aircraft industries is a development of transonic aircraft. Supercritical airfoil⁽¹⁾ is one of the airfoil candidate for such application. The name supercritical is given to such airfoil based on fact that the flow on an extensive region of the upper surface is supersonic flow. The purpose of supercritical airfoil is to increase the value of drag-divergence Mach number M_{dd} . Supercritical airfoil is characterized by the flatness of the upper surface, while on the lower surface there is cusplike shape near the trailing edge to produce lift. Especially thick supercritical airfoil forms an interesting subject to be studied. Thick airfoil will create more space for equipment, fuel etc. The other possibility is to create passenger cabin inside the wing section. The application of such airfoil may be found such as in the Blended-Wing-Body Commercial Transport⁽²⁾. To design such airfoil is really a challenge task. At high subsonic or

transonic speed, there is a high possibility that strong shocks will appear both on the upper and lower surfaces. Especially the presence of the shock on the lower surface could make it more difficult to design the thick airfoil.

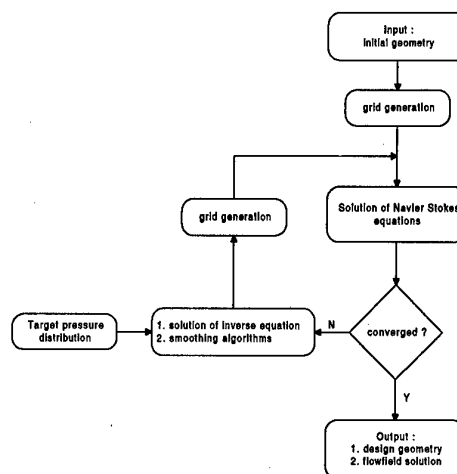


Figure 1. Flowchart of Inverse design procedure

The problem of airfoil design has been existed since the time when man started thinking about 'flying' until the present time. The solution of this problem is by applying the direct method or the inverse method. In direct method the airfoil design engineer working directly with the airfoil geometry. The geometry is modified and calculated and/or tested to obtain the aerodynamics performance. The process is repeated until the desired results are obtained.

In the inverse approach the solution begins with designing a target pressure distribution based on the required aerodynamic performances. Figure 1 shows the general illustration of the inverse design process. One of the available inverse method algorithms is the one developed by Takanashi⁽³⁾, which used the inverse formulated of transonic small perturbation equation to reduce the difference between the target pressure distribution and the computed pressure distribution of a given airfoil.

The first step of the inverse design procedure is to design the target pressure distribution based on the required aerodynamic performance. The pressure difference between the initial and the target forms an input of the inverse formulated transonic small perturbation equations. The solutions of the

* Graduate Student, Department of Aeronautics and Space Engineering

** Professor, Department of Aeronautics and Space Engineering, Member of JSASS

*** Associate Professor, Department of Aeronautics and Space Engineering, Member of JSASS

equations provide the geometry's correction Δz , which are used to modify the initial geometry to form a new geometry. The flow solutions of this new shape may be obtained by applying the Navier-Stokes equations. If, after having checked the convergence, the design requirement are not satisfied, the design cycle is repeated with the new geometry as the new initial geometry. The process is repeated until the pressure different is minimized.

In this study Takanashi's inverse method is applied to design thick supercritical airfoils, with the objective to design airfoil with the maximum thickness ratio around 18% at design Mach number of around 0.75. The potential problem of designing thick supercritical airfoil is that there is a possibility that small distortion or oscillation will occurs on the surface during design cycle⁽⁴⁾ due to shock waves. To prevent this from happening, a smoothing scheme is added to the process. The other problem is the determination of the target pressure distribution. In this paper, some guidelines to achieve the thick supercritical airfoil are discussed.

Smoothing Scheme

To add the stability of the inverse design process by means of preventing the occurring of distortion on the surfaces, a smoothing algorithm is added to the inverse design scheme. There are many smoothing algorithms available, such as polynomial fit, Bezier curve etc. In this study a possibility of applying airfoil parameterization to reduce the distortion on the airfoil surface is studied.

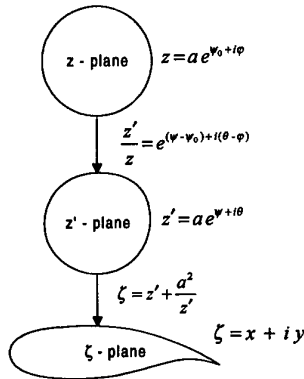


Figure 2. Illustration of transforming a circle into an airfoil shape

It is well known that a circle can be transformed into a curve which represents an airfoil shape^(5,6). Figure 2 gives the illustration of transformation process of a circle into wing section.

The circle in the z -Plane is transformed into a near circle shape in the z' -Plane, then this shape is transformed into a wing shape. In this study the latter transformation is utilized.

The transformation,

$$\zeta = z' + \frac{a^2}{z'}$$

transforms a circle in z' plane into a curve resembling a wing

section. The coordinate of z' and ζ are defined by:

$$z' = e^{\psi + i\theta}$$

$$\zeta = x + i y$$

Combines all these equations yield :

$$x = 2 a \cos \psi \cos \theta \quad (1)$$

$$y = 2 a \sin \psi \sin \theta$$

or :

$$\cos \psi = \frac{x}{2 a \cos \theta} \quad (2)$$

$$\sin \psi = \frac{y}{2 a \sin \theta}$$

The necessary calculations to obtain smooth airfoil from a given airfoil are as follows :

- The coordinates of a given airfoil are determined with respect to line joining point midway between the nose of the section and its center of curvature and its trailing edge. The coordinate of this point are taken as $(-2a,0)$ and $(2a,0)$ respectively. The value of a can be chosen simply as unity.
- From the given airfoil shape computes the function $\psi(\theta)$ using eq. 1 and 2.
- Construct Fourier Series $\bar{\psi}(\theta)$ which represents the function $\psi(\theta)$
- Computes the smoothed airfoil coordinate by using this Fourier Series.

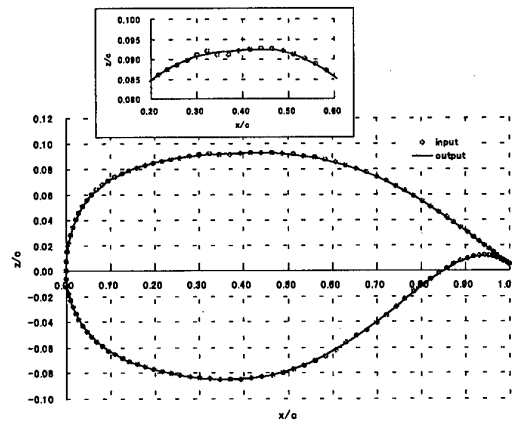


Figure 3. Results of smoothing by parametric representation

Figure 3 gives an example of the smoothing results. For a study purpose some points on the original airfoil's surface are shifted to give distortion in the airfoil shape. On the upper surface the distortion is added at the location between 30% and 50% chord, while on the lower surface between 60% and 80% chord. Looking at this figure, it shows that the smoothing process is working quite well.

The smoothing algorithms should suppress the distortion, while still resembles the originally shape. By using above algorithms the accuracy of the smoothing process depend on the number of parameter in the Fourier series. If the number of

parameter is not enough the accuracy of the resembling airfoil shape will not be good enough. The required number of parameter depends on the airfoil shape. To allow the smoothing process runs automatically a simple logic to determine the required parameters is used in the smoothing algorithms. At some chosen points the different between the Fourier Series $\bar{\psi}(\theta)$ and the target function $\psi(\theta)$ in equation 2 are calculated. If the absolute value of those different are higher than a small value ε , the number of parameter is increased.

Target pressure distribution

The main problem of utilizing inverse method as a design tool is the determination of achievable target pressure distribution. Although every airfoil shape has its corresponding pressure distribution, it does not mean that the prescribed pressure distribution will be achieved by the inverse design process. Especially for thick airfoil there is a high possibility that shock wave will appear on the lower surface which could make more difficult to design the target pressure distribution. At high value of Mach number the presence of the shock wave will be unavoidable. In designing the target pressure distribution the shock wave strength is minimized instead of eliminating. The typical characteristic of the supercritical airfoil (figure 4) will be used as a reference for the designing of the target pressure distribution.

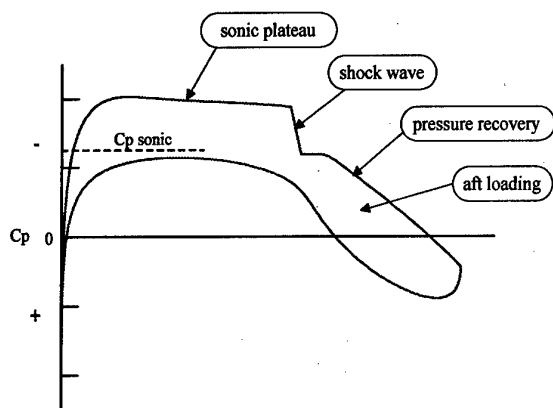


Figure 4. Typical characteristic of supercritical airfoil

The supercritical airfoil is recognized by the presence of the **sonic plateau**⁽¹⁾. On the upper surface the sonic plateau extends from near leading edge to the start of the aft pressure recovery and on the lower surface from near the leading edge to the recompression region entering into the cusp. The rearward extent of the upper surface plateau depends on the thickness of the airfoil. The thicker the airfoil, the forward the aft pressure recovery must begin. It is required that the gradient of the aft pressure recovery be gradual enough to avoid local separation problems near the trailing edge. The pressure plateau behind the shock wave is also necessary to stabilize the boundary layer.

Another problem is how to design target pressure distribution which could lead to desired properties, that is in this study, how to achieve the target thickness ratio. The constraint needed to estimate the thickness ratio based on pressure

distribution is defined by⁽⁷⁾:

$$\hat{t} = -\frac{\sqrt{1-M_\infty^2}}{2} \int_0^1 \frac{(C_{p_l} + C_{p_u})}{2} dx \quad (3)$$

where subscripts *l* and *u* indicate lower surface and upper surface respectively. The lift coefficient is estimated by using a relation:

$$C_L = \int_0^1 (C_{p_l} - C_{p_u}) dx \quad (4)$$

From the relation in equations 3 and 4 it is understandable that a combination of high C_L and \hat{t} at high Mach number will results in high pressure jump in the shock wave where in turn produces high drag value. This means that for thick airfoil at high Mach number the lift coefficient is limited to prevent high drag value. The pressure jump could be estimated by a relation⁽⁷⁾:

$$\Delta C_p = 0.6 \left[C_{p_u} + \frac{1}{0.7 M_\infty^2} \right] \frac{7(M_\infty^2 - 1)}{6}$$

where *us* denotes upstream of the shock. The shock wave is getting stronger when the speed ahead of the shock is becoming high. The sonic plateau encourage a region of supersonic flow with lower local Mach number.

By making comparison the value of \hat{t} for two different airfoil with different C_L at the same Mach number, apparently the values of \hat{t} were different and not the same with its physical value.

Based on this observation the following additional guidelines to achieve the target thickness ratio is applied:

- Starting with a known airfoil having desired thickness ratio at design Mach number chosen as a reference airfoil, compute \hat{t} and C_L .
- Design target pressure distribution where the value of \hat{t} and C_L are same with the ones of the reference airfoil.

The above-mentioned guidelines still will not guaranty that the resulted target pressure distribution is achievable. The prescribed target pressure distribution may still need to be adjusted until an acceptable airfoil shape is obtained.

Design result

In the evaluation of the aerodynamic performance of the airfoil, the full Navier-Stokes equations were solved using C-type mesh contains 129x91 grid points in the flow and normal to the surface direction respectively. The boundary layer on the airfoil was assumed to be fully turbulent and the Baldwin-Lomax turbulence was used.

Case 1.

In first case, the reference airfoil is 18% thickness ratio supercritical airfoil NASA **sc(2)_0518**⁽²⁾. The original airfoil has blunt trailing edge, but for the purposed of this study the airfoil is modified to form sharp trailing edge. The flow conditions were freestream Mach number of 0.74 and Reynolds number of 1.5×10^7 . The angle of attack was set at 0. The NACA 0014 was

chosen as the initial geometry. At design flow conditions the reference airfoil NASA sc(2)_0518 shows a strong shock on the upper surface, while on the lower surface shows a relatively weak shock. Those shocks result in high value of the drag. The objective of target pressure distribution is to improve the performance of the reference airfoil, by reducing the shock wave strength to reduce the drag value, meanwhile the value of lift coefficient and estimated maximum thickness ratio are kept same with the ones of the reference airfoil.

Figure 5 shows the design result, target and performance comparison with the reference airfoil. The inverse design process was ended after 15 cycles, because there was no change when the process was continued.

	t/c	C_L	C_D
Design	17.7%	0.408	0.012
NASA sc(2)_0518	18%	0.404	0.020

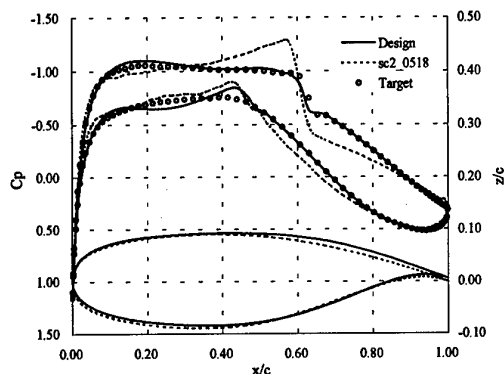


Figure 5. Design wing geometry and corresponding performances in comparison with supercritical airfoil NASA sc(2)_0518 at $M=0.74$

Although there is some discrepancy, especially near the shock location and on the lower surface, in general the target pressure could be achieved quite well. As a result the design airfoil has lower drag, while the lift coefficient and maximum thickness ratio corresponding to the ones of the reference airfoil.

Case 2.

As in the first case, NASA sc(2)-0518 was chosen as the reference airfoil. The flow condition remains the same except that the Mach number is increased to 0.76. Based on the results of case 1, different approach of designing the target pressure distribution was applied. The target pressure in case 1 was designed to try to eliminate the shock wave on the lower surface, which were not completely successful. In case 2 shock wave was also generated on the lower surface. To reduce the drag, the lift coefficient was designed to be lower than the reference airfoil. In compensation the value of \hat{t} became higher than the one of the reference airfoil. This was done to ensure that the thickness ratio of the design airfoil reached the target which was 18%.

Figure 6 shows the design result, target and performance comparison with the reference airfoil. The prescribed target pressure distribution could be achieved. The design result has lower lift coefficient than the reference airfoil, on other hand the drag is quite less than the one of the reference airfoil. The

maximum thickness ratio of the design airfoil is a fraction lower than the desired thickness ratio.

Concluding Remark

Takanashi's inverse method forms a powerful design tool for designing airfoil shape. This study shows the possibility of utilizing Takanashi's inverse method to design thick airfoil at high subsonic speed. The main problem of utilizing inverse method is designing the achievable target pressure design. Although the exact relation between the value of \hat{t} and C_L in their relation with the thickness ratio of an airfoil is not known, it has been shown that the target thickness ratio could be achieved by designing target pressure distribution in such way that the values of \hat{t} and C_L are comparable with the one of the reference airfoil. This study also shows the possibility of using airfoil parameterization as a smoothing algorithm.

References

1. Charles D. Harris, 'NASA Supercritical Airfoil, A Matrix of Family-Related Airfoils', NASA TP-2969, March 1990
2. R.H. Liebeck, M.A. Page and B.K. Rawdon, 'Blended Wing Body Subsonic Commercial Transport', AIAA 98-0438, 1998
3. S. Takanashi, 'Iterative Three-Dimensional Transonic Wing Design Using Integral Equations', Journal of Aircraft, Vol. 22, No. 8, August 1985, pp. 655-660
4. Wolf Bartelheimer, 'An Improved Integral Equation Method for The Design of Transonic airfoils and wings', AIAA paper 95-1688-CP, 1995
5. Ira H. Abbott and Albert E. von Doenhoff, 'Theory of Wing Section', Dover Publications, 1959
6. T. Theodorsen and I.E. Garrick, 'General Potential Theory of Arbitrary Wing Sections', NACA Report, No. 452, 1933
7. Shigeru Obayashi, Susumu Takanashi, 'Genetic Optimization of Target Pressure Distributions for Inverse Design Method', AIAA journal, Vol. 34, No. 5, pp. 881-886, May 1996

	t/c	C_L	C_D
Design	17.60%	0.323	0.013
NASA sc(2)_0518	18%	0.356	0.030

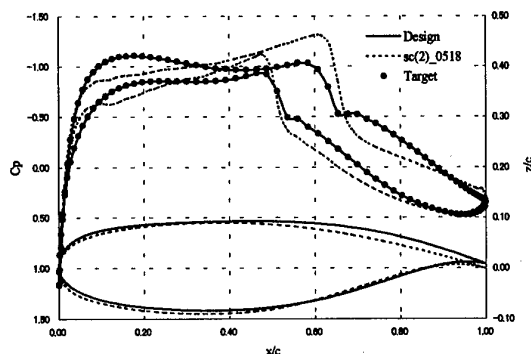


Figure 6. Design wing geometry and corresponding performances in comparison with supercritical airfoil NASA sc(2)_0518 at $M=0.76$

Unsteady Supersonic Cavity Flow Simulations Using Navier-Stokes Equations and $k-\omega$ SST Turbulence Model

Jianbo ZHANG * and Etsuo MORISHITA **

Department of Aeronautics and Astronautics
Graduate School of Engineering
The University of Tokyo
7-3-1, Hongo, Bunkyo-ku, Tokyo

Key Words: Unsteady flow, Compressible flow, Turbulent flow

ABSTRACT

Unsteady supersonic flow over cavity of length-to-depth ratio 3 at 2.5 is simulated using mass-averaged Navier-Stokes equations and Menter's $k-\omega$ SST turbulence model with cell-centered finite volume method in a two-block grid system. The numerical algorithm is based on the Roe's finite-difference-splitting scheme for the inviscid flux and central difference for the viscous flux. The equation is advanced in time with Jameson's 4-step Runge-Kutta method. The computed narrow-band tones are compared with experiment.

1. INTRODUCTION

Compressible flow oscillations over cavity-like geometry such as grooves, wheel wells, bomb bays, and cutouts occur widely in aerospace vehicles. The existence of a number of complex flow phenomena in the flow field and their potential hazardous effects on the performance, integrity and stability of the vehicles have stimulated extensive experimental, theoretical and computational researches over the years. The flow field features boundary layer separation, shear layer instability, vortex flow, acoustics radiation, shock/expansion wave interaction and self-sustained pressure oscillation.

After decades of experimental and theoretical works, it is widely believed that the discrete acoustic tones associated with the cavity flows are a result of the instability of the separating shear layer that spans the cavity, enhanced by the acoustic feedback.

The upstream boundary layer separates at the leading edge of the cavity. A shear layer is formed. The flow instability waves of the shear layer are excited and grow as they propagate downstream. The fluctuating motion of the shear layer induces a periodic mass injection and ejection at the trailing end of the cavity. This mass inflow and outflow act as the source of acoustic radiation. The acoustic disturbances propagate upstream and interact with the shear layer, thereby close the feedback loop.

The frequencies at which these tones occur can be predicted with a semi-empirical equation known as the modified Rossiter equation^[5]

$$\frac{f_m L}{U_\infty} = \frac{m - \alpha}{M_\infty / \sqrt{1 + [(\gamma - 1)/2] M_\infty^2} + 1/k_c} \quad (1)$$

where f_m is the frequency of a given lengthwise acoustic mode; L , the cavity length; U_∞ , the free-stream velocity; M_∞ , the free-stream Mach number; m , the longitudinal mode number; α , the phase shift between the vortices and the acoustic pulses, and k_c , the ratio of convection velocity of vortices to free-stream velocity. The two empirical parameters α and k_c are given values of 0.25 and 0.57.

With the development of the computational fluid dynamics and the increase of the power of the computer, numerical simulation has been becoming a viable alternative to experimental investigation of complex flow. Over the years, many efforts have been taken to simulate the cavity flow field numerically. As the cavity flows of practical interest are highly turbulent, the effects of turbulent mixing have to be properly addressed if accurate prediction of the pressure field is to be achieved. Up to now, several types of turbulence models, such as Baldwin-Lomax algebraic model, $k-\epsilon$ two-equation model, $k-\omega$ two-equation model have been used in the numerical simulation of the cavity flow, with different level of success. Menter's $k-\omega$ SST model is a recently proposed two-equation eddy-viscosity turbulence model, and is found to perform well in a variety of complex flow involving separation, even under strong adverse pressure gradient. The primary purpose of this paper is to assess the performance of this model in predicting the unsteady cavity flow field and the associated discrete acoustic tones.

2. NUMERICAL METHOD

A. Governing Equations and Solution Algorithm

Mass-averaged Navier-Stokes equations, casted in a Cartesian coordinate system read:

*Ph.D. student, Department of Aeronautics and Astronautics

**Professor, Department of Aeronautics and Astronautics

$$\begin{aligned} & \frac{\partial}{\partial t} \begin{pmatrix} \rho \\ \rho u \\ \rho v \\ \rho e \end{pmatrix} + \frac{\partial}{\partial x} \begin{pmatrix} \rho u \\ \rho u u + p \\ \rho u v \\ \rho u e + p u \end{pmatrix} + \frac{\partial}{\partial y} \begin{pmatrix} \rho v \\ \rho v u \\ \rho v v + p \\ \rho v e + p v \end{pmatrix} \\ &= \frac{\partial}{\partial x} \begin{pmatrix} 0 \\ \tau_{xx} \\ \tau_{xy} \\ u \tau_{xx} + v \tau_{xy} + q_x \end{pmatrix} + \frac{\partial}{\partial y} \begin{pmatrix} 0 \\ \tau_{xy} \\ \tau_{yy} \\ u \tau_{xy} + v \tau_{yy} + q_y \end{pmatrix} \quad (2) \end{aligned}$$

Normalized variables are used in Eq.(2). Length is normalized by cavity depth D , density by ρ_∞ , velocity by a_∞ , temperature by T_∞ , pressure and total energy by $\rho_\infty a_\infty^2$, time by D/a_∞ , and viscosity by μ_∞ . Normalized state equation is $p = \rho T / \gamma$. Total energy per unit mass $e = \frac{T}{\gamma(\gamma-1)} + \frac{u^2 + v^2}{2}$. The stress terms are

$$\begin{aligned} \tau_{xx} &= \frac{2(\mu_l + \mu_t)M_\infty}{3 \text{Re}_\infty} \left(2 \frac{\partial u}{\partial x} - \frac{\partial v}{\partial y} \right) \\ \tau_{xy} &= \frac{(\mu_l + \mu_t)M_\infty}{\text{Re}_\infty} \left(\frac{\partial u}{\partial y} + \frac{\partial v}{\partial x} \right) \\ \tau_{yy} &= \frac{2(\mu_l + \mu_t)M_\infty}{3 \text{Re}_\infty} \left(2 \frac{\partial v}{\partial y} - \frac{\partial u}{\partial x} \right) \end{aligned} \quad (3)$$

And heat flux terms are

$$\begin{aligned} q_x &= \frac{M_\infty}{(\gamma-1)\text{Re}_\infty} \left(\frac{\mu_l}{\text{Pr}} + \frac{\mu_t}{\text{Pr}_t} \right) \frac{\partial T}{\partial x} \\ q_y &= \frac{M_\infty}{(\gamma-1)\text{Re}_\infty} \left(\frac{\mu_l}{\text{Pr}} + \frac{\mu_t}{\text{Pr}_t} \right) \frac{\partial T}{\partial y} \end{aligned} \quad (4)$$

The molecular viscosity is calculated using Sutherland's law:

$$\mu_l = T^{1.5} \left(\frac{1 + 110.4/\tilde{T}_\infty}{T + 110.4/\tilde{T}_\infty} \right) \quad (5)$$

A $k-\omega$ SST model due to Menter^[1] is used to calculate the turbulent eddy viscosity μ_t .

The governing equations are solved in the framework of cell-centered finite volume method. The inviscid fluxes are evaluated with Roe's finite-difference-splitting(FDS) scheme^[2], while central-difference-like scheme is used for the viscous fluxes. To preserve monotonicity the mini-mod flux limiter is used. The equations are advanced in time with Jameson's 4-step Runge-Kutta method^[3], which is of second order accurate in time. Rather than fixing the size of the time step throughout the computation, each update determines its own time step that is allowed by the current flow field. The unevenly sampled data is processed with a special form of discrete Fourier transformation^[4] to extract the narrow-band tones in

the power spectrum. In such a way, the simulation can proceed much more efficiently.

B. Code Validation

Two simple test cases are chosen to evaluate the temporal and spatial accuracy of the authors' code. The first case is the propagation of an inviscid normal shock wave in a shock tube. The shock wave has a Mach number of 2 and is initially placed at -0.4. Fig. 1 shows the density variation along the shock tube at time 0.283. Computed position of the shock wave agrees well with the theoretical value, which is represented by the straight line.

The second test case is turbulent compressible boundary layer over a flat plate at Reynolds number 5×10^6 and external Mach number 2.0. As is evident in Fig. 2, the compressible law of wall is accurately reproduced by the $k-\omega$ SST model of Menter.

C. Cavity Configuration and Flow Conditions

The cavity flow to be simulated is chosen from the test cases in ref[6]. The depth of the cavity is 15mm and the length is 45mm. The Mach number of external flow is 2.5. The free-stream air temperature is 128.9K and static pressure is 12390.7 psi. The oncoming boundary layer has a thickness of 5mm, a displacement thickness of 0.328mm and a momentum thickness of 0.129mm. The skin friction coefficient is 1.79×10^{-3} .

In the numerical simulation below, one-seventh power distribution of the tangent velocity is imposed at the inlet. The distribution of the temperature at the inlet is deduced from the Crocco-Busemann integral with adiabatic walls. Pressure is held constant, and normal velocity is assumed zero across the inlet. Inflow turbulent kinetic energy k and turbulent specific dissipation rate ω is taken the same as that in ref[6], namely $1.258 \text{m}^2/\text{s}^2$, and $2.567 \times 10^4/\text{s}$ respectively.

D. Grid System

Two grid blocks are employed to discretize the solution field, one inside the cavity, and the other outside the cavity(Fig.3). Due to limited computer resources, rather coarse grids are used(30*30,70*40). The interface between these two blocks shares the same set of edges. The unknowns at the buffer cells of the interface are interpolated from the solutions of the other block. To ensure the conservation of the inviscid fluxes, the conserved variables to the right and left of the edges on the interface, necessary for the evaluation of the flux with Roe's scheme, is set to the same for both blocks after an update.

For the block outside the cavity, the viscous effects are confined to a thin layer near the lower boundary. Solution gradients normal to this boundary dominate that in the tangent direction. Therefore, simplified thin-layer Navier-Stokes equations can be employed. On the other hand, the flow inside the cavity is characterized by a number of recirculating vortices. The full Navier-

Stokes equations have to be used.

3. RESULTS AND DISCUSSIONS

Solutions are developed till the initial transient flow passed away and the self-sustained oscillation of the flow field is achieved. As explicit integration method is employed in the current simulation and the grid is intended for turbulent calculation, time-step is severely limited by the CFL stability constraint. Tens of thousands of time step is required to reach a stable self-sustained oscillation, which is monitored by the pressure history on several sampling points along the cavity wall.

After the flow field reached the stable self-sustained oscillation, the computation was carried on for some additional cycles, during which snapshots of the flow field were taken and pressures along the cavity wall were recorded for further analysis.

Fig. 4 and Fig. 5 show the density and pressure contours at one moment of a oscillation cycle. From the density contours, it is evident that the boundary layer separate at the upstream lip of the cavity. A shear layer is formed that spans the open end of the cavity. The shear layer flows downstream, deflecting up and down and striking the trailing edge of the cavity. From the pressure contours, it is evident that a strong pressure discontinuity is formed just in front of the trailing edge of the cavity. The pressure waves propagate upstream. The net propagating velocity of the acoustic waves should be the sum of the sound speed and the fluid velocity. The flow outside the cavity is supersonic, inside is subsonic. Therefore, the pressure waves propagate upstream faster inside the cavity than outside. While the pressure waves inside the cavity is roughly parallel to the vertical cavity wall, those outside the cavity take the typical angle of a Mach cone at the same free-stream Mach number.

Fig. 6 and Fig. 7 reveal the strong and complex vortex flow inside the cavity. Fig. 6 shows the velocity vector field. While the magnitude of the velocity in the left part of the cavity is small, that at the right part is quite large. Actually, the Mach number of the flow at the right part is at high subsonic regime. Fig. 7 depicts the instantaneous streamlines at the same moment of Fig. 6. Clearly, there is a strong and big vortex at the right part of the cavity, with a size of the depth of the cavity. There is one small vortex at the right-bottom corner of the cavity, another one below the shear layer near the leading edge of the cavity. The lower part of the shear layer deviate deeply into the cavity, though at small velocity. These figures are just snapshots of the flow field at one moment. Actually, vortices inside the cavity undergo violent oscillations as the flow field evolves. They might exert significant influence on the whole dynamics process. However, in all of the theoretical models that so far have been proposed, no flow inside the cavity is assumed, and the effect of these

strong vortices on the feedback and the shear layer is neglected.

Fig. 8 records the pressure history over several oscillation cycles on the mid-point on the front, rear, and bottom walls of the cavity. Lomb's method of discrete Fourier transformation for unevenly sampled data^[4] is employed to extract narrow-banded tones in the power spectrum. The measured tones frequencies for the first three modes are 3467Hz, 6787Hz, and 10010Hz. The corresponding values predicted with modified Rossiter's formula are 2777Hz, 6479Hz and 10182Hz. Those predicted with the current numerical simulation are 4120Hz, 8533Hz and 14021Hz. There exists large discrepancy. Inappropriate inflow boundary conditions and/or relatively coarse grids may be the reasons to blame. Further works are needed to improve the numerical prediction.

4. CONCLUSION

Salient features in cavity flows, such as the deflecting shear layer, the radiating sound waves, the oscillating pressure field, and the complex vortex flow inside the cavity, had been captured. However, the predicted discrete tones did not compare well with that obtained from the experiment. This does not mean that the $k-\omega$ SST turbulence is deficient for this case. Instead, the boundary conditions at the inlet should be refined and the grid resolution should be further increased. To cope with the increased overhead from the increased grid dimensions, efficient implicit time-accurate algorithm needs to be developed and implemented. Efforts are being undertaken to improve the numerical prediction.

REFERENCES

- [1] Menter F.R., AIAA Journal, vol. 32, No. 8, August, 1994, pp1598-1605.
- [2] Roe, P., Journal of Computational Physics, Vol. 43, 1981.
- [3] Jameson, A. et al, AIAA Paper 81-1259, 1981.
- [4] Lomb, N.R. Astrophysics and Space Science, vol. 39, 1976, pp. 447-462.
- [5] Heller, et al, J. Sound & Vib, vol 18, Oct. 1971, p545-553.
- [6] Xin Zhang, AIAA Journal, vol 33, No. 8, August, 1995, pp1404-1411.

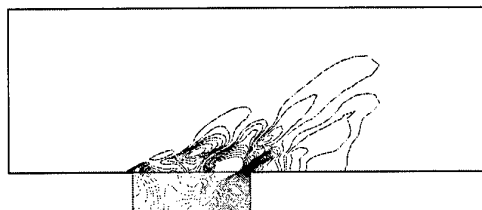
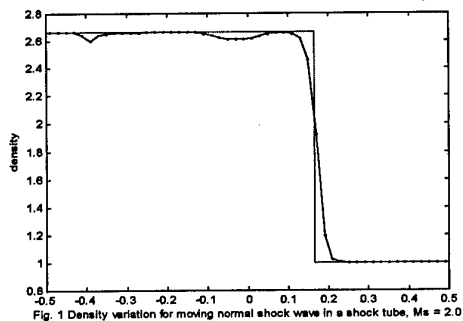


Fig. 5 Pressure contours at one moment of a oscillation cycle

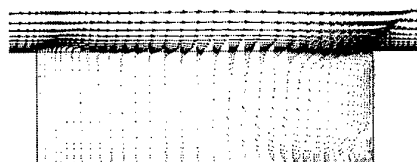
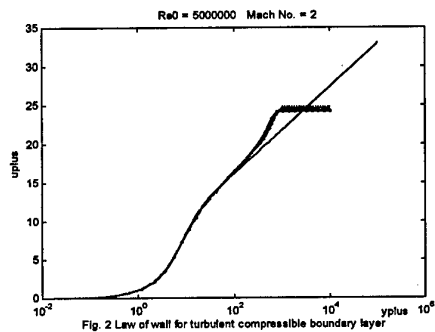


Fig. 6 Velocity vectors at one moment of a oscillation cycle

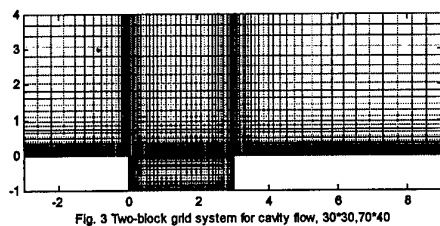


Fig. 3 Two-block grid system for cavity flow, $30^\circ 30.70^\circ 40$

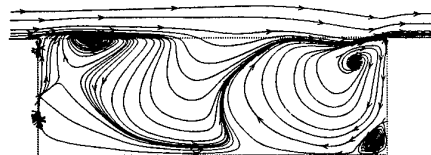


Fig. 7 Instantaneous streamlines at one moment of a oscillation cycle

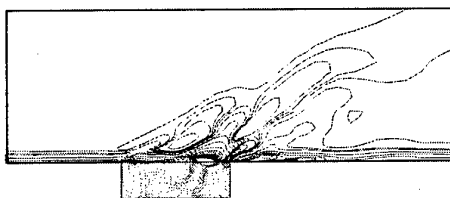
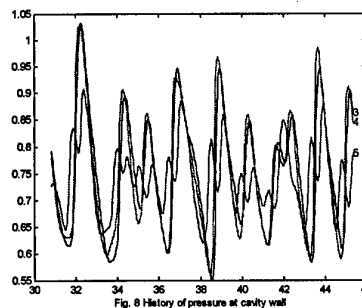


Fig. 4 Density contours at one moment of the oscillation cycles



A Study on Shock Wave/Boundary Layer Interaction Phenomena with Chemically Nonequilibrium

A. Matsumoto** and S. Aso*

Department of Aeronautics and Astronautics, Kyushu University,
Hakozaki, Higashi-ku, Fukuoka 812-8581, JAPAN

Key Words : Shock Wave/Boundary Layer Interaction, High Enthalpy Flows

Abstract

Numerical simulation is performed to investigate high temperature effects in shock-wave/boundary-layer interacting flow fields. Shock-wave/boundary-layer interacting flow fields near a compression corner are numerically simulated by solving the two-dimensional full Navier-Stokes equations. Surface pressure, heat flux and shear stress are intensively investigated and relations among those physical properties are discussed. Moreover, effects of wall catalysis and freestream pressure to shock-wave/boundary-layer interaction flow fields are also discussed.

1. Introduction

Development of hypersonic transport has been strongly conducted. Hypersonic transport vehicles consist of many modules. So their body shape is complicated. Then, shock wave interference problems become very important [6]. It is significant problem for structural design to predict higher local peak of surface heat flux and pressure generated in interaction regions for those interference problems. Moreover, those problems are very complicated including high temperature effects for vehicles flying higher Mach number. Many researches have been conducted on those problems, researches including high temperature effects are quite insufficient. High temperature effects drastically affects flow field. Especially, dissociation and surface recombination play very important roles in a shock-wave/boundary-layer interaction flow field.

Schematics of shock-wave/boundary-layer interaction region at a two-dimensional compression corner is shown in Fig. 1. A strong normal shock wave impinges on a ramp

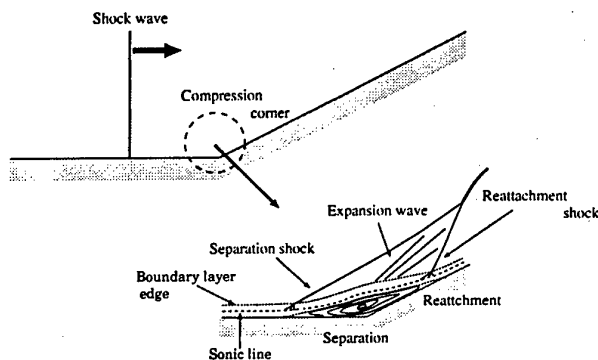


Fig. 1: Schematics of shock-wave/boundary-layer interaction near a two-dimensional compression corner

*Graduate student, Dept. Aero. & Astro., Kyushu Univ.

**Professor, Dept. Aero. & Astro., Kyushu Univ.

surface, and reflects on the surface. Then steady flow is induced behind a normal shock wave. The flow separates due to inverse pressure gradient at compression corner. Then shock-wave/boundary-layer interaction region is formed.

2. Numerical methods

Unsteady shock reflection process is numerically simulated to investigate structure of shock wave-boundary layer interaction flow field generated near a compression corner in chemical nonequilibrium. Incident normal shock wave is reflected by ramp. The shock wave is not so strong compared to reentry condition, but freestream temperature is enough high for molecular components of air (N_2 , O_2) to dissociate behind normal shock wave. Therefore, it is required for governing equation to include chemical nonequilibrium.

First, following assumptions are made to introduce basic equations.

1. Viscous and laminar flow
2. Chemically reacting flow (chemical nonequilibrium flow)
3. Dissociated air consists of 5 chemical species (N_2 , O_2 , NO , N , O) : Ionization is neglected
4. Electronic excitation mode is neglected
5. Thermal equilibrium flow ($T_{tr} = T_{rot} = T_{vib}$)

The governing equation is consist of conservative equations as follows [3] :

1. Global mass conservation
2. Mass conservation of each chemical species
3. Momentum conservation (x, y direction)
4. Total energy conservation

17 reactions shown in Table 1 are considered as elemental reactions for air 5-species. Chemical reaction rate for each reaction are evaluated by Arrhenius law importing Blotter's rate coefficients [2]. Transport properties for sin-

Table 1: Elemental Chemical reactions

r	Reactants	Products	M(Third Body)
1	$O_2 + M_1$	$\rightleftharpoons 2O + M_1$	O, N, NO, O_2, N_2
2	$N_2 + M_2$	$\rightleftharpoons 2N + M_2$	O, NO, O_2, N_2
3	$N_2 + N$	$\rightleftharpoons 2N + N$	
4	$NO + M_3$	$\rightleftharpoons N + O + M_3$	O, N, NO, O_2, N_2
5	$NO + O$	$\rightleftharpoons O_2 + N$	
6	$N_2 + O$	$\rightleftharpoons NO + N$	

gle species are evaluated equations from Chapman-Enskog theory with Lennard-Jones potential [1] [4]. Viscosity for multicomponent gas is evaluated by Wilke's mixture formula. Thermal conductivities for molecules are corrected

by Eucken's relation, then Wilke's mixture formula is applied for multicomponent gas. Diffusivities for multicomponent gas are evaluated from binary diffusion coefficients with pressure and thermal diffusion is neglected.

Governing equations are extended to generalized coordinate system, and solved by finite difference method. Conservative variables are defined at cell vertex. Harten-Yee's non-MUSCL modified flux type TVD scheme [5] is applied to evaluate numerical flux for convective terms. Conventional Roe's average [7] is applied to determine the cell centered physical variables. For viscous terms a central difference scheme is applied. For chemically reacting source term familiar point implicit scheme is not applied, because stiffness due to chemically reacting source term is not so serious by the assumption of thermal equilibrium flow in the present calculations. chemically reacting source term can be explicitly treated. Time integration is performed by Strang-type fractional time step method to maintain second order time accuracy for unsteady problem.

Initial condition is obtained by solving steady inviscid one-dimensional conservative equations by Runge-Kutta method. For boundary conditions zero derivatives of physical variables are imposed at incoming, upper and exit boundary. Zero derivative of pressure, non-slip, constant wall temperature and fully catalytic or non catalytic wall conditions are imposed at wall boundary.

3. Results and discussion

Flow conditions are shown in Table 2. Difference be-

Table 2: Flow conditions

	p_∞	T_∞	M_s	θ_w	Re
case 1	50 Torr	2,000 K	5	30°	5.8×10^4
case 2	20 Torr	2,000 K	5	30°	2.4×10^4

tween two cases is only downstream pressure. At downstream, species concentrations can be approximately set as $C_N = C_O = C_{NO} = 0$, $C_{N_2} = 0.788$, $C_{O_2} = 0.222$ (dissociation at downstream is neglected because of small dissociation degree). For each cases chemically frozen flow and chemical nonequilibrium flow (thermal equilibrium) are assumed. For chemical nonequilibrium flow two extreme conditions; fully catalytic ($k_w = \infty$) or non catalytic ($k_w = 0$) wall conditions are imposed as species condition at a wall.

Typical shock reflection pattern through the computations is shown in Fig. 2. Shock reflection pattern shows double Mach reflection (DMR). A flow is separated near a compression corner and λ shape shock wave is formed. Slip line is formed from primary triple point and interacts to secondary Mach stem, then flow field is complicated.

3.1 Calculated results and discussions of case 1 ($p_\infty = 50$ Torr)

Instantaneous temperature contours around a compression corner are shown in Fig. 3. From the figures length of separation region, separation point and reattachment point are different from each other. Comparing frozen case with nonequilibrium case, reattachment point is far from a corner in nonequilibrium case. It can be said, the difference is due to angle of separation shock wave; angle of separation shock wave in frozen case is larger than that of

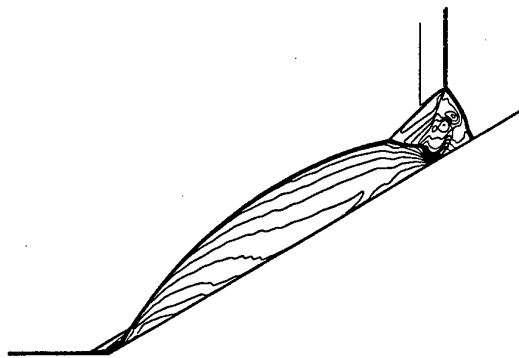


Fig. 2: Typical shock reflection pattern (Instantaneous density contours), Double Mach reflection, chemical nonequilibrium flow (case 1, FCW)

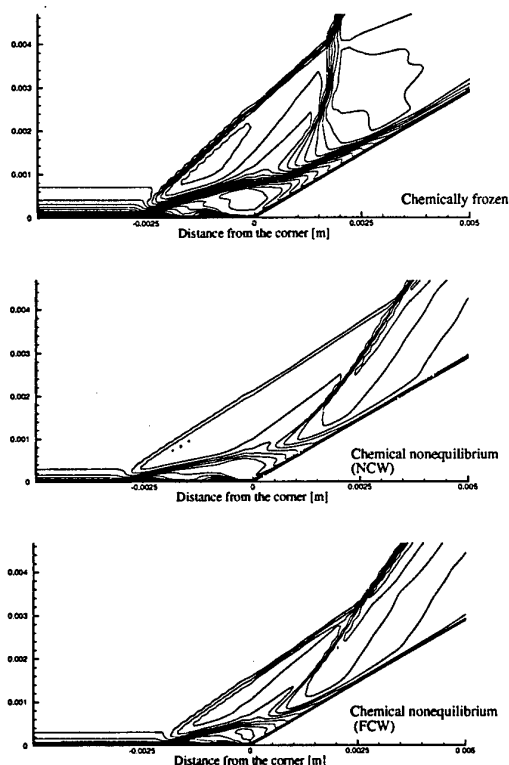


Fig. 3: Instantaneous temperature contours around a separation region

nonequilibrium case, then momentum exchange rate to enthalpy is larger than that of nonequilibrium case. So a flow reattaches downstream compared with nonequilibrium case. The matter will be discussed later related to shear stress distributions.

Distributions of surface heat flux, shear stress and surface pressure are shown Fig. 4. Large heat flux is observed at reattachment point. Comparing two nonequilibrium cases, difference of distributions are observed as effects of

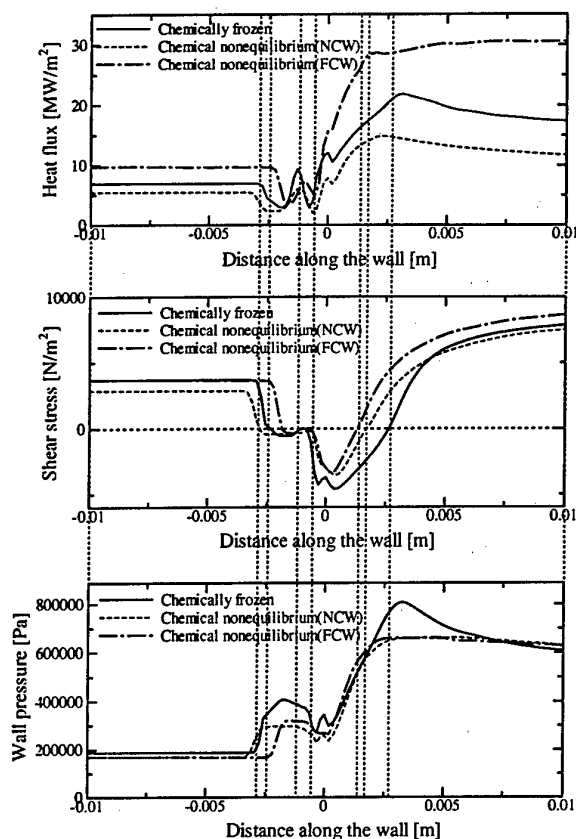


Fig. 4: Instantaneous distributions of surface heat flux, shear stress, and surface pressure

wall catalysis. Difference of between the two cases is quite large. Under fully catalytic wall condition, almost twice as large heat flux as that with non catalytic wall is observed. Heat flux has approximately half value between two nonequilibrium cases near the reattachment point in chemically frozen case. Secondary separation is also observed in the shear stress distributions as positive value region of shear stress in negative region. Separation point, reattachment point and separation length are measured from the figures. The results are shown in Table 3. The result shows

Table 3: State of separation

	x_{sep}	x_{reat}	L_{sep}	unit : [mm]
Frozen	-2.59	2.59	5.18	
Non-eq. (NCW)	-2.96	1.66	4.62	
Non-eq. (FCW)	-1.85	1.29	3.10	

that nonequilibrium effects affect angle of separation shock wave and its position, then a reattachment point is slightly near from the corner in nonequilibrium case. Besides it is observed wall catalysis affects separation point due to its enhancement of surface recombination of atoms. Therefore separation region has smallest value under nonequilibrium and fully catalytic wall condition. Largest surface pressure in interaction region is observed under frozen flow case. Two nonequilibrium cases do not show large difference near a reattachment point under the downstream con-

dition (case 1 condition in Table 2) except local pressure due to change of separation and reattachment point.

3.2 Calculated results and discussions of case 2 ($p_{\infty}=20$ Torr)

Instantaneous temperature contours around a compression corner are shown in Fig. 5. They show same tendency

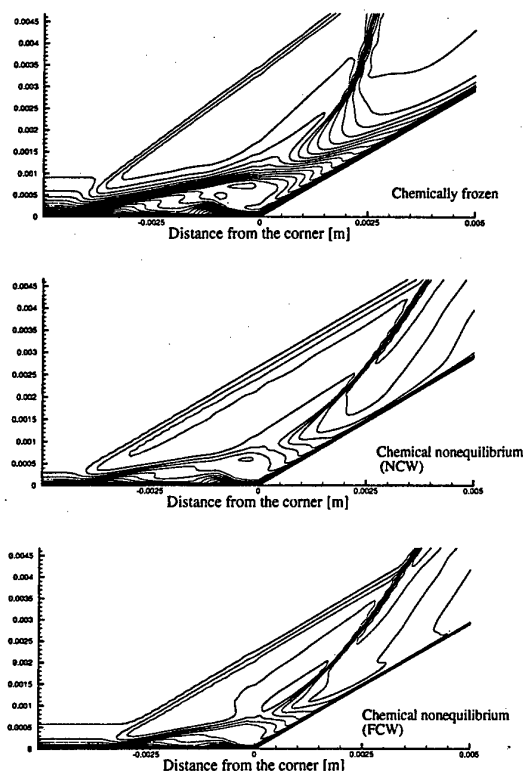


Fig. 5: Instantaneous temperature contours around a separation region

that separation length is larger than those of case 1 calculation, and viscous effects is less near a surface in comparative low Reynolds number flow. Secondary separation is clearly observed compared to previous case. Separation point, reattachment point and separation length show same tendency as shown Fig. 4. Under chemical nonequilibrium and fully catalytic wall condition a separation point is nearest to a corner, reattachment point is nearest to a corner and separation length is smaller than those of under any other conditions. Distributions of surface heat flux, shear stress and surface pressure are shown Fig. 6. Difference from flow assumption is clearly recognized than previous case. So it can be considered that downstream pressure have some correlation to flow field, especially near a reattachment point. Heat flux distribution shows largest peak at the reattachment point under nonequilibrium flow and fully catalytic wall condition. Shear stress distributions have same tendency in previous calculation. Separation point, reattachment point and separation length are evaluated from the distributions. The result is shown in Table 4. The result also shows same tendency as case 1 calculation. Separation point is nearest, reattachment point is nearest

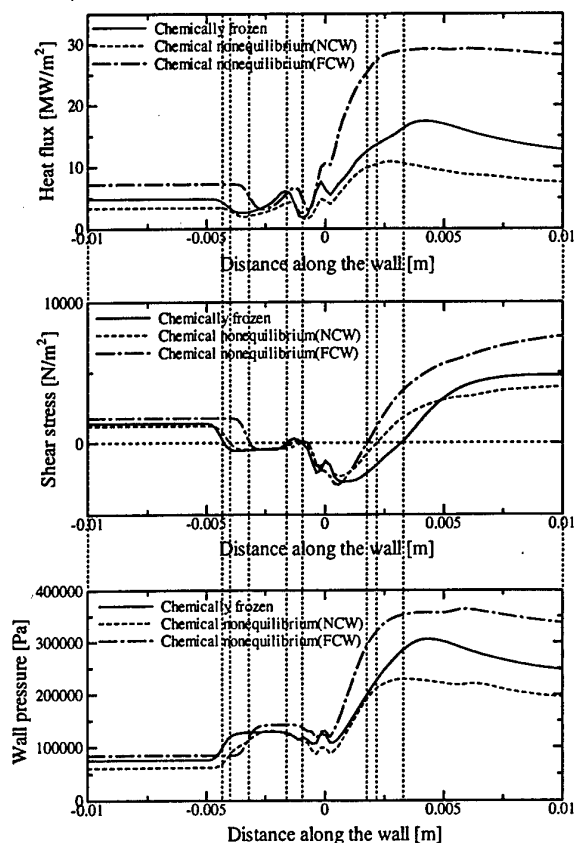


Fig. 6: Instantaneous distributions of surface heat flux, shear stress and surface pressure

Table 4: State of separation

	x_{sep}	x_{reat}	L_{sep}	unit : [mm]
Frozen	-4.24	3.15	7.39	
Non-eq. (NCW)	-4.06	2.21	6.27	
Non-eq. (FCW)	-3.15	1.84	4.99	

to the corner, and length of separation region is shortest than any other cases under nonequilibrium and fully catalytic wall condition. In the surface pressure distributions, pressure plateau region (separation bubble region) is longer than that in case 1. The pressure level near a reattachment point is larger than that in case 1.

In two nonequilibrium conditions of case2, the peak pressure with fully catalytic wall is twice as large as that with non catalytic wall near reattachment point, which is quite different from case 1. In case 1 almost no difference is found in peak pressure near reattachment point for a non catalytic wall and fully catalytic conditions of case 1. Effects of nonequilibrium and wall catalysis effects also affects surface pressure distribution, especially near reattachment points.

4. Summary

Shock-wave/boundary-layer interacting hypersonic high enthalpy flow is numerically simulated assuming thermal equilibrium and chemical nonequilibrium condition. From the results of numerical simulation, effects of chemi-

cal nonequilibrium and downstream pressure in a shock-wave/boundary-layer interaction flow field can be observed. They are summarized as below.

1. Chemical nonequilibrium on the flow properties in shock-wave/boundary-layer interaction is significant.
2. Chemical reaction affects angle of separation shock wave. Then the flow structure changes due to chemical reactions. Especially in fully catalytic wall condition, the size of separation region becomes smaller than that of non catalytic condition.
3. In case 1 ($p_{\infty} = 50$ Torr) pressure distributions show pressure plateau just after separation point and peak pressure near reattachment point. Almost similar pressure distributions are observed under non catalytic and fully catalytic wall conditions. Fully catalytic and non catalytic conditions show peak heating near reattachment point. Peak heating with fully catalytic wall is twice as large as that of non catalytic wall condition. The results show wall catalysis is quite important.
4. In case 2 ($p_{\infty} = 20$ Torr) almost same tendency as in case 1 is observed in heat flux distributions. However in pressure distributions significant difference between fully catalytic wall and non catalytic wall is observed.
5. The size and extent of separation region of case 2 are larger than those of case 1. The results might be caused by viscous and nonequilibrium effects.

Reference

- [1] Bird, R.B., Stewart, W.E. and Lightfoot, E.N., "Transport Phenomena", John Wiley & Sons, Inc., 1960.
- [2] Blottner, F.G., "Viscous Shock Layer at The Stagnation Point with Nonequilibrium Air Chemistry", AIAA Journal Vol. 7, No. 12, pp. 2281-2288, 1969.
- [3] Gnoffo, P.A., Gupta, R.N. and Shinn, J.L., "Conservation Equations and Physical Models for Hypersonic Air Flows in Thermal and Chemical Nonequilibrium", NASA TP-2867, 1989.
- [4] Gupta, R.N., Yos, J.M., Thompson, R.A. and Lee, K.-P., "A Review of Reaction Rates and Thermodynamic and Transport Properties for 11-Species Air Model for Chemical and Thermal Nonequilibrium Calculation to 30,000 K", NASA RP-1232, 1990.
- [5] Harten, A., "High Resolution Schemes for Hyperbolic Conservation Laws", Journal of Computational Physics, Vol. 49, pp. 357-393, 1983.
- [6] Korkegi, R.H., "Survey of Viscous Interactions Associated with High Mach Number Flight", AIAA Journal, Vol 9, No. 5, pp. 771-784, 1971.
- [7] Roe, P.L., "Approximate Riemann Solvers, Parameter Vectors, and Difference Schemes", Journal of Computational Physics, Vol. 43, pp. 357-372, 1981.

FLOW CONTROL METHOD USING UNSTEADY SENSITIVITY ANALYSIS

Hyoung-Jin Kim*, Chongam Kim**, and Oh-Hyun Rho***
Seoul National University, Seoul, 151-742 Korea

Key Words: Unsteady Flows, Flow Control

ABSTRACT

This paper presents a method for active feedback control of compressible flows utilizing discrete aerodynamic sensitivity analysis. Unsteady sensitivity code and adjoint code are developed via direct differentiation method and adjoint method, respectively, by hand-differentiation from a two-dimensional unsteady compressible Navier-Stokes solver. Active flow controls are conducted by minimizing unsteady objective function. Unsteady sensitivity derivatives of the objective function are calculated by the unsteady sensitivity codes, and optimization is conducted utilizing a linear line search method at every physical time level. Several flow control examples validate that the present active flow control method utilizing the unsteady sensitivity analysis is robust and problem-independent.

Introduction

With the recent development of numerical optimization and sensitivity analysis techniques in computational fluid dynamics, optimal flow control methods utilizing Navier-Stokes equations and sensitivity analysis methods are getting much more attention than before. Optimal flow control methods make it possible to conduct feedback flow control without any a priori knowledge of unsteady flow characteristics.

Optimal flow control methods have been mainly developed for incompressible low Reynolds number flows since the governing equations are much simpler than compressible flows.^{1,2} On the other hand, few works have been done for compressible high Reynolds number flows. Mohammadi³ recently reported a flow control method for high speed flows using incomplete sensitivity derivatives. It was assumed that the sensitivity derivatives with respect to flow variables can be neglected if objective function is based on local information around the body surface. However, a general flow control method using complete sensitivity information has not been reported.

The objective of the present study is to develop a general active flow control method utilizing unsteady complete sensitivity analysis for compressible laminar or turbulent flows. Unsteady sensitivity analysis codes are developed for discrete unsteady Navier-Stokes equations with Baldwin-Lomax alge-

braic turbulence from steady sensitivity codes developed in the previous research of the authors⁴. At each physical time step, objective function and its gradient are calculated, and control input required to minimize the objective function is determined by a linear line search method, which can be easily replaced with a more sophisticated gradient based algorithms at the cost of computational time. In this approach, an active feedback flow control is interpreted as an unsteady design optimization problem so that the versatility of the direct optimization methods can be fully utilized.

Flow Analysis

A two-dimensional unsteady Navier-Stokes solver developed and validated in Ref.[5,6] was used for the flow analysis. Unsteady Reynolds-averaged two-dimensional compressible Navier-Stokes equations in generalized coordinates are used in the conservation form based on a cell-centered finite volume approach, given as

$$\frac{1}{J} \frac{\partial Q}{\partial t} = -R \quad (1)$$

, where t represents physical time, Q is a four-element vector of conserved flow variables as $Q = \{\rho, \rho u, \rho v, e\}^T$, and R is the residual vector as $R = (E-E_v)_\xi + (F-F_v)_\eta$. E and F are inviscid flux vectors and E_v and F_v are viscous ones of chordwise and normal directions, respectively. Roe's FDS scheme was adopted for the space discretization in the inviscid flux terms, and MUSCL approach with Koren limiter is employed to obtain a third order accuracy. The central difference method is used for viscous flux terms. Turbulence effects were considered using the Baldwin-Lomax algebraic model.

For the temporal discretization, the dual time stepping method is employed to obtain a second order temporal accuracy as follows.

$$\frac{1}{J} \frac{\partial Q}{\partial \tau} = -R^{n+1,s+1} - \frac{3Q^{n+1,s+1} - 4Q^n + Q^{n-1}}{2J\Delta t} \quad (2)$$

where τ represents pseudo time, n the physical time level, and s the pseudo time level. The above equations are discretized in pseudo time using the Euler implicit method and linearized by employing the flux Jacobian. This leads to a large system of linear equations in delta form at each pseudo time step as

$$\left(\frac{1}{J\Delta \tau} + \left[\frac{\partial R}{\partial Q} \right] + \frac{1.5I}{J\Delta t} \right) \Delta Q = -R^{n+1,s} - \frac{3Q^{n+1,s} - 4Q^n + Q^{n-1}}{2J\Delta t} \quad (3)$$

In the implicit part, Beam & Warming's AF-ADI method is used, and van Leer's FVS is employed with a first order accuracy.

* Graduate Student, Dep't of Aerospace Eng. Currently, Postdoctoral

Research Fellow, Dep't of Aeronautics and space Eng., Tohoku Univ.

** Assistant Professor, Dep't of Aerospace Eng.

*** Professor, Dep't of Aerospace Eng.

Unsteady Sensitivity Analysis

Direct Differentiation (DD) Method

The discrete residual vector for nonlinear aerodynamic analysis of unsteady problems with the dual-time stepping method at $(n+1)th$ time level can be written symbolically as

$$R^{n+1}[Q, X, \beta] + \frac{3Q^{n+1}[\beta] - 4Q^n + Q^{n-1}}{2\Delta t} = 0 \quad (4)$$

where X is the grid position vector, β the vector of design variables at $(n+1)th$ time level. Equation (4) is directly differentiated with respect to β_k to yield the following equation.

$$\left(\left[\frac{\partial R}{\partial Q} \right] + \frac{1.5I}{J\Delta t} \right) \left[\frac{dQ}{d\beta_k} \right]^{n+1} + \left[\frac{\partial R}{\partial X} \right] \left[\frac{dX}{d\beta_k} \right]^{n+1} + \left[\frac{\partial R}{\partial \beta_k} \right]^{n+1} = 0 \quad (5)$$

In order to find the solution $\{dQ/d\beta_k\}^{n+1}$ of the unsteady sensitivity equation (5), a pseudo time term for $\{dQ/d\beta_k\}^{n+1}$ is added as in Eq.(2).

$$\frac{1}{J} \frac{\partial}{\partial \tau} \left[\frac{dQ}{d\beta_k} \right] = - \left(\left(\left[\frac{\partial R}{\partial Q} \right] + \frac{1.5}{J\Delta t} \right) \left[\frac{dQ}{d\beta_k} \right]^{n+1} + \left[\frac{\partial R}{\partial X} \right] \left[\frac{dX}{d\beta_k} \right]^{n+1} + \left[\frac{\partial R}{\partial \beta_k} \right]^{n+1} \right) \quad (6)$$

And the same time integration scheme with the flow solver is adopted to obtain the following form.

$$\left(\frac{1}{J\Delta \tau} + \left[\frac{\partial R}{\partial Q} \right] + \frac{1.5I}{J\Delta t} \right) Q = - \left(\left(\left[\frac{\partial R}{\partial Q} \right] + \frac{1.5}{J\Delta t} \right) \left[\frac{dQ}{d\beta_k} \right]^{n+1} + \left[\frac{\partial R}{\partial X} \right] \left[\frac{dX}{d\beta_k} \right]^{n+1} + \left[\frac{\partial R}{\partial \beta_k} \right]^{n+1} \right) \quad (7)$$

, where Q' represents $dQ/d\beta_k$. The above equations are solved with the AF-ADI scheme which is used for the flow solver.

When the flow variable sensitivity vector $\{dQ/d\beta_k\}^{n+1}$ is obtained, the total derivative of the unsteady system response of interest, F^{n+1} can be calculated. F^{n+1} is a function of flow variables Q , grid position X , and design variables β at $n+1$ time level, i.e.,

$$F^{n+1} = F^{n+1}(Q^{n+1}(\beta), X^{n+1}(\beta), \beta^{n+1}). \quad (8)$$

The sensitivity derivative of the cost function F with respect to the k^{th} design variable β_k is given by

$$\left[\frac{dF}{d\beta_k} \right]^{n+1} = \left[\frac{\partial F}{\partial Q} \right]^T \left[\frac{dQ}{d\beta_k} \right]^{n+1} + \left[\frac{\partial F}{\partial X} \right]^T \left[\frac{dX}{d\beta_k} \right]^{n+1} + \left[\frac{\partial F}{\partial \beta_k} \right]^{n+1}. \quad (9)$$

Adjoint Variable(AV) Method

Since the total derivative of the unsteady flow equations is null in the $(n+1)th$ time level as can be seen in Eq.(5), we can introduce adjoint variables and combine Eq. (5) and (9) to obtain

$$\left[\frac{dF}{d\beta_k} \right] = \left[\frac{\partial F}{\partial Q} \right]^T \left[\frac{dQ}{d\beta_k} \right] + \left[\frac{\partial F}{\partial X} \right]^T \left[\frac{dX}{d\beta_k} \right] + \left[\frac{\partial F}{\partial \beta_k} \right] + \lambda_k^T \left(\left(\left[\frac{\partial R}{\partial Q} \right] + \frac{1.5}{J\Delta t} \right) \left[\frac{dQ}{d\beta_k} \right]^{n+1} + \left[\frac{\partial R}{\partial X} \right] \left[\frac{dX}{d\beta_k} \right]^{n+1} + \left[\frac{\partial R}{\partial \beta_k} \right]^{n+1} \right) \quad (10)$$

Coefficients of flow variable sensitivity vector $\{dQ/d\beta_k\}$ form the following adjoint equation.

$$\left(\left[\frac{\partial R}{\partial Q} \right] + \frac{1.5}{J\Delta t} \right) \lambda_k + \left[\frac{\partial F}{\partial Q} \right] = 0 \quad (11)$$

If we find the adjoint variable vector $\{\lambda_k\}$ that satisfies the above adjoint equation, we can obtain the sensitivity derivative of F with respect to β_k by the following equation without any information about the flow variable sensitivity vector $\{dQ/d\beta_k\}$.

$$\left[\frac{dF}{d\beta} \right] = \left[\frac{\partial F}{\partial X} \right]^T \left[\frac{dX}{d\beta} \right] + \left[\frac{\partial F}{\partial \beta} \right] + \lambda_k^T \left(\left[\frac{\partial R}{\partial X} \right] \left[\frac{dX}{d\beta_k} \right] + \left[\frac{\partial R}{\partial \beta_k} \right] \right). \quad (12)$$

As in Eqs.(3) and (7), the adjoint equation (11), after adding pseudo time term, is also converted to the following system of linear algebraic equations and is solved with the AF-ADI scheme.

$$\left(\frac{1}{J\Delta \tau} + \left[\frac{\partial R}{\partial Q} \right] + \frac{1.5I}{J\Delta t} \right) \lambda_k = - \left(\left(\left[\frac{\partial R}{\partial Q} \right] + \frac{1.5I}{J\Delta t} \right) \lambda_k + \left[\frac{\partial F}{\partial Q} \right] \right)^T \quad (13)$$

The subscript 'VL' of the transposed flux Jacobian $[\partial R / \partial Q]^T$ in the LHS of Eq.(13) refers to van Leer's FVS flux jacobian.

Strategy for Flow Control

We employed the following two procedures to minimize an unsteady objective function F with an assumption that the objective function F is non-negative and behaves linearly with respect to the variation of $\{\beta\}$.

- Strategy I :** 1. Calculate F^{n+1} for $\{\beta\} = \{\beta\}^n$ by the Flow Solver.
2. Calculate $\{\nabla F^{n+1}\}$ for $\{\beta\} = \{\beta\}^n$.
3. Obtain $\{\beta\}^{n+1}$ as follows.

$$\{\Delta \beta\} = - \frac{F}{|\nabla F|^2} \{\nabla F\}, \quad \{\beta\}^{n+1} = \{\beta\}^n + \{\Delta \beta\}$$

4. $n = n + 1$, go to S1.

Strategy II : The following step is added to the Step 3 of Strategy I.

- 3-1. Update F^{n+1} for $\{\beta\} = \{\beta\}^{n+1}$ by the Flow Solver.

Results and Discussion

Cylinder Lift Control

The first example is the lift control of a cylinder lift, in which we attempt to remove the lift of the cylinder due to vortex shedding by adjusting the rotational speed of the cylinder. Flow conditions are $M_\infty = 0.3$, $Re = 200$, where asymmetric von Karman vortex is generated in the wake region behind the cylinder. O-type grid system of 169×169 is employed here.

Firstly, we validate the sensitivity codes developed in the previous sections. In order to validate the direct and adjoint unsteady sensitivity codes, unsteady sensitivity derivatives are compared with those calculated by the following finite difference approximation.

$$\frac{dC_l}{d\alpha} \approx \frac{C_{l,\alpha+\Delta\alpha}^{n+1} - C_{l,\alpha}^{n+1}}{\Delta\alpha}, \quad (14)$$

where α is a nondimensional rotating speed defined as $\alpha \equiv \omega R/U_\infty$, and R is a cylinder radius. The step size $\Delta\alpha$ for the finite difference calculation is set to be 1.0×10^{-4} . The L2 norm of residual is reduced by 6 and 4 orders of magnitude from the initial value for flow solver and sensitivity codes, respectively at every physical time step. The physical time step Δt is set to be 0.2 for the cylinder cases.

Fig.1 shows the time history of C_l' ($=dC_l/d\alpha$). The sensitivity derivatives by the finite difference and DD and AV methods almost exactly coincide one another. This implies that the steady sensitivity codes developed in Ref.[4] are successfully converted to unsteady ones by the present method.

An objective function is defined as follows to remove the lift of the cylinder.

$$\text{Minimize } F = 0.5 \times C_l'^2 \quad (15)$$

In this case, we tried both the strategy I and II for the flow control. In order to compute the required sensitivity derivatives, we adopted the DD code since only one control parameter, the rotating speed α , is used in this case and the AV code requires about two times the computational time taken by the DD code.⁵

Fig.2(a) shows a lift history before and after the flow control is activated, and Fig.2(b) shows variation of the rotating speed α . The lift and the rotating speed α controlled by the strategy I oscillate, while the lift controlled by the strategy II is successfully removed and α does not oscillate. This implies that the linear assumption adopted for the calculation of the control parameter variation worked well in this case. Since the time lag of the strategy I causes oscillation of the objective and the control parameter, we used the strategy II for remaining examples.

Cylinder Vortex Shedding Control

In this example, the present flow control method is applied to the vortex shedding control of a circular cylinder. Flow conditions are same as those of the previous cylinder lift control case. We define the objective function as the difference between the target surface pressures and the computed surface pressures of the cylinder, as follows.

$$\text{Minimize } F = \frac{1}{2} \int_0^{2\pi} (C_p - C_{pt})^2 R d\theta \quad (16)$$

The target pressures C_{pt} are specified as those of the inviscid flow given as $1-4\sin^2\theta$, where θ is the circumferential coordinate of the polar coordinate system. We employed blowing/suction velocities along the cylinder surface as control parameters. Since there are a large number of control parameters, the adjoint sensitivity code is used here.

Although not shown here, F is reduced to about one-tenth compared with the value without control. Also, fluctuations of the cylinder lift and drag are removed and magnitudes of those are remarkably reduced. We can see clearly the effect of the vortex shedding control in Fig.3, which compares streamlines of the cylinder flow without and with control. The unsteady vortex shedding is removed by the control, and parallel streamlines are obtained behind the cylinder.

Airfoil Shock Buffet Control by Flap Deflection

The objective of this example is to remove the lift fluctuation of SC(2)-0714 airfoil in a buffet flow condition of $M_\infty = 0.725$, α (incidence angle) = 3.5 and $Re = 15 \times 10^6$. A C-type grid system with 169x61 points is used. The objective function is defined as follows.

$$\text{Minimize } F = |C_l - C_{l0}|, \quad (17)$$

where C_{l0} is a lift coefficient at the moment when the control is activated.

Lift oscillation caused by the shock buffet is removed by adjusting a deflection angle of a plain flap as can be seen in Fig.4(a). Clockwise deflection angle is defined to be positive. We used the DD code for the calculation of sensitivity derivatives since only one control parameter is adopted here.

Fig.4(b) shows the lift history of the airfoil. The lift coefficient is kept constant by the control. It is clear from Fig.4(c) that the unsteady flow has become a steady one by the appropriate deflection of plain flap. The deflection angle of -3.17 deg. is equivalent to a reduction of the incidence angle by about 1 deg., and the airfoil is now out of the buffet flow condition by decreasing the incidence angle.

Concluding Remarks

A robust flow control method based on unsteady aerodynamic sensitivity analysis via direct differentiation and adjoint methods is presented. Formulations of the discrete unsteady sensitivity analysis are presented, and the unsteady sensitivity codes are developed from the steady ones. Unsteady sensitivity derivatives computed by the sensitivity codes almost exactly coincide with those of the finite difference method. Successful control examples show that the present flow control method is promising for the application to various flow control problems.

References

1. Joslin, R. D., Gunzburger, M. D., Nicolaides, R. A., Erlebacher, G., and Hussaini, M. Y., "A Self-Contained, Automated Methodology for Optimal Flow Control," *AIAA J.*, Vol.35, No.5, pp.816-824, 1997.
2. Teman, R., Bewley, T., and Moin, P. "Control of Turbulent Flows," Proceedings of the 18th IFIP TC7 Conference on System Modelling and Optimization, Detroit, MI, July 1997.
3. Mohammadi, B., "Flow Control and Shape Optimization in Aeroelastic Configurations," AIAA 99-0182, Jan.1999.
4. Kim, H. J., Kim, C., Rho, O. H., and Lee, K., "Aerodynamic Sensitivity Analysis for Navier-Stokes Equations," submitted for publication in *Computers and Fluids*, 1999, see also AIAA99-0402, Jan. 1999.
5. Hwang, S. W. and Rho, O. H., "Numerical Simulation of Supersonic Flow over Double Cavity," AIAA 94-2206, June, 1996.
6. Kim, H. J. and Rho, O. H., "Dual-Point Design of Transonic Airfoils using the Hybrid Inverse Optimization Method," *J. of Aircraft*, vol.34, No.5, pp.612-618, 1997.

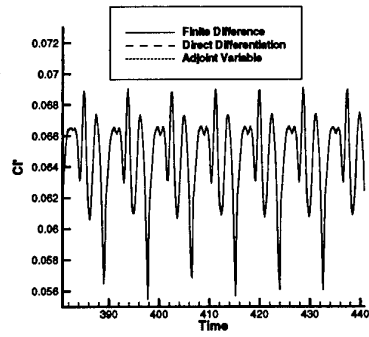
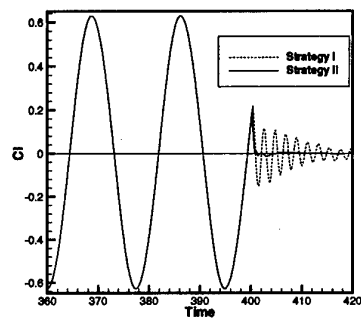
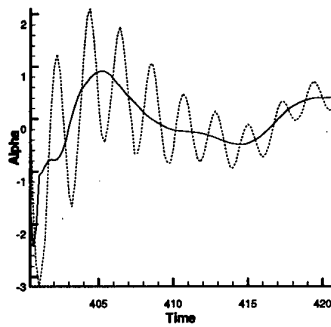


Fig.1 Validation of unsteady sensitivity analysis codes

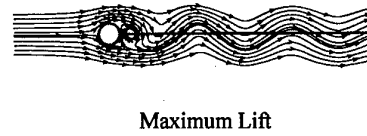


(a) Time history of lift coefficient
(flow control was started at $t = 400.4$)



(b) variation of control parameter α

Fig.2 Cylinder lift control results ($Re = 200$, $M_\infty = 0.3$)

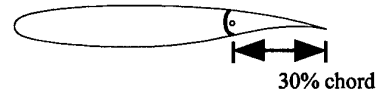


(a) Before Control

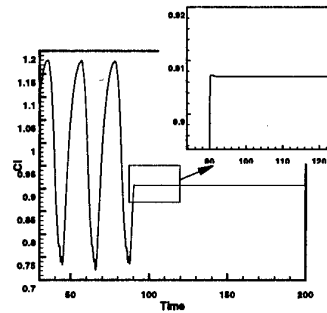


(b) After Control

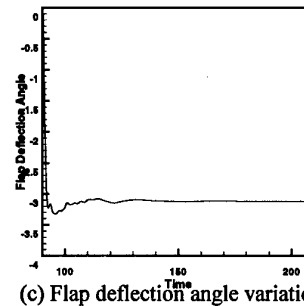
Fig.3 Vortex shedding control results:
comparison of streamlines around the cylinder



(a) Plain flap of SC(2)-0714 of 30% chord length



(b) Lift history



(c) Flap deflection angle variation

Fig.4 Shock buffet control results with plain flap deflection

A CFD PROCEDURE FOR AEROSPACE APPLICATIONS

Robert W. MacCormack
 Department of Aeronautics and Astronautics
 Stanford University
 Stanford, CA 94305-4035
 USA

Key Words: Fluid Dynamics, Compressible Flows, Shock Waves, Viscous Flows, Unsteady Flows

Abstract

An implicit procedure for minimizing the error introduced by approximate factorization¹ in solving the unsteady Euler or Navier-Stokes equations is presented. Also, a procedure for controlling numerical disturbances is described that adds numerical viscosity directly to the natural viscosity, similar in concept to that of an eddy viscosity. This approach preserves the frame independence of the governing equations even when solved in arbitrary curvilinear coordinate systems. High convergence rates of approximately 0.8 are achieved upon application to a wide range of problems. The implicit procedure can be combined with a multigrid procedure for further convergence acceleration.

Introduction

Implicit numerical methods for fluid dynamics in general first approximate the governing partial differential flow equations with a matrix equation and then replace, by approximate factorization, the original matrix with a sequence of efficiently invertible matrix factors. In addition, these methods often add artificial dissipation to control numerical instability. The difference between the original equations to be solved and those actually solved numerically represents computation error. This error is introduced through

- 1 discretization of derivatives by finite difference quotients,
- 2 approximate factorization of the original matrix equation, and
- 3 the addition of artificial dissipation.

The governing equations should be discretized to as high an order as is practical. The errors introduced by approximate factorization may require the use of relatively small time steps to contain their growth, which in turn causes slow convergence. Artificial dissipation if introduced in large amounts or in a frame dependent manner can degrade the accuracy of the numerical solution. The strategy for overcoming these difficulties is given herein. First we examine the governing equations.

Governing Equations

Consider the unsteady equations of compressible viscous flow in two dimensions represented in general coordinates ξ and η as follows.

$$\frac{\partial U}{\partial t} + \frac{\partial F}{\partial \xi} + \frac{\partial G}{\partial \eta} = 0 \quad (1)$$

A finite difference/volume equation, written in *delta* law form, approximating the above equation, is given by Eq. (2) below

$$\left\{ I + \Delta t \left(\frac{D_{\cdot}}{\Delta \xi} \bar{A}^n_{i+1/2,j} + \frac{D_{\cdot}}{\Delta \eta} \bar{B}^n_{i,j+1/2} \right) \right\} \delta U^{n+1}_{i,j} \\ = -\Delta t \left(\frac{F^n_{i+1/2,j} - F^n_{i-1/2,j}}{\Delta \xi} + \frac{G^n_{i,j+1/2} - G^n_{i,j-1/2}}{\Delta \eta} \right)$$

where \bar{A} and \bar{B} are the matrix Jacobians of the flux vectors F and G with respect to state vector U , respectively, and the dots, \cdot , appearing in the equation indicate that the difference operators operate on all factors to the right. Upon application of the difference operators an equation of the following form is usually obtained.

$$B_{i,j} \delta U^{n+1}_{i,j+1} + A_{i,j} \delta U^{n+1}_{i,j} + C_{i,j} \delta U^{n+1}_{i,j-1} \\ + D_{i,j} \delta U^{n+1}_{i+1,j} + E_{i,j} \delta U^{n+1}_{i-1,j} = \Delta U^n_{i,j} \quad (3)$$

where $A_{i,j}$, $B_{i,j}$, $C_{i,j}$, $D_{i,j}$ and $E_{i,j}$ are block matrix elements and

$$\Delta U^n_{i,j} = \\ -\Delta t \left(\frac{F^n_{i+1/2,j} - F^n_{i-1/2,j}}{\Delta \xi} + \frac{G^n_{i,j+1/2} - G^n_{i,j-1/2}}{\Delta \eta} \right)$$

Eq. (3) can also be expressed in full matrix form.

$$M \cdot [\delta U] = [\Delta U]$$

with

$$M'_\xi = \begin{bmatrix} x & \cdot & x & \cdot & \cdot & \cdot & \cdot \\ \cdot & x & \cdot & x & \cdot & \cdot & \cdot \\ x & \cdot & x & \cdot & x & \cdot & \cdot \\ \cdot & \bar{D} & \cdot & \bar{A} & \cdot & \bar{E} & \cdot \\ \cdot & \cdot & x & \cdot & x & \cdot & x \\ \cdot & \cdot & \cdot & x & \cdot & x & \cdot \\ \cdot & \cdot & \cdot & \cdot & x & \cdot & x \end{bmatrix}$$

$$M'_\eta = \begin{bmatrix} x & x & \cdot & \cdot & \cdot & \cdot & \cdot \\ x & x & x & \cdot & \cdot & \cdot & \cdot \\ \cdot & x & x & x & \cdot & \cdot & \cdot \\ \cdot & \cdot & \bar{B} & \bar{A} & \bar{C} & \cdot & \cdot \\ \cdot & \cdot & \cdot & x & x & x & \cdot \\ \cdot & \cdot & \cdot & \cdot & x & x & x \\ \cdot & \cdot & \cdot & \cdot & \cdot & x & x \end{bmatrix}$$

and diagonal matrix

$$D = \begin{bmatrix} x & \cdot & \cdot & \cdot & \cdot & \cdot & \cdot \\ \cdot & x & \cdot & \cdot & \cdot & \cdot & \cdot \\ \cdot & \cdot & x & \cdot & \cdot & \cdot & \cdot \\ \cdot & \cdot & \cdot & \bar{A} & \cdot & \cdot & \cdot \\ \cdot & \cdot & \cdot & \cdot & x & \cdot & \cdot \\ \cdot & \cdot & \cdot & \cdot & \cdot & x & \cdot \\ \cdot & \cdot & \cdot & \cdot & \cdot & \cdot & x \end{bmatrix}$$

The block matrix elements appearing above are again defined by Eq.(4) with the exception that the parameter α has now been set to 2.

In three dimensions M can be decomposed by

$$M \simeq M'_\xi \cdot [D]^{-1} \cdot M'_\eta \cdot [D]^{-1} \cdot M'_\zeta$$

Although the original *nonzero* elements of matrix M are returned exactly by the above MAF decomposition procedure, other formerly *zero* elements are disturbed and can contribute to both error and reduced convergence speed. The following section describes an iterative procedure for eliminating or further reducing this remaining decomposition error.

Removal of Decomposition Error

Eq.(6) can be expanded as follows.

$$M \simeq M'_\xi \cdot [D]^{-1} \cdot M'_\eta = M + P$$

The equation actually solved, instead of Eq.(3), is

$$M \cdot [\delta U] + P \cdot [\delta U] = [\Delta U] \quad (7)$$

The difference between Eq.(3) and Eq.(7) is the decomposition error term $P \cdot [\delta U]$. We now present an iterative procedure for removing this decomposition error.

The decomposition error term is fed back into the matrix equation on the right hand side for self cancellation. A k -step iterative modified approximate factorization algorithm¹, MAF(k), is defined as follows.

MAF(k) Algorithm

$$M \cdot [\delta U^{(k)}] + P \cdot [\delta U^{(k)}] = [\Delta U] + P \cdot [\delta U^{(k-1)}]$$

where $[\delta U^{(0)}] = [0] \quad k = 1, 2, 3, \dots$

MAF(1) is the same as Eq. (7) above. For this iterative procedure to work, each MAF iteration must be numerically stable and the sequence must converge. For it to be efficient, the number of iterations must be kept small, ideally at two. A stability analysis and examples showing sequence convergence have been given¹. The optimum value for the maximum number of k sub-iterations per time step was shown to be two for flows going to steady states.

Added Numerical Dissipation

Numerical dissipation is the fundamental requirement for numerical stability. It has to be present to obtain numerical solutions. It is introduced by the choices made in discretization. When this is insufficient, more must be added. This section presents a rational way to add numerical dissipation.

One would like to preserve the physical balance of the Navier-Stokes stress tensor, which is frame independent. It is hopeless to add artificial viscosity in multidimensional curvilinear coordinate systems and simultaneously preserve this physical balance - with few exceptions.

One exception is to use the already frame independent Navier-Stokes viscous stress tensor itself as a vehicle to add numerical dissipation. Similar to the concept of an eddy viscosity used to include the effects of turbulent mixing in the Reynolds Averaged Navier-Stokes equations, the addition of numerical viscosity by augmenting the natural viscosity can be used in the frame independent Navier-Stokes stress tensor, even when solving the Euler equations, to control numerical instability.

$$\mu \leftarrow \mu_{\text{physical}} + \mu_{\text{numerical}} \quad (8)$$

Numerical difficulties arise at the foot of shock waves and in regions where oscillation occurs in the convection velocity within subsonic flow.

(1) Along the shock wave, the numerical viscosity can be chosen to be

$$\mu_{\text{numerical}_i} = 1/2 \cdot \Delta h_{\xi_i} \cdot \rho_i c_i \quad (9)$$

where Δh_{ξ} represents the grid spacing distance in the ξ direction, assumed crossing through the shock, and

ρ is the density. At both points adjacent to the shock the viscosity is augmented as shown above in Eq.(8).

(2) Within subsonic regions with oscillation in convection speed q_n .

$$\mu_{\text{numerical}_i} = 0.05 \cdot \min \{ \Delta h_\xi, \Delta h_\eta, \Delta h_\zeta \} \cdot (\rho_1 |q_{n1}| + \rho_2 |q_{n2}|) \cdot \frac{|q_{n3} - 3(q_{n1} - q_{n2}) - q_{n4}|}{|q_{n3}| + 3(|q_{n1}| + |q_{n2}|) + |q_{n4}| + \epsilon} \quad (10)$$

where points 1, 2, 3 and 4 are adjacent point about grid point $i = "1"$ and $\epsilon \simeq 10^{-9}$ is added to prevent division by zero in motionless regions. The quotient factor is bounded by one and is proportional to $\frac{1}{8q_n} \cdot \Delta \xi^3 \cdot |\frac{\partial^3 q_n}{\partial \xi^3}|$. The above value of numerical viscosity is added, as in Eq.(8), at points i (1) and $i+1$ (2).

Computational Results and Conclusion

The method just described was successfully applied to several aerodynamic flows^{4,5}, ranging from low subsonic to hypersonic Mach numbers - (1) The Euler equations at Mach 0.2 for flow past an ellipse, Fig. 1, (2) the Reynolds Averaged Navier-Stokes equations for transonic flow past an airfoil, Fig. 2, (3) the Navier-Stokes equations for Mach 5 flow past a sphere, Fig. 3, and real gas equilibrium flow past a sphere at Mach 18, Fig. 4.

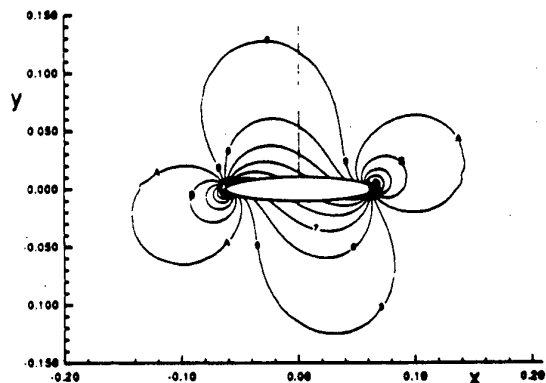


Figure 1. Pressure contours for subsonic flow about an ellipse.

References

- 1 MacCormack, R.W., "A New Implicit Algorithm for Fluid Flow," *AIAA Paper No. 97-2100*, 1997.
- 2 Stone, H.L., "Iterative Solution of Implicit Approximations of Multidimensional Partial Differential Equations," *Siam J. Numer. Anal.*, Vol. 5, No. 3, Sept., 1968, pp. 530-558.
- 3 Bardina, J. and C.K. Lombard, "Three Dimensional Hypersonic Flow Simulations with the CSCM Implicit Upwind Navier-Stokes Method," *AIAA Paper No. 87-1114*, 1987.

⁴ MacCormack, R.W., "Assessment of a New Numerical Procedure for Fluid Dynamics," *AIAA Paper No. 98-2821*, 1998.

⁵ MacCormack, R.W., "A Fast and Accurate Method for Solving the Navier-Stokes Equations," *21st ICAS Congress*, Melbourne, Australia, Sept. 13-18, 1998.

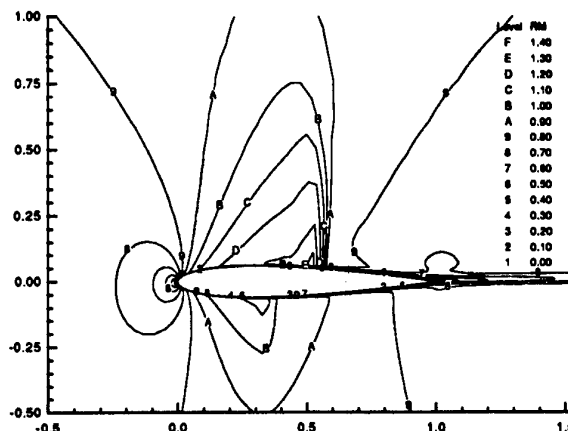


Figure 2. Mach contours for transonic flow past an airfoil.

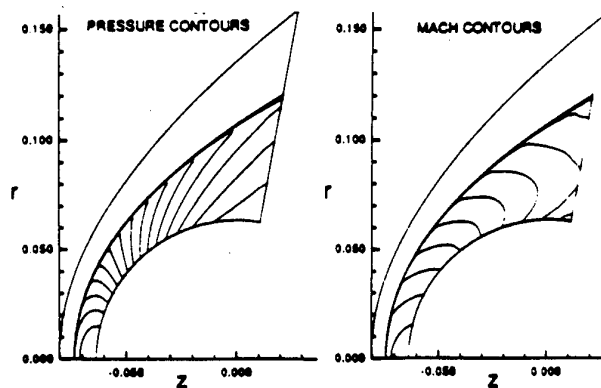


Figure 3. Pressure and Mach contours for supersonic flow past a sphere.

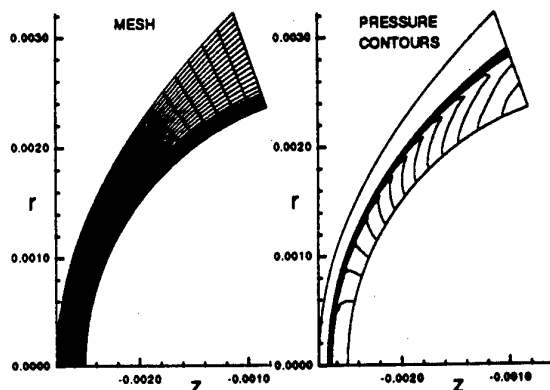


Figure 4. Mesh and pressure contours for Mach 18 real gas flow past a sphere.

Estimation of Tilt Rotor Dynamics and Aerodynamics in Low Speed Forward Flight

Ken Itoh* and Tomoari Nagashima**

Department of Aerospace Engineering, The National Defense Academy

1-10-20 Hashirimizu, Yokosuka, 239-8686 Japan

Key Words : Tilt Rotor, Blade Flapping, Parameter Identification

Abstract

For a better understanding of dynamic and aeromechanical behaviors of a tilt rotor during low speed transition state, a new approach to predict its induced flow field and blade flapping motions is formulated based on system identification technique. This is composed by two stage estimation processes, one for the state estimation (blade flapping deflection and velocity) and the other for the parameter identification to define induced velocity distribution over the rotor disc at arbitrary tilt angle. The state variables are estimated by the kinematic observer by incorporating measured blade flapping data detected with the blade mounted potentiometer and accelerometers. The induced velocity distribution over the disc at arbitrary tilt angle is approximated by the extended Glauert distribution and its undetermined coefficients are identified by applying the generalized least square method to simultaneous linear algebraic equations which originally describe blade flapping equation of motion. In this presentation, after brief introduction of typical experimental results obtained by the dynamic running test of the model rotor, benefits and difficulties experienced in the course of implementation of system identification to the aeromechanical problem are described. By comparing estimated and numerical blade flapping motions calculated with estimated induced velocity distributions, it is ascertained that the proposed

procedure are useful and practical approach for predicting aeromechanical behaviors of a tilt rotor during transition.

1. Introduction

With a steady progress of rotorcraft technology, rotorcraft based VTOL airplanes are expected to be most promising airvehicles in the next century. It is needless to say that the key factor for their successful designs and operations is to establish mathematical model which predicts precisely aeroelastic behavior of the rotor system during transition. In our laboratory, several basic researches to clarify aeromechanical characteristics of a tilt rotor system have been conducted using the dynamic running test facility.

In this paper, a new prediction method based on system identification technique for a blade flapping motion of a tilting motion at low speed forward flight is proposed and its usefulness and benefits as a practical design tool as well as active control devices are discussed.

2. Sensor Equation of the Blade Mounted Accelerometer

Consider an accelerometer mounted on a blade, as shown in Fig. 1. Let the blade be hinged at a distance e from the axis of rotation. The rotor shaft rotates with constant angular velocity Ω in C.W

* Graduate Student, National Defense Academy

** Professor, National Defense Academy

direction while the rotor assembly is tilting with constant pitching rate q (nose up is positive) about the horizontal axis located downward h from the hub center. The accelerometers are arranged along the blade C.G. axis, which coincide with the feathering and the blade elastic axes, with orientating their sensitive axes to the out-of-plane direction. Output of accelerometer mounted at $r=r_i$ is given as:

$$G_i = \left[\ddot{Z} + (r+e)\ddot{\Theta} + 2\dot{q}(r+e)\sin\Theta + g\cos\Theta + g\frac{dZ}{dr}\sin\Theta\cos\Theta \right]_{r=r_i} \quad (1)$$

where Θ and g are the rotor tilt angle and the gravity acceleration. Let expand the blade out-of-plane deflection $Z(r,t)$ by eigen functions as:

$$Z = \sum_{k=1}^n \gamma_k(r) \eta_k(t) \quad (2)$$

and transpose the 3rd and 4th terms into L.H.S, then, equation (1) becomes;

$$G_i' = \sum_{k=1}^n \left[\gamma_k(r) \ddot{\eta}_k(t) + \left\{ g\sin\Theta\cos\Theta + (r+e)\ddot{\Theta} \right\} \frac{d\gamma_k(r)}{dr} \eta_k(t) \right]_{r=r_i} \quad (3)$$

($i \geq 2k$)

Equation (3) constitute the sensor equations which determine modal deflection η_k and modal acceleration $\ddot{\eta}_k$ of the blade. It is understand from equation (3) that if the blade deflection is approximated by superposition of k th eigen functions, more than $2k$ sensors must be mounted on the blade to decompose η_k and $\ddot{\eta}_k$ definitely from the measured data.

3. Estimation of Flapping States and Identification of Induced Velocity Distributions

3.1. State Estimation

Though there are a lot of state estimation procedures, in this study, the kinematic observer proposed by McKillip is utilized because of its simple structure. When the blade deflection is approximated by the rigid mode and neglecting any elastic deformations, the kinematic observer is given as follows:

$$\frac{d}{dt} \begin{pmatrix} \hat{\beta} \\ \hat{\dot{\beta}} \end{pmatrix} = \begin{bmatrix} 0 & 1 \\ 0 & 0 \end{bmatrix} \begin{pmatrix} \hat{\beta} \\ \hat{\dot{\beta}} \end{pmatrix} + \begin{pmatrix} K_1 \\ K_2 \end{pmatrix} (\beta_{meas} - \hat{\beta}) + \begin{pmatrix} 0 \\ \hat{\beta}_{meas} \end{pmatrix} \quad (4)$$

where $(\hat{\cdot})$ and subscript "meas" indicate estimated and measured values, respectively. K_1 and K_2 are observer gains. Let us define the estimation error as:

$$e = \beta_{meas} - \hat{\beta}$$

and substitute it into equation (4), we have following error equation

$$\ddot{e} + K_1 \dot{e} + K_2 e = 0 \quad (5)$$

After several try and error calculations, combination of $K_1=144$ and $K_2=6400$ are selected as the observer gains. It should be noted that in equation (4), the blade flapping states can be estimated only by measured values of β and $\dot{\beta}$ both of which can be reduced from the sensor equation (3) and there is no necessary to know a priori the accurate blade equation of motion.

3.2. Identification of Induced Velocity Distributions

From the blade element theory, for a rigid and uniform blade, the flapping equation of motion of a tilting rotor blade is given as:

$$\begin{aligned} \beta'' + C_1 \beta' + C_2 \beta &= -2(1+\epsilon)\bar{q} \sin \Psi - \epsilon_s \cos \Theta + \frac{\gamma}{8} (C_3 \beta + C_4) - \frac{\gamma}{2} \int_{x_0}^x (x-\bar{x}) x \lambda_{(x,\Psi)} dx \\ C_1 &= \frac{\gamma}{8} \left\{ (1-x_0^4) \left(1 - \frac{8\bar{\epsilon}(1-x_0^2)}{3(1-x_0^4)} + \frac{2\bar{\epsilon}^2}{1+x_0^2} \right) \right. \\ &\quad \left. - \frac{4(1-x_0^2)}{3} \left(1 - \frac{3\bar{\epsilon}(1-x_0^2)}{1-x_0^2} \right) (\bar{h}\bar{q} - \mu \cos \Theta) \sin \Psi - (1-x_0)^2 \bar{\epsilon}^2 \mu \cos \Theta \sin \Psi \right\} \\ C_2 &= (1+\epsilon) + \epsilon_s \sin \Theta \cos \Psi + \frac{\gamma}{6} (1-x_0^2) \left(1 - \frac{3\bar{\epsilon}(1-x_0^2)}{2(1-x_0^2)} \right) \mu \cos \Theta \cos \Psi \\ C_3 &= (1-x_0^4) \left\{ 1 - \frac{4\bar{\epsilon}(1-x_0^2)}{3(1-x_0^4)} \right\} - \frac{8(1-x_0^2)}{3} \left(1 - \frac{3\bar{\epsilon}(1-x_0^2)}{2(1-x_0^2)} \right) (\bar{h}\bar{q} - \mu \cos \Theta) \sin \Psi \\ C_4 &= (1-x_0^4) \left\{ 1 - \frac{4\bar{\epsilon}(1-x_0^2)}{3(1-x_0^4)} \right\} \bar{q} \cos \Psi + \frac{4(1-x_0^2)}{3} \left(1 - \frac{3\bar{\epsilon}(1-x_0^2)}{2(1-x_0^2)} \right) \mu \sin \Theta \end{aligned} \quad (6)$$

where Ψ is the blade azimuth angle and $(\cdot)'$ means differentiation with respected to Ψ . $x=r/R$, $x_0=r_0/R$, $\bar{\epsilon}=e/R$, $\bar{h}=h/R$, $\bar{q}=q/\Omega$, $\mu=V/R\Omega$ and $\lambda=v/R\Omega$ are nondimensional radius position, root cut out, hinge offset, distance between hub center and tilt axis, pitching rate, forward speed and induced velocity, respectively. γ is a blade Lock's Number. As for the induced velocity distribution over the rotor disc at an arbitrary tilt angle, the extended Glauert formula given below is adapted

$$\lambda_{(x,\Psi)} = \lambda_0 + x\lambda_c \cos \Psi + x\lambda_s \sin \Psi \quad (7)$$

and its unknown coefficients (λ_0 , λ_c and λ_s) are identified by applying a recursive least-squares method to equation (6) after rearranging it to the linear algebraic equations with regard to λ_0 , λ_c and λ_s by putting $q=0$ and substituting blade flapping states for

their estimated values.

4. Model Rotor and Instrumentation

Dimension of the model blade and its planform are shown in Fig. 2. The blades were made up laminated balsa with an aluminum spar and had a cross section of NACA0015. Three accelerometers were allocated along the blade C.G. line as shown in Fig. 2 and they are designated as G30, G50, and G80, respectively depending on their radial positions. As easily anticipated, operational environment of the blade mounted accelerometer is very severe, it was selected to satisfy the following specification: measurement range: 200G, transverse sensitivity: less than 3%, over-range limit: 1000G, frequency response: 0 to 3.5kHz, size: L15×W10×H4.6mm, and weight: 1.2grams.

General arrangement of the model rotor is illustrated in Fig. 3. The rotor is a two bladed articulated rotor and powered by 400 Watts, speed controlled AC servo-motor. On the hinge axis, a potentiometer was installed and measured blade flap angle at the root. As for tilting and alternation of rotor tilt angle, another AC servo-motor was utilized. The model rotor assembly was installed on the tip of the support arm being cantilevered to the running carriage which moves along the guided rail with constant / programmed speed. Output signals of the potentiometer and accelerometers were picked up through the slip ring and after filtering with cut-off frequencies of 100Hz, they were stored to computer memory at 2kHz sampling rate.

The dynamic running test was conducted with various combinations of carriage velocity from 0 to 4.2m/s, blade pitch angle from 4 to 10 degrees, and tilt angle of -10 to 100 degrees for the case of fixed tilt angle and pitching rate of $\dot{q}=0\sim\pm 0.4\text{rad/s}$.

5. Measured Data and Estimation Results

Typical data measured by a potentiometer and accelerometers are shown in Fig. 4(a). In Fig. 4(b), blade flap deflection and acceleration reduced from the sensor equation (3) are also shown, together with the estimated flapping states obtained from the kinematic

observer. Parameter identification processes for the nondimensional induced velocity coefficients using the recursive parameter estimation are depicted in Fig. 5(a) and in Fig. 5(b), their converged values are plotted as a function of the tilt angle. It is shown that induced velocity coefficients decrease exponentially with an increase of the tilt angle and a symmetrical distribution can be obtained at $\Theta = 90^\circ$ which warrants a quasi-steadiness of a flow field around the rotor. In Fig. 6, examples of measured and calculated time histories of the blade flapping motion during transition are plotted. Figures depicted in the left side are those for the downward tilting motion from vertical to horizontal, while figures in the right side, those for the upward tilting motion. Finally, phase plane trajectories of flapping motion under the same condition in the case of Fig. 6 are shown in Fig. 7. Observing these figures, it is understood that calculated results predict such effect as the induced velocity distribution variations due to variable tilt angle and difference of gyro-moment depending on the direction of the pitching motion fairly well, but there remains a space to improve prediction accuracy by taking into account dynamic effect due to tilting motion on the induced velocity distribution.

6. Conclusions

- (1) Kinematic Observer, using measured data of potentiometer and blade mounted accelerometers, is effective tool for a prediction of dynamical behavior of a tilting rotor.
- (2) Because of high G environment of the model rotor blade, to keep measurement accuracy as higher possible it is desired, to adapt accelerometer to be able to satisfy the following specification: measurement range: less than 30G, transverse sensitivity: less than 1%, over-range limit: about 1000G, frequency response: more than 1kHz, size: within L10×W10×H5mm, and weight: less than 1gram.

Reference

- 1) R. McKillip, Jr.: Kinematic Observer for Active Control of Helicopter Rotor Vibration, *Vertica*, 12(1988), pp.1-11.

- 2) R. McKillip, Jr.: Periodic Control of the Individual-Blade-Control Helicopter Rotor, Vertica, 9(1985), pp.199-225.
- 3) R. McKillip, Jr.: Experimental Studies in System Identification of Helicopter Rotor Dynamics, Vertica, 9(1988), pp.329-336.
- 4) N.D.Ham: Helicopter Individual-Blade-Control, Thirty-First Japanese Aircraft Symposium, 10(1993)
- 5) K.Itoh & T.Nagashima: An Experimental Study on the Cross Coupling Effects of a Helicopter Rotor in Low Advance Ratio Using the Dynamic Running Test Facility, J.JSASS, 45(1997), pp.575-583.

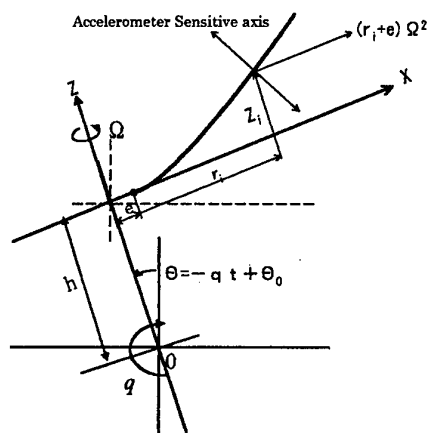


Fig. 1. Coordinate System

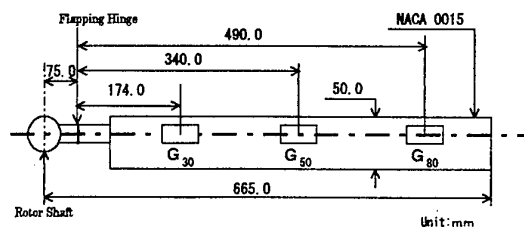


Fig. 2. Model Rotor Blade Geometry

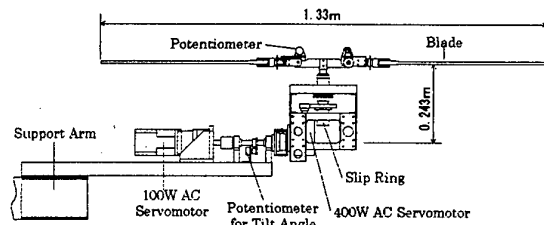


Fig. 3. General Arrangement of Model Rotor Assembly

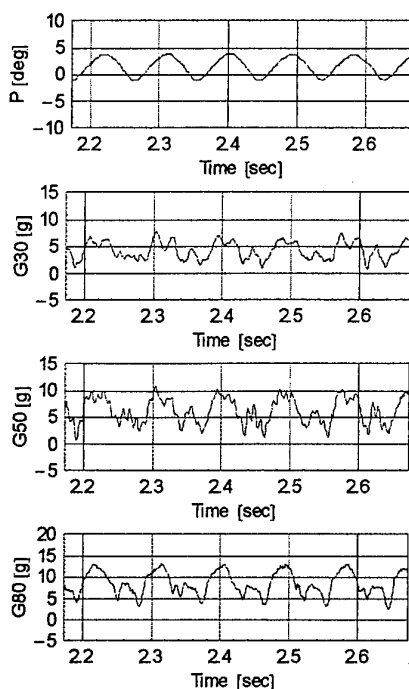


Fig. 4(a) Measured Data
($V=3.14\text{m/s}$, $\theta=9.2^\circ$, $\Theta=0^\circ$)

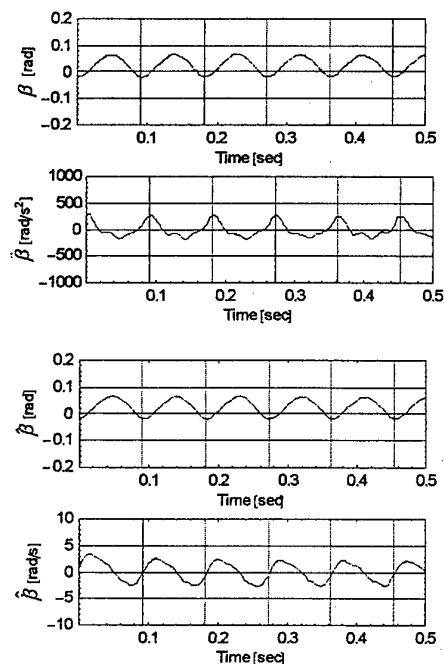


Fig. 4(b). Decomposed Results of Measured Data and
Estimated Blade Flapping State
($V=3.14\text{m/s}$, $\theta=9.2^\circ$, $\Theta=0^\circ$)

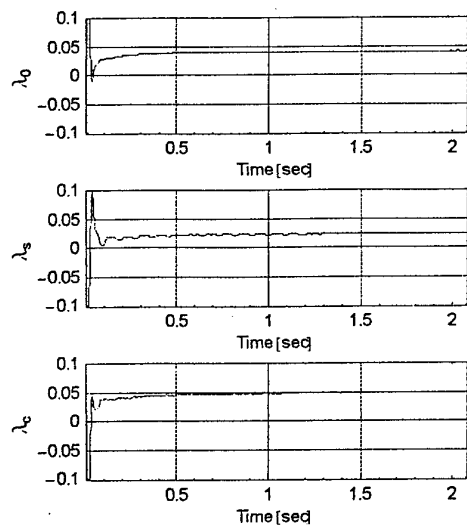


Fig. 5(a). Estimation Processes of Induced Velocity Coefficients
($V=3.14\text{m/s}$, $\theta=9.2^\circ$, $\Theta=0^\circ$)

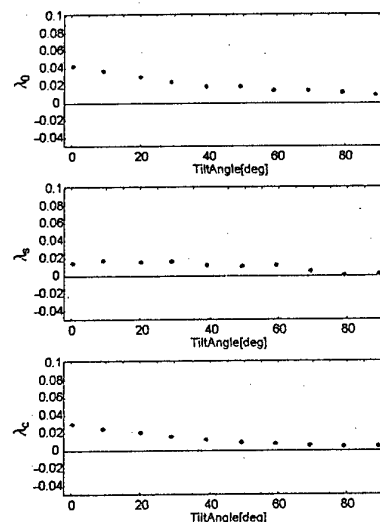
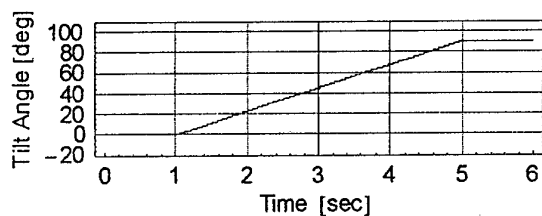
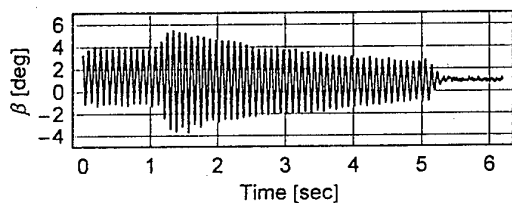


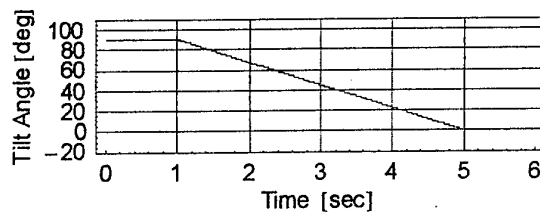
Fig. 5(b). Estimated Induced Velocity Coefficient at Various Tilt Angle
($V=3.14\text{m/s}$, $\theta=9.2^\circ$)



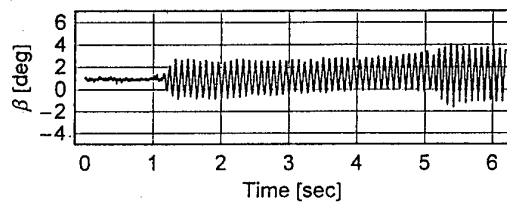
(a) Calculated



(b) Measured Data
(1) $q=-0.4\text{rad/s}$

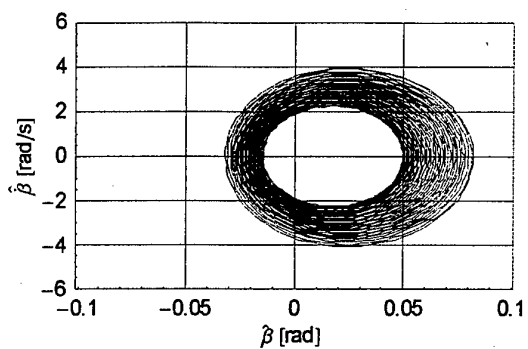


(a) Calculated

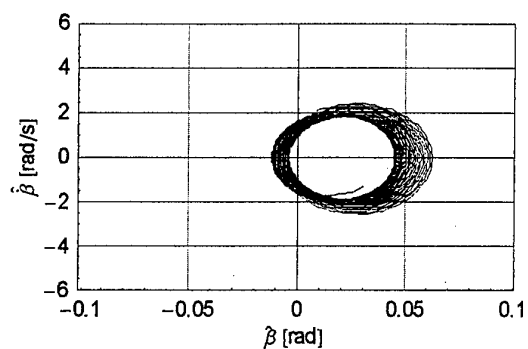


(b) Measured Data
(2) $q=0.4\text{rad/s}$

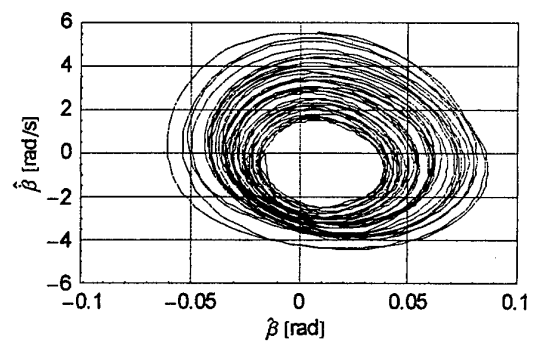
Fig. 6. Measured and Calculated Blade Flapping Motions of a Tilt Rotor during Transitions
($V=3.14\text{m/s}$, $\theta=9.2^\circ$)



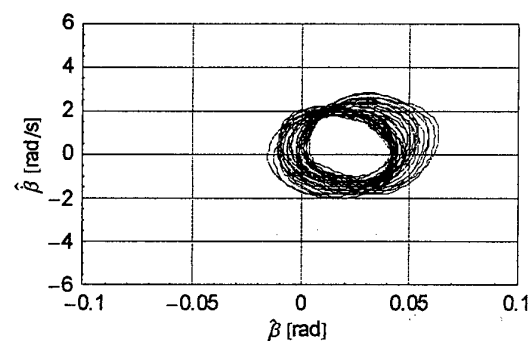
(a) Calculated



(a) Calculated



(b) Measured
(1) $q = -0.4 \text{ rad/s}$



(b) Measured
(2) $q = 0.4 \text{ rad/s}$

Fig.7. Phase Plane of Trajectories of Blade Flapping Motions during Transitions

($V = 3.14 \text{ m/s}$, $\theta = 9.2^\circ$)

Simulation of A Flexible Aircraft Dynamics

Hamid Reza KHEIRANDISH¹ and Jiro NAKAMICHI²

¹Research Center of Computational Mechanics, Inc, Tokyo, Japan hamid@rccm.co.jp

²National Aerospace Laboratory, Tokyo, Japan jiro@nal.go.jp

Key Words: Aeroelasticity, Flutter, SST

Abstract

Numerical flutter simulation of the experimental SST in transonic region is presented. The elasticity of the aircraft's wing and fuselage is taken into account by utilizing 24 symmetric and anti-symmetric natural modes in solving structural equations. The Euler and structural equations were integrated simultaneously to obtain SST responses. The aileron flutter, like the linear theory, was found the most critical one for this configuration. The flutter boundaries are estimated lower than those obtained by the linear theory for the range of Mach number 0.6-1.0.

Introduction

The estimation of flutter boundary of high-speed aircraft plays an essential role in the structural design concepts and parameters. Its role gets more importance in the case of supersonic transport because relatively thin wing-sections or control surfaces are necessarily used for these configurations. Therefore an interactive relation between design parameters and flutter boundary suggested by experiment or CFD is highly requested at primarily steps of structural design. With remarkable progresses in computing speed and numerical methods, the CFD is now of much current interest to do this request. Linear methods can predict the flutter boundary with relatively high accuracy in all the flows except for transonic region where the flow is highly nonlinear or when the flow is highly separated. In these regions the nonlinear methods should be employed for accurate prediction.

The authors have developed a CFD Code to numerically simulate unsteady coupled fluid-structure problems based on Navier-Stokes/Euler equations. This code has been used and verified in several large scale problems such as 3-D high aspect ratio wings^{1,2}, and Arrow wing configuration³. This report describes numerical simulation of aeroelastic responses of the NAL Supersonic Transport(SST) experimental aircraft around transonic region. The unsteady Euler equations coupled with structural equations were solved to obtain flutter boundary of SST. The results were obtained either with and without structural damping and were compared with linear theory results when available.

Governing Equations

The computation is based on unsteady Euler equations for governing flow field and a modal approach form of equations for structural side(Eqs. 1). These equations can be described in non-dimensional form as

$$\frac{\partial \hat{Q}}{\partial \alpha} + \frac{\partial \hat{F}}{\partial \xi} + \frac{\partial \hat{G}}{\partial \eta} + \frac{\partial \hat{E}}{\partial \zeta} = 0$$

$$m_i \ddot{q}_i + k_i^2 m_i q_i = \bar{Q} \iint (-C_p n_z) \Phi_i dS \quad (1)$$

where q_i are generalized coordinates: Φ_i , m_i and k_i are the natural modes, generalized masses and natural reduced frequencies corresponding to the i 'th mode, respectively. \bar{Q} is the nondimensionalized dynamic pressure and n_z is the z -direction component of normal vector to the wing surface. The double integration symbol implies the integration over the whole aircraft surface. The structural equations of motion are derived by the assumption that the deformation of the body under consideration can be described by a separation of variables involving the summation of free vibration modes weighted by generalized displacements. For more information on obtaining governing equations see Ref 4-5. The integration of governing equations are implemented using a second order upwind TVD scheme^{6,7} for the flow equations and Wilson's θ implicit method⁸ for the structural ones. The procedure of unsteady computations can be carried out as follows:

1. Compute steady state solution at a given Mach number
2. Assume dynamic pressure
3. Assume initial value for some of generalized velocities
4. Solve structural equations and update surface geometry and corresponding surfaces and internal grids
5. Update flow field solution
6. Repeat steps 4 To 5 for many cycles and save time history of generalized coordinates.

To find flutter boundary at a given Mach number, repeat steps 3 to 6 for a range of dynamic pressures and find stable and unstable regions by analyzing mode responses.

Characteristics of Experimental Model

A plan-view of this model is given in Figure 1. The dimensions and typical parameters of the are as follows; Fuselage length 11.5m, wing root chord-length 4.2m, span length 4.72m, aspect ratio 2.1 and swept-back angles 24°-28.8°. The structural dynamics characteristics, natural mode shapes and frequencies of this model were found, using NASTRAN, by FHI. The flutter boundary, except at transonic regions, was also determined using linear theory. They found that the aileron flutter is the most critical one. The first 24 symmetric and anti-symmetric modes of fuselage and wings are shown in Table 1. The modes which contain aileron motion are marked by '*'.

Senior Eng., Technical Development Dept.
Head, Aeroelasticity Div.

Table 1. Vibration Characteristic of Experimental Model

Mode No.	Frequency	Dominant
	Hz	Mode Shape
1	0.0	Rigid Pitching
2	0.0	Rigid Heaving
3	0.0	Rigid Rolling
*4	8.7	FLaB, WB
5	11.5	FLaB
*6	16.5	WB-s
*7	26.0	FLaB, Aileron T-s
*8	27.4	WB-a
*9	29.6	Aileron T-a
10	30.2	Aileron T-s
11	34.1	FLaB
12	38.1	FLaB T
13	42.4	V
14	42.9	FLaB
15	47.7	H-a
16	48.7	H-s
17	56.3	W-s
18	62.5	W-a
19	67.9	W-s
20	71.0	W-a, V
21	72.2	W-s, Aileron B
22	76.9	W-s, Aileron T
23	83.0	V
24	89.1	V

F:Fuselage W:Main Surface H:Horizontal Tail V:Vertical Tail
B:Bending T:Torsion
Lo: Longitudinal La: Lateral -s: Symmetric -a: Anti-symmetric
* Mode indicated in Figures

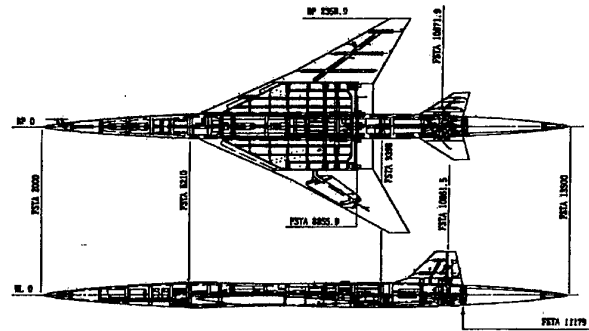


Fig 1. Plan-View of SST Experimental Model

The flight envelope of SST experimental aircraft in a frame of Altitude vs. Equivalent Air Speed (EAS) is illustrated in figure 2. This figure shows the rocket launching path and also free flight path. Our objective is to investigate that the flight path is free of flutter specially in transonic region.

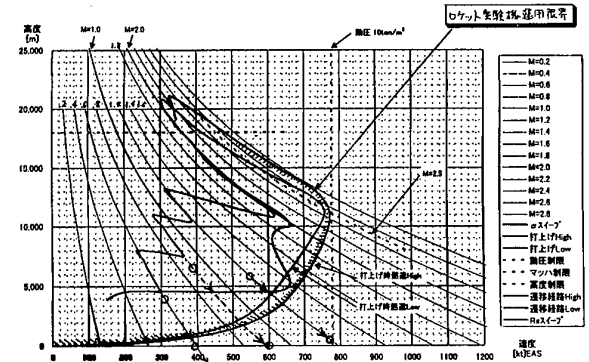


Fig 2. Flight Envelope of SST

Numerical Results and Discussions

A H-H type mesh with 126x121x80 grid points was generated around full SST configuration for these computation. The mesh generator is based on elliptic methods. The minimum size of grid in normal direction is of order of .005 based On the wing root

chord length. The outer boundaries are put at least 15 times the wing root chord length away from the surfaces in the stream-wise and normal directions and 3 times the half-span length in span-wise direction. A schematic view of grids around the half-span of SST is shown in Fig 3.

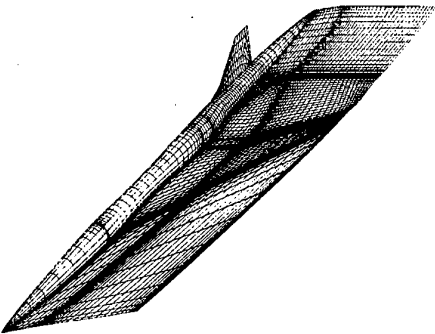


Fig 3. Grid Distributions on SST

The first 24 modes, which were found by NASTRAN, were considered in the computations. These modes contain symmetric modes as well as ant-symmetric modes. The SST responses in Mach number range 0.6 to 1.2 at several dynamic pressures with or without structural damping were found. The results are illustrated as selected generalized modes(dominant modes) vs. non-dimensional time at each Mach number and dynamic pressure to investigate the SST responses. For the sake of convenience modes marked by "*" in table 1 are only illustrated in this paper. They are mode 4: fuselage and main surface bending, mode 6: main surface symmetric bending, mode 7: fuselage bending and aileron torsion-symmetric, mode8: main surface bending-anti-symmetric, and mode 9: aileron torsion- anti-symmetric modes. The first three rigid modes are not considered here.

An example of steady state pressure distributions on four different semi-span stations(0.0%, 30%, 50%, 70%) at Mach number 0.9, obtained by present computation and linear theory, are given in Figure 4. The 0.0% semi-span stations, corresponds to body-symmetric line.

Hereunder steady numerical computation results will be shown and discussed. At all the numerical simulations, structural damping is set to 0.0 unless mentioned.

The results at Mach number 0.6, where dynamic pressures are 100kPa and 80kPa, respectively are given in figures 5-6. This figures show the time histories of some dominant generalized coordinates. It can be seen from figure 6 that only those modes which contain aileron mode(ie; mode7 and 8) will be diverged first by a 20kPa increase in dynamic pressure. Other modes show positive damping at this range of dynamic pressure.

Figure 7-9 show simulation results at Mach number 0.9. The dynamic pressures are set at 90kPa, 60kPa and 25kPa. At this Mach number simulations with structural damping equal to 0.02 were also carried out. These results are given in figures 10-11. As the previous case, modes 7 and 8 are the modes which show instability first by an increase in dynamic pressure. The inclination is similar for the case with structural damping 0.02, too. The critical dynamic pressure(the dynamic pressure at which flutter occurs) is about less than 60kPa without structural damping while it increases to 70kPa when structural damping is 0.02.

The SST response at Mach number 1.0 and dynamic pressure 90kPa is shown in figure 12. The modes 7 and 8 are already

diverged at this dynamic pressure. Other modes are still show convergence.

The results at Mach number 1.2, dynamic pressures 130kPa and 100kPa are given in figures 13-14. The response is stable at 100kPa while some modes(ie; mode 7 and 8) seems to be unstable at 130kPa. The tendency of modes are similar to the previous cases..

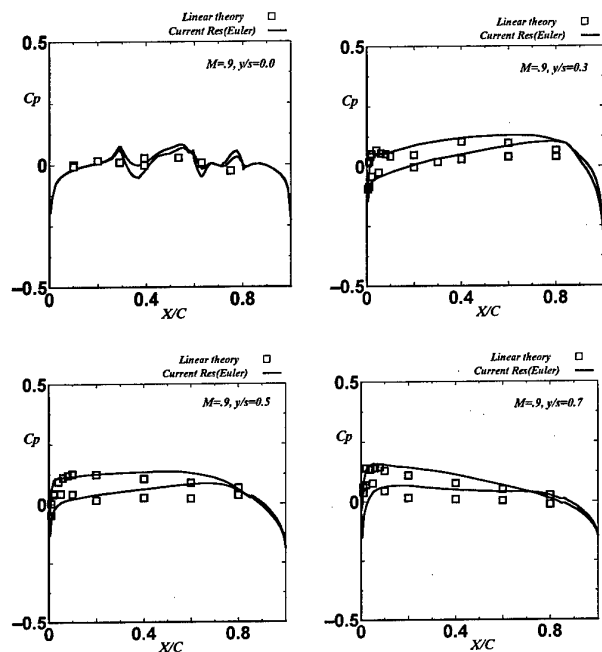


Fig 4. Steady State Pressure Distributions, $M=0.9$, $A=0.0$

Figure 15 shows the main surface flutter boundary obtained by present method and linear-theory. The vertical and horizontal axes are: equivalent air speed and Mach number, respectively. In this Figure main surface and aileron flutter boundaries obtained by linear theory are illustrated by dashed line. The triangles show the data computed by present method. The results are agreed together only at Mach number 1.2. The flutter speed obtained by present simulations are lower than those estimated by linear-theory for Mach numbers less than 0.9. A dip-like curve is obtained by present method although no shock waves were seen in all the computations.

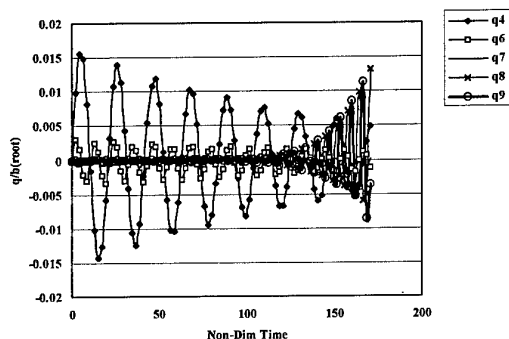


Fig.5 SST Response at $Dp=100\text{kPa}$, $M=0.6$

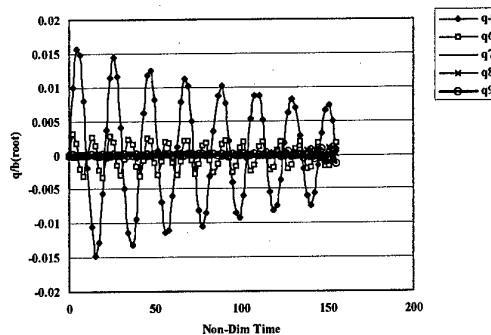


Fig.6 SST Response at $Dp=80\text{kPa}$, $M=0.6$

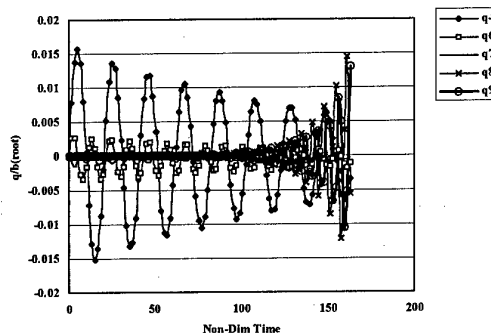


Fig.7 SST Response at $Dp=90\text{kPa}$, $M=0.9$

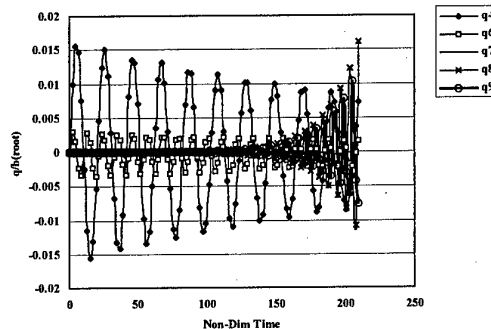


Fig.8 SST Response at $Dp=60\text{kPa}$, $M=0.9$

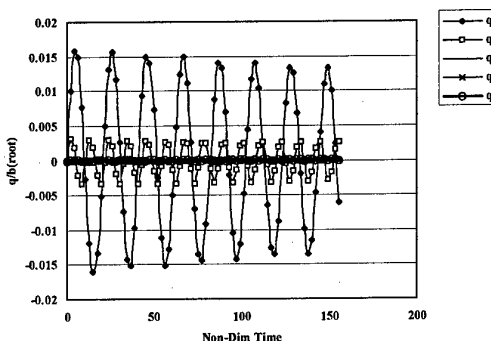


Fig.9 SST Response at $Dp=25\text{kPa}$, $M=0.9$

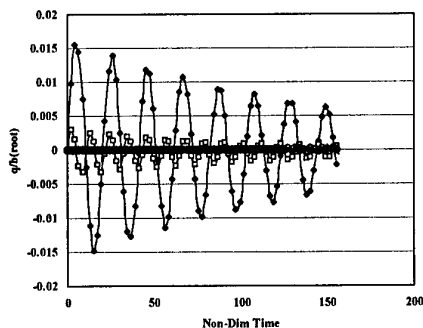


Fig.10 SST Response at $D_p=60\text{kPa}$, $M=0.9$, $g=.02$

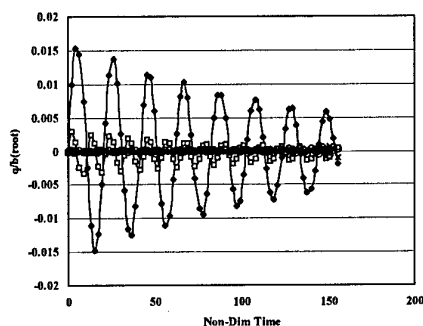


Fig.11 SST Response at $D_p=70\text{kPa}$, $M=0.9$, $g=.02$

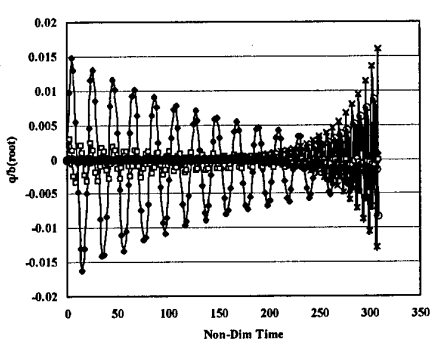


Fig.12 SST Response at $D_p=90\text{kPa}$, $M=1.0$

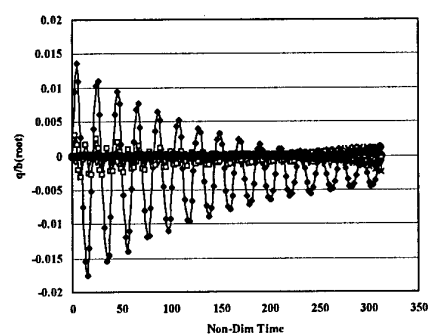


Fig.13 SST Response at $D_p=130\text{kPa}$, $M=1.2$

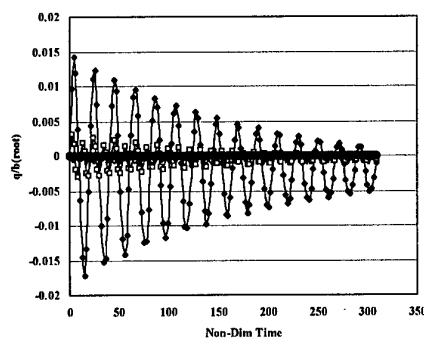


Fig.14 SST Response at $D_p=100\text{kPa}$, $M=1.2$

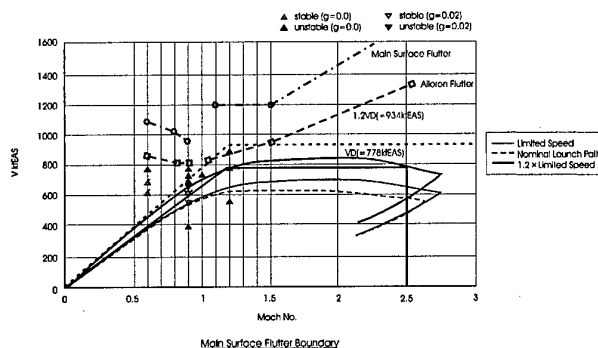


Fig.15. Main surfaces Flutter Boundaries

Conclusion

Numerical flutter simulation of full-SST configuration has been carried out using Euler solution at transonic region. The aileron flutter was found as the most critical one. The flutter speeds obtained by the present code do not agree well with those of linear-theory except at Mach number 1.2.

The authors thank Fuji Heavy Industries for their offering the results of vibration analysis for the present studies.

REFERENCES

- [1] H. Kheirandish, G. Beppu and J. Nakamichi, Numerical Simulation of Viscous Unsteady Flow around Wings Oscillation in Elastic Modes, JSCS Symposium, Tokyo, Japan (1996)
- [2] H. Kheirandish, G. Beppu and J. Nakamichi, Computational Investigation of Wings Flutter To be published in "International Journal of Computational Fluid Dynamics, 99/10"
- [3] H. Kheirandish, and J. Nakamichi, Inter-Code Validation between NAL and DLR in the Aeroelastic Simulation for SST Configuration, CEAS/ICAS/AIAA/NASA Langley International forum on Aeroelasticity and structural Dynamics (Virginia-Williamsburg), 1999/6/21-25
- [4] T.H. Pulliam and J.L. Steger, Recent Improvements in Efficiency, Accuracy, and Convergence for Implicit Approximate Factorization Algorithms, AIAA Paper 85-0360, (1985)
- [5] R.L. Bisplinghoff, H. Ashley, Principles of Aeroelasticity, Dover Pubns (1975)
- [6] H. Yee and A. Harten, Implicit TVD Schemes for Hyperbolic Conservation Law in Curvilinear Coordinates, AIAA paper 85-1513 also AIAA Journal, Vol.25, No.2, (1987), pp.266-274
- [7] H. Yee and G.H. Klopfer and J.L. Montagne, High-Resolution Shock-Capturing Schemes for Inviscid and Viscous Hypersonic Flows, NASA TM-100097 (1988).
- [8] K.J. Bate and E.L. Wilson, Numerical Methods in Finite Element Analysis, Prentice-Hall (1976)

STRUCTURAL FATIGUE LIFE EXTENSION AND DAMAGE TOLERANCE USING HOLE COLD EXPANSION TECHNOLOGY

Len Reid*

Fatigue Technology Inc., 100 Andover Park West, Seattle, WA 98188 USA

Key Words: Aircraft, Airworthiness

ABSTRACT

To meet fatigue life or durability and damage tolerance requirements, structural fatigue life enhancing methods are often used in aircraft and rotorcraft structures. Pre-stressing fastener holes and holes in attaching structures or lugs by hole cold expansion is widely used to prevent growth of cracks originating at holes. The residual compressive stresses generated shield the hole from cyclic loads and reduce the stress intensity factor associated with crack growth. The overall fatigue life and damage tolerance is enhanced on both new and aging aircraft structures. The paper describes the cold expansion process and benefits as well as derivative processes and applications.

1. INTRODUCTION

Aircraft and rotorcraft are designed using good safety, durability and structural integrity principles. They are also required to have long fatigue lives and low operating and maintenance costs. A number of different design techniques and principles are used to ensure basic structural integrity. Structural fatigue life enhancing methods are often used to meet design durability and fatigue life.

Most conventional aircraft structures require fastened joints in wings and fuselages as integral parts of the design to facilitate manufacture and assembly. The structure also includes attaching lugs and clevises for joining structural sub-assemblies and mounting components. Due to their complexity and loading, all of these "joints" are a point of high stress concentration. Since most fatigue cracks originate at holes subjected to cyclic tensile loading they are also the primary source of structural fatigue problems.

Good detail design of joints is necessary to achieve the required fatigue life and structural endurance under expected in-service loads. The installation of high interference fit fasteners and pins can improve fatigue life of the joint however, it is highly dependent on the fit of the fastener. Alternatively, pre-stressing the hole to induce beneficial residual compressive stresses around the hole can greatly enhance the fatigue resistance of the joint by preventing cracks from growing from the hole. Split-sleeve hole cold expansion is the most widely used and proven cost effective method of pre-stressing the holes. The resulting residual compressive stresses effectively shield the hole from the cyclic tensile loads that cause cracks to grow. Furthermore, when used on older aircraft structure, these beneficial stresses retard crack growth by reducing the stress intensity factor

associated with a pre-existing crack. The overall fatigue life and damage tolerance of the structure is greatly enhanced by using this technology.

2. SPLIT SLEEVE COLD EXPANSION PROCESS

Split Sleeve Cold Expansion is a proven technology for increasing the fatigue life of holes in aircraft structures [1-3]. Since its development in the 1960s by Boeing, and later by Fatigue Technology Inc. (FTI), it has been used to cold expand millions of holes in almost every military and commercial aircraft flying today. Furthermore, it is used in design to reduce weight, and extend inspection thresholds in structure designed to meet damage tolerance requirements.

The process, shown in Figure 1, improves the fatigue life of holes in metallic structure by generating a large, controllable zone of permanent residual compressive stress around the hole. It is a one sided process accomplished by pulling a tapered solid mandrel, pre-fitted with a split sleeve, through a hole. The action of drawing the mandrel through the hole causes the hole to permanently deform, producing an annular zone of compressive stress next to the hole. The residual compressive stress created by split sleeve cold expansion significantly increases fatigue life by reducing the stress concentration produced at the hole by in-service loads.

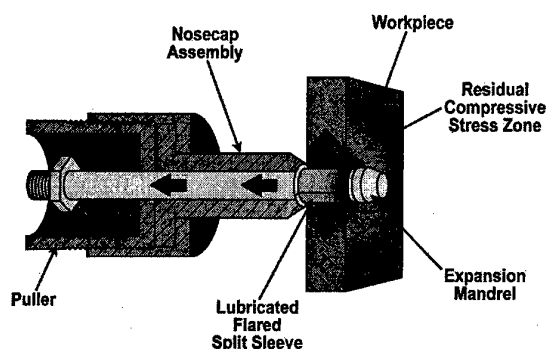


Figure 1 Split Sleeve Cold Expansion Process

* Vice President, Engineering

The magnitude of the peak residual compressive circumferential stress is about equal to the compressive yield stress for the material and typically spans one radius to one diameter from the edge of the hole. A balancing tensile stress zone with a peak stress of 10-15 percent of the material tensile yield strength lies just beyond the compressive stress region. Fatigue life improvement from this process usually ranges from 3 to 10 times in typical aircraft structures as shown in Figure 2 for aluminum alloy [3] and Figure 3 for titanium [3].

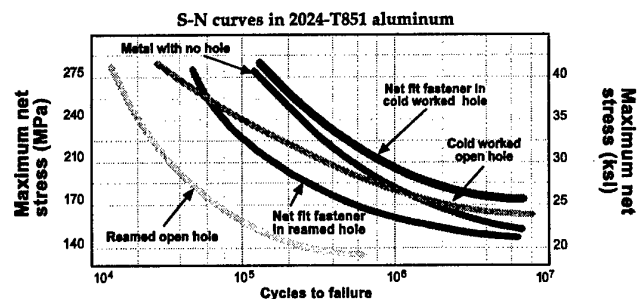


Figure 2 Fatigue Life Improvement - 2024-T851 Aluminum Alloy

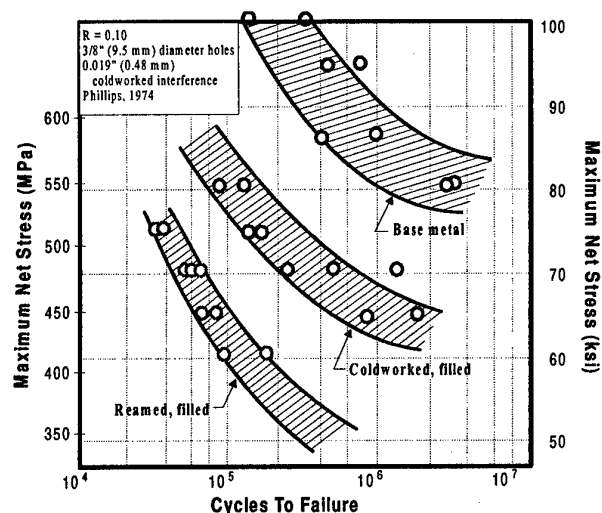


Figure 3 Fatigue Life Improvement - Titanium (6Al-4V)

Optimal fatigue performance is achieved when the hole is expanded by at least 3 percent for aluminum, and at least 4.5 percent for titanium and high strength steels, in typical hole diameters (up to 25mm) and plate thickness. Larger holes up to 110mm (4.5 inches) diameter have been cold expanded. FTI has also developed a method for cold expanding non-circular hole configurations. It is also worth noting that holes may be re-cold expanded should there be a requirement to further rework structure.

3. EFFECT ON CRACK GROWTH

The cold expansion residual stresses reduce crack growth rates by reducing the stress intensity factor range (ΔK) [4] and the stress ratio (R , min. stress/max. stress). The effect is shown in Figure 4. The stress intensity factor is a measure of the stresses acting at the crack tip. Additionally, the presence of residual stresses may change the critical crack length for unstable fracture, because it reduces the static stress intensity factor. The reduction in crack growth rate and the increased critical crack length significantly improves the damage tolerance of the structure.

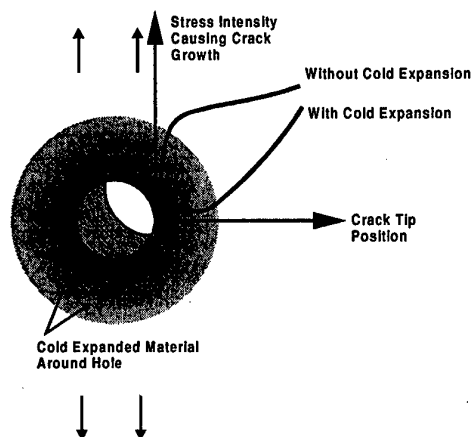


Figure 4 Reduction in Stress Intensity Factor Range Under Residual Compressive Stress

Figure 5 shows that cracks about 1mm in length growing from a 6mm (1/4 inch) diameter hole in 7075-T6 aluminum alloy, under 248 MPa (35 ksi) net stress, are totally arrested when subjected to the same applied cyclic loads [5]. The residual compressive stress zone acts like a strong clamp on the material around the crack minimizing crack opening displacement, thereby preventing growth.

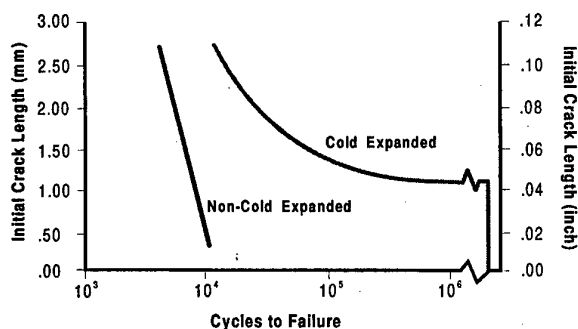


Figure 5 Effect of Cold Expansion on Stopping Crack Growth (7075-T6 Aluminum)

4. DURABILITY AND DAMAGE TOLERANCE

Most airworthiness authorities require inspection thresholds be established for single-load path structures based on crack propagation analysis assuming a small manufacturing flaw exists at critical holes. In the past, particularly on military aircraft, initial manufacturing damage was simulated by a 0.050-inch radius corner crack or "rogue flaw." In addition, 0.005-inch cracks were assumed to exist at each fastener hole, representative of equivalent initial quality, for continuing damage calculations.

When fatigue-enhancing systems such as hole cold expansion are used, the rogue flaw (0.050-inch crack) has been simulated by a smaller crack because of the known reduction in crack growth due to the residual compressive stresses. Because the cold expansion residual stresses and their effect on fatigue life are difficult to predict analytically, the United States Air Force (USAF) damage tolerance specifications allow the design of a cold expanded (Cx) hole to be based on analysis for the same size non-cold expanded (NCx) hole with a reduced initial assumed flaw. In this case it is typically a 0.005-inch radius corner flaw. The result is a very conservative approach, as shown in the example at Figure 6 for 2024-T3 aluminum alloy.

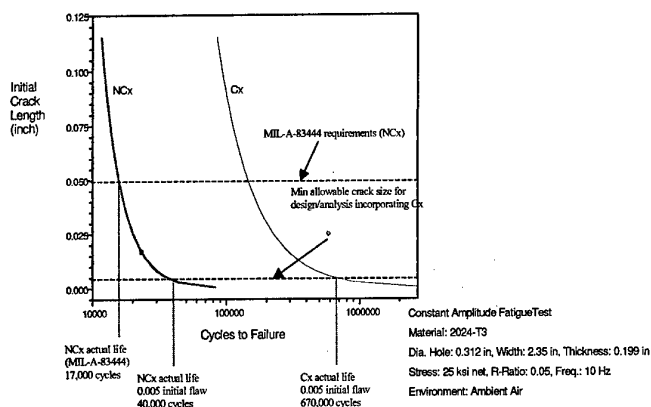


Figure 6 Reduced Initial Flaw Assumption Versus Test for Pre-Cracked Cold Expanded Holes

Although some benefit is allowed for cold expansion, actual test results show the process is far more effective in preventing crack growth from pre-cracked holes. This benefit is due to the residual compressive stresses reducing the stress intensity factor at the crack tip and also the reduction in mean stress. In many tests, coupons with pre-cracked holes that were cold expanded would not fail because of the increase in fatigue strength due to the residual stresses. A new analytical method to account for the benefits of hole cold expansion that modifies the stress intensity factor is being developed by FTI and discussed in reference [6].

5. DERIVATIVE PROCESSES

The method of cold expanding holes has been further adapted for expanding bushings into mounting lugs, hinges and fittings. Bushings installations have also been used to repair or resize holes that have been damaged by fatigue cracks, fretting or elongation. The two techniques known as ForceMate® (FmCx™) (shown in Figure 7) and BushLoc® (BICx™), developed by FTI [7], involve radially expanding an initially clearance fit bushing

or insert into the hole thereby imparting a high level of interference. In most cases, this process also cold expands the material around the hole to generate a residual compressive stress zone around the bushing. Bushings made from a variety of materials (steel, stainless steel, beryllium copper, aluminum nickel bronze, etc.) in diameters up to 114mm have been successfully installed using these processes. These processes greatly enhance the integrity of a bushed hole or fitting.

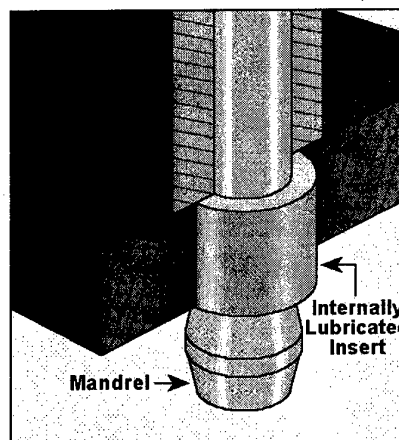


Figure 7 The ForceMate Bushing Installation Process

In both methods, bushings have proven to be very effective in eliminating fatigue cracks (Figure 8) and bushing migration and movement, which induces fretting. In addition to the other benefits, the FTI bushing installation methods reduce corrosion caused by installation damage (galling and scoring of the hole). ForceMate bushings are used in aircraft engine pylon attachments, landing gear attachments, wing fold fittings and rotating components in helicopters. Both hole cold expansion and ForceMate bushing installation have been successfully demonstrated and used in gas turbine engine components to meet stringent low cycle fatigue (LCF) requirements [8].

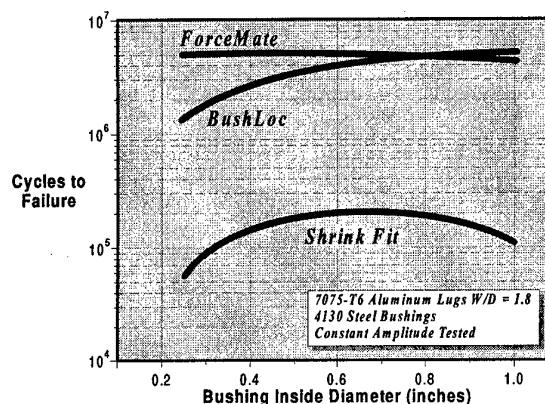


Figure 8 Fatigue Life Comparison of Bushing Installation Methods

A further derivative process is a unique rivetless style nut plate, adapted from the previous bushing installation methods which utilizes a nut retainer that is split sleeve cold expanded into the fastener hole. The ForceTec® (FtCx™) system is shown in Figure 9. The retainer has an integral "basket" and clip which retains a

standard floating nut after the retainer is installed. The combined effect of high interference and residual compressive stresses from cold expansion, prevent rotation of the retainer and also provide significant fatigue and crack growth life improvement of the structure.

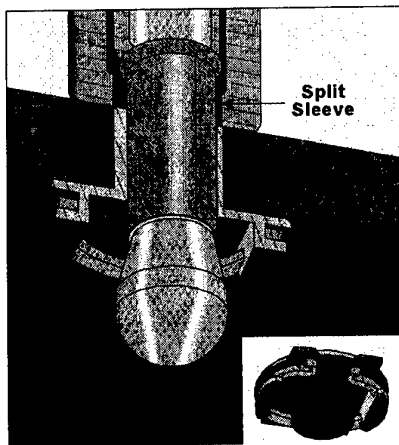


Figure 9 Schematic of ForceTec Retainer Expansion

The ForceTec system has been designed to meet the performance specifications defined in military specification MIL-N-25027. It can accommodate fastener sizes from 3/16 to 9/16 inch diameter (5 to 14 mm) in materials as thin as 2mm (0.80 inch). It is an effective blind nut attachment where fatigue is a problem or where a large number are required because they can be installed in much less time than other nut plates.

6. CONCLUSION

Split Sleeve Cold Expansion is a measurable and quantifiable way of improving the fatigue life and quality of a hole without relying on the integrity of the fastener fit. The overall result is enhanced fatigue life, which can allow an aircraft to fly or to be operated beyond its original fatigue limit.

Benefits derived from use of this process include: (1) added safety and operational assurance through improved structural integrity, both in production and repair; (2) reduced maintenance costs by eliminating fatigue problems associated with fastened joints; (3) reduced inspection costs, by extending inspection intervals resulting from the enhanced durability and damage tolerance of the structure; and (4) possible structural weight savings.

Derivative processes such as ForceMate or BushLoc high interference bushing installation prevent bushing migration, fretting and corrosion and enhance the overall durability of bushing installations and assemblies. The ForceTec rivetless nut plate improves blind nut plate installations and removes a potential source of structural fatigue failure. All processes are being used on both commercial and military aircraft.

7. REFERENCES

- [1] FTI Split Sleeve Cold Expansion Process Specification FTI 8101C, September 1994 (first issued June 1981).
- [2] Champoux, R.L., "Fatigue of Aircraft Structures," Fatigue Prevention and Design, Chameleon Press Ltd., London, 1986, pp. 41 et seq.
- [3] Phillips, J.L., "Sleeve Coldworking Fastener Holes," Vol. I, 1974, Air Force Materials Laboratory Report AFML-TR-74-10.
- [4] Clark, G., "Modeling Residual Stresses and Fatigue Crack Growth at Cold Expanded Fastener Holes," Fatigue Fracture of Engineering Materials Structures, Vol. 14, No. 5.
- [5] Petrak, G.J. and Stewart, R.P., "Retardation of Cracks Emanating from Fastener Holes," Engineering Fracture Mechanics, Vol. 6, Pergamon Press, 1974, pp. 275-282.
- [6] Reid, L.F., et al, "The Evaluation of a Modified Stress Intensity Factor for Cold Expanded Holes," International Committee on Aeronautical Fatigue Conference Proceedings, Seattle, Washington USA, July 12-16, 1999.
- [7] Champoux, R.L., and Landy, M.A., "Fatigue Life Enhancement and High Interference Bushing Installation Using the ForceMate Bushing Installation Technique," 1986 American Society for Testing and Materials (ASTM) Report STP 927, pp. 39-52.
- [8] Rufin, A.C., "Extending the Fatigue Life of Aircraft Engine Components by Hole Cold Expansion Technology," International Gas Turbine and Aeroengine Congress and Exposition, Cologne, Germany, June 1-4, 1992, ASME 92-GT-77.

SAAB Aerospace: An Overview of Full Scale Testing Programs

Gene R. Woelffer

MTS Systems Corporation
14000 Technology Drive
Eden Prairie, MN 55344 USA

Key Words: SAAB, Aerospace

Abstract:

An overview of the recent structural testing programs performed at SAAB Aerospace including the SAAB 340 and 2000 commercial transports, and the Gripen fighter. Presentation will cover the various full scale testing equipment on all 3 programs, including controls, mechanical loading, and fixtures used.

Structural Testing Facilities at SAAB

Static-, Fatigue- and Damage Tolerance Testing

Facilities:

5 Laboratories

Total area of 2900 m²

12 Component facilities

4 Fullscale facilities

Test Stations:

340 286 Test Stations

330 Control channels

Station size: 1-115 channels

1850 Data acquisition ch.

75 Acoustic emission ch.

Test Equipment:

300 400 Actuators

7 10 Hydraulic supply units

Capacity up to 650 l/min

Testing at Saab

Unequal area actuators

Hydraulic safety manifolds

Five port servo valves

2 or 3 bridge loadcells

Control system

Data acquisition system

Restrained test article

Both compression and tension whiffle trees

Three stage valve driver to control home built air valve

Paging system to monitor test

Present Commercial Testprojects

Saab 2000 Fatigue

Wings, fuselage excluding cockpit and tail.

56 channels, cabin pressurization

MTS Aero-90

Saab 2000 Tail

8 load channels

MTS Aero-90

Saab 340 Damage Tolerance Test

52 load channels 1 airp.

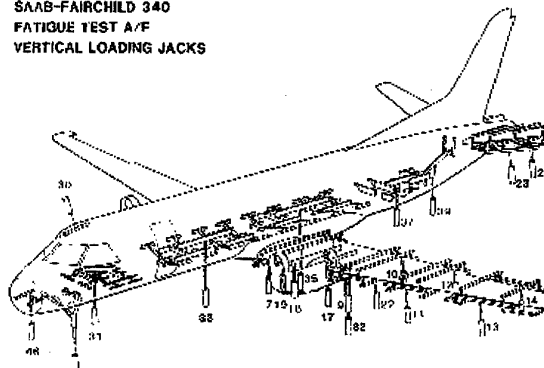
MTS RT11 +450 Electronic

Component Tests

Various

MTS Aero-90LT+older equipment

SAAB-FAIRCHILD 340
FATIGUE TEST A/F
VERTICAL LOADING JACKS



Present Military Testprojects

JAS 39 Gripen Fullscale Fatigue

82 load ch., 2 disp., 9 airpress. 5 hardpoints

MTS TSC 872

JAS 39 Gripen Two Seater Fatigue

44 load ch., 5 air, 5 hardpoints

MTS Aero-90

Component Tests

Various

MTS Aero-90LT

"SAAB is a good customer"

Operations Manager

Aerospace Structures and Materials Division

Structures Testing Concept

Requirements: Static Test (Full Scale)

Demonstrate 150% LL (180% LL for CFRP) with no failure

Demonstrate no permanent deformation at LL

Measure load in primary load paths (calibration)

Verify the design concept and the global FE-model by measuring strain and deflection for comparison

Demonstrate strength beyond the designed strength (secondary)

Structure Testing Concept

Requirements: Fatigue Tests (Full Scale)

Demonstrate 4 times the service life without damages

At least 4 times (during test) ahead of the fleet leading a/c

Scheduled inspection to detect cracks or other damages

Use flight per flight spectra (same database as in analysis)

Structure Testing Concept

Requirements: Damage Tolerance Tests

Demonstrate 2 times the service life followed by 120%

LL residual strength for critical parts

Artificial defects introduced at critical locations

All defects measured and documented

Scheduled inspection during test to detect possible crack propagation and/or to follow crack propagation

Structure Verification Concept

The Solution: Load Spectrum

A sequence of 313 missions corresponds to 200 flh and contains about 480000 states

Of the 313 missions, 32 are unique

Of the 480000 states, about 15000 are unique

Local spectra generated from the global FE-model

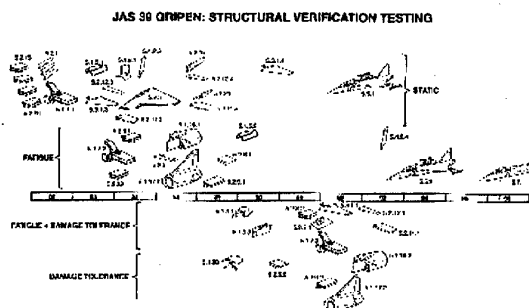
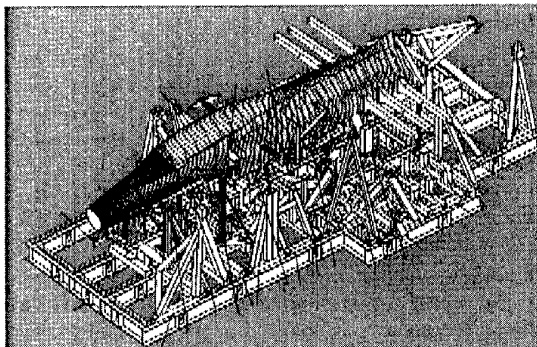
In house developed tools for fatigue and damage tolerance analysis with access to the local spectra

About 150 critical parts analysed at 1000 locations of defects

Conclusion:

39 Gripen Testing

55 different static, fatigue and damage tolerance tests have been done, from small part tests to full scale fatigue tests, over a 15 year period.



The Role of Aeroelasticity in Recent German and European Aircraft Research and Development

H. Hönlinger*, F. Kießling**, R. Voß***

* Director

** Section Head, Aeroelastic Simulation

*** Section Head, Unsteady Aerodynamics

DLR Institute of Aeroelasticity, Bunsenstr. 10, D-37073 Göttingen

Key Words: Aircraft, Airworthiness, Aerodynamics, Unsteady Flows, Wings and Airfoil Sections, Stability and Control

Abstract

The increasing performance requirements and the economical pressure to reduce Direct Operational Costs (DOC) of new aircraft designs can no longer be met by applying traditional sequential design methods. This holds especially true when considering aeroelasticity. The impact of its effects on the design of new high-performance transport or fighter aircraft demands the use of multidisciplinary design concepts and optimization strategies even in the preliminary design phase.

In Germany, a multidisciplinary research program focused on the development of key-enabling technologies for the so-called lead concept Megaliner was initiated as an innovative cooperation between the industry, research establishments, and universities.

In this paper, aeroelastic design principles for the passive airframe and for actively controlled advanced aircraft with highly sophisticated fly-by-wire flight control systems are presented.

The challenging problems in aeroelasticity are pointed out and the impetus of major disciplines in the development of advanced computational simulation is highlighted. The focus is primarily on the transonic regime and on the study of related nonlinear effects.

1 Situation in the European Aerospace Industry

Aerospace industries worldwide belong to those industries with the highest investment in research and development. In Europe – and especially in Germany – aerospace technology is one of the most important technologies with a high transfer potential to other industries. This transfer has to be improved systematically in order to remain competitive in the market.

Trend analyses indicate a doubling of global air traffic within the next decade. The air space in which airplanes fly, however, is limited. In order to overcome this problem, the idea of a Megaliner was born, a very large transport aircraft with more than 500 tons take-off weight capable of carrying 530 to 700 passengers. The Airbus Industries project is named A3XX, Fig. 1.

The development of such a type of aircraft with a span of about 80 m is a challenge with many unknowns. Aeroelasticity belongs to the main design drivers the more the flexibility of the airframe increases due to its dimensions. It seems that the size of the Megaliner approaches the limit of what is feasible; see Ref. 1.

However, not only technological challenges are associated with this project. The Megaliner must also be economical competitive which simply means: it must be better, faster, and cheaper than other products already in the air. To achieve this goal, aerospace industries have developed a dual strategy based on acceleration of the development process to reduce marketing time and on innovation driven by a symbiosis of "Technology Push" and "Demand Pull". Fig. 2 shows a strategy to reduce the time from early planning to certification. The basic idea is to overlap as much as possible the processes of research, development, design, and manufacturing. Efficient overlapping of R&D alone is not sufficient. Also key-enabling technologies must be available to the industry earlier than thus far. As a means for achieving this, the industry has defined so-called "lead concepts" to concentrate

academia, industrial R&D, and research establishments on the development of key-enabling technologies. In this context, the Megaliner is the lead concept supporting the A3XX project.

2 Cooperate Research Program DYNAFLEX

To stimulate the development of key-enabling technologies, the German Ministry of Education and Research (BMBF) initiated the "Programm Luftfahrtforschung und Technologie", a national program for aeronautical research and development to support the industries. About 10 % of the funding was dedicated to academia and research establishments like the German Aerospace Center (DLR) for research work focused on lead concepts. The DLR Institute of Aeroelasticity was tasked to establish such a novel cooperative research program called DYNAFLEX for the Megaliner, Ref. 2.

Structural flexibility resulting in large static and dynamic deformations will be characteristic for a Megaliner. The classical design philosophy would try to solve the resulting problems of control efficiency, handling qualities, flutter, and coupling of flight mechanic modes with elastic modes by using a stiff structural design. This solution, however, is no longer feasible due to the aircraft's huge dimensions. A paradigm shift is required in the design philosophy. The structural flexibility must become a positive and integral design element.

Multidisciplinary design and optimization (MDO) was found to be a key element in solving many challenges of the Megaliner, and high-fidelity modeling of the flying flexible aircraft in the design process is a prerequisite for this approach. For DYNAFLEX a catalog of questions and tasks was agreed upon between DLR and DASA Airbus (now DaimlerChrysler Aerospace) in order to focus the research activities on:

- Modeling methodology and accuracy for the "flying flexible aircraft" with respect to flight control system design and structural optimization
- Improvements of non-linear unsteady aerodynamics necessary for the transonic flight regime and for control law design
- Improvement of the multidisciplinary optimization process in the conceptual as well as detailed design phase
- Validation of numerical aeroelastic simulations
- Integrated control law design for handling and active control functions like flutter suppression and load alleviation
- Interactions between handling qualities, control concepts, and resulting structural loads
- Validation of the various control laws by real-time simulation in a flight simulator.

A matrix of interdependent tasks was developed by DLR and DASA on the basis of the catalog of questions. This matrix addressed the following tasks:

- system modeling
- aeroelasticity and unsteady aerodynamics
- flight control laws and handling qualities
- conceptual design and structural optimization
- validation of results

For the execution of these tasks, two common models and data sets supplied by DASA were used by all partners. The first set described an already existing large transport aircraft. This set had to be used in the first phase of program for validation. The second data set represents current A3XX design data. Thus, the results can be directly applied in this project. The data sets were handled by DLR in close contact with DASA.

In addition to the project management DLR provided all partners with software codes and unsteady aerodynamics data and supervised the multidisciplinary research process. A common work plan was created including five work packages for the university partners

- Technical University of Berlin (B),
- Technical University of Braunschweig (BS),
- Technical University of Munich (M),
- University of Siegen (SI),
- University of Stuttgart (S)

For the practical work three workgroups were organized:

- Simulation of fluid/structure interaction and of flight maneuvers (BS, M, DLR)
- Multidisciplinary design optimization with aeroelastic constraints (BS, SI, DLR)
- Flight mechanics modeling, control law design, and handling qualities (B, S, DLR)

In following, the role of aeroelasticity in aircraft design is shown and some topics of research work in this field at the DLR Institute of Aeroelasticity are outlined.

3 Aeroelasticity in Aircraft Design

3.1 Definition and Classification

Aeroelastic problems of aircraft structures result from interactions between the static or dynamic deformations of the elastic airframe and the induced steady or unsteady aerodynamic loads. In modern aircraft with fly-by-wire flight control and active systems, additional interactions between the airframe and the control system are possible. Thus, airframe flexibility is fundamentally responsible for a variety of aeroelastic phenomena and related problems. As long as the strength requirements are fulfilled, structural flexibility itself is not necessarily objectionable.

The aeroelastic interactions, however, may not only strongly influence the vehicle's dynamic response and stability, but also the overall performance and handling qualities. Therefore, in the conceptual and preliminary design phase of an aircraft, the application of aeroelastic design criteria becomes imperative.

The whole spectrum of aeroelastic phenomena to be considered during the design process can be classified by means of Collar's well-known aeroelastic triangle of forces, Ref. 3, illustrated in Fig. 3. Three types of forces - aerodynamic, elastic, and inertial - are involved. Generally, aeroelastic phenomena can be divided in two main groups:

- static phenomena on one edge of the triangle, i. e. divergence, control surface effectiveness, and load distribution influenced by aeroelastic effects,
- dynamic phenomena in the triangle center involving all three types of forces, i. e. flutter, buffeting, and dynamic response or dynamic stability of the flexible aircraft.

All of them have profound effects on the aircraft design. The resulting stiffness requirements become increasingly important design criteria which govern the optimization processes in aircraft development.

3.2 Basic Aeroelastic Design Criteria

In the following the most important aeroelastic design criteria for

high-performance aircraft ranging from glider to fighter to large transport aircraft are addressed. Due to the fact that aeroelastic phenomena like flutter and divergence can result in fatal accidents and can reduce control effectiveness required for maneuvering or can raise the drag and thus fuel costs, the following design criteria have, among others, become the standard for any aircraft design (e. g. military specifications and FAR/JAR regulations):

- the aircraft must be free of flutter, divergence, and aeroservoelastic instability within its flight envelope
- the control effectiveness of combinations of controls must be above a given minimum to assure safe flight operation within the envelope

In addition the following goals should be met:

- the flight shape of the wing should have minimum aerodynamic drag and sufficient effectiveness for all configurations
- the planform of a weight competitive wing should have maximum aerodynamic efficiency (aspect ratio) provided by advanced aeroelastic design.

This can be accomplished by improving conceptual sizing and layout processes to reflect the enhanced configuration freedom provided by advanced aeroelastic design.

3.3 Airframe Design

The airframe is the passive load and mass carrying structure of an aircraft including all control surfaces. From an aeroelastic point of view, special attention has to be paid to the control surface attachment. Manually actuated control systems are treated as mechanical spring/mass systems. In the case of hydraulically driven control surfaces, actuator transfer functions with limited bandwidth must be considered.

3.3.1 Improvement of Flutter Behavior

Modern transonic transport or fighter aircraft wings are swept back. This feature eliminates wing torsional divergence, but from the beginning of design, attention had to be paid for bending-torsion flutter. To eliminate this instability or move the flutter boundary out of the flight envelope, the stiffness and mass properties of flutter-prone components must be considered. Flutter optimization consists in finding the stiffness and mass distribution with minimum weight under the following constraints:

- fulfillment of all static requirements derived from design loads (strength and buckling),
- no change in the external geometric/aerodynamic shape,

During the preliminary design process, when this type of optimization is normally required, the design is already frozen to a certain degree. This means that the design space is rather limited. Typical design variables in the preliminary design are:

- thickness or cross-section properties of structural elements
- geometric shape
- location of concentrated masses (for flutter).

To enhance the optimization process, the aeroelastic design principles have to be defined in such a manner that they can be formulated as proper constraints. They can be found by considering the expected flutter mechanisms. For the classical wing bending-torsion flutter, the following two rules for flutter prevention are known, Fig. 4:

- The frequencies of modes which can couple resulting in a flutter case, e. g. wing bending and wing torsion, must be far apart. The further the frequencies are separated, the larger is the airspeed for flutter on-set.
- Concerning the shape of the flutter-critical wing torsion, rearward nodal locations are found to cause lower critical speeds than forward nodal locations. This is an additional

information for optimization of stiffness or mass distribution to improve flutter stability.

Flutter optimization of conventional primary structures usually lead to a local increase of the stiffness distribution of the initial design. In most cases, flutter stability under the given constraints must be improved accepting some additional weight. An example of the application of these aeroelastic principles is given in the study of a transport aircraft wing structure Ref. 4. In this analysis, areas of optimum structural reinforcement for achieving the necessary flutter margins were identified. The optimized design is compared with the initial (fully stressed) design in Fig. 5. With a structural mass increase of only 95 kg the required margin between flutter speed and flight envelope has been obtained.

Manually controlled aircraft are prone to control surface flutter. Based on the knowledge about this typical flutter mechanisms with limited ranges of instability, the problems can often be eliminated by appropriate mass balancing and sufficient control system stiffness. Similar to the case mentioned above, optimization to meet the required safety margins with minimum weight results in proper stiffness distributions, light-weight control surface structures, stiff control systems, and some additional balance masses. This procedure was applied to the German STRATO 2C High Altitude Aircraft shown in Fig. 6. Despite of its large dimensions (wing span 56.5 m), it is a manually controlled aircraft, Ref. 5.

3.3.2 Improvement of Control Efficiency

Lifting surfaces with large aspect ratios show a beam-like structural behavior. Fig. 7 shows the deflections of a swept wing of an airliner compared to those of an unswept high performance sailplane wing. For unswept wings the aeroelastic effect on static deformation is entirely dependent on torsional stiffness and the elastic axis location. Wing bending stiffness is not a factor at all. Swept wings of modern transonic transport or fighter aircraft, however, show a more complicated behavior. For a backward swept wing, upward bending will cause a nose-down rotation (wash-out) of streamwise wing sections, i. e. a change in the local angle of attack. The drag and lift distribution of the wing, in turn, is dependent on the angle of attack distribution. For large transport aircraft the wing contributes to 60-65 % of the total drag and therefore the structural behavior of the wing has a significant impact on aerodynamic efficiency, e. g. fuel consumption.

In addition, wash-out reduces aileron control effectiveness and reversal becomes possible inside the flight envelope. To counter this problem, the wing box stiffness has to be increased. The optimization task is to generate required flight shape (local angle of attack distribution) and aileron effectiveness with a minimum structural weight penalty observing all other constraints (e. g. flutter stability, minimum drag, or maximum root bending moment). Thus, aerodynamic and flight control benefits can be achieved by aeroelastic means if the stiffness distribution of the conventional wing box is changed taking the mentioned coupling effects of swept wings into account.

3.3.3 Aeroelastic Tailoring

From an aeroelastic point of view, the major advantage of composite material is its anisotropic property which offers additional design freedom (additional design variables are the fiber directions and layer thicknesses of the composite material). Aeroelastic tailoring is the embodiment of the directional stiffness into an aircraft structural design to control aeroelastic deformation, static or dynamic, in such a fashion as to affect the aerodynamic and structural performance of that aircraft in a beneficial way, Ref. 6.

Static and dynamic phenomena can be influenced by aeroelastic

tailoring. In this paper, only static examples are considered. Fig. 8 shows the result of a design study for a generic transport aircraft. This swept wing consists of a metal inner wing and a composite outer wing interfaced at 60 % wing span. The study assessed the potential of composite material and aeroelastic tailoring applied to the outer wing with respect to a pure metal wing design. The comparison of the three investigated cases clearly shows the possibilities for drag reduction. The relative twist change between flight and jig shape is only about half compared to that of the metal reference wing. Also it can be noticed that the aeroelastically tailored wing is less sensitive to wing fuel loading.

Concerning aileron control effectiveness the improvements in low speed range and cruise are satisfactory. In the high speed range, however, the benefit of aeroelastic tailoring is limited and can not compensate the detrimental effect of washout. Even with an optimization including the metal structure of the inner wing the required effectiveness is achieved only with a large structural weight penalty, Fig. 9.

3.4 Design of Aircraft with Active Controls

An active aircraft structure is any airframe with integrated active elements like computer-controlled, hydraulically driven flight control surfaces which can be used to improve performance. A general scheme is given in Fig. 10. Sensors at designated points measure the local motion consisting of rigid-body motions and elastic deformations. The signals of the sensors are fed into the control system computer (controller) which, in turn, generates via control laws the input signals for the control surface actuators or any other actuating devices.

3.4.1 Benefits of Active Control Functions

The integration of modern electronic flight control systems (EFCS) with fly-by-wire technology opens the opportunity to implement beneficial active control functions, see Ref. 7, as outlined in the following table.

Active Functions	Benefits
care-free handling	structural weight reduction
maneuver load control (MLC)	structural weight reduction
gust load alleviation (GLA)	structural weight reduction
fatigue life enhancement	maintenance cost reduction
deformation and elastic mode control	aerodynamic drag reduction
flutter suppression	dynamic stability improvement
ride comfort improvement	passenger comfort

Proper implementation of these active control functions enables the aircraft to function beyond the performance range of classical passive structures. Gust load alleviation (GLA) systems, for example, reduce the additional loading produced by gusts by proper control surface deflections. Usually, the design of transport aircraft wings is driven by gust load cases and, consequently, applied GLA leads to less structural weight.

In a similar manner, fatigue life enhancement functions lead to less structural weight by damping of the fatigue life consuming vibration modes. The active control functions mentioned above can be used to minimize unwanted external forces, leading to less structural weight. In this case, the optimization task is to design the control laws with respect to stress constraints as well as with other constraints like minimum control energy or controller robustness.

In another application of active functions the properties of the structure itself are changed to improve the stability. Optimization is used to generate control laws which increase the flutter margin (active flutter suppression).

3.4.2 Dynamic Stability of Active Systems

In all control law optimization procedures, the dynamic stability of the active aircraft in flight and on the ground must be observed. The interaction between the aircraft's structural dynamics, unsteady aerodynamics, automatic flight control, and active functions has emerged as an important design consideration. This field of merging disciplines is called aeroservoelasticity, as illustrated by Fig. 11. In this aeroservoelastic triangle, the left leg represents the classical dynamic aeroelastic interaction which does not include the interaction with an active system. Similarly, the lower leg of the triangle represents a classical aeroservodynamic control system synthesis. Finally, the right leg represents the important dynamic servoelastic coupling between the elastic modes of the aircraft and the active control system. This coupling, together with the unsteady aerodynamic feedback inputs from servo-actuated active control surfaces, results in an aeroservoelastic interaction which is also known as structural coupling.

In many cases, active functions are implemented as high-gain control systems. The control surface areas generally used for active functions are small fractions of the total wing area. Thus, high-gain systems are necessary. These systems, however, bear the risk of instability problems with higher vibration modes involved. Dangerous aeroservoelastic instabilities may occur if the sensor signals are not filtered and fed back correctly. Aeroservoelastic instabilities turn out to be as dangerous as classical flutter instabilities.

3.4.3 Integrated Flight Control System Design

Faced with the above mentioned problems, an integrated design of the EFCS and all active functions is necessary to determine the EFCS gains, phase-advance filters and notch filters to minimize structural coupling in a single global optimization process. The EFCS shall be designed observing aircraft rigid body mode and structural mode coupling stability requirements for each control system loop. Structural coupling will be minimized by notch filters or other measures and the EFCS must robust to cover all aircraft configurations and all kinds of non-linearities of the complete system. This integrated design is based on the assumption that the flexible aircraft characteristics are accurately predictable.

The integrated optimization process of EFCS and its additional active functions, is considered in two steps. In a first step, the active components of the control system should be optimized with respect to aeroservoelastic criteria:

- optimization of sensor locations and directions (e. g., the gyro platform should be put into the place of zero slope of the first fuselage bending mode shapes, where the elastic pitch/yaw rate is at a minimum; see Fig. 12)
- optimization of the actuator transfer functions (a strong decay in the actuator transfer function from medium to high frequency would minimize the coupling effects)
- minimization of inertia forces (high-frequency structural coupling effects are small with light-weight control surfaces).

The second step is the optimization of the filters in the control loops. There are two interdependent types of filters which should be optimized together. Phase advance filters correct the low-frequency phase shift of notch filters and other delays. But the major tool for decoupling the aircraft control system from aeroservoelastic influences is notch filter optimization. In the optimization procedure the coefficients of the filter transfer functions act as design variables, and aeroservoelastic stability, control power, control authority, etc. are the constraints. The block diagram in Fig. 13 shows the scheme of active control feedback paths of a modern fighter flight control system.

The full potential of reducing structural weight and of improving dynamic stability and handling qualities by ACT can be exploited if it is used from the very beginning of the design. The implementation of ACT after design freeze, however, results in a so-called "repair solution" which is obviously sub-optimal.

Active Aeroelastic Wing technology (AAW) is a multidisciplinary, synergetic technology integrating aircraft aerodynamics, active controls, and structures to maximize aircraft performance. In comparison with ACT and its improvement, AAW uses wing flexibility for a net benefit and thus enables the use of weight competitive high-aspect-ratio and thin swept wings which are aeroelastically deformed into shapes for optimum multi-point performance. AAW turns wing flexibility into a benefit through the use of multiple leading and trailing edge control surfaces activated by a digital flight control system. At higher dynamic pressures the AAW control surfaces are used as „tabs“ which are forcing wing twist instead of reducing it.

3.5 Multidisciplinary Design Optimization

The need for increasing integration of aerodynamics, structures, and control system design in a Multidisciplinary Design Optimization (MDO) environment is evident both from past design trends and predictions of future directions, see Ref. 8.

The most pressing issue for the structural designer's daily work is the gap in fidelity between aerodynamics used in performance calculations, flight dynamics and aeroelasticity. Fluid/structure interaction techniques are needed to use Euler- and Navier/Stokes-methods in early design for more reliable load and maneuver performance predictions. High performance computing will enable the practical use of these methods.

In the very near future, however, loosely coupled MDO strategies will be used in the industrial environment. Software framework tools supporting these approaches exist but need to be refined, extended, and validated for serious application. Reliable, robust software for generic model and design space approximation is missing. When this is accomplished, MDO methods like Concurrent Subspace Optimization need to prove applicability to industrial use. Successful implementation might be the key to the required cultural change in industry towards concurrent engineering.

4 Aeroelastic Simulation Technologies

4.1 Structural Modeling

Today, the Finite Element Method is a robust standard tool for establishing sophisticated static and dynamic structural models. Thanks to available pre- and postprocessing software with graphical user interaction, the set up of large models is considerably facilitated. In Fig. 14 the left half model used in the first phase of the DYNAFLEX program is shown. Nevertheless, it was found useful, to develop compatible reduced models based on larger ones with a smaller number of unknowns especially for optimisation studies.

Despite of the increasing finite element modeling capabilities, there is a continuing demand for experimental validation. Even for the Megaliner it can be foreseen, that a ground vibration test will be performed to check the analytical predictions of the natural vibrations. Due to the very low frequencies of the fundamental elastic modes, the realization of a proper suspension of the huge aircraft will be a demanding task.

4.2 Unsteady Aerodynamics

The major objective in the development of unsteady CFD codes for low angle-of-attack, high subsonic-to-transonic flow is the prediction of aeroelastic response and, more specifically, flutter.

For aircraft operating close to the transonic buffet-onset boundary, the required flutter margin extends deep into the transonic flow regime. Wind tunnel measurements have shown that additional parameters may strongly affect the dynamic behavior near the flutter boundary. To accurately predict the most critical flutter conditions in the transonic speed range, as well as control surface efficiency, buzz, and buffeting response characteristics, reliable aerodynamic codes are required for the calculation of the steady and unsteady air loads on both the stationary and oscillating lifting systems.

More detailed CFD models will result in considerable demands for computer resources. For viscous flow modeling, the coupling of lower-level inviscid CFD methods with boundary layer models becomes attractive. Such inviscid-viscous interaction methods using TSD, Full Potential, and Euler codes are capable of treating important transonic effects and have attracted much interest for aeroelastic simulation in industry Ref. 9. Further development on 3D flows involving shock-induced separating and reattaching flows remains an important research topic.

Fast flutter computations are needed in the design and especially in optimization. The Doublet Lattice Method (DLM) widely used for generating subsonic unsteady aerodynamic models does not account for transonic effects and loses its accuracy for transonic wing designs with Mach numbers of 0.85 and more. The Transonic Doublet Lattice Method (TDLM) developed by DLR is a direct extension of DLM to the transonic flow around harmonically oscillating wings (Fig. 15). TDLM was expanded to determine aerodynamic influence coefficient (AIC) matrices for complete aircraft and allows for the computation of transonic generalized air loads for arbitrary mode shapes. These matrices are independent from the structural model, as long as the geometrical shape is kept constant. The TDLM-based flutter boundary compares favorably with the result of a nonlinear time-accurate CFD method (harmonic air loads from the Full Potential code and boundary layer coupling obtained by Fourier analysis), see Ref. 10.

4.3 Fluid/Structure Interaction

The main objective in the development of methods for fluid/structure interaction is the correct transfer of physical information (motion and pressure) between the fluid and the structure. Aerodynamic and structural models do not use conforming grids at their interface. In general, the aerodynamic pressures are computed at points of boundary-fitted CFD grid while the structural displacements are computed at the nodes of an interior finite element model. From the whole load carrying structure only the wing box is often modeled in greater detail.

It is convenient to provide the user with a modular tool for fluid/structure coupling. This tool allows the use of different CFD grids and codes as well as different finite element analyses and models. DLR's Full Potential and Euler codes with and without boundary layer coupling has been tested in this context.

With DLR's fluid/structure interaction software CAESAR the user may choose between different coupling methodologies. Interpolation methods on scattered data like the volume spline and the so-called method of the "Euclidian Hat" with useful local properties. Another method accomplishes the data transfer by the kinematics of rigid beam elements fulfilling force and moment equilibrium. Finally, a newly developed method based on "finite interpolation elements" is available, which conserves virtual work. Results of these different coupling methods have been compared and their sensitivities investigated. Details are presented in Ref. 11. Fig. 16 shows the result of computed static deformation for the reference wing with the center section of the fuselage and the iterative behavior of the computation.

5 Nonlinear Aeroelasticity

Since approximately five decades, dynamic aeroelastic analyses, in particular flutter analyses, have been routinely performed in modal form in the frequency domain by applying Lagrange's equations of motion. This routine, based on the assumption of linearity of inertia, elastic, and aerodynamic forces with respect to the motion, will continue to maintain its importance in aircraft design, Ref. 12. However, there are a number of inherent nonlinear aerodynamic and aeroelastic phenomena such as transonic buzz, stall flutter, heavy buffeting, and wing rock.

The straightforward application of higher-level, nonlinear unsteady CFD methods and the inclusion of strong structural nonlinearities in aeroelastic analyses requires the solution of correspondingly nonlinear aeroelastic equations in the time domain. This calls for a simultaneous time integration of the coupled fluid and structural dynamic equations of motion applying adequate solution algorithms. In Fig. 17 the time history leading to a limit cycle oscillation of a 2D airfoil with control surface is shown. In this case, the integration in time is achieved along with the finite-difference, time-marching CFD solution of the flowfield. Aeroelastic stability and response characteristics are then deduced from the free decay records, identical in concept to those measured during wind tunnel or flutter flight testing.

5.1 Structural Nonlinearities

Structural nonlinearities, such as free-play in the control surface attachments and nonlinear aeroservoelastic behavior arising from actuators and control systems, may strongly influence the characteristics of flight vehicles. Often these nonlinearities are not distributed but concentrated at specific locations. This property facilitates the analytical treatment considerably. Using the method of describing functions even multiple interacting nonlinear elements can be handled efficiently in the frequency domain, if the requirements of the harmonic balance method are met.

Ref. 13 reports on a study of an airfoil with a control surface and different nonlinear characteristics of the control surface attachment, see Fig. 18, for example. Also different aerodynamic theories were used in the time domain simulations. It was found, that the branching of the flutter boundary according to a sub- or supercritical Hopf bifurcation does not only depend on the type of nonlinearity but also on the general aeroelastic properties of the system. Quite complicated behavior can be observed even with this small aeroelastic model.

5.2 Aerodynamic Nonlinearities

Ref. 14 presents the results of extensive simulations of a transonic 2D airfoil section including control surface and chordwise flexibility leading to camber, for example. The aerodynamic model was an inviscid one based on the Euler equations. In Fig. 19 the computed points for identifying the flutter boundary and regions of limit cycle oscillations are shown. The transonic dip has a quite complex shape caused by changes in the characteristics of the flutter motion. A picture of the flow field corresponding to point (f) is also shown, indicating shock movement across the hinge line of the control surface.

Nevertheless, linearized flutter analysis will play an important role in the transonic regime as long as the shock non-linearity is manifested in steady flow and vibration-induced unsteady pressures behave linearly for small motions. Thus, it is sufficient to accurately know the steady flow field including the static shock strength and location, and to consider small perturbations about this steady flow field to determine the stability boundaries (transonic dip) with classical flutter analysis.

5.3 Wind Tunnel Experiments

As mentioned above, nonlinear effects play a dominant role in aerodynamics and aeroelasticity of the transonic flow regime. Due to compressibility effects, the unsteady pressures induced by small motions on the wing can change appreciably in the range of transonic Mach numbers and influence the aeroelastic stability behavior. The nonlinearity of the flow is the reason why this instability behavior is not yet completely understood. Flutter oscillations often exhibit a limit cycle behavior: the oscillation amplitude attains a finite value. The underlying limiting mechanism has not been clarified entirely up to now. Thus the analytical prediction of limit cycle amplitudes is a topic of future research which must include accurate validation experiments in a wind tunnel. The set-up of such an experiment is shown in Fig. 20. It was performed in the transonic wind tunnel at DLR Göttingen (TWG). The main goal of the study presented in Ref. 15 can be outlined as follows:

- measurement of unsteady air loads and pressure distributions on a constant-chord supercritical wing model (NLR7301) performing heave and pitch oscillations,
- experimental investigation of transonic flutter in a pure state of two-dimensional motion,
- recording of time series and unsteady pressure distributions of limit cycle oscillations.

The limit cycle amplitudes were found to be significantly smaller than those predicted by computer simulations with Euler codes. This is an indication that treatment of regions of viscous flow may be an important part of accurate analyses.

6 Conclusions

With DYNAFLEX a novel kind of cooperative research program was initiated by BMBF and managed by DLR, focusing on the lead concept Megaliner to support the A3XX project. All partners used the same geometrical and structural model as well as aerodynamic data set supplied by DASA and provided by DLR. This concept was found to be very efficient. For all partners, this type of cooperative program was a new, exciting, and successful experiment.

For the design of high-performance aircraft, aeroelastic design criteria will become increasingly important and will need to be considered in the conceptual design phase. Multidisciplinary design optimization procedures are essential for the efficient application of aeroelastic design criteria and to ensure minimum drag, the control effectiveness of metal and composite structures, as well as dynamic stability. Active control technology must be applied to extend structural aircraft performance beyond the structural limits of the passive airframe. The AAW is an advanced example of consequent application of this technology.

Although numerous encouraging papers (mainly for 2D aeroelastic models) have been published in the challenging field of computational aeroelastic simulation, the overall work is still in the beginning stages. The frame in which further progress is anticipated is given by the available computer resources, which are raising rapidly. Computer power is obviously not the major problem in the long run. The primary objective of computational aerospace applications seem to be the appropriate software and the high performance network, which will enable multidisciplinary analysis and design of advanced aerospace systems. In this context there is no doubt that – in trying to make full use of the capabilities of higher-level CFD codes and high fidelity FE modeling – Computational Aeroelastic Simulation remains a main challenge in the next century with a great technical and economical impact on future flight vehicle design.

References

1. Försching, H.: New Ultra-High Capacity Aircraft (UHCA) – Challenges and Problems from an Aeroelastic Point of View. International Forum on Aeroelasticity and Structural Dynamics, RAS, Manchester, U. K., 1995.
2. Hönlinger, H.; Voß, R.: Dynamics of Flexible Aircraft (DYNAFLEX) – An innovative cooperation between the industry, research establishments, and universities. International Forum on Aeroelasticity and Structural Dynamics, Williamsburg, Virginia, USA, June 22-25, 1999.
3. Collar, A. R.: The Expanding Domain of Aeroelasticity. J. Roy. Aeron. Soc., Vol. L, August 1946, pp. 613-634.
4. Snee, J. M. D.; Zimmermann, H.; Schierenbeck, D.; Heinze, P.: Simultaneous Stress and Flutter Optimization for the Wing of a Transport Aircraft Equipped with Four Engines. AGARD R-784, 1991, paper 13.
5. Kießling, F.; Rippl, M.; Hönlinger, H.: Status on STRATO 2C Flight Flutter Testing Activities. AGARD SMP Meeting: Advanced Aeroservoelastic Testing and Data Analysis. Rotterdam, The Netherlands, May 8-10, 1995, paper 5.
6. Shirk, M. H.; Hertz, T. J.; Weisshaar, T. A.: Aeroelastic Tailoring – Theory, Practice, and Promise. J. Aircraft, Vol. 23, No. 1, January 1986, pp. 6-18.
7. Hönlinger, H. G.; Hutin, P.-M.; Pendleton, E. W.: The Benefits of the Passive and Active Aeroelastic Design of Aircraft Structures. The American Society of Mechanical Engineers: Optimization in Industry, Palm Coast, Florida, USA, March 23-27, 1997, pp. 259-281.
8. Hönlinger, H.; Krammer, J.; Stettner, M.: MDO Technology Needs in Aeroelastic Structural Design. AIAA Symposium, St. Louis, Missouri, USA, September 1998.
9. Wegner, W.: Aerodynamics for Oscillating Wings using the Virtual Grid Deformation Method. AGARD SMP Workshop on Numerical Simulation and Unsteady Aerodynamics and Aeroelastic Simulation, Aalborg, Denmark, October 13-17, 1997, AGARD R-822, paper 4.
10. Voß, R.: Transonic Flutter Computations with the TDLM Method. Aeroelastik-Tagung der DGLR, Göttingen, Germany, June 29-30, 1998, DGLR Bericht 98-01, pp. 417-425.
11. Beckert, A.: Ein Beitrag zur Strömungs-Struktur-Kopplung für die Berechnung des aeroelastischen Gleichgewichtszustandes. DLR FB 97-42, 1997 (in German).
12. Försching, H.; Hönlinger, H.: The Expanding Domain of Aeroelastic Simulation. Euromech-Colloquium 349: Simulation of Structure Fluid Interaction, DLR, Göttingen, Germany, September 16-18, 1996, Paper 1, pp. 1-14.
13. Schulze, S.: Simulation of Nonlinear Airfoil/Control-Surface Flutter at Subsonic Speeds Using Classical Unsteady Aerodynamics and an Euler Method. International Forum on Aeroelasticity and Structural Dynamics, Williamsburg, Virginia, USA, June 22-25, 1999.
14. Schulze, S.: Transonic Aeroelastic Simulation of a Flexible Wing Section. AGARD SMP Workshop on Numerical Simulation and Unsteady Aerodynamics and Aeroelastic Simulation, Aalborg, Denmark, October 13-17, 1997, AGARD R-822, paper 10.
15. Knipfer, A.; Schewe, G.: Investigations of an Oscillating Supercritical 2D Wing Section in a Transonic Flow. 37th Aerospace Sciences Meeting & Exhibit, Reno, Nevada, January 11-14, 1999. AIAA 99-0653.

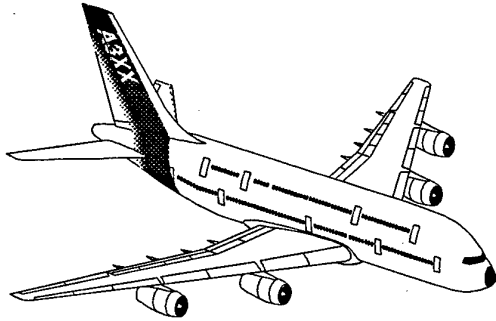


Fig. 1: Lead concept Megaliner

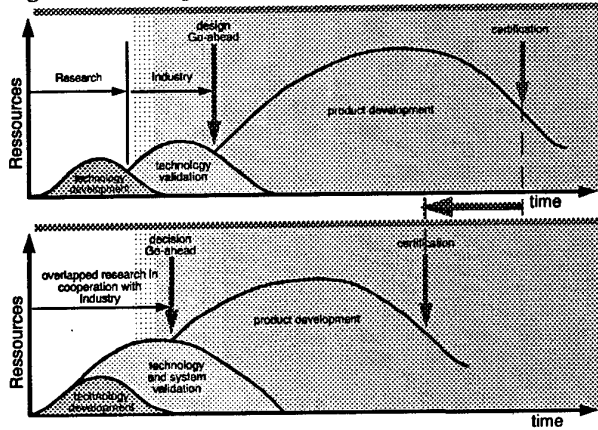


Fig. 2: Time and cost reduction by overlapping

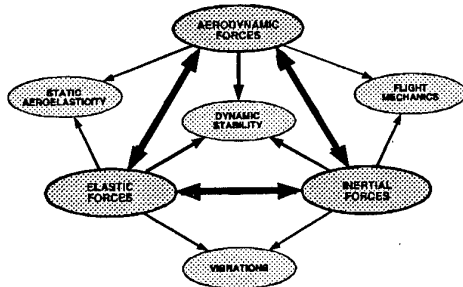


Fig. 3: Aeroelastic Triangle

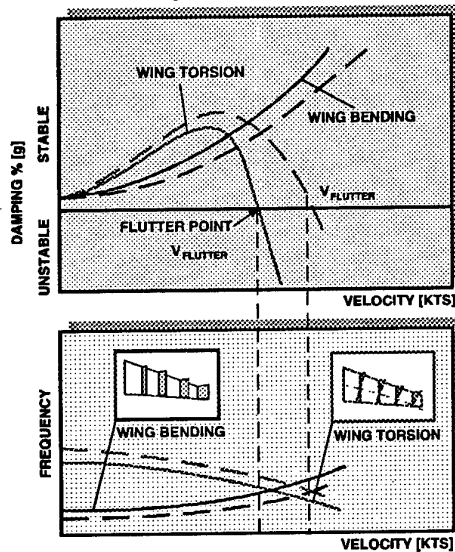


Fig. 4: Bending/torsion flutter mechanism

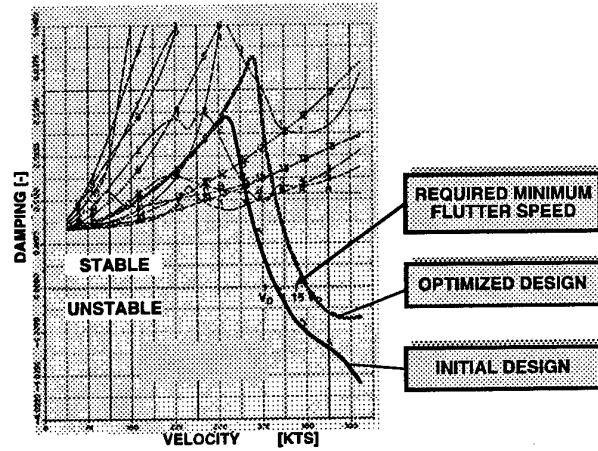


Fig. 5: Flutter optimization (mass increase 92.8 kg) (Ref. 4)

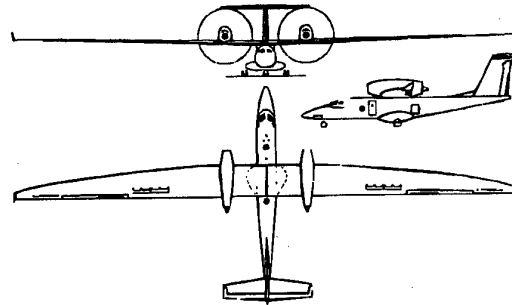


Fig. 6: STRATO 2C with manual controls

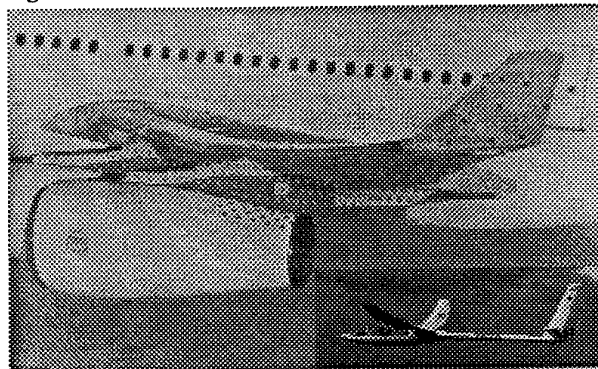


Fig. 7: Wings under air load

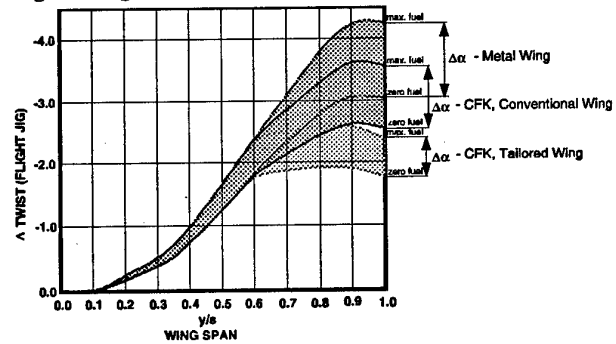


Fig. 8: Flight shape and aeroelastic tailoring

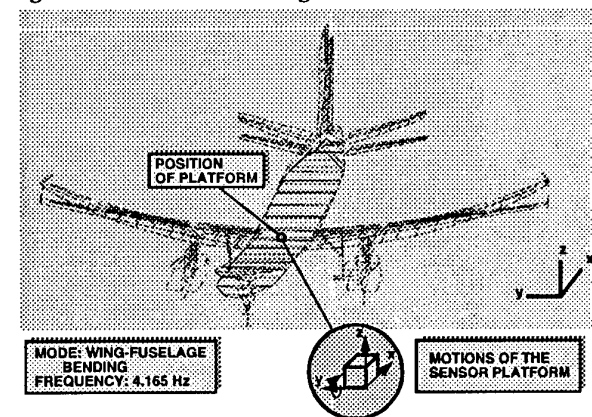
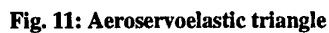
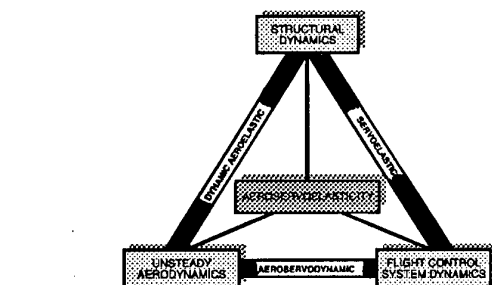
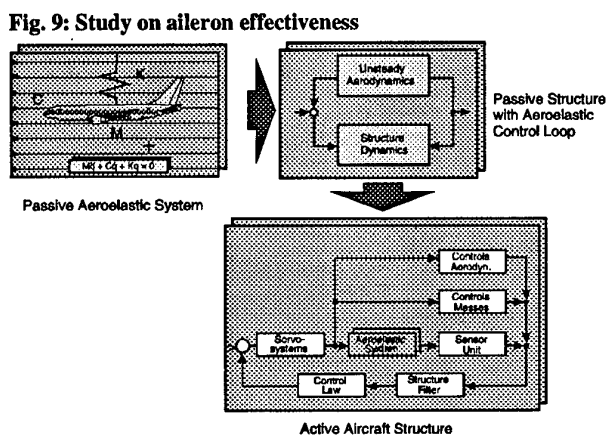
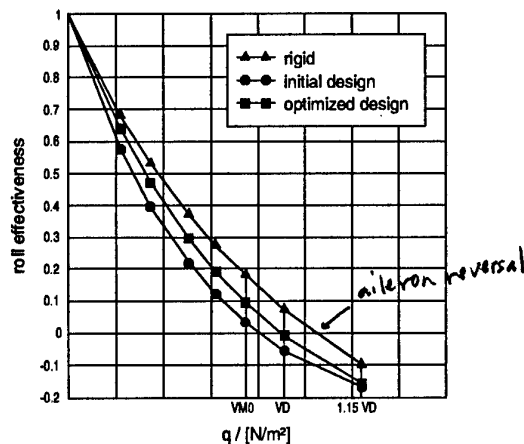


Fig. 12: Influence of vibration modes on sensor placement

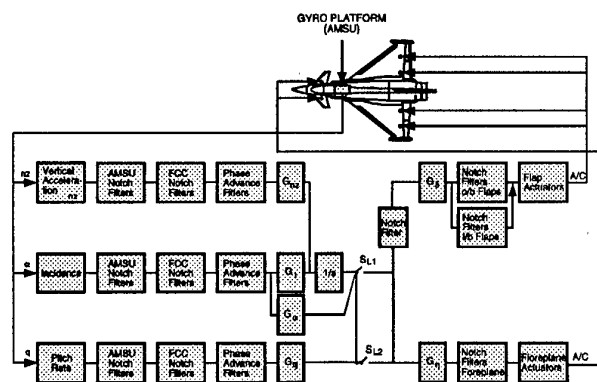


Fig. 13: Flow chart of longitudinal control of a flighter

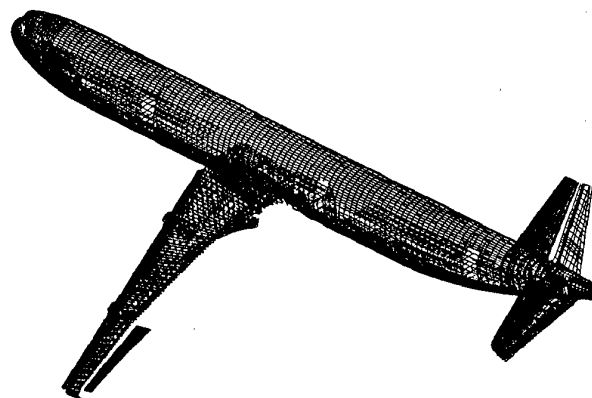


Fig. 14: Reference finite element model of DYNAFLEX

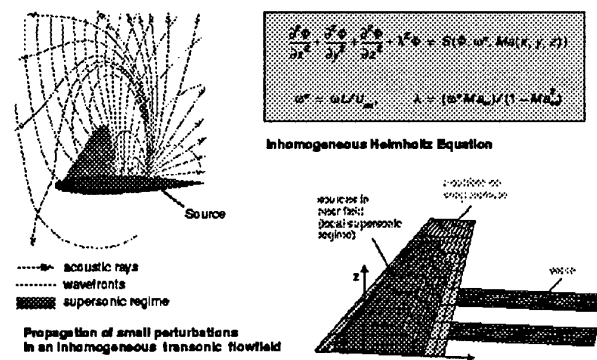


Fig. 15: Transonic Doublet Lattice Method

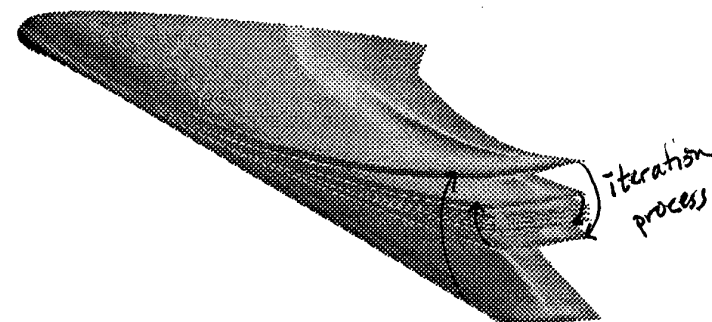


Fig. 16: Iteration of static aeroelastic deformation

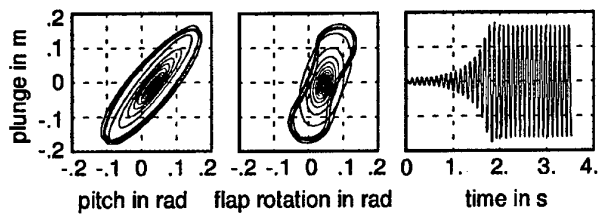


Fig. 17: Limit cycle flutter (airfoil with control surface)

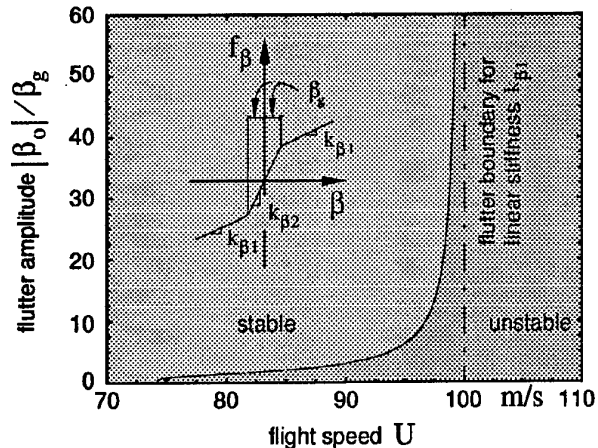
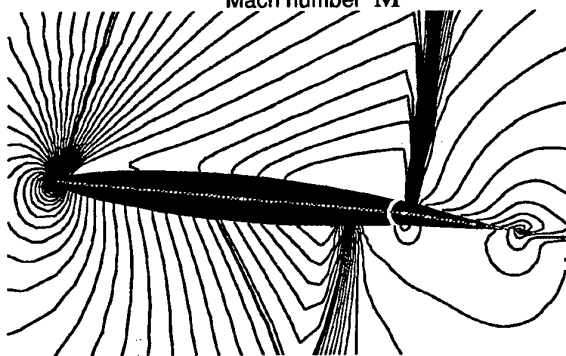
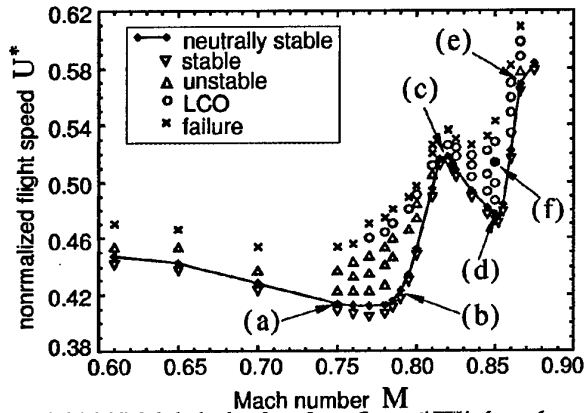


Fig. 18: Stability boundary with structural nonlinearity



(f) $M = 0.85$

Fig. 19: Transonic aerodynamic nonlinearities

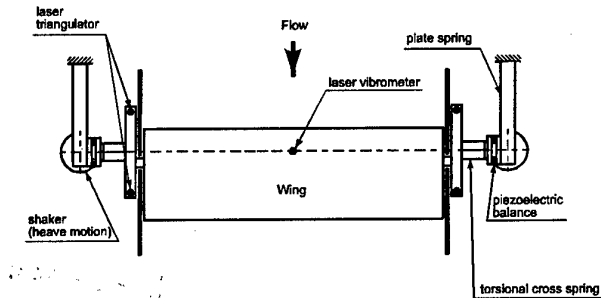


Fig. 20: 2D wind tunnel model test set up in the TWG



On the Dynamic Stability of a Completely Free Stiff-Edged Cylindrical Shell Subjected to a Follower Force

Si-Hyoung Park* and Ji-Hwan Kim**

Seoul National University,
San 56-1, Shinrim-Dong, Kwanak-Ku, Seoul 151-742, Korea
Seoul National University,
San 56-1, Shinrim-Dong, Kwanak-Ku, Seoul 151-742, Korea

Key Words : Stability and Control

ABSTRACT

The dynamic stability of a completely free cylindrical shell under a follower force is analyzed. By attaching rings on both side of a shell, we describe the behavior of rockets or missiles more exactly. Using orthogonality, the analysis is performed about each circumferential wave number. The kinetic analysis and the static analysis are used according as the circumferential wave number is one or not.

1. INTRODUCTION

Rockets and launch vehicles have a large thrust for the purpose of flying deeper into space or accelerating rapidly. For these objects, there are efforts to reduce the mass of the structures, which result in decrease of structural stiffness. A large thrust and a flexible structure may be the principal cause of dynamic instability, as natural frequencies vary with the thrust.

A thrust can be treated by a follower force, but there are several questions about the most effective structural model of rockets or launch vehicles. Beam theories have been widely used and a beam with a concentrated mass has been sometimes dealt with[1,2]. There are studies[3] investigating the stability of a plate under a thrust, in which the plate can be regarded as not a full model of rockets or launch vehicles but a model of a part. In general, rockets are similar to cylindrical shells rather than beams or plates and thus should be modelled by a shell. However, taking the computational difficulties in analysing a shell into account, the shell model may not be useful if the beam model can predict the critical instabilities efficiently. This paper explores some of these issues.

The literature on the dynamic stability of a beam under a thrust is vast and will be reviewed in the case of work on a free-free beam such as flying vehicles. Beal[1] first investigated a free-free beam under a constant thrust and a pulsating thrust using the Euler-Bernoulli beam theory, where the instability types under a constant follower force were divided into two categories, which are a flutter type and a divergence type. In his work, it was found that a divergence does not take place before a flutter without a thrust control. Park and Mote[2] studied the effect of a concentrated mass on the critical load and the instability type, where they found that a concentrated mass can

induce a divergence without a thrust control and reduce the critical load substantially.

Several studies on dynamic stability of a completely free shell or plate under a follower force are available in the literature. Kim and Park[3] treated a plate model which is subjected to a intermediate follower force, but the plate in their work can not be regarded as a full model of rockets or launch vehicles. A shell model was first employed by Bismarck[4] to analyze the stability of structures under follower forces. In addition to the free edge condition, various boundary conditions were treated in this paper, but it deals with a shallow shell like a curved plate. Park and Kim[5] analyzed the dynamic instability of a completely free cylindrical shell under a constant and a pulsing follower force, where the results of a shell model were compared with those of a beam model. They discussed the effects of shell dimensions on the usefulness of a beam model and concluded that a cylindrical shell model is necessary for some ranges of shell dimensions. However, they applied no stiffening structure to the cylindrical shell and thus it was found that instabilities are induced under a low load by Rayleigh and Love modes with low frequencies which the stiffening element can eliminate in the vehicle structures.

In the present work, we analyze the dynamic stability of a completely free cylindrical shell under a follower force. Assuming that the edge of a shell is movable but not freely-deformable, we describe the behavior of rockets or missiles more exactly. In other words, the circular shape of a cylindrical shell is not varied on the edge at which the follower force is acting, as the aft of a missile is fixed fast to a engine mount. The follower force acts on the plane which is generated by the edge circle of the shell. At the other edge, the deformation of the shell is restrained by a stiff ring but rather flexible than the forced edge, as the nose of a missile behaves like a stiffening element.

2. GOVERNING EQUATIONS

Figure 1 shows a cylindrical shell of length L , thickness h and radius R with rings on both sides. One of the rings is assumed to be rigid and the other is flexible. The x -axis is taken along a generator, the circumferential arc length subtends an angle θ , and the z -axis is directed radially outwards, where the z -axis is measured from the neutral surface. The rings are assumed to have rectangular cross sections and the same radius that the shell has. A follower force with the

* Research Assistant, Department of Aerospace
** Associate Professor, Department of Aerospace

magnitude P is assumed to be distributed along a edge ring and tangential to the deformed generator.

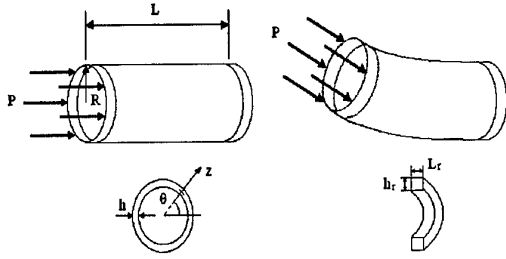


Figure 1. Shell and ring geometry

2.1 Shell equations

The present analysis is based on the assumptions such as, small deflections, linear elasticity and isotropic material. The reliable prediction of the small deflection response of moderately thick shells requires the use of shear deformation theories. In Ref. [11], it was found that the frequency predicted by the first order shear deformation theory can be good approximations with a error under about 1.8% for a moderate thickness ratio ($h/R < 0.18$), which agrees with the shell dimension considered in the present analysis. Therefore, if we include only first-order shear deformation, the displacement field can be written as in Ref. [6].

$$\begin{aligned} u &= u_0(x, \theta) + z\phi(x, \theta) \\ v &= v_0(x, \theta) + z\psi(x, \theta) \\ w &= w_0(x, \theta) \end{aligned} \quad (1)$$

where u_0 , v_0 and w_0 are the displacements of the middle surface, and ϕ and ψ are the changes of slope of the normal to the middle surface. From equation (1), we get the kinetic energy as

$$\begin{aligned} T &= \frac{1}{2} \rho \int_0^{2\pi} \int_0^L \int_{-\frac{h}{2}}^{\frac{h}{2}} (\dot{u}_0^2 + \dot{v}_0^2 + \dot{w}_0^2 \\ &\quad + 2z \dot{u}_0 \dot{\phi} + 2z \dot{v}_0 \dot{\psi} + z^2 \dot{\phi}^2 + z^2 \dot{\psi}^2) \\ &\quad (R+z) dz dx d\theta \end{aligned} \quad (2)$$

where ρ is the mass density of the shell material. The strain energy is written as

$$V = \frac{1}{2} \int_0^{2\pi} \int_0^L \int_{-\frac{h}{2}}^{\frac{h}{2}} \epsilon^T Q \epsilon (R+z) dz dx d\theta \quad (3)$$

where

$$\epsilon = \begin{bmatrix} \epsilon_{xx} \\ \epsilon_{\theta\theta} \\ \gamma_{x\theta} \\ \gamma_{xz} \\ \gamma_{\theta z} \end{bmatrix} = \begin{bmatrix} \frac{\partial u_0}{\partial x} + z \frac{\partial \phi}{\partial x} \\ \frac{1}{R+z} \left(\frac{\partial v_0}{\partial \theta} + w_0 \right) + \frac{z}{R+z} \frac{\partial \psi}{\partial \theta} \\ \frac{\partial v_0}{\partial x} + z \frac{\partial \psi}{\partial x} + \frac{1}{R+z} \frac{\partial u_0}{\partial \theta} + \frac{z}{R+z} \frac{\partial \phi}{\partial \theta} \\ \phi + \frac{\partial w_0}{\partial x} \\ \psi + \frac{1}{R+z} \left(\frac{\partial w_0}{\partial \theta} - v_0 \right) - \frac{z}{R+z} \phi \end{bmatrix} \quad (4)$$

$$\sigma = Q \epsilon = \begin{bmatrix} \sigma_{xx} \\ \sigma_{\theta\theta} \\ \sigma_{x\theta} \\ \sigma_{xz} \\ \sigma_{\theta z} \end{bmatrix} \quad (5)$$

Equation (4) is based on Ref. [6] and the stiffness matrix Q includes the shear correction factor and the material properties such as Young's modulus E and Poisson's ratio ν .

2.2 Ring equations

The major effects of a ring are displacement constraints for the deformation of the shell, which are radial, tangential and axial. Assuming that the axial constraint between shell and ring is ignored in the same manner as described in Ref. [7] and discussed in Ref. [8] and that the deformation of the ring includes the first order shear such as the shell equations, the ring has three unknowns, the displacements of in tangential direction $v_{r,i}$, in radial direction $w_{r,i}$ and the change of slope $\phi_{r,i}$, where the subscript r indicates that the parameters are related to the ring and i denotes the ring location ($i=0, L$). Analogously to the shell equations, the strain-displacement relation of a ring are expressed as follows:

$$\epsilon = \begin{bmatrix} \epsilon_{\theta\theta} \\ \gamma_{\theta z} \end{bmatrix} = \begin{bmatrix} \frac{1}{R+z} \left(\frac{\partial v_{r,i}}{\partial \theta} + w_{r,i} \right) + \frac{z}{R+z} \frac{\partial \phi_{r,i}}{\partial \theta} \\ \phi_{r,i} + \frac{1}{R+z} \left(\frac{\partial w_{r,i}}{\partial \theta} - v_{r,i} \right) - \frac{z}{R+z} \phi_{r,i} \end{bmatrix} \quad (6)$$

The strain and kinetic energy of the ring takes the similar form to equation (2) and (3), where h , ρ , ϵ , v_0 , w_0 and ϕ are replaced with $h_{r,i}$, $\rho_{r,i}$, $\epsilon_{r,i}$, $v_{r,i}$, $w_{r,i}$ and $\phi_{r,i}$ respectively and the integral $\int_0^L dx$ is simplified into the ring width $L_{r,i}$ for the reason that the displacement fields of a ring is assumed to be constant through the width in general. In addition, the stiffness matrix Q in equation (3) is modified into a 2 by 2 matrix $Q_{r,i}$ with the material properties of the ring and the terms with u_0 or ϕ are excluded in equation (2).

2.3 Follower force contribution, discretizations and matching conditions

An extended Hamilton's principle is applied to a ring-stiffened shell subjected to a tangential follower force as follows :

$$\int_{t_1}^{t_2} (\delta T_{total} - \delta U_{total} + \delta W_f) dt = 0, \quad (7)$$

where δW_f is the virtual work of the follower force. If we assume that the influence of the ring width on each side of the shell is negligible and take the acceleration of the shell and ring by the follower force into account, we can assume that the axial stress is linearly distributed along the longitudinal direction and that the stress resultant $f(x)$ is smaller than the follower force magnitude P at $x=0$ and larger than zero at $x=L$, due to the ring acceleration, as is presented in Figure (2). In

addition, assuming that the axial stress is uniformly distributed in the thickness direction, δW_f is expressed as

$$\delta W_f = \int_0^{2\pi} \int_0^L f(x) \left(\frac{\partial \delta w_0}{\partial x} \frac{\partial w_0}{\partial x} + \frac{\partial \delta v_0}{\partial x} \frac{\partial v_0}{\partial x} \right) R dx d\theta + \int_0^{2\pi} P \left(\delta w_0 \frac{\partial w_0}{\partial x} + \delta v_0 \frac{\partial v_0}{\partial x} \right) R d\theta \Big|_{x=0} \quad (8)$$

where the dimension of P and $f(x)$ is force per unit length.

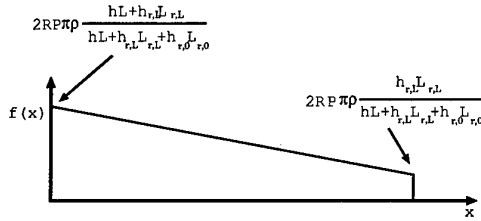


Figure 2. Axial compression distribution

From the above assumption that the effect of the ring width is negligible, the matching conditions are expressed as follows:

$$\begin{aligned} w_0(0, \theta, t) &= w_{r,0}(\theta, t), & v_0(0, \theta, t) &= v_{r,0}(\theta, t) \\ \phi_0(0, \theta, t) &= \phi_{r,0}(\theta, t), & w_0(L, \theta, t) &= w_{r,L}(\theta, t) \\ v_L(0, \theta, t) &= v_{r,L}(\theta, t), & \phi_0(L, \theta, t) &= \phi_{r,L}(\theta, t) \end{aligned} \quad (9)$$

To solve the variational form, equation (7), we introduce the circumferential base function as [12]

$$\begin{aligned} u_0 &= \sum_{m=0}^{\infty} U(x) \cos(m\theta) e^{i\omega t}, & v_0 &= \sum_{m=0}^{\infty} V(x) \sin(m\theta) e^{i\omega t} \\ w_0 &= \sum_{m=0}^{\infty} W(x) \cos(m\theta) e^{i\omega t}, & \phi &= \sum_{m=0}^{\infty} \Phi(x) \cos(m\theta) e^{i\omega t} \\ \psi &= \sum_{m=0}^{\infty} \Psi(x) \sin(m\theta) e^{i\omega t} \end{aligned} \quad (9)$$

for $m=0, 1, 2, \dots$

The above discretization in the circumferential direction has the orthogonal property about the virtual work of a follower force, the ring kinetic energy and the ring strain energy. Therefore, the stability analysis can be performed for each m . From this condition, the ring equation, the work of the follower force and the matching condition are simplified according as $m=1$ or not. If $m=1$, the shell behaves like a beam and thus the rings play a role only like concentrated masses in total energy. In other words, the shell can not be stiffened by the ring. If $m \neq 1$, the strain energy of the ring is also important in addition to the kinetic energy. In this case, from the assumption that the ring on the side, which a follower force is applied to, is rigid, the matching condition at $x=0$ is changed as follows:

$$w_0(0, \theta, t) = v_0(0, \theta, t) = \phi_0(0, \theta, t) = 0 \quad (10)$$

In addition, the second integral term in equation (8) is zero due to the fact that $\delta w_0, \delta v_0 = 0$.

With the above shape functions for the circumferential direction, the 4-node Lagrangian element can be used for the longitudinal direction. The discretized equation is

$$\mathbf{M}^{(m)} \ddot{\mathbf{q}}^{(m)} + \mathbf{K}^{(m)} \mathbf{q}^{(m)} + PS^{(m)} \mathbf{q}^{(m)} = 0 \quad (11)$$

for $m=0, 1, 2, 3, \dots$

This equation is solved by an eigenvalue problem as

$$(-\omega^2 \mathbf{M}^{(m)} + \mathbf{K}^{(m)} + PS^{(m)}) \mathbf{q}^{(m)} = 0 \quad (12)$$

The follower force is known as a non-conservative force and therefore the stability analysis must be a kinetic approach rather than a static approach. However, in the case $m \neq 1$, the non-conservative part in equation (8) is absent. In linear stability problems of the non-gyroscopic conservative type, all the critical loads are supplied not only by the kinetic approach but also by the energy approach [9]. This means that the stability analysis in the case $m \neq 1$ is a static buckling problem and the stability check by the frequencies of equation (11) is required only for the case $m=1$.

3. NUMERICAL RESULTS AND DISCUSSIONS

The non-dimensional equation of motion is required for a parametric study. By non-dimensionalizing by the radius R , following equation is induced from equation (11).

$$(-\lambda^2 \bar{\mathbf{M}}^{(m)} + \bar{\mathbf{K}}^{(m)} + \beta \bar{\mathbf{S}}^{(m)}) \bar{\mathbf{q}}^{(m)} = 0 \quad (13)$$

where $\beta, \lambda^2, \bar{\mathbf{M}}$ and $\bar{\mathbf{K}}$ are expressed as follows:

$$\beta = P \frac{(1-\nu^2)}{Eh} \quad (14)$$

$$\lambda^2 = \omega^2 \frac{(1-\nu^2)\rho R^2}{E} \quad (15)$$

$$\bar{\mathbf{M}} = \bar{\mathbf{M}}_s + \mu_a \bar{\mathbf{M}}_{r,0} + \mu_n \bar{\mathbf{M}}_{r,L} \quad (16)$$

$$\begin{aligned} \bar{\mathbf{K}} &= \bar{\mathbf{K}}_s + k_n \bar{\mathbf{K}}_{r,L} & m \neq 1 \\ \bar{\mathbf{K}} &= \bar{\mathbf{K}}_s & m = 1 \end{aligned} \quad (17)$$

where $\bar{\mathbf{M}}_{r,0}, \bar{\mathbf{M}}_{r,L}$ and $\bar{\mathbf{K}}_{r,L}$ are non-dimensional matrices of the rings at $x=0, L$. The ring contribution parameters μ_a, μ_n and k_n are

$$\mu_{a(n)} = \frac{\rho_{r,0(L)} L_{r,0(L)}}{\rho L} \quad (18)$$

$$k_n = \frac{E_{r,L} L_{r,L} (1-\nu^2)}{EL} \quad (19)$$

In equation (14) and (15), the assumption $h=h_r$ is used for simplicity and μ_a, μ_n and k_n are the parameters that vary the relative ring stiffness and mass ratio to the shell. If $m \neq 1$, $\bar{\mathbf{M}}$ is not used for the stability analysis as explained above.

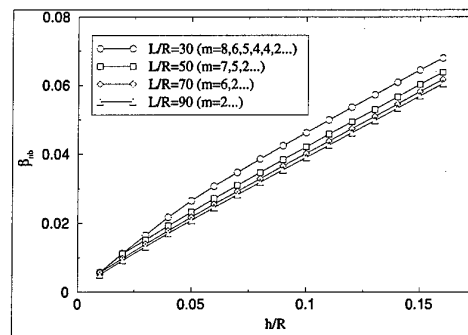


Figure 3. Buckling load ($m \neq 1, k_n = 0$)

The buckling loads β_{nb} for the case $m \neq 1$ are presented in Figure 3. The circumferential wave numbers

which induce instability are also presented. β_{nb} increases almost linearly with increasing thickness ratio and the increase of length ratio reduces the buckling load. The circumferential wave number, which induces instability, decreases with increasing length ratio and thickness ratio, but is not reduced to zero.

The ring stiffness ratio k_n has no effect on β_b and thus the effect is not presented. The buckling mode shapes are shown in Figure 4 for the case $k_n=0$. As x approaches L , the deformation of shell is almost zero. The stiffening ring therefore does not influence β_b .

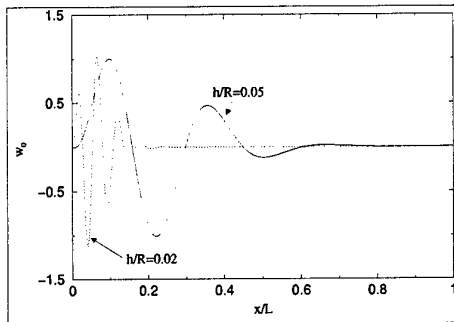


Figure 4. buckling mode shape ($L/R=50$, $k_n=0$)

Figure 5 shows the typical instability types for the case $m=1$. It is shown that both divergence and flutter can occur depending on μ_a and μ_n and that the thickness ratio has no effect on the stability. It is notable that divergence is the same phenomenon as buckling in the present work.

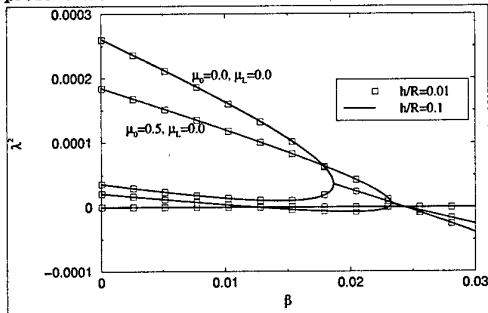


Figure 5. Eigenvalue curves ($m=1$, $L/R=50$)

In Figure 6 and 7, are presented the flutter or divergence loads β_b . It is shown that a flutter occurs only for low μ_a and μ_n . At the transition points from flutter to divergence, β_b decreases discontinuously. The thickness ratio, at which the buckling occurs for the case $m \neq 1$, is appended at the right side of axis, as the critical load is the smaller value between β_b and β_{nb} . It is shown that the critical load is found at $m=1$ modes only for long and thick shells, where a beam theory can predict the critical load efficiently. It is also found that the ranges of length and thickness ratio where a beam theory can be applied are larger than those of Ref. [5]. This is due to the edge ring which stabilizes the modes with a higher circumferential wave number ($m > 1$).

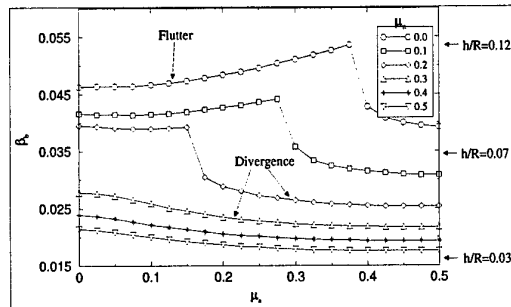


Figure 6. Divergence and flutter load ($m=1$, $L/R=30$)

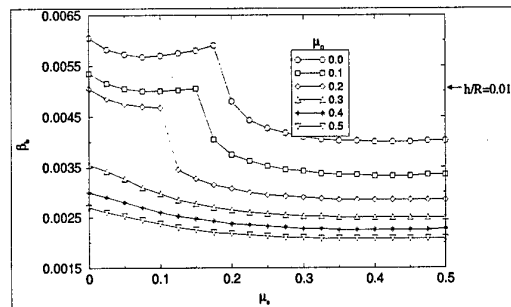


Figure 7. Divergence and flutter load ($m=1$, $L/R=90$)

4. REFERENCE

1. Beal, T. R., "Dynamic Stability of a Flexible Missile under Constant and Pulsating Thrust," AIAA Journal, 3-3, pp. 486-494, 1965
2. Park, Y. P. and Mote, C. D., "The Maximum Controlled Follower Force on a Free-free Beam Carrying a Concentrated Mass," Journal of Sound and Vibration, 98-2, pp. 247-256, 1985
3. Kim, J. H. and Park, J. H., "On the Dynamic Stability of Rectangular Plates Subjected to Intermediate Follower Force," Journal of Sound and Vibration, 209-5, pp. 882-888, 1998
4. Bismarck, M. N., "Dynamic Stability of Shallow Shells Subjected to Follower Force," AIAA Journal, 33-2, pp. 355-360, 1995
5. Park, S. H. and Kim, J. H., "On the Dynamic Stability of a Completely Free Cylindrical Shell Subjected to a Follower Force," Proceedings, 40th Structures, Structural Dynamics and Materials Conference, St. Louis, Missouri, pp.446-455, 1999.
6. Soedel, W., "Vibrations of Shells and Plates," New York: Marcel Dekker
7. Garnet, H and Levy, A., "Free Vibrations of Reinforced Elastic Shells," Journal of Applied Mechanics, 36-4, pp. 835-844, 1969
8. Huang, S. C. and Hsu, B. S., "Vibration of Spinning Ring-Stiffened Thin Cylindrical shells," AIAA Journal, 30-9, pp. 2291-2298, 1992
9. Ziegler, H., "Principles of Structural Stability," Massachusetts: Blaisdell Publishing Company, 1968.

Parametric Instability of a Viscoelastic Composite Beam under a Periodic Force

Tae-Woo Kim* and Ji-Hwan Kim**

Seoul National University
Shinrim-Dong, Gwanak-Ku, Seoul, 151-742, Korea

Keyword: Stability and Control

Abstract

Parametric instability of a composite beam subjected to a periodic loading is studied considering viscoelastic properties of the material. Governing equations are derived within linear viscoelastic constitutive equation and stability boundaries are determined by using the method of multiple scales. It is shown that viscoelasticity of material expands the stable area of the system.

Introduction

Composite materials with polymeric matrices are being used widely in aerospace structures because of their efficient load carrying capabilities. Particularly, advanced continuous fiber composites such as graphite-epoxy or boron-epoxy are being used to an increasing extent, replacing the more conventional structural materials such as steel or aluminum. However polymeric matrices, when used in unidirectional laminates, are expected to exhibit strong viscoelastic effects especially at high temperature and moisture, namely the response is time, as well as history, dependent. In particular, properties transverse to the fibers and shear properties are matrix controlled and show strong viscoelastic behavior. The potential long-term viscoelastic response to mechanical or thermal loading must be anticipated and accommodated at the design stage.

There are some studies dedicated to the analysis of the parametric instability of structures where time dependent material properties are considered. Stevens^[1] investigated approximately some of the qualitative aspects of the parametric excitation of a viscoelastic column subjected to harmonically varying axial load. He showed that in some cases the instability regions are broadened significantly and shifted toward lower values of the exciting frequencies, as the material becomes more viscoelastic in nature. For the determination of whether a viscoelastic homogeneous plate subjected to a harmonic in-plane excitation is stable, Aboudi *et al.*^[2] utilized the concept of Lyapunov exponents. Cederbaum and Mond^[3] used an analytical approach to study the stability boundaries of a viscoelastic column subjected to a periodic longitudinal load. Fung^[4] studied the dynamic stability of a simply supported viscoelastic beam, which is subjected to harmonic and parametric excitations simultaneously, considering the large deflection and non-linear effects of inertia, stiffness, damping.

The present paper deals with the parametric stability of a composite beam under a periodic loading where the viscoelastic properties of composites are incorporated. In the

study, the time dependent properties of the materials are defined by the constitutive equations of the linear viscoelastic theory of hereditary type. The finite element analysis is used for the formulation of the problem and stability boundaries are determined by means of the method of multiple scales.

Governing Equations

Fig.1 shows a composite cantilever beam under a periodic loading. In the theory of first order shear deformation and linear strain, the displacement field and displacement-strain relationship is expressed respectively as,

$$\begin{aligned} u(x, z, t) &= u_0(x, t) + z\varphi_y(x, t) \\ w(x, t) &= w_0(x, t) \end{aligned} \quad (1)$$

and

$$\begin{aligned} \varepsilon_{xx}(x, z, t) &= u_{0,x}(x, t) + z\varphi_{y,x}(x, t) \\ \varepsilon_{zx}(x, t) &= w_{0,x}(x, t) + \varphi_y(x, t) \end{aligned} \quad (2)$$

where $u_0(x, t)$, $w_0(x, t)$ represent the displacements at the neutral axis, $\varphi_y(x, t)$ the rotation of a line perpendicular to the neutral axis in z - x plane and $()_{,a}$ the partial derivative with respect to a ($a: x$ or z). For the constitutive equation, we will use the Boltzmann's superposition principle as linear viscoelastic theory. So the constitutive relations at k -th layer of the laminated beam, with zero initial values, can be written as follows^[5],

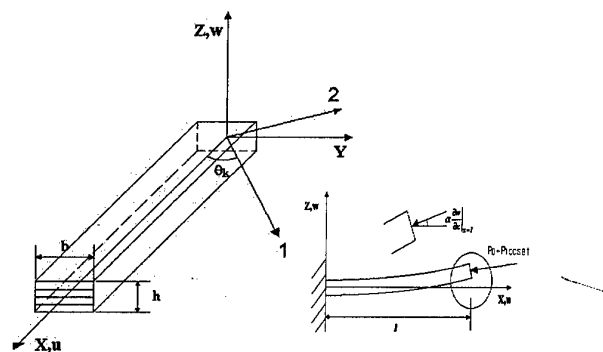


Fig. 1 Geometric Configuration

* Research Assistant, Department of Aerospace Engineering

** Associate Professor, Department of Aerospace Engineering

$$\begin{aligned}\sigma_{xx}^k(x, t) &= \int_0^t \{\bar{Q}_{11}^k(t-\tau) + \bar{Q}_{12}^k(t-\tau)P_{21}^k(t-\tau) \\ &\quad + \bar{Q}_{16}^k(t-\tau)P_{61}^k(t-\tau)\} \dot{\epsilon}_{xx}^k(x, \tau) d\tau \\ \sigma_{xx}^k(x, t) &= \int_0^t \{\bar{Q}_{45}^k(t-\tau)P_{45}^k(t-\tau) \\ &\quad + \bar{Q}_{55}^k(t-\tau)\} \dot{\epsilon}_{xx}^k(x, \tau) d\tau\end{aligned}\quad (3)$$

where the Poisson effects^[6] P_{21} , P_{61} and P_{45} are time dependent. However, in cases of cross-ply laminated beams they have constant values as,

$$P_{61}^k(t-\tau) = P_{45}^k(t-\tau) = 0, \quad P_{21}^k(t-\tau) = \begin{cases} -\frac{Q_{12}(0)}{Q_{22}(0)} & \theta_k = 0 \\ -\frac{Q_{12}(0)}{Q_{11}} & \theta_k = \frac{\pi}{2} \end{cases} \quad (4)$$

And the equations of motion are derived from the extended Hamilton's principle as in reference 7,

$$\delta \int_{t_1}^{t_2} (T + W_c) dt + \int_{t_1}^{t_2} (\delta W_{nc} - \delta U) dt = 0 \quad (5)$$

where T is the kinetic energy, δU the virtual work done by internal forces corresponding to the deformation energy of a elastic case, W_c the work done by the conservative portion of the loading and δW_{nc} the virtual work by the nonconservative portion of the loading. They can be expressed respectively as follows,

$$\begin{aligned}T &= \frac{1}{2} \int_A \{I_0(\dot{u}_0^2 + \dot{w}^2) + I_2\varphi_y^2\} dA, \\ \delta U &= \int_A \{N\delta u_{0,x} + M\delta\varphi_{y,x} + Q(\delta\varphi_y + \delta w_{,x})\} dA, \\ W_c &= \frac{1}{2} \int_0^l q w_{,x}^2 dx + q u_0|_{x=l}, \\ \delta W_{nc} &= -\alpha q w_{,x}|_{x=l} \delta w\end{aligned}\quad (6)$$

where N is normal force resultant, M moment resultant, Q shear force resultant, α a parameter that indicates the direction of loading, A cross section area and I_0 , I_2 moments of inertia written as,

$$(I_0, I_2) = \int_{-h/2}^{h/2} b\rho(1, z^2) dz \quad (7)$$

where ρ is density of the material.

Finite Element Formulation

In the finite element analysis of beam, the in-plane displacement u_0 , deflection w , and normal rotation φ_y can be represented by

$$u_0 = \sum_{j=1}^m u_0^j \Phi_j, \quad w = \sum_{j=1}^m w_j \Phi_j, \quad \varphi_y = \sum_{j=1}^m \varphi_y^j \Phi_j \quad (8)$$

where u_0^j , w_j are displacements, φ_y^j is rotation at node j and Φ_j denotes the shape function at node j .

Substituting Eqn 2- Eqn 4 into Eqn 5, one can obtain

following equations for homogeneous solution in matrix form,

$$[\bar{M}]\{\ddot{\bar{x}}\} + \int_0^t [\bar{K}(t-\tau)]\{\dot{\bar{x}}\} d\tau + ([\bar{W}_c(t)] + [\delta\bar{W}_{nc}(t)])\{\bar{x}\} = 0 \quad (9)$$

where $\{x(t)\}$ is the global nodal displacement vector and $[\bar{M}]$, $[\bar{K}(t)]$, $[\bar{W}_c(t)]$, $[\delta\bar{W}_{nc}(t)]$ are the global mass matrix, the time dependent global stiffness matrix, the global stiffness matrices from the work done by a pulsating external force respectively.

In this paper, the time dependent relaxation moduli in the principal material directions, Q_{ij} , are represented by the sum of exponentials, which is practically one of the widely used models for approximation of the viscoelastic behavior of material. Hence, without considering the effects of temperature and moisture they can be given as follows,

$$Q_{ij}(t) = Q_{ij}^0 + \sum_{r=1}^{n_{ij}} Q_{ij}^r e^{\alpha'_{ij} t} \quad (10)$$

where α'_{ij} denotes time constant and n_{ij} number of time constants of Q_{ij} when expressed by the exponential series. We further assume as in reference 8 that $Q_{55} = Q_{66}$ and time function for Q_{12} is equal to the one for Q_{22} . Now, Q_{11} is taken to be constant since it is generally controlled by fiber properties. Also, the time function for Q_{44} is taken the same as that for Q_{55} . When the time dependency is given by one exponential function, corresponding to the three-parameter solid model, the relaxation moduli are as follows,

$$\begin{aligned}Q_{11}(t) &= Q_{11} & Q_{22}(t) &= Q_{22}^0 + Q_{22}^1 e^{c_2 t} \\ Q_{12}(t) &= \frac{Q_{12}(0)}{Q_{22}(0)} Q_{22}(t) & Q_{44}(t) &= Q_{44}^0 + Q_{44}^1 e^{c_4 t} \\ Q_{55}(t) &= \frac{Q_{55}(0)}{Q_{44}(0)} Q_{44}(t) & Q_{66}(t) &= Q_{55}(t).\end{aligned}\quad (11)$$

For simplicity, following non-dimensionalized parameters are introduced,

$$\begin{aligned}S &= \frac{l}{h}, \quad \Omega = \theta \sqrt{\frac{\rho l^2}{Q_{11}}}, \quad \tau = t \sqrt{\frac{Q_{11}}{\rho l^2}} \\ \zeta &= \frac{P_0}{P_{cr}}, \quad \varepsilon_1 = c_2 \sqrt{\frac{\rho l^2}{Q_{11}}}, \quad \varepsilon_2 = c_4 \sqrt{\frac{\rho l^2}{Q_{11}}}, \quad \varepsilon_3 = \frac{P_1}{P_{cr}}.\end{aligned}\quad (12)$$

where P_{cr} is the elastic critical load under a constant axial force. Thus, with Eqn 11 and Eqn 12, Eqn 9 can be cast into following form :

$$\begin{aligned}[M]\{\ddot{\bar{x}}\} &+ \int_0^\tau ([K_0] + e^{\varepsilon_1(\tau-t')}[K_1] + e^{\varepsilon_2(\tau-t')}[K_2])\{\dot{\bar{x}}\} dt' \\ &+ (\zeta + \varepsilon_3 \cos \Omega \tau)[W]\{\bar{x}\} = 0\end{aligned}\quad (13)$$

Stability Analysis

In general parametric instability problems of elastic structures, solutions are usually expanded in terms of a small parameter, particularly pulsating load parameter ζ . When viscoelastic behavior of widespread material is incorporated, there appear another small parameters due to time

dependence of material properties that develop slowly with time. Then solutions can be sought in the form of expansions in these parameters as well as ζ .^{[3], [9]} Assuming that $\varepsilon_1, \varepsilon_2$ is small, we expand the Eqn 13 in power series in $\varepsilon_1, \varepsilon_2$. Retaining only terms of lowest order in $\varepsilon_1, \varepsilon_2$, one gets the following equations:

$$[M]\{\ddot{x}\} + ([K_0] + [K_1] + [K_2] + [W])\{x\} + (\varepsilon_1[K_1] + \varepsilon_2[K_2])\int_0^\tau \{x\}dt' + \varepsilon_3 \cos \Omega \tau [W]\{x\} = 0 \quad (14)$$

We introduce the linear transformation $\{x\} = [\Phi]\{\eta\}$, where $[\Phi]$ is the normalized right modal matrix. Multiplying each term of Eqn 14 by transpose of the normalized left modal matrix, $[\Psi]^T$ we obtain,

$$[I]\{\ddot{\eta}\} + [\Lambda]\{\eta\} + (\varepsilon_1[\Psi]^T[K_1][\Phi] + \varepsilon_2[\Psi]^T[K_2][\Phi])\int_0^\tau \{\dot{\eta}\}dt' + \varepsilon_3 \cos \Omega \tau [\Psi]^T[K_2][\Phi]\{\eta\} = 0 \quad (15)$$

where $[I], [\Lambda]$ denote the identity matrix and spectral matrix respectively and in component form,

$$\ddot{\eta}_n + \Omega_n^2 \eta_n + \sum_{m=1}^N (\varepsilon_1 g_{1nm} + \varepsilon_2 g_{2nm}) \int_0^\tau \dot{\eta}_m dt' + \varepsilon_3 \cos \Omega \tau \sum_{m=1}^N f_{nm} \eta_m = 0 \quad (16)$$

Now, in order to eliminate the secular terms that increases infinitely in regular perturbation expansions in $\varepsilon_1, \varepsilon_2$ and ε_3 , the method of multiple scales is employed by introducing three new time scales $T_1 = \varepsilon_1 \tau, T_2 = \varepsilon_2 \tau, T_3 = \varepsilon_3 \tau$ in first order expansion in terms of small parameters.^[10] Noting $T_0 = \tau$, we seek solutions to Eqn 16 in the form,

$$\eta_n(T_0, T_1, T_2, T_3) = \eta_{n0}(T_0, T_1, T_2, T_3) + \varepsilon_1 \eta_{n1-1}(T_0, T_1, T_2, T_3) + \varepsilon_2 \eta_{n1-2}(T_0, T_1, T_2, T_3) + \varepsilon_3 \eta_{n1-3}(T_0, T_1, T_2, T_3) + H.O.T. \quad (17)$$

Substituting Eqn 17 into Eqn 16 and equating each of the coefficients of $\varepsilon_1, \varepsilon_2$ and ε_3 to zero, we have

$$D_0^2 \eta_{n0} + \Omega_n^2 \eta_{n0} = 0 \quad (18)$$

$$D_0^2 \eta_{n1-1} + 2D_0 D_1 \eta_{n0} + \Omega_n^2 \eta_{n1-1} + \sum_{m=1}^N g_{1nm} \int_0^{T_0} \eta_{m0} dt' = 0 \quad (19)$$

$$D_0^2 \eta_{n1-2} + 2D_0 D_2 \eta_{n0} + \Omega_n^2 \eta_{n1-2} + \sum_{m=1}^N g_{2nm} \int_0^{T_0} \eta_{m0} dt' = 0 \quad (20)$$

$$D_0^2 \eta_{n1-3} + 2D_0 D_3 \eta_{n0} + \Omega_n^2 \eta_{n1-3} + \cos \Omega \tau \sum_{m=1}^N f_{nm} \eta_{m0} = 0 \quad (21)$$

where D_k denotes the partial derivative with respect to T_k . The general solution of Eqn 18 can be written as

$$\eta_{n0} = A_n(T_1, T_2, T_3) \exp(i\Omega_n T_0) + c.c. \quad (22)$$

where *c.c.* stands for complex conjugate. Next, we substitute Eqn 22 into Eqn 19, Eqn 20 and Eqn 21 and obtain equations with secular terms that are unbounded with time. For uniform

expansions these terms must be eliminated and this is accomplished by setting each of the coefficients of troublesome terms equal to zero. When Ω is near $\Omega_p + \Omega_q$, following conditions must be satisfied,

$$D_1 A_n - \frac{1}{2\Omega_n^3} g_{1nm} A_n = 0 \quad (23)$$

$$D_2 A_n - \frac{1}{2\Omega_n^3} g_{2nm} A_n = 0 \quad (24)$$

$$D_3 A_n = 0 \quad (n \neq p, q)$$

$$D_3 A_n - \frac{if_{pq}}{4\Omega_n} \bar{A}_n \exp(i\mu T_3) = 0 \quad (n = p, q) \quad (25)$$

where \bar{A}_n is the complex conjugate of A_n and μ is the detuning parameter for expressing the nearness of Ω to $\Omega_p + \Omega_q$ defined by,

$$\Omega = \Omega_p + \Omega_q + \varepsilon_3 \mu \quad (26)$$

To satisfy Eqn 23 to Eqn 25, we let

$$A_n(T_1, T_2, T_3) = a_{n1}(T_1) a_{n2}(T_2) a_{n3}(T_3) \quad (27)$$

and by inserting Eqn 23 to Eqn 25, we obtain

$$a_{n1} = \alpha_{n1} \exp\left(\frac{1}{2\Omega_n^3} g_{1nm} T_1\right) \quad (28)$$

$$a_{n2} = \alpha_{n2} \exp\left(\frac{1}{2\Omega_n^3} g_{2nm} T_2\right) \quad (29)$$

and when $n=p, q$,

$$a_{p3} = \alpha_{p3} \exp(-i\lambda T_3) \quad (30)$$

$$a_{q3} = \alpha_{q3} \exp\{i(\bar{\lambda} + \mu) T_3\}$$

where

$$\lambda = -\frac{1}{2}(\mu \pm \sqrt{\mu^2 - \frac{1}{4}\Lambda_{pq}}) \quad (31)$$

and

$$\Lambda_{pq} = \frac{f_{pq} f_{qp}}{\Omega_p \Omega_q} \quad (32)$$

It follows from Eqn 28, Eqn 29 and Eqn 30 that when $n=p, q$, the solutions of order zero are represented as

$$\eta_{n0} = A_{n0} \exp(i\Omega_n T_0) \exp\left(\frac{1}{2\Omega_n^3} g_{1nm} T_1\right) \exp\left(\frac{1}{2\Omega_n^3} g_{2nm} T_2\right) \exp(-i\lambda T_3) + c.c. \quad (33)$$

Rewriting Eqn 33 in terms of τ , we see that instability occurs when

$$\frac{1}{\Omega_n^3} |g_{1nm} \varepsilon_1 + g_{2nm} \varepsilon_2| \leq \sqrt{\frac{1}{4}\Lambda_{pq} - \mu^2} \varepsilon_3 \quad (34)$$

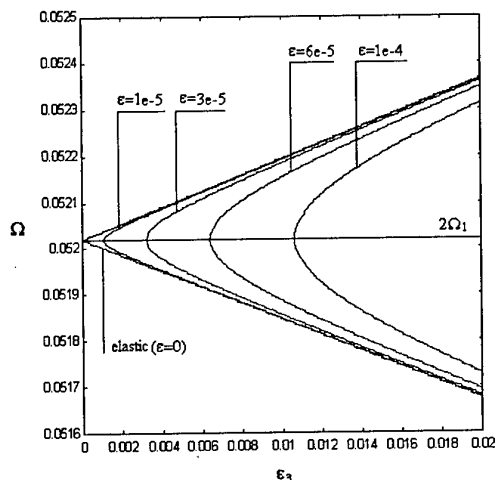


Fig.2 Variation of stability boundaries due to viscoelastic properties ($\epsilon_1=\epsilon_2=\epsilon$)

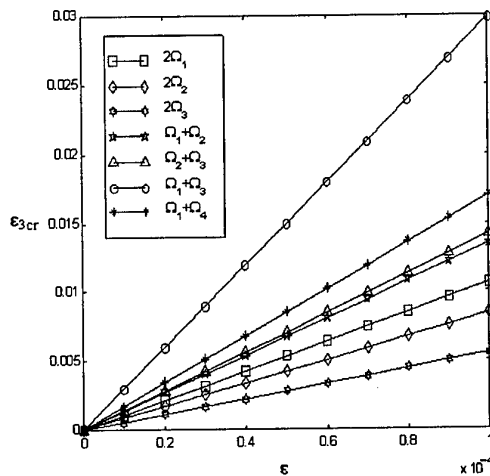


Fig.3 Minimum parameter values for instability in various resonance cases ($\epsilon_1=\epsilon_2=\epsilon$)

The transition curves in the $\epsilon_3\Omega$ -plane that separate stable from unstable solutions are defined by

$$\Omega = \Omega_p + \Omega_q \pm \sqrt{\frac{1}{4} \frac{\Lambda_{pq}^2}{\Omega_n^6} (g_{1nn}\epsilon_1 + g_{2nn}\epsilon_2)^2} \quad (35)$$

When $\epsilon_1=\epsilon_2=0$, in pure elastic case, we have the known results for elastic stability boundaries.

Numerical Results and Discussion

Fig.2 shows stability boundaries of a [0/90/90/0] beam with $\alpha=0$, $S=30$ and $\zeta=0.3$ in case Ω is near $2\Omega_1$. As can be seen, the stable region is enlarged when material becomes more viscoelastic in nature and there exist a critical value of the excitation parameter, ϵ_{3cr} , for instability, which is defined from Eqn 35 by,

$$\epsilon_{3cr} = \frac{2(g_{1nn}\epsilon_1 + g_{2nn}\epsilon_2)}{\Omega_n^3 \sqrt{\Lambda_{pq}}} \quad (36)$$

In Fig.3 these critical values are plotted against the viscoelastic parameter for various resonance forms. The critical values for combination resonance of different frequencies are more sensitive to the viscoelastic parameter than for primary resonance. Furthermore, one can see that among primary resonance, that of low frequency has critical values more dependent on viscoelasticity. Besides, the effect of other parameters on the stability, like slenderness ratio, stacking sequence and constant loading parameter, has been investigated.

References

1. Stevens, K.K., "On the Parametric Excitation of a Viscoelastic Column", *American Institute of Aeronautics and Astronautics Journal*, Vol. 4, pp. 2111-2116, 1966.
2. Aboudi J., Cederbaum G. and Elishakoff I., "Stability of Viscoelastic Plates by Lyapunov Exponents", *Journal of Sound and Vibration*, Vol. 139, No. 3, pp. 459-467, 1990.
3. Cederbaum G. and Mond M., "Stability Properties of a Viscoelastic Column Under a Periodic Force", *Journal of Applied Mechanics*, Vol. 59, pp. 16-19, 1992.
4. Fung R.F., Huang J.S. and Chen W.H., "Dynamic Stability of a Viscoelastic Beam Subjected to Harmonic and Parametric Excitations Simultaneously", *Journal of Sound and Vibration*, 198(1), pp. 1-16, 1996.
5. Yi, S. and Hilton, H.H., "Dynamic Finite Element Analysis of Viscoelastic Composite Plates in the Time Domain", *International Journal for Numerical Methods in Engineering*, Vol. 37, pp. 4081-4096, 1994.
6. Chandrashekhara, K. and Bangera, K.M., "Free Vibration of Composite Beams Using a Refined Shear Flexible Beam Element", *Computers and Structures*, Vol. 43, No. 4, pp. 719-727, 1992.
7. Chen, T.M., "The Hybrid Laplace Transform/Finite Element Method Applied to the Quasi-Static and Dynamic Analysis of Viscoelastic Timoshenko Beams", *International Journal for Numerical Methods in Engineering*, Vol. 38, pp. 509-522, 1995.
8. Yi, S. and Hilton, H.H., "Nonlinear Thermo-Viscoelastic Analysis of Interlaminar Stresses in Laminated Composites", *Journal of Applied Mechanics*, Vol. 63, pp. 218-224, 1996.
9. Szyszkowski, W. and Glockner, P.G., "The Stability of Viscoelastic Perfect Columns: A Dynamic Approach", *International Journal of Solids and Structures*, Vol. 21, No. 6, pp. 545-559, 1985.
10. Nayfeh A.H and Mook D.T., *Nonlinear Oscillations*, John Wiley & Sons, 1979.

BVI Noise Predictions using Euler/FW-H Method

Akio Ochi*, Eiji Shima*, Takashi Aoyama†, and Shigeru Saito†,

* Advanced Technology Institute of Commuter-helicopter, Ltd. (ATIC), Kakamigahara, Gifu, Japan

† National Aerospace Laboratory (NAL), Chofu, Tokyo, Japan

Key Words: Helicopters, Aerodynamics

ABSTRACT

The predictions of helicopter Blade-Vortex Interaction (BVI) noise are performed using a combined method of an unsteady Euler code with an aeroacoustic code based on the Ffowcs Williams and Hawkings formulation. A moving overlapped grid method is employed in the Euler code. Three types of grids, blade grid, inner and outer background grids are used. The calculated waveform of BVI noise clearly showed the distinct spikes caused by the interaction between blade and tip vortex. The carpet noise contours calculated by the present method was compared with the experimental data obtained by Advanced Technology Institute of Commuter-helicopter, Ltd. The calculated noise level showed good agreement with the measured data.

1. INTRODUCTION

Over the past years, noise problems have been becoming serious with the increase of use of rotorcrafts. Blade-Vortex Interaction (BVI) noises cause serious noise problems for helicopters. It is an aeroacoustic noise generated by interactions between rotor blades with vortices shed from their blade tip during descending flight for landing approach.

Through the progress of Computational Fluid Dynamics (CFD) and computer technologies, advanced CFD techniques enable us to calculate whole rotor configuration by using Finite Difference Method (FDM) or Finite Volume Method (FVM). These kinds of computations can handle both vortex wake geometry and aerodynamic features such as blade surface pressure at the same time without wake modeling.

The primary objective of this paper is to present a procedure to predict BVI noise by an advanced CFD method. The procedure consists of a Euler code based on FDM and an aeroacoustic code based on FW-H formulation. This Euler code was developed under the collaborative research between Advanced Technology Institute of Commuter Helicopter (ATIC) and National Aerospace Laboratory (NAL). ATIC was established in 1994 to research and develop technologies in aeroacoustic field to reduce helicopter external noise and in flight control field for flight safety.

2. NUMERICAL METHOD

The procedure of BVI noise prediction consists of two phases. The first phase is a CFD computation of the rotor aerodynamics. The second one is an acoustic computation to obtain far field acoustic data using the blade surface pressure computed in the first phase.

The governing equations of the aerodynamic computation are the unsteady Three-dimensional Euler equations. The inertial force terms by the rotation are included in the calculation of the blade grid.

Grid system

A moving overlapped grid approach is employed to treat rotating rotor blades. The blade grid rotates in the Cartesian background grid. In this study, a new grid topology is employed to concentrate grid points near the rotor disk. The Cartesian background grid is divided into the two parts. One is the inner background grid and the other is the outer background grid. The inner background grid is placed around the rotor disk. The outer background grid covers whole computation region and has sparse grid density. The grid system for a 5-bladed configuration is sketched in Fig. 1 and 2. Huge number grid points are distributed to the inner background grid to achieve higher resolution, because the density of grid directly affects the strength of numerical viscosity. Table 1 shows the numbers of grid points.

Table 1. Grid specifications.

	(x × y × z)
Inner background grid	450 × 400 × 80 = 14,400,000
Outer background grid	83 × 79 × 49 = 321,293
Blade grid	(chord × normal × span) × blade (79 × 40 × 160) × 5 = 2,528,000
Total	17,249,293
Grid spacing of Inner background grid in rotor disk	0.11c (= 0.006R)

Numerical method for Cartesian background grid

A high accuracy explicit scheme is utilized in the background Cartesian grid. The compact TVD scheme is employed for spatial discretization. MUSCL cell interface value is modified to achieve 4th-order accuracy. The time integration is carried out by the four stages Runge-Kutta.

Numerical method for blade grid

The numerical method for the blade grid calculation is an implicit finite-difference scheme. The Euler equations are discretized in the delta form using Euler backward time differencing. The accuracy of this solver in space and in time is 2nd-order and 1st-order, respectively. In order to obtain the unsteady solution in forward flight conditions, the Newton iterative method is also used. In order to reduce the residual at each time-step, six iterations are used.

Treatment of blade motion

The dynamic blade motions such as flapping, feathering, and lagging are defined by the input data. The present code accepts azimuth-wise data or 1st harmonic function data obtained by measurements or other codes (e.g. CAMRAD). In the present calculation, the collective pitch, cyclic pitch, flapping, and lagging angles measured by the wind tunnel experiment by ATIC are used. The inertial forces by these dynamic motions have not considered yet in the present flow solver.

Noise analysis

The pressure distribution on the blade surface calculated by the CFD code is stored every 0.5 degrees in azimuth-wise direction as the input data in noise calculation. The aeroacoustic code is based on the FW-H formulation without the quadruple term.

3. CALCULATION CONDITIONS

Three cases of shaft tilt angle are selected to evaluate the capability of our code to predict BVI noise. The operating conditions are summarized in Table 2. The shaft tilt angles are corrected by the Heyson's method.

Table 2. Operating conditions.

	Case 1	Case 2	Case 3
Corrected shaft tilt angle, α_c	2.49°(aft)	4.50°	6.43°
Shaft tilt angle, α_s	4.02°(aft)	5.97°	7.93°
Collective pitch angle	4.91°	4.28°	3.78°
Lateral cyclic pitch angle	-2.66°	-2.68°	-2.52°
Longitudinal cyclic pitch angle	1.89°	1.73°	1.56°
Flapping angle (inc. coning)	1.74°	2.83°	1.74°
Tip Mach number, M_{tip}	0.626	0.625	0.625
Advance ratio, μ	0.157	0.157	0.157

4. RESULTS AND DISCUSSION

Numerical computations are performed by the present method for the realistic rotor system, which has five blades with high aspect ratio. The CPU time is about 20 hours per revolution using 30 PEs of Numerical Wind Tunnel

(NWT) in NAL. The periodic solution is obtained after 4 revolutions. The required memory sizes are 8GB.

Figure 3 presents calculated thrust distributions on the rotor disk. It shows distinct thrust fluctuations caused by BVI near the azimuth angles of 80° and 280°. Tip vortices are clearly captured by our code as shown in Fig. 4. The computed and measured pressure coefficient (C_p) histories on blade surface are plotted in Fig. 5. Although quantitative discrepancies are recognized, the fluctuations caused by BVI are successfully captured. The sudden changes of pressure coefficient are observed in the advancing side (from 0° to 90°) and the retreating side (from 270° to 360°).

Figure 6 shows the microphone position in the experiment. The microphone was placed downward front of the rotor center. The calculated sound pressure level (SPL) is compared with the experimental data in Fig. 7. The solid lines show calculated data and averaged experimental data. The background crowd shows raw (non-averaged) data to indicate the fluctuation of measured data. The calculated SPL waveform shows distinct spikes caused by BVI. The difference between calculated and measured waveforms is due to the disagreement of intensity and location of BVI. The predicted and measured carpet noise contours on the horizontal plane 2.3m below the center of the rotor for three shaft tilt angle cases are compared in Fig. 8. These results show good agreement in both qualitatively and quantitatively. The predicted results well capture the trend that the BVI lobe location moves downstream with the increase of shaft tilt angle.

5. CONCLUSIONS

The predictions of helicopter BVI noise are performed using a combined method of an unsteady Euler code with an aeroacoustic code based on the Ffowcs Williams and Hawkings formulation. The waveform of calculated sound pressure level showed the distinct spikes caused by BVI. The predicted carpet noise contours by the present method showed reasonable agreement with the experimental data obtained by ATIC. These results indicate that advanced CFD method has considerable potential for BVI noise prediction.

REFERENCES

- Ochi, A., Shima, E., Aoyama, T., Saito, S., and Yamakawa, E., "BVI Noise Predictions by Moving Overlapped Grid Method," AHS 55th Annual Forum, Montréal, Quebec, Canada, May 25-27, 1999.
- Ahmad, J., Duque, E. P. N., and Strawn, R. C., "Computations of Rotorcraft aeroacoustics with a Navier-Stokes/Kirchhoff Method," 22nd European Rotorcraft Forum, Brighton, UK, Sep 1996.

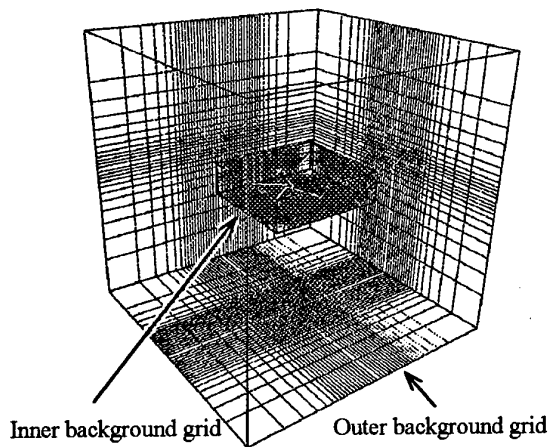


Fig. 1. Blade grids, inner background grid, and outer background grid.

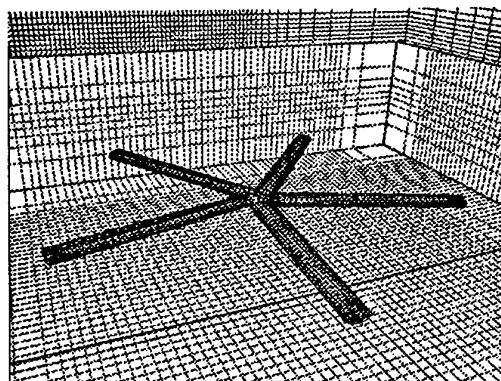


Fig. 2. Blade grids and background grids. (close up)

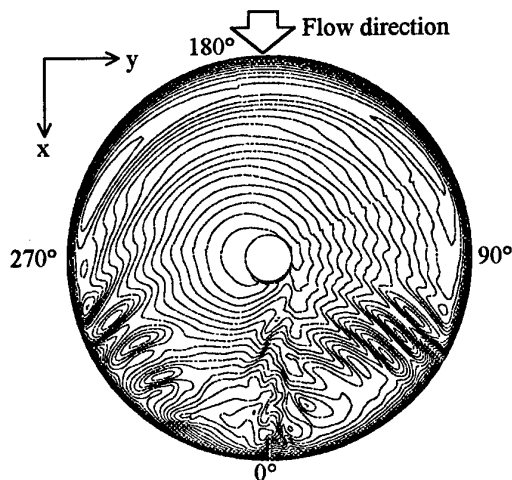


Fig. 3. Thrust distributions on rotor disk for case 2

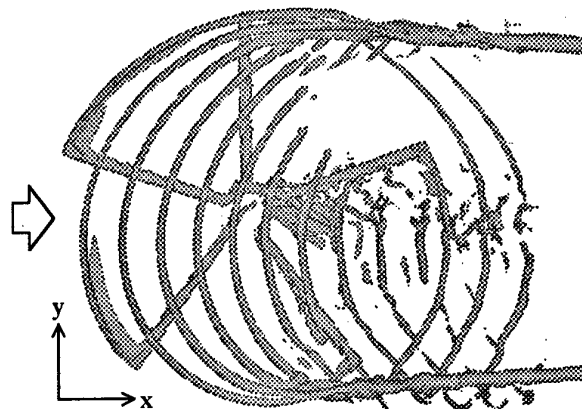


Fig. 4. Visualized tip vortices by iso-surface of vorticity for case 2.

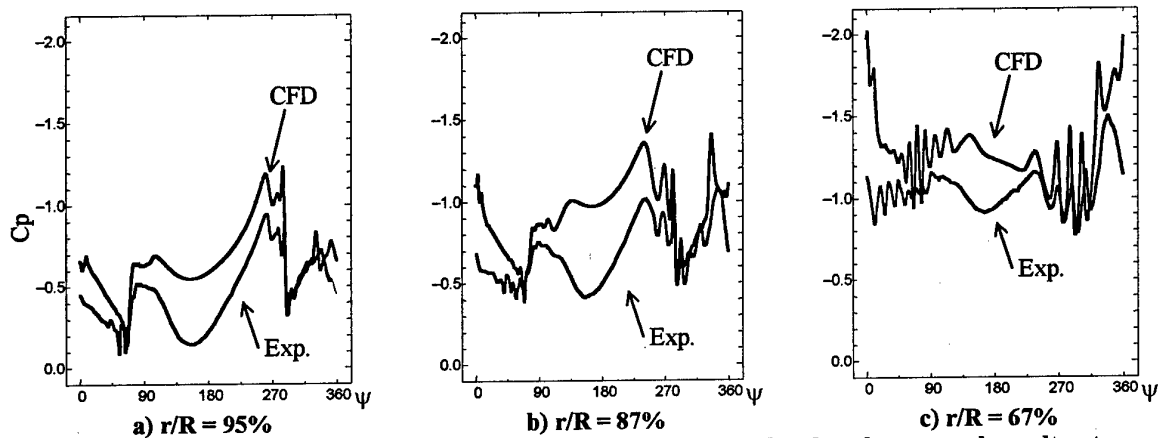
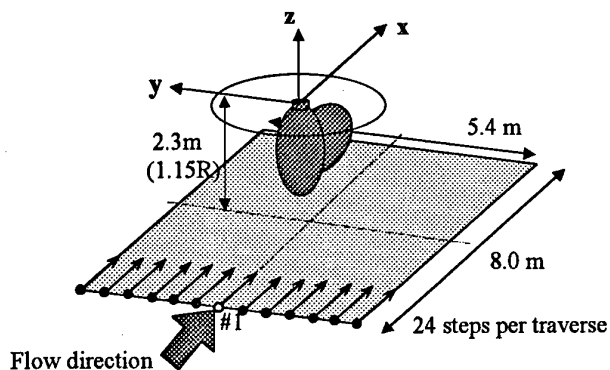


Fig. 5. Comparisons of pressure coefficient histories between calculated and measured results at upper surface of blade on different span stations for Case 2 ($\alpha_c = 4.50^\circ$). Chord-wise position x/c is 4%.



13 traverse microphones to
measure carpet noise contours

Acoustic data :
mean value during
about 43 revolutions

Microphone positions in Fig. 15
#1: $x=-4.0\text{m}$, $y=0\text{m}$, $z=-2.3\text{m}$

Fig. 6. Microphone setting for noise measurement in ATIC model rotor test.

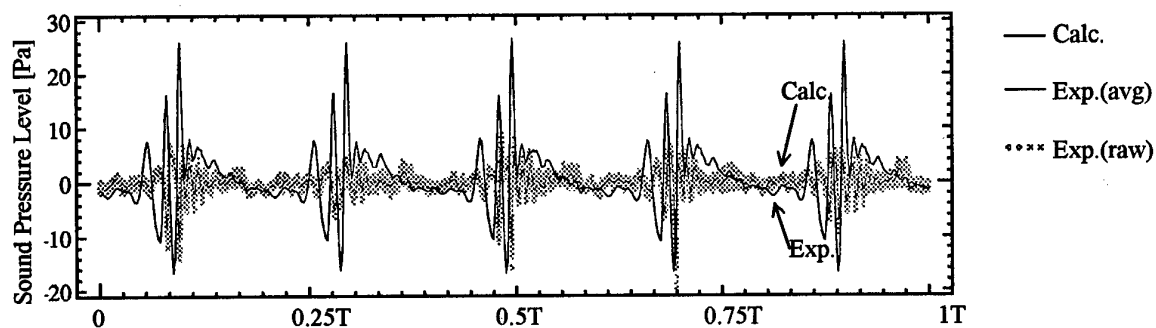


Fig. 7. Comparison of Sound Pressure Level (SPL) histories between calculation and measurement for Case 2.

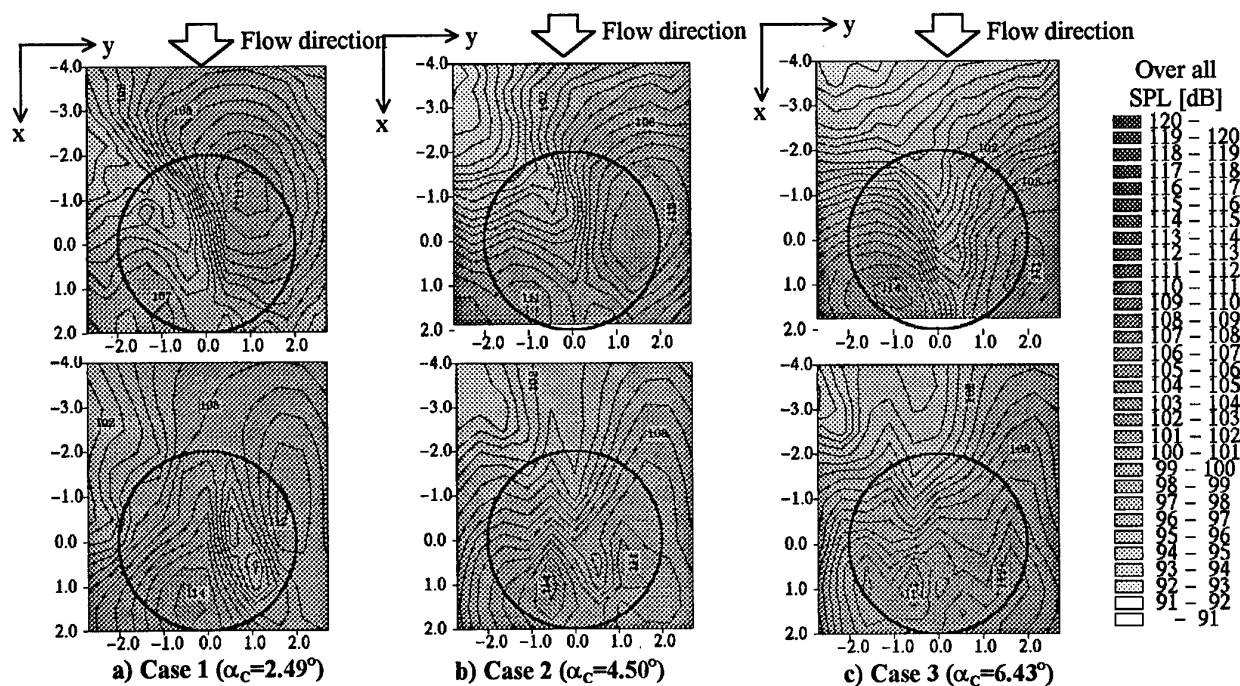


Fig. 8. Comparisons of carpet noise contours between calculated and measured results for three cases. Open circle shows rotor disk.

A Study on Aerodynamic Characteristics Improvement of Modified Arrow Wing of Next-Generation SST due to Lateral Blowing

Makoto KAMISHITA* and Shigeru ASO**

Kyushu University, 6-10-1 Hakozaki, Higashi-Ku, Fukuoka 812-8581, JAPAN

Keiichi KARASHIMA†

Nishinippon Institute of Technology, 1633 Aratsu, Kanda-Machi, Miyako-Gun, Fukuoka 800-0344, JAPAN

Kiyoshi SATO‡

ISAS, 3-1-1 Yoshinodai, Sagamihara, Kanagawa 229-0022, JAPAN

Key Words Aerodynamic Characteristics, Lateral Blowing, Flow Control, SST

Abstract

An experimental study on the improvement of aerodynamic characteristics of a modified arrow wing by lateral blowing in low and high-speed flow has been conducted. A modified arrow wing, which is one of the baseline configurations of the proto-type of next-generation SST, is selected for the experiments. The testing model is the combination of a body of a circular cylinder and ogive and a modified arrow wing with aspect ratio of 1.91. The lateral blowing is realized by injecting a pair of steady jets parallel to the trailing edge of the wing. The experiments have been conducted with the transonic and supersonic wind tunnel of ISAS under the testing conditions of M_∞ (free-stream Mach number) = 0.3 ~ 2.3, Re (unit Reynolds number) = $1.06 \times 10^7 \sim 3.10 \times 10^7$ [1/m], α (angle of attack) = $15^\circ \sim 30^\circ$ and C_j (jet momentum coefficient) = 0.0084 ~ 0.0316. The results show that the C_L and L/D is increased by lateral blowing while C_D is slightly increased for positive α . The results suggest that the lateral blowing can be useful for the improvement of aerodynamic characteristics of the arrow wing in low and high-speed flow.

Nomenclature

C_L	Lift coefficient
C_D	Drag coefficient
C_{My}	Pitching moment coefficient
L/D	Ratio of lift to drag
C_j	jet momentum coefficient
Re	Reynolds number per length [1/m]
P_j	jet-plenum stagnation pressure [Pa]
P_s	free-stream static pressure [Pa]
S_j	area of jet nozzle exit
S_w	area of wing planform
α	angle of attack
M_∞	free stream Mach number
D	diameter of jet-nozzle exit
Subscript	
∞	free stream
j	jet blowing

* Graduated student, Dept. of Aero. & Astro., Kyushu University

** Professor, Dept. of Aero. & Astro., Kyushu University

† Professor, Nishinippon Institute of Technology

‡ ISAS

1. Introduction

Recently research of developing the supersonic transportation becomes very active. It is said that high L/D performance is requested at all flight regime. There are many techniques for the increment of L/D , such as leading flaps and trailing flaps. However these high lift devices are passive method for high L/D . In the present study active control of aerodynamic characteristics of SST wing is investigated by using the lateral blowing. Significant increase of L/D is obtained by lateral blowing in the present study. Also the aerodynamic effects by applying lateral blowing at Mach number from 0.3 to 2.3 is confirmed.

2. Experimental apparatus and Procedures

2.1 Wind tunnel

The tests were conducted with transonic and supersonic wind tunnel of ISAS (Institute of Space and Astronautical Science). Each tunnel has a 600mm × 600mm square test section and is blowdown type. The transonic and supersonic wind tunnels are capable of Mach numbers sweep from 0.3 to 1.3 and from 1.5 to 4.0 respectively. The sting type of force balance is used and is put in the testing model, which is mounted by the sting.

2.2 Model and Instrumentation

The testing model is the wing-body combination as shown in Fig.1. The body consists of a circular cylinder and conical apex and the planform of the wing configuration is an arrow wing. In addition, the wing has no twist, camber or dihedral. Wing parameters are shown in Table 1.

The feasibility of lateral blowing was suggested by an early investigation of the technique performed by K.Karashima on a trapezoidal wing (swept angle of 45°) at Mach number 0.3. Lateral blowing is realized by injecting a pair of sonic-jets in parallel to the trailing edge of the wing⁽¹⁾. Then the nozzle is located at the junction between the trailing edge of wing and the fuselage of the model. The jet is injected parallel to the trailing edge. The schematic diagram of experimental system is shown in Fig.2. An air compressor is located out of the test section, and compressed air is provided to the nozzle in the model through the tube as shown in Fig.2.

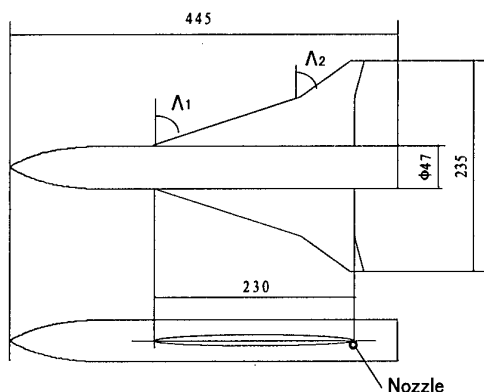


Fig.1 Model configuration (unit mm)

Aspect ratio	1.91
Swept angle Λ_1	72.7°
Λ_2	52.2°
Section	Circular arc airfoil
Thickness ratio	6%
Root chord length	230mm
Semi span length	94mm

Table 1 Wing Parameters

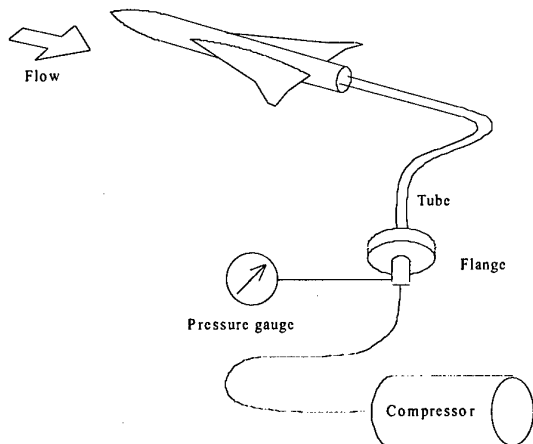


Fig.2 Schematic of experimental diagram

2.3 Test conditions

Test conditions for the present experiment are shown in Table 2. Lift, drag and pitching moment are measured both in subsonic and supersonic flows. Also, the surface oil flow pictures on the wing have been taken at Mach number of 0.3. The primary parameter to identify blowing rate is the jet momentum coefficient, as follows ;

$$C_j = \frac{\dot{m}_j u_j}{\frac{1}{2} \rho U_\infty^2 S_w} = \frac{2 p_j S_j}{\gamma p_s S_w M_\infty^2}$$

P_j means plenum stagnation pressure for jet pressure. At case from ① to ③, the value of P_j equals 1.078×10^6 Pa. The effects of C_j is investigated by changing P_j in case of from ④ to ⑥.

I Forces and moment

	M_∞	α	D
①	0.3, 0.4, 0.5	-15.0° ~ +30.0°	2 mm
②	0.7, 0.9, 1.0, 1.1, 1.3	-15.0° ~ +15.0°	2 mm
③	1.5, 1.7, 2.0, 2.3	-12.5° ~ +12.5°	2 mm
④	0.3	-5.0° ~ +15.0°	3 mm
⑤	0.9	-5.0° ~ +15.0°	3 mm
⑥	1.5, 2.0	-5.0° ~ +12.5°	3 mm

II Oil flow visualization of surface flowstream

M_∞	α	D
0.3	10°, 20°, 30°	2 mm

Table 2 Test conditions

3. Results and discussion

In cases of ① through ③, P_j is kept constant 1.078×10^6 Pa. So, C_j is smaller as free stream Mach number is increased. (Fig.3)

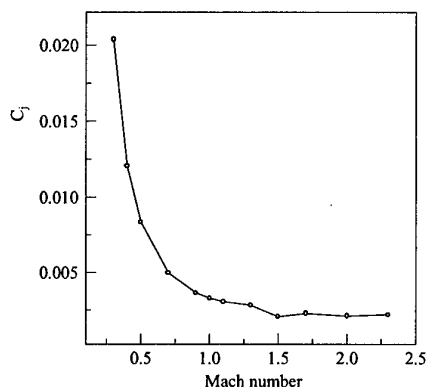


Fig.3 C_j vs Mach number as the case of $P_j = 1.078 \times 10^6$ Pa

The effects of lateral blowing on lift, drag, ratio of lift to drag and pitching moment curves at Mach number of 0.3 are presented in Fig.4 through Fig.7 respectively.

Fig.4 shows that uniformly increase of C_L due to lateral blowing is observed between $\alpha = -15^\circ$ and $\alpha = 30^\circ$. The increase of C_D is small for lower positive α and large for higher positive α . And C_D characteristics shows that blowing curve intersects no blowing's near $\alpha = 0^\circ$. As a result, significant increase of L/D is observed at lower angle of attack between -5° and 5° . In Fig.7 pitching-down tendency is observed. The features of C_L , C_D , L/D and C_{My} curves are almost similar in all subsonic region.

Aerodynamic characteristic for various Mach numbers at $\alpha = 2.5^\circ$ are shown in Fig.8 to Fig.11. The increase of C_L by lateral blowing is observed for all Mach number region. Higher increase is observed especially in subsonic flow. While C_D increases in subsonic region, in supersonic C_D decreases. So, L/D also increases for all Mach number region. In the pitching moment characteristics, the nose of the model is pitching downward by lateral blowing. As shown those figures, effects of lateral blowing are verified from Mach number of 0.3 to 2.3, though the rate of change is smaller as Mach number increases.

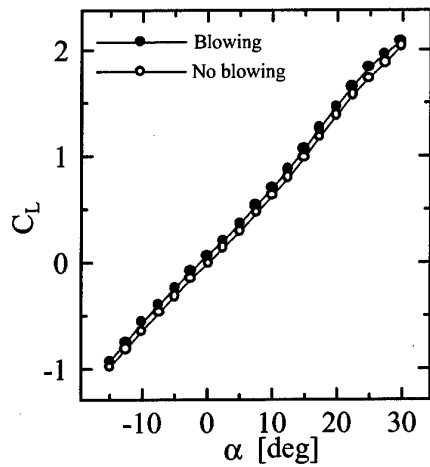


Fig.4 C_L vs α at Mach 0.3

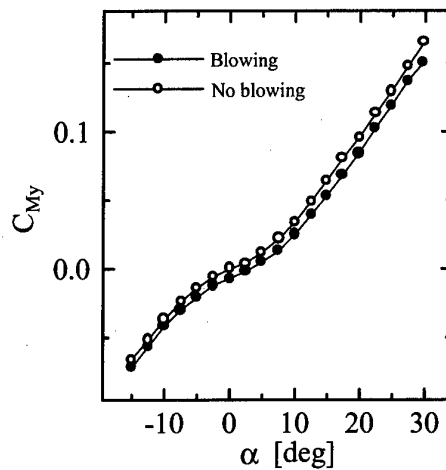


Fig.7 C_{My} vs α at Mach 0.3

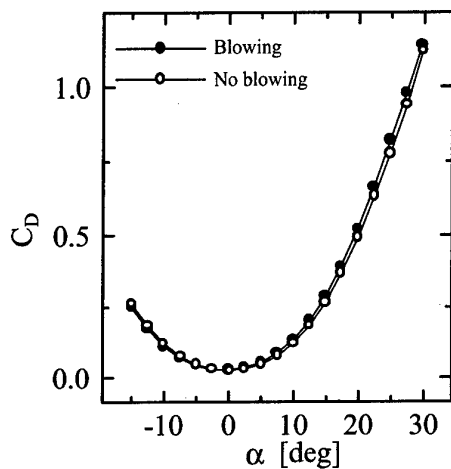


Fig.5 C_D vs α at Mach 0.3

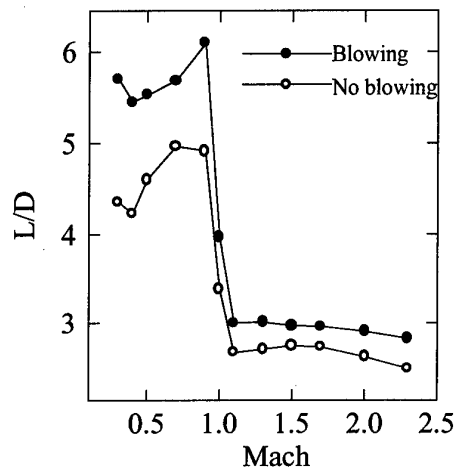


Fig.10 L/D vs Mach at $\alpha=2.5$ deg

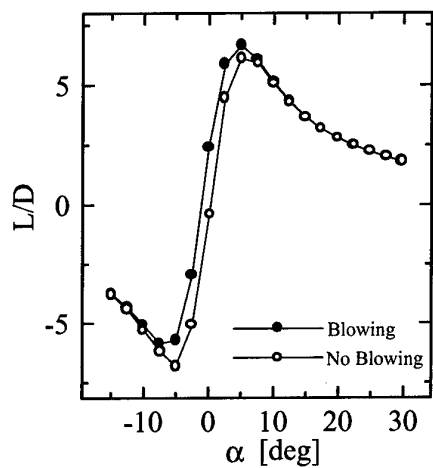


Fig.6 L/D vs α at Mach 0.3

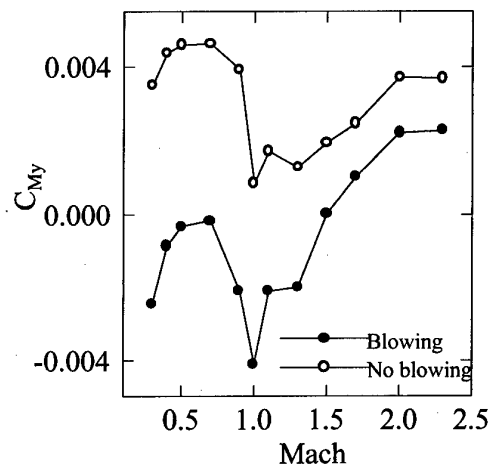


Fig.11 C_{My} vs Mach at $\alpha=2.5$ deg

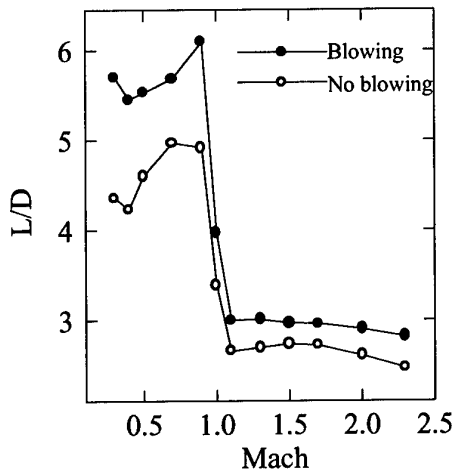


Fig.10 L/D vs Mach at $\alpha=2.5$ deg

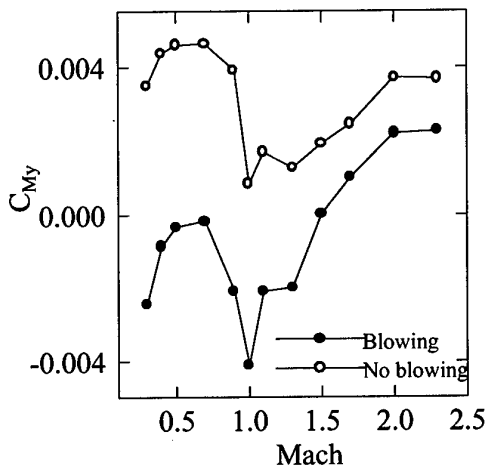


Fig.11 C_{My} vs Mach at $\alpha=2.5$ deg

Next, the surface streamlines are observed by oil flow technique. Comparing those pictures with and without lateral blowing, it is clear that two streamlines are different. Side view of those pictures with lateral blowing shows downward flow near the trailing edge. The downward flow increase lift. Also top view of lateral blowing shows slightly converging surface flow over the wing into the root of the wing is observed. As flow on the lower surface of the wing near the trailing edge is dammed by lateral blowing, pressure on the lower of wing becomes larger. The increase of pressure at lower surface also increase lift.

The influence of jet momentum is also investigated. The experimental results with various C_j are shown in Fig.12. As C_j is increased, the increment of C_L is larger. However the contribution by increasing C_j becomes small. So, the effective value of C_j might have some upper limit. Since C_j is related with jet flow structure, it is necessary to capture the behavior of the jet flow structure to reveal the mechanism.

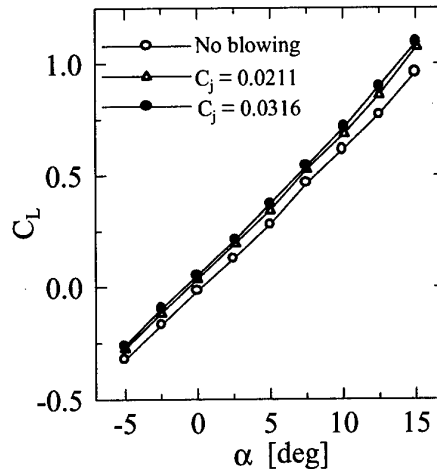


Fig.12 Effects of C_j about C_L vs α at Mach 0.3

4. Concluding remarks

A study has been conducted to examine the aerodynamic effects by applying lateral blowing to the SST model. The conclusions of the present study are summarized as follows:

- 1) Significant increase of L/D is observed at lower angle of attack at Mach number from 0.3 to 2.3.
- 2) In supersonic region drag coefficient decreases somewhat slightly by lateral blowing.
- 3) From the surface flow observation the downward flow near the trailing edge and the pressure increase at lower surface of the wing increase the lift of the wing.

For further study

Surface pressure measurement on the arrow wing in order to understand the flowfield formed by interaction among lateral blowing, arrow wing and shock wave are in progress. Also flow visualization of the jet wake for the understanding of the vortex structure to approach the mechanism is in progress. Those efforts are devoted to the understanding of the flow mechanism of lateral blowing. The detailed results will be presented on the Symposium.

References

- [1] K.KARASHIMA; Improvement of Aerodynamic Characteristics of a wing with low aspect ratios by trailing edge blowing, The 28th Fluid Dynamics Conferences, 1996(In Japanese)
- [2] Chiang Shih and Zhong Ding; Trailing-Edge Jet Control of Leading-Edge Vortices of a Delta Wing, AIAA., 34, (1996), pp.1447-1457
- [3] John S.Hong, Zeki Z.Celik and Leonard Roberts; Effect of Leading-Edge Lateral Blowing on Delta Wing Aerodynamics, AIAA., 34, (1996), pp.2417-2478

ON REYNOLDS AND MACH NUMBER EFFECTS AT TWO-DIMENSIONAL WIND TUNNEL TESTING

Boško Rašuo*

Faculty of Mechanical Engineering, University of Belgrade,
27 Marta 80, Belgrade, Yugoslavia

Key Words: Aerodynamics, Aerodynamic Characteristics, Airfoil Sections

ABSTRACT

In this paper, experimental results of wind tunnel measurements for conventional, symmetrical airfoil NACA 0012 obtained from the trisonic wind tunnel of Aeronautical Institute VTI Zarkovo, Belgrade are presented. The measurements of lift coefficient and lift-curve slope are presented. The results were obtained from tests and integrations of surface static-pressure data over a model of the NACA 0012 airfoil section. Data for the NACA 0012 airfoil were obtained for a free-stream Mach number range of 0.25–0.8 and a chord Reynolds number range of 2×10^6 to 25×10^6 . The essential results of these measurements along with the results from other authors are presented and evaluated. The principal factors which influence the accuracy of two-dimensional wind tunnel test results are analyzed. The influences of Reynolds number, Mach number and wall interference with reference to solid and flow blockage (blockage of wake) as well as the influence of side-wall boundary layer control are analyzed.

1. INTRODUCTION

For the successful aerodynamic designing of a new modern aircraft it is necessary to know the accurate aerodynamic characteristics of the whole aircraft, as well as of its individual constituent parts. Since there is no adequate mathematical model of turbulent flows, we cannot solve completely the problem of aerodynamic designing by computer simulation and calculation. We still have to solve many problems related to aerodynamic designing by making tests in wind tunnels. However, wind tunnel simulation is connected with many problems which cause many distortions of flow conditions around the tested models, which finally results in inaccuracy of the measured aerodynamic values. There are many reasons for that, but it is quite understandable that even the best wind tunnels cannot provide conditions for the simulation of the flows around the model which would be identical to the flows in the free air. Therefore, the resolving of the problem related to the definition and elimination of the wind tunnel wall interference is a lasting task to be solved through experimental and theoretical research, either during the construction of new wind tunnels or during their exploitation.

A special group of problems are related to the simulation of flows around the airfoil, i.e. to the provision of two-dimensional flow conditions. It is an extremely complex task to create correct two-dimensional flow conditions in wind tunnels during aerodynamic testing. In the transonic range of speeds this conclusion has proved to be related to the wind tunnels of all types and dimensions. I would point

out the following principal factors which have an impact on the accuracy of the results and which contribute to the uncertainty of the measured values obtained in wind tunnels. First, this is the effect of the Reynolds number, the effect of the Mach number, the wind tunnel wall interference, i.e. the influence of solid and flow blockage (blockage of wake) and the influence of side-wall boundary layer (the problem of creating correct two-dimensional flow conditions).

The purpose of this paper is to point out the principal factors which contribute to the greatest extent to the inaccuracy and diversity of results of measuring aerodynamic values expressed through lift-curve slope of conventional symmetrical NACA 0012 airfoil. Accordingly, an analysis have been made of the available results of tests and theoretical studies made in the major international aeronautical research centers (up to Mach number $M=0.55$ and Reynolds number $MRe=10$), as well as of an extensive experimental and theoretical study made by the VTI-Aeronautical Institute and the Faculty of Mechanical Engineering of the University of Belgrade, with the aim to extend the existing scope of analysis concerning the Mach numbers effects to the transonic speed range (up to $M=0.8$), and the range of the Reynolds numbers effects even to $MRe=35$.

On the basis of the results of this study, an attempt has been made to give an answer to the question: What is the actual lift-curve slope of the conventional symmetrical NACA 0012 airfoil according to the Mach and Reynolds flow numbers?

2. FACILITY DESCRIPTION

The VTI-Aeronautical Institute trisonic blowdown wind tunnel has a transonic test section with two- and three-dimensional inserts [1]. The inserts have 60° inclined-hole porous walls with variable porosity adjustment capability. Mach number is nominally set using either the second throat or flexible nozzle contour, depending on whether the flow is to be subsonic or supersonic. Final Mach number trimming is done using a blowoff system (with ejector assist if required) in which air reenters the circuit in the wide-angle diffuser just before the exhaust stack. Fig. 1 shows a schematic of the circuit airline. Each of the four parallel walls of two-dimensional insert are 4.6 m long: side-walls are 1.5 m wide and the upper and lower wall are 0.38 m. Upper and lower wall consists of a pair of perforated plates with holes inclined 60° to the vertical. Variable porosity is achieved by sliding the backplate to throttle the hole opening, the range being 1.5–8%. Motion of the throttle plate is forward from full-open; i.e. cutoff is from the down-stream edge of

*Professor, Aeronautical Department

each hole. A hole size is of 12.8 mm, and the combined two-plate thickness 14 mm. A splitter plate 2 mm thick is integral with each hole in the main plate-splitters are not incorporated into the throttle plate. Fig. 2 shows the hole

geometry and "finger" region where the porosity is gradually developed on a wall. A reference static hole ("ref." in Fig. 2) located on one wall is used for control of nominal Mach number during a test run.

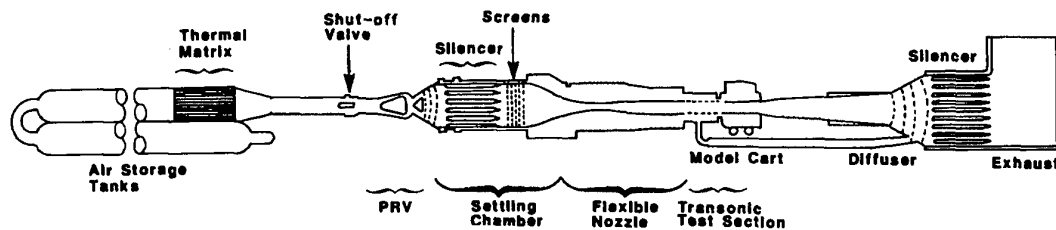


Figure 1: - Schematic of trisonic wind tunnel (PRV - Pressure Regulating Valve)

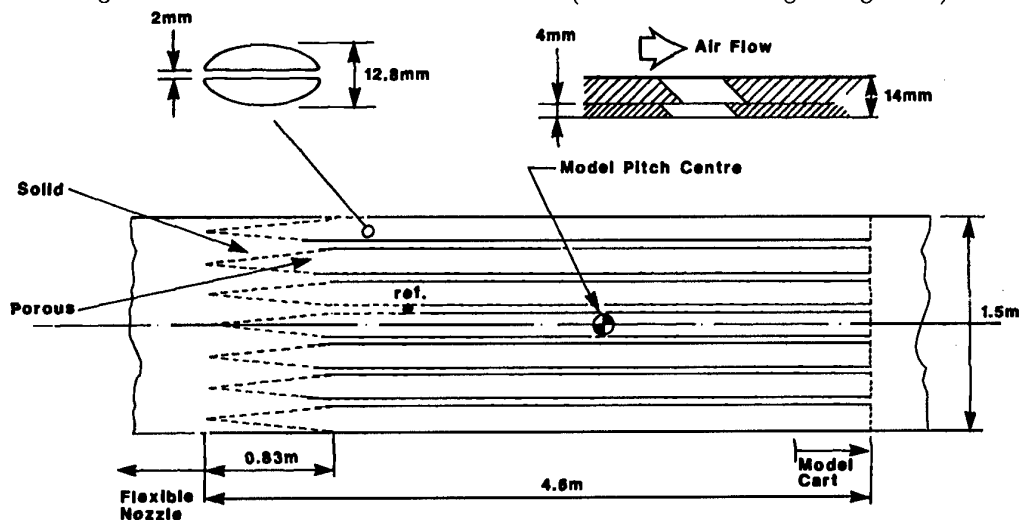


Figure 2: - Schematic of test-section walls

3. THE REYNOLDS NUMBER EFFECTS

Real nature, controversy and complexity of the problem we are faced with are evident in Fig. 3. There are so many solutions for one at the first sight simple question of lift-curve slope for the simplest NACA 0012 airfoil. One of the first attempts to clarify and explain in detail this problem was made at the gathering of experts called "Wall Interference in Wind Tunnels" held in London in 1982 [2]. On that occasion the attention was drawn for the first time to an interesting problem of mutual interdependence of the Reynolds number effects on the test model and the Reynolds number effects on the facility, i.e. wind tunnel. The present dilemma about this interdependence can be also illustrated by posing the similar question. What is actually the lift-curve slope $a = dc_L/d\alpha$ of the conventional symmetrical NACA 0012 airfoil in the function of the Reynolds number? In order to give an answer to this question an analysis should be made of the available results of wind tunnel tests which are published in international literature about such a subtle premature as lift-curve slope of airfoil [3].

First, in order to exclude from the analysis the effect of the Mach number, the range of subsonic flow (up to March number 0.55) has been analyzed at small angles of attack only, because of which the possibility of creating and separating the flows and shock waves have been eliminated. Then the Mach number effects have been included in the analysis. In both cases the effect of the Reynolds numbers to the mod-

els and wind tunnels has been also analyzed.

The results of this analysis are presented in Fig. 3 for NACA 0012 airfoil. They are grouped according to 21 sources of quotation. Many of these results have been achieved by the outstanding and widely known international aerodynamic institutions. For example, an analysis has been made of some old wind tunnel low speed tests made by NACA Institute (symbols 2-4), contemporary results of the NASA (1,5 and 6), the results achieved in the very good industrial facilities (10-12), detailed studies of the NPL and RAE (13-15), the results achieved by AGARD working group 04 DATA BASE (17), the results of ONERA (16-19), of the VTI and the Faculty of Mechanical Engineering (21), etc.

According to this illustration there is a great diversity in the achieved results, as a consequence of the strong influence of the Reynolds numbers effects on the test models and wind tunnels, of inadequate conditions of two-dimensional flows in the test section and the wall interference in the test section of wind tunnel. Wishing to complete this study, the analysis has been extended to the transonic speed range and it has incorporated new tests made by the VTI as well as the calculation of wall corrections made at the Faculty of Mechanical Engineering [4,5].

Experimental tests have been made in blowdown trisonic wind tunnel T-38 with transonic two-dimensional working section of dimensions 0.38×1.5 m with changeable perforation of walls from 1.5 to 8% (see Figures 1 and 2). Aerodynamic coefficients have been calculated by measuring the

distribution of the static pressure in 80 equally distributed tested points along the upper and lower side of NACA 0012 model with a chord of 0.254 m. For this measuring, the complete most modern equipment for aerodynamic measur-

ing has been used. In Ref. 4 the selected results of the measurement of the distribution of the static pressure along the upper side and lower side of the airfoil at angle of attack of 2.0° at Mach number of 0.8 have been presented.

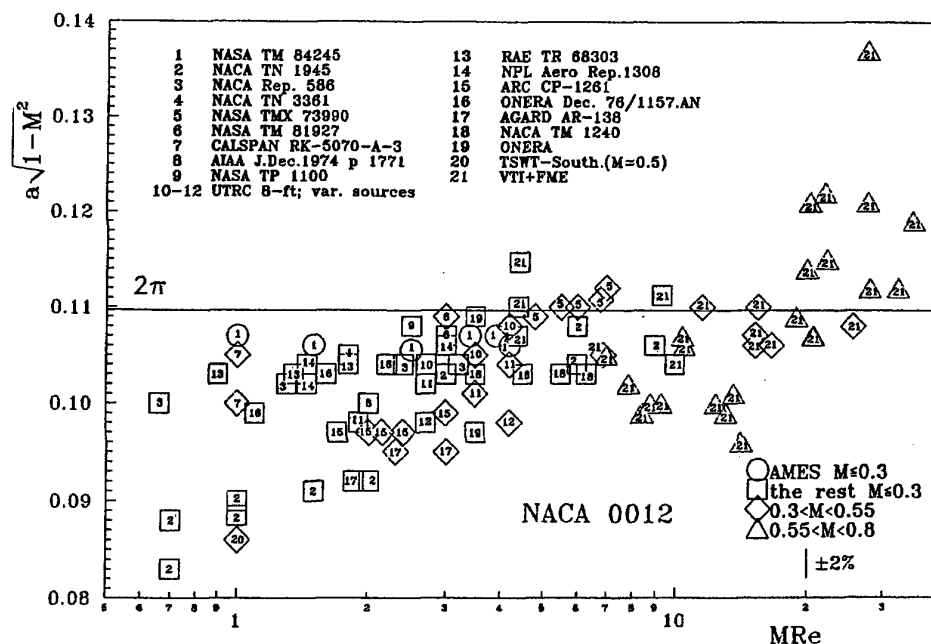


Figure 3: - Illustration of the collected results of the tests of lift-curve slope in the function of the Reynolds number

This additional experimental study has included the Mach test number from 0.25 to 0.8 and the Reynolds model numbers from 2 to 35 MRe. It has corroborated the conclusions made at the beginning about the influences of the Reynolds number in the subsonic speed range and at the same time it has expended them to the transonic range, i.e. to the Mach number effects to the results of the wind tunnel tests.

4. THE MACH NUMBER EFFECTS

In the case of the simulation of transonic flow, the situation becomes even more complex when defining the aerodynamic flow parameters. The effects of solid and flow blockage are even more evident, the side-wall boundary layer becomes thicker, the areas of separated flow and shock waves are created, which cannot be eliminated even by the full presence of the ventilated transonic walls. All this makes it even more difficult to define the exact aerodynamic parameters measured in wind tunnels. All controversy and uncertainty of the achieved results can be seen in Figures 3 and 4.

The Prandtl-Glauert theory which in the early stage of the development of aviation could satisfy for many years the needs of the experts in aerodynamics, in the last few decades could not remain the mainstay for the modern researches carried out all around the world. This dependency which does not contain in itself the Reynolds number effects either to the model or to the facility, can serve today only as a standard measure for classic thinking and assessments in this field of the experimental and mathematical aerodynamics. Such conclusion is applied on the classic experiments made in the first stage of the development of wind tunnels, like the classic experiment made by Göthert (Fig. 4).

The experiments and theoretical studies carried out recently by Murman, Kacperzynski, Chan, Jones and Cather-

all and the latest tests made in NASA, Canada, by the VTI and the Faculty of Mechanical Engineering illustrate an exceptionally great interdependence of the Mach and Reynolds number effects, side-wall suction and the influence of the wind tunnel walls on test results in transonic wind tunnels. These conclusions are completely evident in the results of the lift-curve slopes tests made by the VTI, as well as in the corresponding results achieved in the world and presented in Figures 3 and 4 [3].

5. WALL TUNNEL INTERFERENCE

In all analyses of tests results achieved in wind tunnels, the question of wall tunnel interference has been always raised. It has been manifested that, irrespective of the increased dimensions of the test section, i.e. of the Reynolds number effects on the wind tunnel, the effects of solid and flow blockage, i.e. the wind tunnel wall interference cannot be eliminated. If we look at the results of the tests carried made by the VTI, with high Reynolds numbers and different Mach numbers which are presented in Fig. 4, we can establish that these results, if not corrected, are completely useless from the point of view of an engineer. Only when the wall tunnel influence is calculated, for example by the methods presented in the papers, these test results could be accepted as real results which are achieved in the world today and which could be expected in the conditions of free air flow.

During all tests made by the VTI, the calculation of the perforated wall interference of transonic T-38 wind tunnel has been made by the Fourier's method used to solve the Dirichlet's problem in the rectangle of the wind tunnel test section [4,5].

In order to create correct two dimensional flow conditions and uniform spanwise loading of the airfoil model, it

is necessary to apply side-wall suction, i.e. the control over the boundary layer along the side walls of the wind tunnel. In the case that the control of boundary layer along the side walls is not ensured, this will certainly result in a loss of lift (and difference in drag) caused by the two basic effects of the complex flow. First, the loss of lift is caused by the decreased speed near the wall (by the decreased circulation). This effect can be significantly diminished if the side-wall boundary layer is reduced to the value which is very small in comparison with the spanwise of the model. Second, the influence of the airfoil pressure range will cause nonuniform increase of boundary layer along the side walls which will result in the creation of some three-dimensional effects in the flow around the airfoil [6].

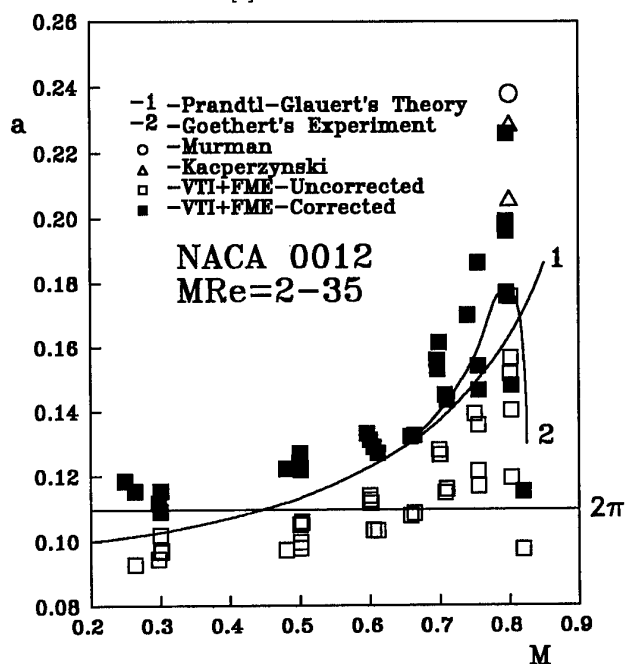


Figure 4: - Results of the test of the dependence of the lift-curve slope from Mach number

The importance of the correct definition of the quantity of the removed air is evident from the ONERA tests presented in Fig. 3 for its results given under point 19. The lower point is the case with inadequate suction and the upper point with right quantity of the removed air. Most frequently the removed quantity of air is expressed through the ratio of normal component of flow velocity through the wall, to the velocity of undisturbed flow (far upstream from the model) V_n/V_∞ . In all tests made by the VTI which are presented in Figures 3-5, the velocity ratio has been within the limits $V_n/V_\infty = 0.0050 - 0.0054$.

6. CONCLUSION

This rather pessimistic picture which one could get on the basis of the presented results can be partially balanced by the new development of corrections of walls and calculation methods which are published and used in the world today, and which, when applied in practice, should increase the confidence in the results of wind tunnel tests. In this context, it is more precise to take the definition of the cor-

rection of walls as "adaptation of walls" which shall incorporate all mentioned factors which have an impact on the quality and accuracy of the flow area of the wind tunnel test section and thereby contribute to the increased accuracy of the measured aerodynamic values. The results achieved in this way (see Fig. 5) could satisfy the users of "accurate" results of two-dimensional aerodynamic tests during the design and fundamental research or the testing of validity of the numerical methods of calculation.

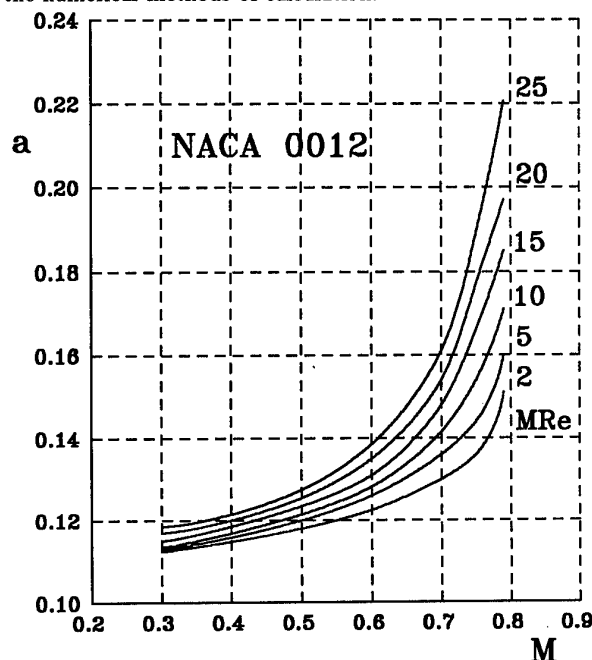


Figure 5: - Dependence of the lift-curve slope from Mach number

REFERENCES

- [1] G.M. Elfstrom, B. Medved & W.J. Rainbird, "Wave Cancellation Properties of a Splitter-Plate Porous Wall Configuration", J. of Aircraft, Vol. 26, No. 10, pp. 920-924, 1989.
- [2] McCroskey, Round Table Discussion on "Wall Interference in Wind Tunnels", AGARD Conference Proceedings No. 335, United Kingdom, pp. RTD-1-10, 19-20 May 1982.
- [3] B. Rašuo, "Experimental and Theoretical Study on Accuracy of Two-dimensional Wind Tunnel Test Results", International Aerospace Congress 1997, University of New South Wales, Sydney, pp. 611-616, 24-27 Feb. 1997.
- [4] B. Rašuo, "A Method for Determining Wall-Interference Corrections in Transonic Wind Tunnels from Measurements of Static Pressure at the Walls", JSASS 12th International Sessions in 36th Aircraft Symposium, Yokosuka, Japan, pp. 627-630, Oct. 12-14, 1998.
- [5] B. Rašuo, "Two-dimensional Wall Interference in Transonic Wind Tunnels", ZAMM, Vol. 77, Akademie Verlag, Potsdam, pp. 275-277, 1997.
- [6] R. Barnwell, "Effect of Sidewall Suction on Flow in Two-dimensional Wind Tunnels", AIAA Journal, Vol. 31, No. 1, pp. 36-41, January 1993.

Suppression of Supersonic Jet Noise by Free Rotating Vane-Type Tab

Mohammed K. IBRAHIM* and Yoshiaki NAKAMURA**

Department of Aerospace Engineering, Nagoya University, Nagoya, 464-8603, Japan

Key Words: Aeroacoustics, Supersonic Jet, Noise Suppression, Tab

ABSTRACT

Flow field and acoustic field measurements have been carried out for supersonic jets perturbed by free-to-rotate vane-type tabs. Four "vane-type tabs" were placed in the nozzle exit plane at diametrically opposite locations. Tangential aerodynamic forces on the vane-tabs rotate the vanes freely. The flow field data were obtained by Pitot probe surveys under automated computer control. The data showed that the center line velocity of a perturbed jet decays faster than the baseline jet. The free rotating vane-tabs alter the shock/expansion structure dramatically. Acoustic measurements showed that the overall sound pressure level, OASPL, was significantly reduced up to 12 dB and screech tones were also suppressed compared with the baseline jet for different values of pressure ratio. The tabs produce streamwise vortices, which have a profound impact on the spreading of the jet in a downstream region. The effects of varying the vane-tab angle from the jet axis and the distance of immersion into the jet on both acoustic and flow fields for both rotating and stationary vanes have been studied.

1. INTRODUCTION

It has been known for a long time that a tab, or a small protrusion in the flow at the exit plane of the nozzle can eliminate screech noise from supersonic jet¹. A screech is a loud tone emitted by a supersonic jet when operated at off-design nozzle pressure ratios. Recently the effect of tabs on suppressing the noise gained considerable attention^{2,3}. The jet spreading rate can be increased and noise can be reduced by using the tabs. In the current investigation the effects of vane-type tabs at the jet exit plane on radiated sound are studied experimentally. The tabs change the vortex formation, the large-scale turbulence structure, and the shock structures in supersonic jets. These effects are examined in this paper for free-to-rotate vane-type tabs to reduce the levels of shock-related noise and turbulent mixing noise. In addition, comparison with stationary vanes will be also presented.

2. EXPERIMENTAL FACILITY

All experiments were carried out in an open jet facility at the Fluid Dynamic Laboratory, Department of Aerospace Engineering, Nagoya University. Figure 1 shows a schematic

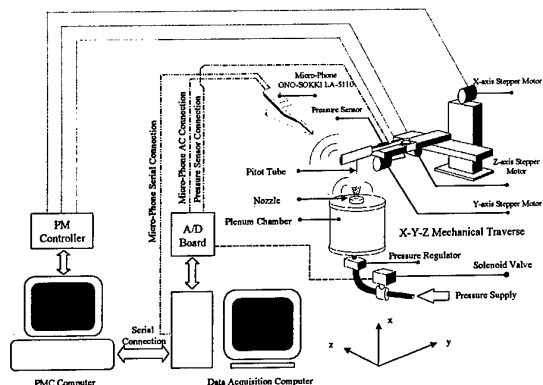


Fig. 1 Schematic diagram of experimental setup

diagram of experimental setup. A nozzle is attached to a cylindrical plenum chamber with a diameter of 200 mm and a length of 400 mm. A pressure regulator is used in order to control the pressure in the plenum chamber. For automatic measurements a XYZ mechanical traverse with three-stepping motors and a solenoid valve in the pressure line are used and controlled by PC. Pressure was supplied from a 12 m³ tank kept at a pressure of 12 kg/cm² and connected to the plenum chamber.

The sound level measuring system with a 0.5-inch condenser microphone (ONO SOKKI LA-5110) with a maximum frequency of 20 kHz and a maximum SPL of 130 dB is employed. The microphone was fixed at a distance of 100D, where D is the diameter of nozzle exit, and 30° from the jet axis. Two pressure sensors with a maximum of 800 Hz

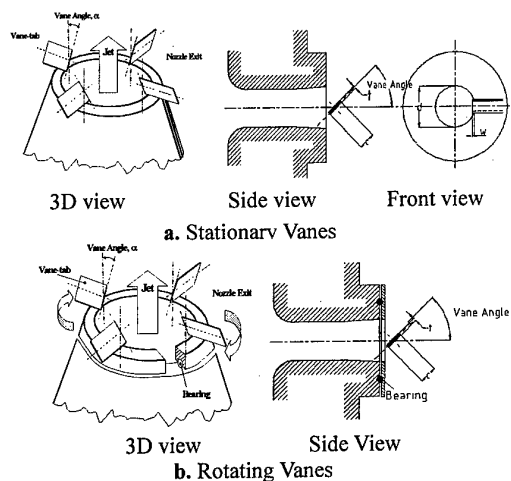


Fig. 2 Schematic of vane type-tab

sampling frequency and a pressure limit of 5 kg/cm² are employed for pressure measurements. Both the pressure sensor and the sound meter were connected to an AD board (ADM 682PCI) with a sampling time of up to 8 μsec. During acoustic measurements the background noise was kept as low

* Graduate Student, Dept. of Aerospace Eng., Nagoya University

** Professor, Dept. of Aerospace Eng., Nagoya University

as 37.5 dB in A weight SPL at the same location as the microphone.

2.1. TAB GEOMETRY

The tab configuration is shown schematically in Fig. 2 for both stationary and rotating modes. The thickness to chord ratio, t/c of the vane is 0.33. The protrusion height into the flow is denoted by w , and the nozzle exit diameter by d . The supersonic nozzle was fabricated of copper and had an exit diameter of 7.8 mm and a throat diameter of 7.5 mm with a design Mach number, M_D of 1.33. Single, two and four vane-type tabs with $w/d = 0.064$ and 0.128 were studied.

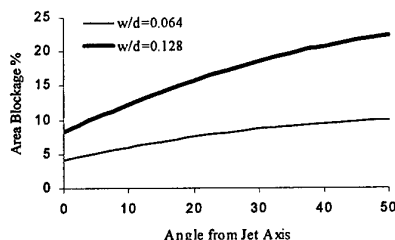


Fig. 3 Area blockage of four vane-type tabs

Figure 3 shows the geometric area blockage due to four tabs for different vane-type tab angles from the jet axis. It should be mentioned here that the geometric area blockage (% area blockage = $(A_{no-tab} - A_{tab})/A_{no-tab} \times 100$) does not necessarily follow the flow blockage² (% flow blockage = $(m_{ideal} - m_{measured})/m_{ideal} \times 100$; $m_{ideal} = \rho_e A_e U_e$). The thrust mainly depends on flow blockage.

4. RESULTS

For supersonic jet, the notation M_j is used to denote the fully expanded Mach number. It is uniquely related to the pressure ratio through the following equation:

$$M_j = \left\{ \left[(P_{io} / P_a)^{\gamma-1/\gamma} - 1 \right] \frac{2}{\gamma-1} \right\}^{0.5}$$

where P_{io} is the chamber pressure and P_a is the ambient pressure. Most of the results are presented here for $P_{io}/P_a = 5$ which corresponds to $M_j = 1.71$.

4.1. JET SPREADING

The parameters, which affect the jet spreading, are the vane mode, rotating or stationary, the number of vanes, the protrusion height w/d and the vane angle from the jet axis. These parameters and their effects are discussed in the following.

Effects vane number: A large increase in the spreading of the jet under the influence of tabs is indicated in Figs. 4 and 5 for both rotating and stationary vanes, respectively with $w/d = 0.064$ and at a vane angle, α of 30° . The measured pressure in a supersonic flow region represents the stagnation pressure P_{t2} downstream of the standing bow shock produced by the Pitot probe itself. In the downstream subsonic flow regions, of course, the measured pressure represents the local stagnation pressure. The results are characterized by wavy

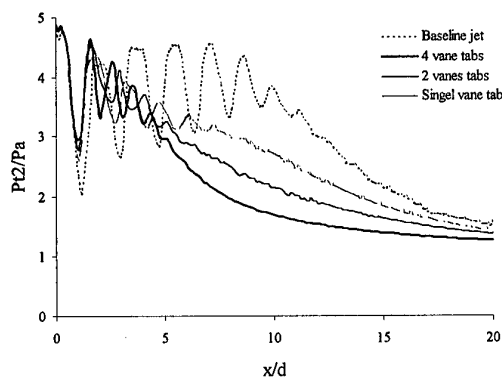


Fig. 4 Effects of vane number on center line stagnation pressure for rotating vanes with $w/d=0.064$ at $\alpha = 30^\circ$ and $M_j = 1.71$

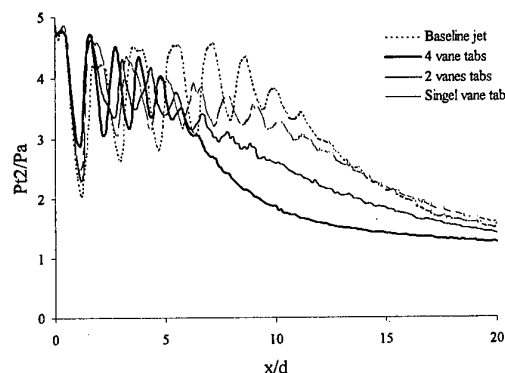
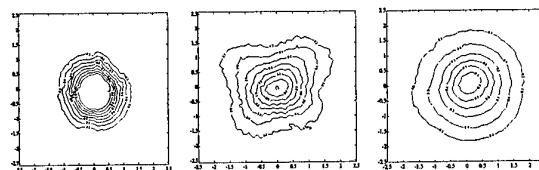


Fig. 5 Effects of vane number on center line stagnation pressure for stationary vanes with $w/d=0.064$ at $\alpha = 30^\circ$ and $M_j = 1.71$



a. Baseline jet b. Stationary vanes c. Rotating vanes
Fig. 6 Mach number contours at $x/d = 10$ for 4 vanes, where $w/d=0.064$, $\alpha = 30^\circ$ and $M_j = 1.71$

patterns due to the standing shock/expansion structure in the jet. The tabs alter and weaken the shock/expansion structure dramatically. The jet centerline stagnation pressure and thus the Mach number is found to decay much faster than that of the baseline jet, which generally implies increase in jet spreading. The effect is most pronounced with four tabs in both modes, rotating and stationary, and the least with a single tab. Rotating tabs are found to decay faster than the corresponding stationary tabs. The maximum observed rotational frequency for the case of four vanes was about 1000 rad/sec. Lower values were observed for two and single vane cases. The rotating vanes generate streamwise vortices which have a rotation frequency equal to that of the vanes unlike the "steady-state" vortices which are produced by

stationary vanes. It has been known that the interaction of these vortices with the jet has a profound impact on the spreading of the jet². The rotation of streamwise vortices around the jet axis was found to have more impact on jet spreading than "steady-state" vortices.

Mach number distributions on a cross-sectional plane of the jet were measured with a Pitot tube for $M_j = 1.71$. These data were taken far enough downstream so that the flow was subsonic everywhere and the static pressure had been relaxed to the ambient pressure⁴. Hence the Mach number could be calculated reliably from only the Pitot tube measurement. Figure 6 shows the Mach number contours at $x/d = 10$ for a baseline jet, four rotating vanes, and four stationary vanes with $w/d = 0.064$ and $\alpha = 30^\circ$. The enormous effects of tabbed cases on the jet spread can be readily appreciated.

Effects of protrusion height: Figures 7 and 8 are for both rotating and stationary vanes, respectively for different values of vane number and w/d ratio at $\alpha = 30^\circ$. As shown from the figures, increase in w/d ratio is found to increase the spread of jet, which is also associated with a decrease in nozzle thrust due to increase in area blockage. The effect is most pronounced with stationary two vanes case with $w/d = 0.128$.

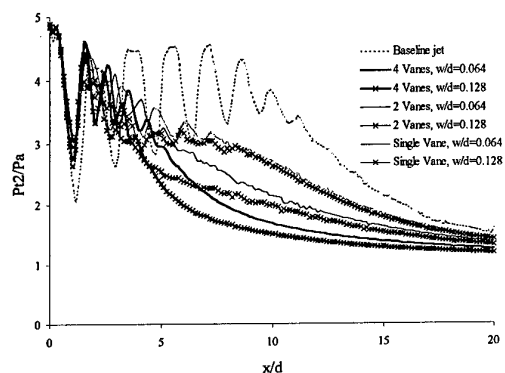


Fig. 7 Effects of w/d and number of vanes on centerline stagnation pressure for rotating vanes at $\alpha = 30^\circ$ and $M_j = 1.71$

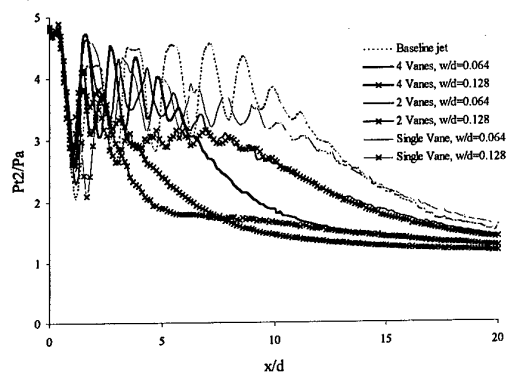
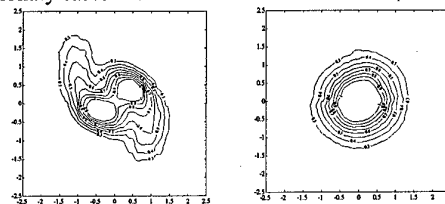


Fig. 8 Effects of w/d and number of vanes on centerline stagnation pressure for stationary vanes at $\alpha = 30^\circ$ and $M_j = 1.71$

However, the distributions along a centerline are not fully representative of actual jet spread. Two vane tabs essentially bifurcate the jet as shown in Fig. 9 which represents the Mach number contours at $x/d = 5$ for both rotating and stationary cases with two vane tabs.



a. Stationary vanes **b. Rotating Vanes**
Fig. 9 Mach contours at $x/d = 5$ for 2 vanes, $w/d = 0.128$, $\alpha = 30^\circ$ and $M_j = 1.71$

Effects of vane angle: Figures 10 and 11 show the effects of the vane angle on the centerline stagnation pressure for both rotating and stationary vanes for four vanes, respectively at $w/d = 0.064$. Increasing the vane angle is found to increase the spread of jet especially for the rotating case. However, increase in vane angle may result in thrust loss due to an increase in area blockage as shown in Fig. 3.

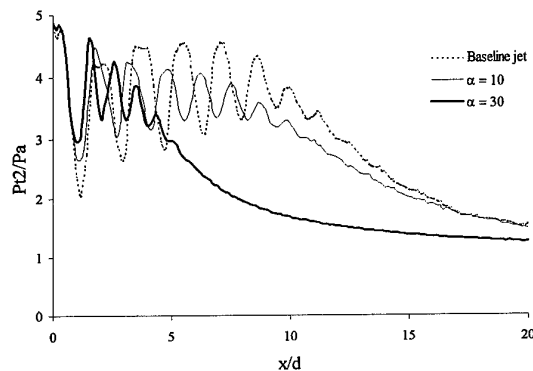


Fig. 10 Effects of vane angle, α , on centerline stagnation pressure for rotating vanes with $w/d = 0.064$ at $M_j = 1.71$

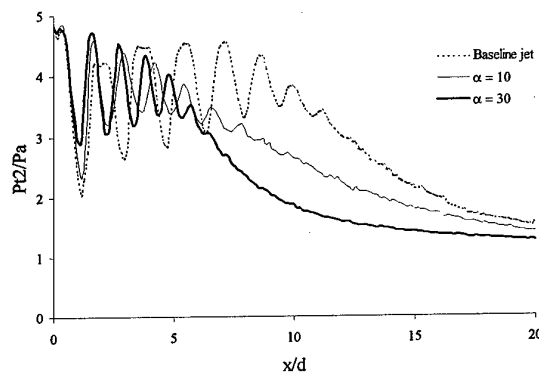


Fig. 11 Effects of vane angle, α , on centerline stagnation pressure for stationary vanes with $w/d = 0.064$ at $M_j = 1.71$

4.2. JET NOISE

The far field noise spectra for four vanes with $w/d=0.064$ and 0.128 are shown for both rotating and stationary modes in Figs. 12 and 13, respectively. Baseline jet spectra also presented in the figures and is clearly marked by a screech component. The fundamental component at about 14.5 kHz corresponds to a Strouhal number of about 0.27, which is in agreement with observations by previous researchers⁵. Thus the vane-type tabs completely eliminate the screech component. In addition the screech component, the broadband levels are also reduced over almost all frequency range.

Figure 14 shows the variation of the overall sound pressure level, OASPL, for both rotating and stationary modes with $w/d = 0.064$ and 0.128 . The OASPL decrease

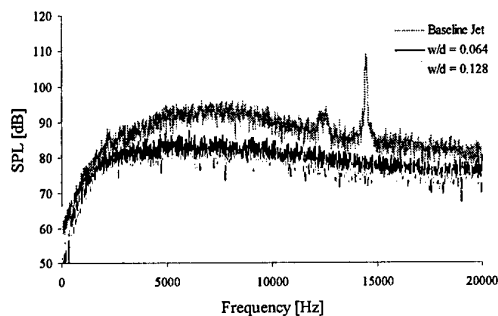


Fig. 12 SPL spectrum for rotating vanes with 4 vanes at $\alpha = 30^\circ$ and $M_j = 1.71$

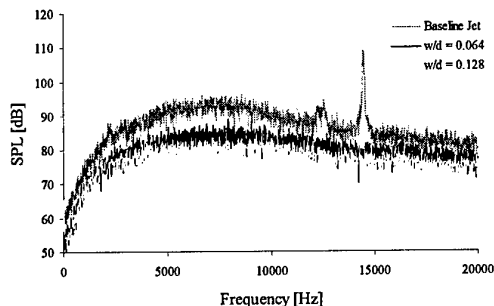


Fig. 13 SPL spectrum for stationary vanes with 4 vanes at $\alpha = 30^\circ$, and $M_j = 1.71$

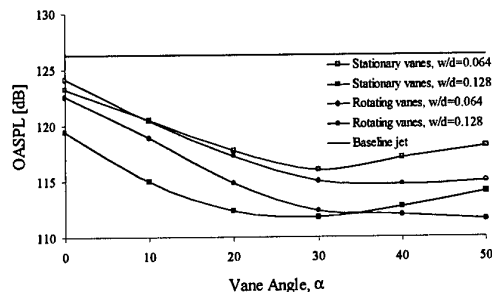


Fig. 14 OASPL for 4 vanes at $\alpha=30^\circ$ and $M_j=1.71$

approximately linearly until $\alpha = 30^\circ$ and then asymptotes or increases again. At $\alpha = 30^\circ$ a maximum reduction in noise of about 10 dB is observed for stationary vanes with $w/d = 0.064$, while a maximum reduction of about 13 dB is observed for the stationary case with $w/d = 0.128$. Regarding the effect of rotation on the OASPL the reduction is about 12 dB for $w/d = 0.064$. This reduction is about 2 dB compared with the similar stationary case of $w/d = 0.064$, whereas it is the same for $w/d=0.128$.

5. CONCLUSION

A vortex generator configuration, referred to as a vane-type tab in two different modes, rotating and stationary, has been found to be quite effective in influencing jet evolution and mixing.

- The centerline stagnation pressure and hence the Mach number for rotating vanes are found to decay faster than the stationary vanes for the tested number of vanes, which generally indicates of increased jet spreading.
- Two stationary vanes with $w/d = 0.128$ bifurcate a jet. This jet bifurcation does not occur for the rotating case.
- A reduction of about 12 dB is observed for four rotating vanes with $w/d = 0.064$ and a vane angle of 30° .
- Further investigation on the effect of the vane-type tabs on thrust penalty is required

6. REFERENCES

1. A. Powell, "On the mechanism of choked jet noise," Proc. Phys. Soc. B 66, 1039, 1953.
2. K.B.M.Q. ZAMAN, "Spreading characteristics of compressible jets from nozzles of various geometries," J. Fluid Mech., vol. 383, 1999, pp 197-228.
3. K. K. Ahuja and W. H. Brown, "Shear flow control by mechanical tabs," AIAA Paper No. 89-0994, 1989.
4. M. Samimy, K. B. M. Q. Zaman and M. F. Reeder, "Effect of tabs at the nozzle lip on the flow and noise field of an axisymmetric jet," AIAA J. 31, pp 609-619, 1993
5. T. D. Norum and J. M. Seiner, "Location and propagation of shock associated noise from supersonic jets," AIAA Paper No. 80-0983, 1980.

Adaptive and Robust Control of Wing Flutter

Takanori DEGAKI* and Shinji SUZUKI†

The University of Tokyo, 7-3-1 Hongo, Bunkyo-ku, Tokyo 113-8656, Japan

Key Words: Flutter, Limit Cycle Oscillation, Adaptive Control, Sliding Mode Control

Abstract

The purpose of this study is to compare the control performance between the adaptive controller and the robust controller (sliding mode controller) for wing flutter suppression. Two-dimensional wing section has plunge and pitch degrees of freedom. Control surfaces are both trailing and leading edges. Linear stiffness for plunge motion and nonlinear stiffness for pitch motion are considered. The steady and quasi-steady aerodynamic theories are employed to calculate the aerodynamic forces. The difference in the aerodynamic theory is used to model aerodynamic uncertainties. Each controller successfully suppresses the wing flutter and shows almost the same control performance, whereas the wing shows limit cycle oscillation without the controller.

1. Introduction

The modern aircraft is emphasized to reduce its weight and maximize the efficiency. The weight reduction, however, leads to the insufficiency of the wing stiffness. One possibility to compensate the insufficiency and prevent from aeroelastic instability is active control technologies.¹⁾

Most of the active control technologies are assured that the wing structure and the aerodynamics are

governed by linear theories and parameter values in aeroelastic equations are completely known. In reality, a wing has structural nonlinearity²⁾ and aerodynamic coefficients involve some uncertainties.

We applied two control techniques for the flutter suppression and compared the performances of those controllers. One is the adaptive controller³⁾; the other is the sliding mode controller⁴⁾. Each controller is applicable to the aeroelastic system that has the structural nonlinearity and the parameter uncertainties.

First, we show the root loci of the linear aeroelastic system as the velocity increases. In the framework of the linear theory, the wing motion grows exponentially with time beyond a critical velocity. Second, we show the limit cycle oscillation due to the structural nonlinearity. Third, the adaptive controller is designed, in which the structural nonlinearity and the unknown aerodynamic coefficients about the pitch axis are considered. Forth, the sliding mode controller is designed on the same condition that the adaptive controller above is designed. Finally, we compare the control performances between the two controllers.

2. Equations of motion

The two-dimensional wing section is shown in Fig.1.

* Graduate student, Department of Aeronautics and Astronautics

† Professor, Department of Aeronautics and Astronautics

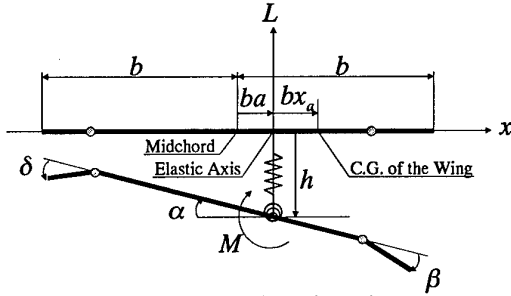


Fig.1 Two-dimensional wing section.

The governing equations of the system is

$$\begin{bmatrix} m & mx_a b \\ mx_a b & I_a \end{bmatrix} \begin{Bmatrix} \ddot{h} \\ \ddot{\alpha} \end{Bmatrix} + \begin{bmatrix} c_h & 0 \\ 0 & c_a \end{bmatrix} \begin{Bmatrix} \dot{h} \\ \dot{\alpha} \end{Bmatrix} + \begin{bmatrix} k_h & 0 \\ 0 & k_a(\alpha) \end{bmatrix} \begin{Bmatrix} h \\ \alpha \end{Bmatrix} = \begin{Bmatrix} -L \\ M \end{Bmatrix} \quad (1)$$

where $k_a(\alpha)$ is the pitching stiffness depends on the pitch angle. That is obtained by fitting the measured displacement-moment data.²⁾ The forth-order polynomial approximation is

$$k_a(\alpha) = 2.82(1 - 22.1\alpha + 1315.5\alpha^2 - 8580\alpha^3 + 17289.7\alpha^4) \quad (2)$$

The lift and moment are calculated using the quasi-steady wing theory as follows:

$$L = \rho U^2 b C_{l\alpha} \left[\alpha + \dot{h}/U + (0.5 - \alpha) \dot{\alpha}/U \right] + \rho U^2 b C_{l\beta} \beta + \rho U^2 b C_{l\delta} \delta \quad (3)$$

$$M = \rho U^2 b^2 C_{m\alpha} \left[\alpha + \dot{h}/U + (0.5 - \alpha) \dot{\alpha}/U \right] + \rho U^2 b^2 C_{m\beta} \beta + \rho U^2 b^2 C_{m\delta} \delta \quad (4)$$

Substituting Eqs. (3-4) into Eq. (1), equations of motion of the wing section are obtained as follows:

$$M\ddot{q} + C\dot{q} + K(q)q = Du$$

$$q = \begin{bmatrix} h & \alpha \end{bmatrix}^T$$

$$u = \begin{bmatrix} \beta & \delta \end{bmatrix}^T$$

$$M = \begin{bmatrix} m & mx_a b \\ mx_a b & I_a \end{bmatrix}$$

$$C = \begin{bmatrix} c_h + \rho U b C_{l\alpha} & \rho U b^2 (0.5 - \alpha) C_{l\alpha} \\ -\rho U b^2 C_{m\alpha} & c_a - \rho U b^3 (0.5 - \alpha) C_{m\alpha} \end{bmatrix}$$

$$K(q) = \begin{bmatrix} k_h & \rho U^2 b C_{l\alpha} \\ 0 & k_a(\alpha) - \rho U^2 b^2 C_{m\alpha} \end{bmatrix}$$

$$D = \begin{bmatrix} -\rho U^2 b C_{l\beta} & -\rho U^2 b C_{l\delta} \\ \rho U^2 b^2 C_{m\beta} & \rho U^2 b^2 C_{m\delta} \end{bmatrix} \quad (5)$$

The wing section properties and the aerodynamic coefficients used in this aeroelastic system are as

follows: $a = -0.6$, $b = 0.135$ m, $C_{l\alpha} = 6.28$, $C_{l\beta} = 2.487$, $C_{l\delta} = -0.087$, $C_{m\alpha} = -0.628$, $C_{m\beta} = -0.334$, $C_{m\delta} = -0.146$, $c_h = 27.43$ Ns/m, $c_a = 0.036$ Ns, $I_a = 0.065$ kgm², $k_h = 2844.4$ N/m, $m = 12.387$ kg, $x_a = 0.247$, and $\rho = 1.225$ kg/m³.

3. Stability analysis

We considered linearized equations of motion to see whether the aeroelastic system is stable or unstable. The linearized equations mean that $k_a(\alpha)$ in Eq. (2) is independent from the pitch angle, $k_a(\alpha) = 2.82$. The eigenvalues of the linearized aeroelastic system show a characteristic behavior as the velocity increases as in Fig. 2.

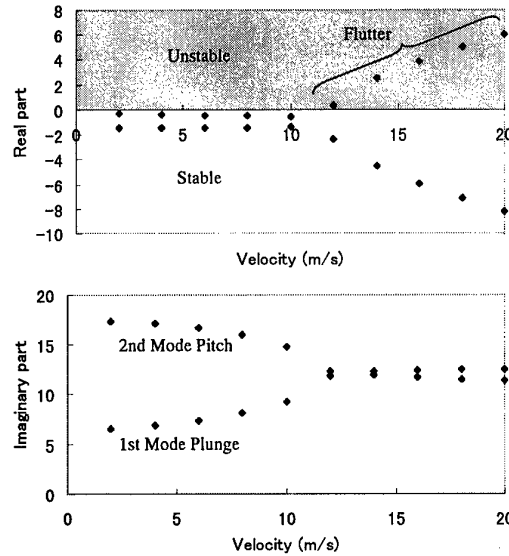


Fig. 2 Root loci of uncontrolled wing as velocity is varied from 2 m/s to 20 m/s with 2 m/s intervals.

The real parts of the two modes separate each other and one mode becomes unstable above a velocity, which is called flutter velocity. On the other hand, the imaginary parts of the two modes come close and coincide. Above the flutter velocity, the wing motion grows exponentially with time as far as the linearized equations of motion are considered. The wing, however, shows a limit cycle oscillation above the flutter velocity, because the structure has the nonlinearity about the pitch moment as of Eq. (2). A limit cycle oscillation of

the plunge displacement in the flow velocity of 20 m/s is in Fig. 3. This oscillation is suppressed using following two controllers respectively.

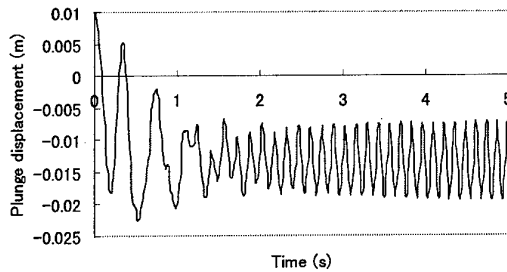


Fig. 3 Limit cycle oscillation of uncontrolled wing for the initial condition of $h=0.01$ m and $\alpha=0$ rad. The flow velocity is 20 m/s.

4. Adaptive control

The adaptive control³⁾ is efficient at a system that has unknown parameters and nonlinearity. In this study, we consider the aerodynamic coefficients about pitch, $C_{l\alpha}$ and $C_{m\alpha}$, as unknown parameters.

The adaptive control is based on Lyapunov stability theory. We select the positive definite function

$$V = \frac{1}{2}(s^T Ms + \Delta a^T \Gamma^{-1} \Delta a) \quad (6)$$

as a candidate of a lyapunov function. When a control law

$$\begin{aligned} u &= D^{-1}(Y_1 \hat{a} + Y_0 - Ks) \\ \dot{\hat{a}} &= -\Gamma Y_1^T s \\ s &= \dot{q} + \Lambda q \end{aligned} \quad (7)$$

$$\begin{aligned} Y_0 &= \left(- \begin{bmatrix} m & mx_a b \\ mx_a b & I_a \end{bmatrix} \Lambda + \begin{bmatrix} c_h & 0 \\ 0 & c_a \end{bmatrix} \right) \dot{x} + \begin{bmatrix} k_h & 0 \\ 0 & k_a(\alpha) \end{bmatrix} x \\ Y_1 &= \begin{bmatrix} \rho U^2 b \alpha + \rho U b \dot{h} + \rho U b^2 (0.5 - a_h) \dot{\alpha} & 0 \\ 0 & -\rho U^2 b^2 \alpha - \rho U b^2 \dot{h} - \rho U b^3 (0.5 - a_h) \dot{\alpha} \end{bmatrix} \end{aligned}$$

is applied, the derivative of the Lyapunov function is

$$\dot{V} = -s^T K s \leq 0. \quad (8)$$

Equation (6) and Eq. (8) indicate that s converges to zero as time approaches infinity. Using the adaptive control law of Eqs. (7), the aeroelastic system is stabilized as the solid line in Fig. 4.

Although all parameters and initial conditions are same as those are in Fig. 3, the wing no longer shows limit cycle oscillation, and smoothly converged to zero within 1 s. For considering the robustness against uncertainty of the aerodynamic model, we design another adaptive controller, in which the steady wing theory

$$L = \rho U^2 b C_{l\alpha} \alpha + \rho U^2 b C_{l\beta} \beta + \rho U^2 b C_{l\delta} \delta, \quad (9)$$

$$M = \rho U^2 b^2 C_{m\alpha} \alpha + \rho U^2 b^2 C_{m\beta} \beta + \rho U^2 b^2 C_{m\delta} \delta \quad (10)$$

is employed for controller design. On the other hand, the quasi-steady wing theory of Eqs. (3) and (4) is employed for the simulation. Whereas we employed the different aerodynamic models between the controller design and the simulation, the controller keeps its good performance as shown in the dashed line of Fig. 4. That indicates the adaptive controller has robustness against the aerodynamic uncertainties.

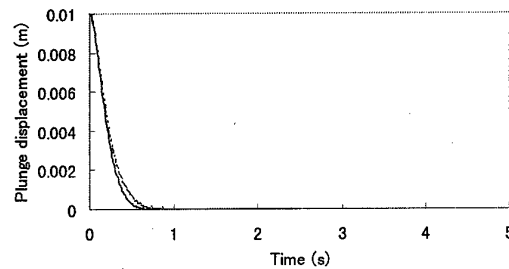


Fig. 4 Wing plunge responses with adaptive controllers. The quasi-steady wing theory is employed for controller design (solid line); the steady wing theory is employed for controller design (dashed line).

5. Sliding mode control

The sliding mode control⁴⁾ is one of variable structure controls. Unlike H^∞ control or μ synthesis, the variable structure controllers are available for even nonlinear systems. Moreover the sliding mode controller accepts model uncertainties and parameter changes if the system satisfy the matching condition.

The state space form of Eq. (5) is

$$\begin{aligned} \dot{x} &= Ax + Bu + \Delta \\ x &= [q \quad \dot{q}] \end{aligned} \quad (11)$$

where Δ are model uncertainties that satisfy the matching condition, i.e., there exists $\tilde{\Delta}$ that satisfy

$$\Delta = B\tilde{\Delta}. \quad (12)$$

In this study, only the linear term of $k_\alpha(\alpha)$, $k_\alpha(\alpha) = 2.82$, is included in the matrix A and the other nonlinear terms are considered to be model uncertainties. The control inputs are determined as

$$\begin{aligned} u &= -(SB)^{-1}SAx - k\sigma/\|\sigma\|, \\ \sigma &= Sx \end{aligned} \quad (13)$$

The row vector S in Eq. (13) is determined to minimize the criterion

$$J = \int_{t_s}^{\infty} (x^T Q x) dt \quad (14)$$

where t_s is the time at which the states reach on the sliding surface and Q is a weighting matrix. The scalar k in Eq. (13) is determined to assure the reachability of the states to the sliding surface, i.e.,

$$k > \|\tilde{\Delta}\|. \quad (15)$$

The response of the aeroelastic system using the sliding mode control input of Eq. (13) is the solid line in Fig. 5.

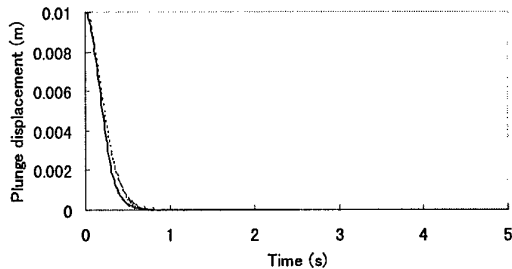


Fig. 5 Wing plunge responses with sliding mode controllers. The quasi-steady wing theory is employed for controller design (solid line); the steady wing theory is employed for controller design (dashed line).

We again consider the robustness evaluation of the sliding mode controller in the same way as that of the adaptive controller. The wing response, in which we use the steady wing theory of Eq. (3)-(4) for controller design and the quasi-steady wing theory of Eq. (9)-(10) for simulation, is shown in the dashed line in Fig. 5.

Even if there exists aerodynamic uncertainties, the controller has the ability to stabilize the motion within 1 s. The sliding mode controller is also robust against the aerodynamic uncertainties similar to the adaptive controller.

6. Conclusion

Based on the present flutter analysis and controller design, the following conclusions are obtained.

Both the adaptive controller and the sliding mode controller are effective for the control of wing flutter that has the structural nonlinearity and the aerodynamic uncertainty. Each controller is stabilized the flutter less than 1 s without limit cycle oscillation. Those two controllers show almost the same control performances under the condition of this study.

When we consider the more complicated flutter problem such as transonic flutter, we must take into account the uncertainties associated with transonic aerodynamics. In the future study, we will apply the sliding mode controller to the transonic flutter problem since it can deal with the uncertainties.

Reference

- 1) Thomas E. Noll, and Franklin E. Eastep, "Active Flexible Wing Program", *Journal of Aircraft*, Vol. 32, No. 1, 1995, p. 9
- 2) Jeonghwan Ko et al., "Stability and Control of a Structurally Nonlinear Aeroelastic Systems," *Journal of Guidance, Control, and Dynamics*, Vol. 21, No. 5, 1998, pp. 718-725.
- 3) Suguru Arimoto, "Dynamics and Control of Robotics," Asakura Shoten, 1991 (in Japanese).
- 4) Kenzo Nonami, and Hongqi Tian, "Sliding Mode Control," CORONA PUBLISHING CO., LTD., 1994 (in Japanese).

Parameter Identification of Spin-Stabilized Projectiles by Using Modified Newton-Raphson Minimization Technique

Zeal-Sain Kuo[†] and Hsiao-Yu Huang^{*}

Chung Cheng Institute of Technology
Tao-Yuan, Taiwan, 33509, R.O.C.
E-mail: zskuo@ccit.edu.tw

Key Words: Flight Dynamics, Stability and Control, Parameter Identification, Spin-Stabilized Projectiles, Modified Newton-Raphson, Maximum Likelihood Criterion, Extended Kalman Filter

ABSTRACT

A modified Newton-Raphson minimization technique for determining aerodynamic coefficients and stability derivatives of spin-stabilized projectiles with a six-degree-of-freedom nonlinear dynamical model was developed. The dynamical model for the projectiles was constructed having process noise in the system and the instrumentation noise in the system outputs. The state equations of the dynamical system were continuous types while the measurement data were discrete. A continuous-discrete type estimation model for the motion of the projectiles was constructed in this paper. The state variables of the system were estimated by the extended Kalman filter and the system parameters were identified by the modified Newton-Raphson technique based on the maximum likelihood criterion. Research results show that parts of the parameters can be identified under proper noise intensity. However, the accuracy of identification is strongly influenced by both process and measurement noise.

1. INTRODUCTION

Identifying the coefficients and derivatives of projectiles from measurement data remains difficult and time consuming, despite the considerable effort that has devoted to it over the year. There is no lack of methods to determine the coefficients of projectiles [1-2]. On the contrary, many methods have been developed, and under idealized conditions or linearization most have been successful [3-5]. Unfortunately, insufficient system mode excitation, instrumentation and measurement noise, and discrepancy of the actual projectiles from the model used for the projectile dynamics generally cause significant errors in the resulting parameter identification. Extracting the aerodynamic coefficients and stability derivatives of flying objects from flight test data has been an importance research field of modern aerodynamics for years. The research of non-linear dynamic characteristics of spin-stabilized projectiles is one of the sophisticated problems in this field. Lately, considering projectiles as a 3 DOF model, Chen [6-7] identified the drag coefficient curve by using measured velocity data from Doppler radar. As for the nonlinear dynamics characteristics of projectiles, identifying all aerodynamic coefficients and stability derivatives such as damping coefficient in roll, lift derivative, pitch moment derivative, etc., is still an area of interests. In this paper, a 6 DOF dynamic model of projectiles is considered. The state variables of the model are estimated by extended Kalman filter (EKF), and the parameters of the model are identified by mNR method based on ML criterion. Two typical projectiles, 20mm and 105mm, are investigated.

2. PROBLEM STATEMENT

Consider a ballistic spin-stabilized projectile with 6 degree-of-freedom (6 DOF). Using standard notations, the equations of motion in body axis can be described as [8-9]

$$\dot{u} = (-D \cos \beta \cos \alpha + C \sin \beta + L \sin \alpha) / m - g \sin \theta + rv - qw \quad (7)$$

$$\dot{v} = (-D \sin \beta - C \cos \beta) / m + pw - ru \quad (8)$$

$$\dot{w} = (-D \cos \beta \sin \alpha - L \cos \alpha) / m + g \cos \theta + qu - pv \quad (9)$$

$$\dot{p} = L_p / I_x \quad (10)$$

$$\dot{q} = (M - I_x pr) / I \quad (11)$$

$$\dot{r} = (N + I_x pq) / I \quad (12)$$

where $L = C_{L\alpha} Q \alpha$ = Lift, $D = (C_{D0} + C_{D2} \eta^2) Q$ = Drag, $C = C_{C\beta} Q \beta$ = Side force, $L_p = C_{lp} Q_1 p$ = Rolling moment, and the pitching and yawing moments are

$$M = C_{m\alpha} Q d \alpha + (C_{mq} + C_{m\dot{\alpha}}) Q_1 q + C_{mp\beta} Q_1 p \beta \quad (13)$$

$$N = C_{n\beta} Q d \beta + (C_{nr} + C_{n\dot{\beta}}) Q_1 r + C_{np\alpha} Q_1 p \alpha \quad (14)$$

The aerodynamic coefficients and stability derivatives are defined in conventional form as given in [10-11], and η is the total angle of attack, $\eta = \cos^{-1}(\cos \beta \cos \alpha)$, α is the angle of attack, β the sideslip angle, $Q = \rho V^2 / 2$ is the dynamical pressure, and $Q_1 \equiv Q S d^2 / V$ a lump parameter, S the reference area, $S = \frac{1}{2} \pi d^2$, and d is the diameter of the projectile. Define the Euler angles (ψ, θ, ϕ) and the axis transformation for angular motion

$$\dot{\theta} = q \quad (15)$$

$$\dot{\psi} = \frac{r}{\cos \theta} \quad (16)$$

and the velocity

$$\begin{bmatrix} \dot{X} \\ \dot{Y} \\ \dot{Z} \end{bmatrix}_I = \begin{bmatrix} \cos \theta \cos \Psi & -\sin \Psi & \sin \theta \cos \Psi \\ \cos \theta \sin \Psi & \cos \Psi & \sin \theta \sin \Psi \\ -\sin \theta & 0 & \cos \theta \end{bmatrix} \begin{bmatrix} u \\ v \\ w \end{bmatrix}_B \quad (17)$$

where $[\cdot]_I$ and $[\cdot]_B$ denote the velocity vector relative to inertia axis system and body axis system, respectively. Equations (1)-(11) describe a highly non-linear dynamical system of general motion for spin-stabilized projectiles. With initial states, aerodynamic coefficients and stability derivatives, The state equations can be written in the form

$$\dot{\mathbf{x}}(t) = \mathbf{f}[\mathbf{x}(t), \Theta; t], \quad \mathbf{x}(0) = \mathbf{x}_0 \quad (18)$$

where $\mathbf{x}(t)$ is the state vector, and Θ is the vector of unknown

[†] Associate Professor, Department of Mechanical Engineering.

^{*} Research Assistant, Department of Mechanical Engineering.

parameters including unknown initial conditions and aerodynamic parameters. The relations of state variables to measurements are listed as follows: the projectile's velocity

$$V = \sqrt{u^2 + v^2 + w^2}, \text{ angle of attack } \alpha = \tan^{-1}(w/u) \approx w/u,$$

$$\text{sideslip } \beta = \sin^{-1}(v/V) \approx v/V, \text{ range } R = \sqrt{X^2 + Y^2 + Z^2},$$

$$\text{elevation } E = \sin^{-1}(-Z/R), \text{ and Azimuth } A_z = \tan^{-1}(Y/X).$$

The measurements of the system output are corrupted by random disturbances. In this paper, the identification problem is the most general model with the presence of additive random process noise in the equations of motion and measurement noise in the system output. Read as

$$\dot{\underline{x}}(t) = f[\underline{x}(t), \underline{\Theta}; t] + \underline{w}(t) \quad (13)$$

$$\underline{y}(t) = g[\underline{x}(t), \underline{\Theta}; t] \quad (14)$$

$$\underline{z}(k) \equiv \underline{y}(k) + \underline{v}(k) = g[\underline{x}(k), \underline{\Theta}; k] + \underline{v}(k) \quad (15)$$

$\underline{w}(t)$ and $\underline{v}(t)$ are Gaussian random vector with uncorrelated zero-mean white noise, and their covariance (Cov.) are $\mathbf{Q}(t)$ and $\mathbf{R}_v(t)$, respectively. It is assumed that the structure of the model is known. The vector of unknown parameters in Eq. (13) is denoted by $\underline{\Theta}$. Thus, $\underline{\Theta}$ includes all unknown aerodynamic coefficients, stability derivatives, and initial states.

3. STATE ESTIMATION BY EXTENDED KALMAN FILTER

Now, for state estimation, since the system under investigation contains process and measurement noise, it is necessary to incorporate a suitable filter for this purpose. In general, the Kalman filter is the optimal filter for linear systems, but for nonlinear system, no optimal filters are practically realizable, except for some linearize or quasi-linearized cases. Therefore, the extended Kalman filter (EKF) is used for estimating the true states from the noisy measurements in nonlinear filtering. For the system model defined in Eqs. (13)-(15), the EKF algorithm can be described as follows:

Initial Conditions: The EKF is started with a priori state estimate $\hat{\underline{x}}(0|0)$ and covariance $\mathbf{P}(0|0)$. The initial conditions are assumed to be Gaussian, and uncorrelated to process and measurement noise.

Prediction Equations:

$$\hat{\underline{x}}(k|k-1) = \mathbf{A}(k-1)\hat{\underline{x}}(k-1|k-1) \\ \approx \hat{\underline{x}}(k-1|k-1) + \int_{k-1}^k f(\underline{x}, \underline{\Theta}; t) dt \quad (16)$$

$$\hat{\underline{z}}(k|k-1) = g[\hat{\underline{x}}(k|k-1), \underline{\Theta}; k] \quad (17)$$

$$\mathbf{P}(k|k-1) = \mathbf{A}(k-1)\mathbf{P}(k-1|k-1)\mathbf{A}^T(k-1) + \mathbf{R}_w(k-1) \quad (18)$$

where $\mathbf{A}(k-1) \equiv \exp(\mathbf{F}(k-1)\Delta t)$, with sampling time

$$\Delta t = t_k - t_{k-1}, \text{ and } \mathbf{F}(k-1) \equiv \left(\frac{\partial f}{\partial \underline{x}} \right)_{\underline{x}=\hat{\underline{x}}(k-1|k-1)}$$

Update Equations:

$$\hat{\underline{x}}(k|k) = \hat{\underline{x}}(k|k-1) + \mathbf{K}(k)\underline{e}(k) \quad (19)$$

$$\mathbf{K}(k) = \mathbf{P}(k|k-1)\mathbf{H}^T(k)[\mathbf{H}(k)\mathbf{P}(k|k-1)\mathbf{H}^T(k) + \mathbf{R}_v(k)]^{-1} \quad (20)$$

$$\mathbf{P}(k|k) = [\mathbf{I} - \mathbf{K}(k)\mathbf{H}(k)]\mathbf{P}(k|k-1) \\ = [\mathbf{I} - \mathbf{K}(k)\mathbf{H}(k)]\mathbf{P}(k|k-1)[\mathbf{I} - \mathbf{K}(k)\mathbf{H}(k)]^T \\ + \mathbf{K}(k)\mathbf{R}_v(k)\mathbf{K}^T(k) \quad (21)$$

where we have defined the residual $\underline{e}(k) \equiv \underline{z}(k) - \hat{\underline{z}}(k|k-1)$

and $\mathbf{H}(k) \equiv \left(\frac{\partial g}{\partial \underline{x}} \right)_{\underline{x}=\hat{\underline{x}}(k|k-1)}$. Note here that the state equations

of the dynamical system are continuous type while the measurement data are discrete. A continuous-discrete type of estimation models for the motion of the projectiles is now constructed by using EKF algorithm for state estimation.

4. PARAMETER IDENTIFICATION BY MODIFIED NEWTON-RAPHSON TECHNIQUE

By combining the ballistic model into a mNR iteration scheme based on ML criterion, the differential correction method for searching aerodynamic coefficients and stability derivatives is applied to determine the unknown parameters from measurements. The ML criterion is obtained by minimization of the negative log likelihood function

$$J = \sum_{k=1}^N \left[\underline{e}^T(k) \mathbf{B}^{-1}(k) \underline{e}(k) + \ln |\mathbf{B}(k)| \right] \quad (22)$$

where $\mathbf{B}(k)$ is the variance matrix of the residual defined by $\mathbf{B}(k) \equiv E[\underline{e}(k)\underline{e}^T(k)]$. To obtain a gradient solution that minimizes J , the following recursive relation is used:

$$\underline{\Theta}_{i+1} = \underline{\Theta}_i + \Delta \underline{\Theta} \quad (23)$$

where the subscript i is the index of the iteration. The mNR is an iterative method for finding a zero of non-linear functions, or in our case a zero of the gradient of the cost function, that is,

$\frac{\partial J}{\partial \underline{\Theta}} = 0$. Suppose $\frac{\partial J_i}{\partial \underline{\Theta}}$ is not equal to zero, but $\frac{\partial J_{i+1}}{\partial \underline{\Theta}}$ is closed to zero. Apply Taylor's series expansions about the i^{th} value of $\underline{\Theta}$.

$$\frac{\partial J_{i+1}}{\partial \underline{\Theta}} \approx \frac{\partial J(\underline{\Theta}_{i+1})}{\partial \underline{\Theta}} = \frac{\partial J(\underline{\Theta}_i + \Delta \underline{\Theta}_i)}{\partial \underline{\Theta}} \\ = \frac{\partial J(\underline{\Theta}_i)}{\partial \underline{\Theta}} + \frac{\partial^2 J(\underline{\Theta}_i)}{\partial \underline{\Theta}^2} \Delta \underline{\Theta}_i + H.O.T \quad (24)$$

Where $\partial^2 J / \partial \underline{\Theta}^2$ is the Hessian matrix of the cost function with respect to $\underline{\Theta}$ at the i^{th} iteration. If $\partial J_i / \partial \underline{\Theta}$ is sufficiently closed to zero, the change in $\underline{\Theta}$ on the $(i+1)$ iteration to make $\partial J_{i+1} / \partial \underline{\Theta}$ approximately zero is

$$\Delta \underline{\Theta}_i = -\mathbf{M}^{-1} \left(\frac{\partial J_i}{\partial \underline{\Theta}} \right) \quad (25)$$

where $\mathbf{M} \equiv \frac{\partial^2 J(\underline{\Theta}_i)}{\partial \underline{\Theta}^2} = \frac{\partial^2 J_i}{\partial \theta_j \partial \theta_l}$, namely, the information matrix. The first gradient of J with respect to θ_j is

$$\frac{\partial J}{\partial \theta_j} = \sum_{k=1}^N \left\{ 2 \underline{e}^T(k) \mathbf{B}^{-1}(k) \frac{\partial \underline{e}(k)}{\partial \theta_j} \right\} \quad (26)$$

and the second gradient is

$$\frac{\partial^2 J}{\partial \theta_j \partial \theta_l} = \sum_{k=1}^N \left\{ 2 \frac{\partial \underline{e}^T(k)}{\partial \theta_l} \mathbf{B}^{-1}(k) \frac{\partial \underline{e}(k)}{\partial \theta_j} + 2 \frac{\partial^2 \underline{e}^T(k)}{\partial \theta_j \partial \theta_l} \mathbf{B}^{-1}(k) \underline{e}(k) \right\} \quad (27)$$

The Newton-Raphson (NR) method has been shown to be very efficient in wide applications. However, it is complex because of the computation of the second gradient matrix. Fortunately, this complexity can be reduced significantly by neglecting the second term in Eq. (27) since the second-order term converges to zero faster than the first term. This reduction in iteration results in the method of modified Newton-Raphson or quasi-linearization. This greatly reduces the computational time, and the approximation improves as the solution is approached.

$$\frac{\partial^2 J}{\partial \theta_j \partial \theta_i} \approx \sum_{k=1}^N \left\{ 2 \frac{\partial e^T(k)}{\partial \theta_i} \mathbf{B}^{-1}(k) \frac{\partial e(k)}{\partial \theta_j} \right\} \quad (28)$$

Then,

$$\Delta \Theta_i = - \left\{ \sum_{k=1}^N \frac{\partial e^T(k)}{\partial \theta_i} \mathbf{B}^{-1}(k) \frac{\partial e(k)}{\partial \theta_j} \right\}^{-1} \left\{ \sum_{k=1}^N e^T(k) \mathbf{B}^{-1}(k) \frac{\partial e(k)}{\partial \theta_j} \right\} \quad (29)$$

It is noted that $e(k)$ and $\mathbf{B}(k)$ have been computed in extended Kalman filter. We need $\frac{\partial e(k)}{\partial \theta_j}$ to compute Eq. (29).

Differential $e(k)$ with respect to Θ , yields

$$\frac{\partial e(k)}{\partial \Theta} = \frac{\partial}{\partial \Theta} [\underline{z}(k) - \hat{\underline{z}}(k|k-1)] = -\mathbf{H}(k) \frac{\partial \underline{x}(k)}{\partial \Theta} \quad (30)$$

The second term in the right hand side is approximated by considering the variation of state variables with respect to a small increment $\delta \theta_j$ in each component of Θ , then

$$\frac{\partial \underline{x}(k)}{\partial \Theta} \approx \frac{\underline{x}_p(k) - \underline{x}(k)}{\delta \Theta} \quad (31)$$

where the perturbed state vector $\underline{x}_p(k)$ is obtained from the perturbed system equation.

5. NUMERICAL EXAMPLES

To evaluate the performance of the identification algorithm, two typical projectiles, 105 mm and 20 mm, are considered. The model of projectiles is highly nonlinear and the data included both process noise and measurement noise are generated through simulation. Numerical experiments were run with different initial conditions and different noise levels to investigate their effects on the parameter identification. The physical properties of the projectiles are given in Table 1 [11].

Table 1. Physical Property of the Projectiles

	Mass (kg)	Diameter (m)	Ix (kg-m ²)	Iy (kg-m ²)
105 mm	14.58	0.105	0.023	0.2264
20 mm	0.1014	0.02	6.154x10 ⁻⁶	3.728x10 ⁻⁵

For state estimation, extended Kalman filter (EKF) is used for the purpose of obtaining the nominal state variables from the noisy measurements. With initial muzzle speed 460 m/s, spin rate 1382 rad/s, and elevation angle 45 deg (0.7854 rad), Fig. 1 shows the convergence of the state variable estimated using the EKF, where the dotted line is the true state generated by pure numerical integration, dashed line the state corrupted by process noise, and solid line is the state estimated by EKF. Since there was not much qualitative difference in the time plots for the state variables, only one of the states is presented.

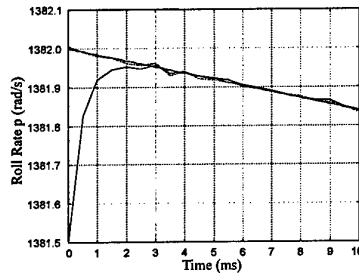


Fig. 1 Time History of Roll Rate p.

We proceed to the parameter identification problems. To keep computer usage to a minimum, no noise biases or initial conditions were determined for the projectile identification, thus

$$\Theta = [C_{D0}, C_{D2}, C_{L\alpha}, C_{lp}, C_{m\alpha}, (C_{mq} + C_{m\dot{\alpha}}), C_{mp\beta}]^T \quad (32)$$

Due to axial symmetry of the spin-stabilized projectiles, we have $C_{e\beta} = C_{L\alpha}$, $C_{n\beta} = C_{m\alpha}$, $C_{np\alpha} = C_{mp\beta}$. The parameter identification results are presented in Tables 2 and 3.

Table 2 Identification of Aerodynamic Coefficients and Stability Derivatives for 105mm Projectile

Parameter	Nominal Value	Moderate noise		Low noise	
		mNR Algo.	Cost Insp.	mNR Algo.	Cost Insp.
C_{D0}	0.39	0.3854	0.385	0.3887	0.389
C_{D2}	8.1	-	-9.4x10 ⁴	-	-8x10 ⁴
$C_{L\alpha}$	1.9	-	11.2	-	2.20
C_{lp}	-0.01	-0.00944	-0.0095	-0.00994	-0.0099
$C_{m\alpha}$	3.85	-	-19.6	-	2.8
$(C_{mq} + C_{m\dot{\alpha}})$	-6.9	-2.197	-2.8	-6.701	-6.69
$C_{mp\beta}$	0.03	-	1.2	-3.489	-3.3

- No convergence even after several iterations.

Starting value $\Theta_0 = [0.6, 12, 3.1, -0.02, 1.9, -3.6, 0.05]^T$

Table 3 Identification of Aerodynamic Coefficients and Stability Derivatives for 20mm Projectile

Parameter	Nominal Value	Moderate noise		Low noise	
		mNR Algo.	Cost Insp.	mNR Algo.	Cost Insp.
C_{D0}	0.25	0.2497	0.25	0.2497	0.25
C_{D2}	2.12	-	-	-	-
$C_{L\alpha}$	2.87	-	-1.6	-	2.0
C_{lp}	-0.02	-0.02	-0.02	-0.02	-0.02
$C_{m\alpha}$	2.07	-	0.30	-	2.0
$(C_{mq} + C_{m\dot{\alpha}})$	-10.99	-	79	-	-13.3
$C_{mp\beta}$	0.37	-	0.4	-	-4.3

- No convergence even after several iterations.

Starting value $\Theta_0 = [0.6, 12, 1.5, -0.01, 4.5, -6, 1]^T$

From Tables 2 and 3, it is seen that C_{D0} and C_{lp} were identified for both moderate and low noise levels. It is to be noted that C_{D0} and C_{lp} are the major factors that dominate the motion of the selected projectiles, and, actually, they can be identified even with larger noise intensity. On the other hand, some of the parameters are not able to converge due to rank deficiency problems [5]. This difficulty motivates our curiosity to study further for the cause of the difficulty. Values in the column of cost inspection are obtained from figures shown later. Figures 2 shows the cost function J as functions of the parameters C_{lp} for various noise levels. From the figure, we found that the intensity of noise influence the lowest point of the cost function.

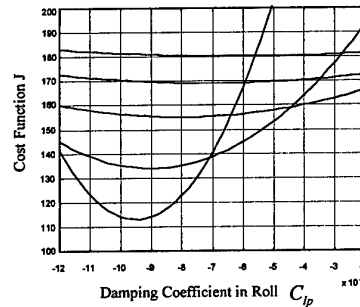


Fig. 2 Cost Function J as Function of Damping Coefficient in Roll for Various Noise Intensity

This drastically affects the accuracy of the identification, since our identification algorithm by mNR searches the lowest point

of J , i.e., $\partial J / \partial \Theta = 0$. Even worse, the cost function with respect to variations of some parameters, say, $C_{L\alpha}$, $C_{m\alpha}$ becomes insensitive or irregular for certain level of noise. Figures 3-6 present the cost function J and the gradient of J as functions of the parameters $C_{L\alpha}$ and $C_{m\alpha}$ for this case. It is obvious that the mNR algorithm fails to converge to the true value, when the situation occurs.

6. CONCLUSION

The modified Newton-Raphson (mNR) method presented here is the most general technique that has been developed for parameter identification problem with both process and measurement noise. It consists of a combination of extended Kalman filter for estimating the states and a mNR iteration procedure for estimating the parameters. Research results show that only parts of the parameters can be identified under proper noise intensity. However, the accuracy of identification is strongly influenced by both process and measurement noise. Moreover, parameter sensitivity to the system behavior is crucial identifiability. It is found that the drag coefficient of zero angle-of-attack and the rolling moment derivative are identified with effective accuracy in a wide range of noise level. On the other hand, other parameters are more difficult to identify, because of the sensitivity and irregularity in the gradient of cost function.

REFERENCE

- [1] Chapman, G. T. and Kirk, D. B., "A method for Extracting Aerodynamic Coefficients from Free Flight Data," *ALAA J.*, 18, 4, pp. 753-758, April 1970.
- [2] Jategaonkar, R. V. and Plaetschke, E., "Algorithms for Aircraft Parameter Estimation Accounting for Process and Measurement," *J. of Aircraft*, 26, 4, pp. 360-372, April 1989.
- [3] Iliff, K. W., and Taylor, L. W., "Determination of Stability Derivatives from Flight Data Using A Newton-Raphson Minimization Technique," NASA TND-6579, 1972.
- [4] Maine, R. E., and Iliff, K. W., "Application of Parameter Estimation to Aircraft Stability and Control," NASA RP-1168, 1986.
- [5] Stepner, D. E., and Mehra, R. K., "Maximum Likelihood Identification and Optimal Input Design for Identifying Aircraft Stability and Control Derivatives," NASA CR-2200, 1973.
- [6] Chen, Y., Wen, C., Gong, Z., and Sun, M., "Drag Coefficient Curve Identification of Projectiles from Flight Tests via Optimal Dynamic Fitting," *Control Engineering Practice*, 5, 5, 1997.
- [7] Chen, Y., Wen, C., Xu, J., and Sun, M., "High-order Iterative Learning Identification of Projectile's Aerodynamic Drag Coefficient Curve from Radar Measured Velocity Data," *IEEE Trans. on Contr. Sys. Tech.*, 6, 4, NJ, 1998.
- [8] Etkin, B., *Dynamic of Atmospheric Flight*, John Wiley & Sons, N.Y., 1972.
- [9] Soong, C. Y. and Kuo, Z. S., "Nonlinear Theoretic Analysis of Flight Stability for Projectiles," National Science Council Report, No. NSC86-2623-D014-006, Taiwan, Sept. 1997.
- [10] Kessler, E. L., et al., "Design for Control of Projectile Flight Characteristics," *U.S. Army Engineering Design Handbook*, AMCP 706-242, 1966.
- [11] Vaughn, H. R., "A Detailed Development of The Tricyclic Theory," *Sandia Laboratory Report*, No. SC-M-67-2933, Albuquerque, 1968.

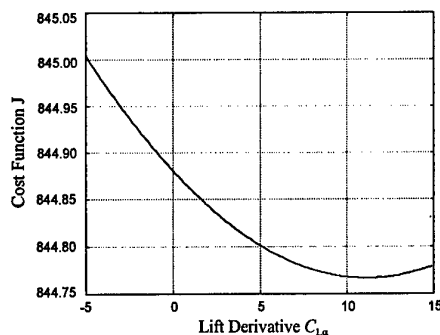


Fig. 3 Cost Function J as Function of Lift Derivative $C_{L\alpha}$

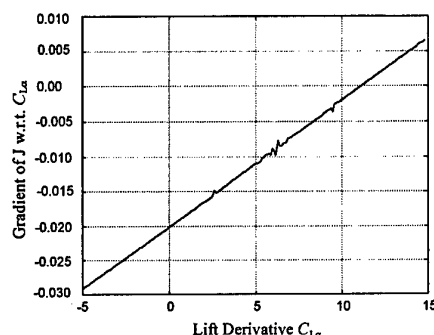


Fig. 4 Gradient of J as Function of Lift Derivative $C_{L\alpha}$

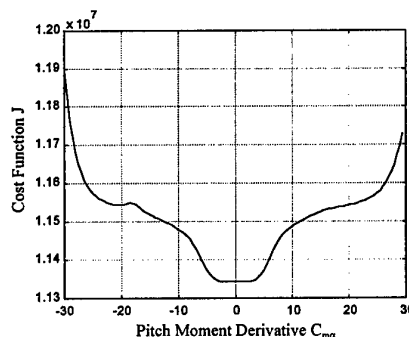


Fig. 5 Cost Function J as Function of Pitch Moment Derivative $C_{m\alpha}$

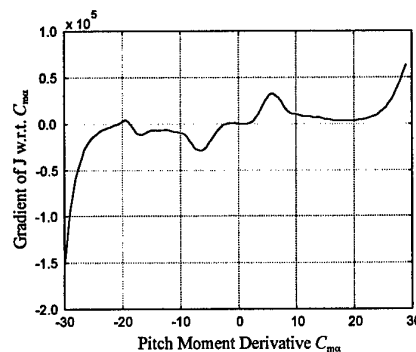


Fig. 6 Gradient of J as Function of Pitch Moment Derivative $C_{m\alpha}$

AN ACCELERATED CO-EVOLUTIONARY ALGORITHM USING NEURAL NETWORKS

Jong-Han Kim*, Chang-Su Park* and Min-Jea Tahk**

Department of Aerospace Engineering
Korea Advanced Institute of Science and Technology(KAIST)
373-1 Kusong-dong, Yuseong-gu, Taejeon, 305-701, Korea

Key Words: flight control, co-evolution, neural network

ABSTRACT

A new co-evolutionary algorithm of which the speed is accelerated by neural networks is proposed in this paper. To reduce the total simulation time, the cost function information is stored in the neural network. After sufficient training is achieved, some of the cost evaluations are replaced by neural network computations, and it leads to reduced computational load. The proposed algorithm is efficient as demonstrated in an autopilot design problem.

1. INTRODUCTION

Recently developed co-evolutionary algorithms are powerful for solving minimax problems[1]. For general minimax problems, the number of cost evaluations of a co-evolutionary algorithm is proportional to the square of the population size, resulting in a heavy computational load. In this paper, we propose a new co-evolutionary algorithm which is accelerated by neural networks.

Cost evaluation is the most time-consuming process in general optimization problems, but standard evolutionary algorithms use cost information only for fitness evaluation. In the new algorithm, the cost information is not discarded but stored in the neural network for further use. The neural network is trained from the early stages of evolution. After sufficient training is achieved, some of the cost evaluations are replaced by the neural network computations. For most practical problems, the computational load required for neural network training is much smaller than that required for the evaluation of the original cost. Therefore the total simulation time is greatly reduced.

In this paper, some fundamentals of the co-evolutionary algorithm are presented first, and the accelerated co-evolutionary algorithm is introduced next. Finally, a robust autopilot design by the accelerated co-evolution is presented for verification.

2. CO-EVOLUTIONARY ALGORITHM

Co-evolutionary algorithms are originally developed for solving minimax problems[2] [3], and applied to optimization problems[1]. It simulates a competitive evolution of two groups of opposite objectives, one tries to minimize the given cost function while the other tries to maximize.

The co-evolutionary process is summarized as follows.

1. Initialization
The initial populations of two groups are generated.
2. Offspring generation
The offspring of each group is generated through recombination and mutation.
3. Match
The two groups have a series of matches for cost evaluations. All the cost evaluations are performed in this step.
4. Fitness evaluation and sorting
All the individuals of two groups check the fitness and sort themselves according to their objectives.
5. Selection
The two groups select new parent populations for the next generation.
6. Termination condition
If the termination condition is satisfied, the co-evolution process is terminated. Otherwise, go to step 2.

3. ACCELERATED CO-EVOLUTIONARY ALGORITHM

For most practical optimization problems, the cost is determined by complicated functions such as integrations and transcendental functions. And the algorithms need cost evaluations very frequently, which results in a heavy computational load and time also.

The accelerated co-evolutionary algorithm(ACEA) is motivated from the universal approximation property of the multilayer feedforward neural networks[4]. In the new algorithm, the cost is reused to train the neural networks. The neural networks are adapted whenever the cost is evaluated. Then, some of the cost evaluations are replaced by the neural network computations.

In the accelerated algorithm, each group evolves in the following way.

1. Initialization
2. Offspring generation
3. Match

* Graduate Student, Department of Aerospace Engineering

** Associate Professor, Department of Aerospace Engineering

In the new algorithm, the matching process has two modes, while the original co-evolutionary algorithm has only one matching mode(the actual cost evaluation). One mode mode performs the actual cost evaluation and neural network training, another mode performs the neural network computation for the cost evaluation. As only one mode is possible per match, we have to select a mode for each match.

- [Mode A] : Actual cost evaluation and neural network training
 - [Mode B] : Neural network computation only
4. Fitness evaluation and sorting
 5. Selection
 6. Termination condition

When the Mode A is on, some computation time is required for the match, as the actual cost is computed. But when the Mode B is on, the computation time required greatly reduces compared to Mode A. - no actual cost is calculated in Mode B. A fast neural network computation completes a matching.

As the groups evolve, the neural network training will reduce the error so that the cost computed by the neural network will become more accurate and reliable. So in the early stages of the evolution, Mode A dominates the match for a generation, and as the co-evolution continues, Mode B is more frequently employed. With increased usage of Mode B, the faster simulation is possible, but some risk of error remains. Because of the risk, some of the matches in a generation should be done by Mode A, not to stop training.

The two modes are switched by the following function. The first N_{ma} matches per generation are performed by Mode A, while the rest are computed by Mode B. N_{ma} at the n -th generation($n \geq 2$) is given by

$$N_{ma}(n) = \text{int}(\{B_L + (1 - B_L)(\frac{E(n-1)}{E(1)})^k\} \cdot N_m) \quad (1)$$

where $E(n)$ is the mean error of the neural network computations, $B_L(0 < B_L < 1)$ is the lower bound of N_{ma} , and N_m is the number of the match per generation.

B_L prevents the domination of Mode B in case the neural network error is very small. A positive constant k is the decay factor. In case E decreases drastically, the decay rate of N_{ma} is controlled by k . A small k leads to slow decay and accurate neural network computations. Note that $k = 0$ for the original co-evolutionary algorithm. In practical problems, a value of k near unity gives good results.

4. APPLICATION

A. Aircraft normal acceleration control

For verification, we design a robust autopilot for F-15 using the proposed algorithm. Fig.2 shows the block diagram for the linearized longitudinal dynamics of F-15, and the appropriate transfer functions are as follows.

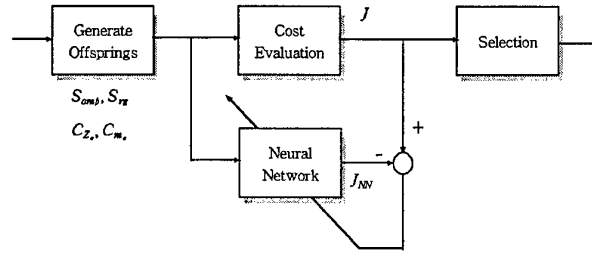


Fig. 1. Flow diagram for the matching

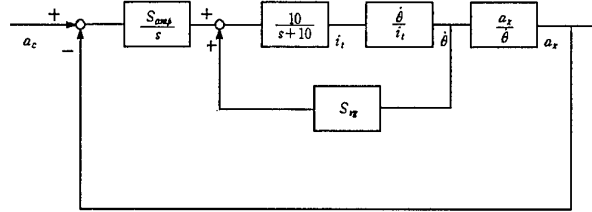


Fig. 2. Aircraft longitudinal dynamics

$$\dot{\theta} = \frac{\frac{mU}{Sq} C_{m_{i_t}} s - C_{m_{i_t}} C_{z_{\alpha}} + C_{m_{\alpha}} C_{z_{i_t}}}{\left(\frac{mU I_y}{(Sq)^2} s^2 - \left(\frac{I_y}{Sq} C_{z_{\alpha}} + \frac{mU}{Sq} \frac{c}{2U} C_{m_q} \right) s + \left(\frac{c}{2U} C_{m_q} C_{z_{\alpha}} - \frac{mU}{Sq} C_{m_{\alpha}} \right) \right)} \quad (2)$$

$$\frac{a_z}{\theta} = \frac{\pi U}{180g} \times \frac{\left(\frac{I_y}{Sq} C_{z_{i_t}} s^2 - \frac{c}{2U} C_{m_q} C_{z_{i_t}} s + C_{m_{i_t}} C_{z_{\alpha}} - C_{m_{\alpha}} C_{z_{i_t}} \right)}{\frac{mU}{Sq} C_{m_{i_t}} s - C_{m_{i_t}} C_{z_{\alpha}} + C_{m_{\alpha}} C_{z_{i_t}}} \quad (3)$$

The F-15's numerical data at a cruising condition are shown in Table 1[5].

The cost function is defined as the following integral form. The cost is zero when the response is identical to the reference model response, and increases as the response deviates from the reference response. Graphically, the cost is the shaded area in Fig.3.

$$J = \int_{t_i}^{t_f} |a_z - a_{z_{ref}}| dt \quad (4)$$

The reference model is selected as a simple second order system whose transfer function is as follows.

$$\frac{A_{z_{ref}}}{A_{z_{comm}}} = \frac{\omega_n^2}{s^2 + 2\zeta\omega_n s + \omega_n^2} \quad (5)$$

The reference model with the natural frequency $\omega_n = 2(\text{rad/s})$ and the damping ratio $\zeta = 0.9$ provides fast dynamics with no overshoot.

Table 1. A cruising condition

h(m)	$V_T(\text{m/sec})$	C_L	$C_{L_{\alpha}}$	$C_{L_{i_t}}$
6,096	189.63	0.24	4.17	0.4
C_D	$C_{D_{\alpha}}$	$C_{m_{\alpha}}$	$C_{m_{i_t}}$	$\frac{c}{2U} C_{m_q}$
0.05	0.35	-0.29	-0.5	-0.0512

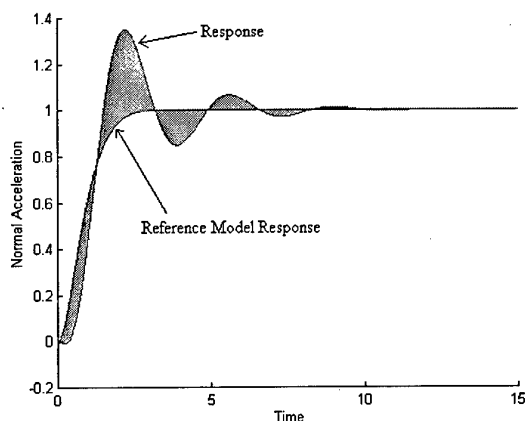


Fig. 3. Cost function(Cost is the shaded area)

B. Computer simulation

Setting and solving the given design problem as a minimax game between the controller gain group and the parameter uncertainty group, we obtain a robust controller for which the performance is fine even under the worst possible case. The aerodynamic parameters $C_{z\alpha}$ and $C_{m\alpha}$ are assumed to be the maximizer group having 10% uncertainties, while the gains S_{amp} and S_{rg} try to minimize the given cost.

Each group consists of 10 parents and 40 offsprings per generation and evolves until the 100th generation. The matching process is followed by the full match rule($40 \times 40 = 1600$ matches per generation) and the (μ, λ) selection is used. The parameters in the mode switching function is selected as, $B_L = 0.2$, $k = 0.5, 1, \text{ or } 2$.

A Gaussian radial basis function(RBF) neural network is used for the cost mapping. All the RBF parameters(w (weights), m (RBF centers), σ (RBF width)) are all adapted by error back-propagation. A single hidden layer with bias is used, for which each of hidden units has the following activation function,

$$H_i(x) = \exp\left(-\frac{(x - m_i)^2}{2\sigma_i^2}\right) \quad (6)$$

Table 2. Co-evolution results

Parameter	CEA(Unaccelerated)	ACEA($k = 0.5$)	ACEA($k = 1$)	ACEA($k = 2$)
S_{amp}	2.2882	2.3004	2.2778	2.2891
S_{rg}	0.1970	0.2037	0.1974	0.1999
$C_{z\alpha}$	-3.7605	-3.7723	-3.7611	-3.7633
$C_{m\alpha}$	-0.2611	-0.2643	-0.2614	-0.2613
$\sigma(S_{amp})$	0.0764	0.0856	0.0417	0.1040
$\sigma(S_{rg})$	0.0109	0.0193	0.0056	0.0172
$\sigma(C_{z\alpha})$	0.0114	0.0338	0.0091	0.0168
$\sigma(C_{m\alpha})$	0.0002	0.0125	0.0006	0.0009
Simulation Time(sec)	11871	5783	4293	3615

C. Results

The optimization result by the accelerated co-evolutionary algorithm(ACEA) with various decay factor k is presented in Table 2, and the result by the original co-evolutionary algorithm(CEA) is also shown for comparison. Both results are obtained by averaging the data from 20 runs each. $\sigma(\cdot)$ denotes the standard deviation and is presented to show the convergence characteristics. A Pentium-II 450 PC is used for computer simulation.

5. CONCLUSIONS

The co-evolutionary algorithm is accelerated by neural networks for numerical efficiency. The proposed algorithm reduces the evolution simulation time, with little degradation in performance. For the controller design example, the simulation time is reduced by 50%, while the convergence properties of the parameters are as good as that of the original algorithm. Both accuracy and speed are provided by proper mode switching. In this paper, the neural network computation error is monitored on line and used in the mode switching function.

ACKNOWLEDGMENT

This work was supported by Korea Science Foundation under Contract 96-0200-04-01-3.

REFERENCES

- [1] M.J.Tahk, "Co-evolution for Engineering Optimization Problems : Minimax Design and Constrained Optimization," *Special Lecture, Proceeding of JSASS Aircraft Symposium*, Yokosuka, Japan, pp.687-690, Oct. 1998.
- [2] C.S.Park, J.Hur and M.J.Tahk, "Aircraft Control System Design Using Evolutionary Algorithm," *Journal of the Korean Society for Aeronautical and Space Sciences*, Vol.27, No.4, pp.104-114, June 1999.
- [3] C.S.Park and M.J.Tahk, "A Co-evolutionary Minimax Solver and its Application to Autopilot Design," *Proceeding of AIAA Guidance, Navigation, and Control Conference*, Boston, USA, pp.408-415, Aug. 1998.
- [4] S.Haykin, *Neural Networks - A Comprehensive Foundation*, 2nd ed., Prentice Hall, 1999
- [5] J.H. Blakelock, *Automatic Control of Aircraft and Missiles*, 2nd ed., Wiley, 1991.

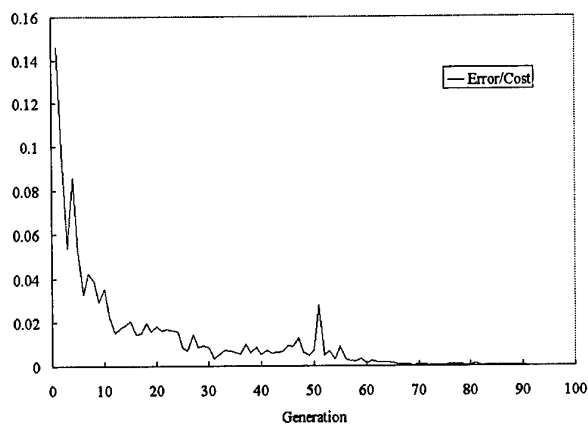


Fig. 4. Neural network computation error

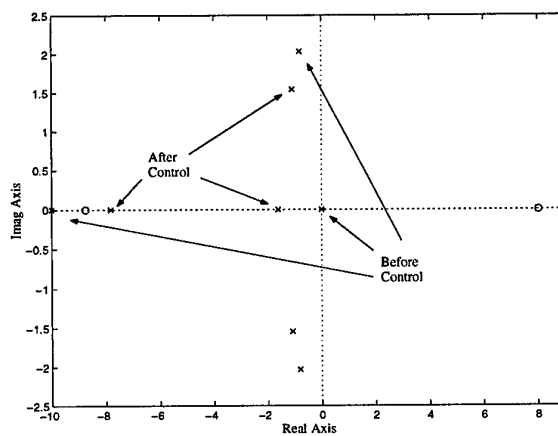


Fig. 7. Pole locations

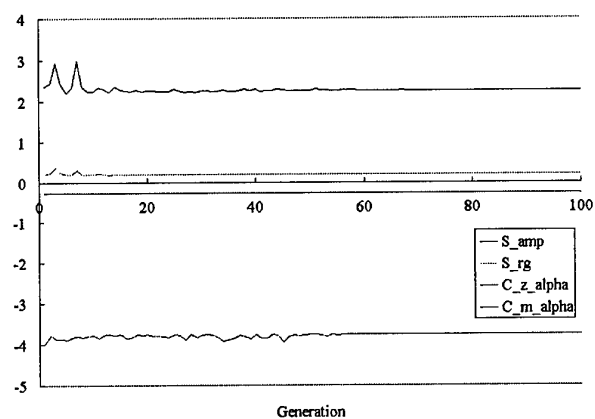


Fig. 5. Co-evolution history by the accelerated algorithm

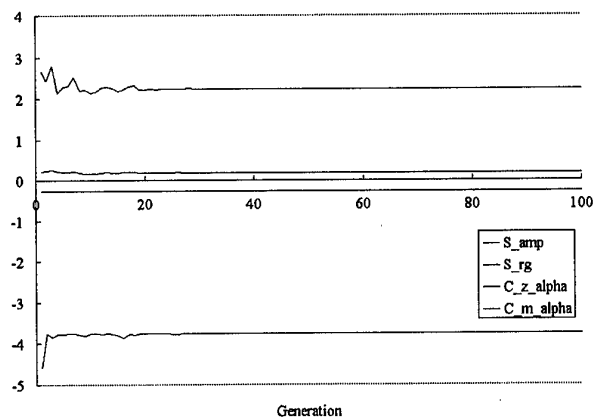


Fig. 8. Co-evolution history by the original algorithm

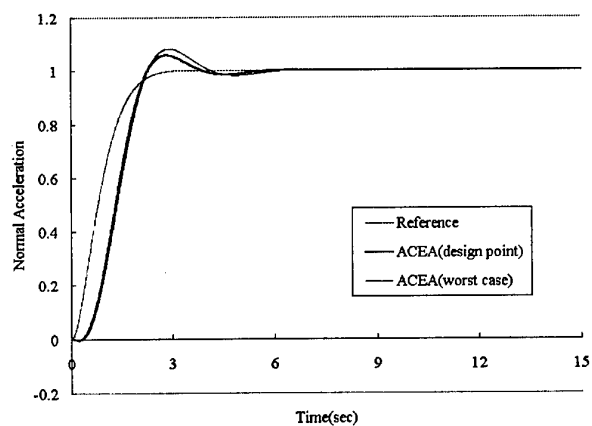


Fig. 6. Response to the step input (designed by the accelerated algorithm)

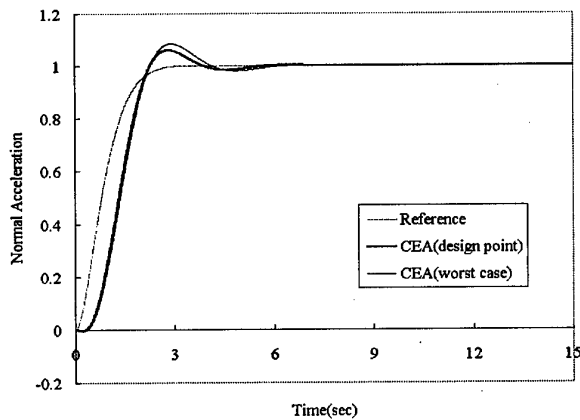


Fig. 9. Response to the step input (designed by the original algorithm)

APPLICATION AND TESTING OF A SQP CODE TO SOME TRAJECTORY OPTIMIZATION PROBLEMS

Marcello Tava* and Shinji Suzuki**

The University of Tokyo, Graduate School of Aeronautics and Astronautics, Bunkyo-ku Tokyo 113

Key Words: Trajectory Optimization, Nonlinear Programming, Sequential Quadratic Programming

ABSTRACT

For the preparation of future optimization analysis, a preliminary testing of a sequential quadratic programming code (BDH) has been conducted with respect to three trajectory optimization problems of known analytical solution.

First, a transfer to a rectilinear path with maximum final velocity was solved. In the second problem a ship cruising in a region of currents had to be driven from an initial to a final point in the least time. The third problem required to find the heading law by which an airplane can enclose the maximum area in a given time when subjected to wind currents.

The analysis was conceived as a benchmark study for the BDH code and sensitivity tests were performed with respect to most of the input parameters the user must provide to the code. Particularly, the sensitivity of the numerical solution versus variations of the initial solution was considered. The analysis taught important lessons on how to prepare a suitable initial solution for optimal control solving.

1. Introduction

Most state-of-the-art methods for solving trajectory optimization problems are based on a two-step procedure. In the first part the optimal control problem is converted into a nonlinear programming (NLP) problem. Then, the resulting NLP problem is solved using some numerical techniques.

The procedure for the first part is generally based on dividing the time domain of the optimal control problem into a number of sub-intervals and by choosing the states and the controls at the nodes as the parameters of the optimization. The dynamic problem is thus transformed into a static problem whose variables are no longer the n state and m control continuous functions, but an array containing $n+m$ parameters at each node. The formulation is known as parameter optimization problem¹ and the process used to set it as transcription². In order to preserve the dynamic features of the original variables, continuity constraints between adjacent sub-intervals must be added to the original set of constraints. This may be done with an integration scheme by a technique named collocation.³ At this point the NLP problem is completely defined and all is needed is a NLP code which iterates on the unknowns until the parameter optimization is solved.

Among the many NLP algorithms, quadratic programming (QP) is one of the most popular. Its formulation derives from observing that an equivalent expression is available to the Kuhn-Tucker (KT) necessary conditions for a

constrained optimum. Given the problem:

$$\text{minimize: } F(X) \quad \text{subject to: } c(X) = 0 \quad (1)$$

and introducing the Lagrangian $L = F(x) - \lambda^T c(x)$, an equivalent solution to the KT optimality conditions is given by solving the quadratic optimal problem:

$$\text{minimize: } \frac{1}{2} p^T H_L p + g^T p \quad \text{subject to: } Gp = -c \quad (\text{QP})$$

where H_L is the Hessian of the Lagrangian ($H_L = \nabla_x^2 L$), G is the constraint gradient ($G = \nabla_x c$), g is the objective function gradient ($g = \nabla_x F$) and p is the search direction from the initial value X_0 to the candidate stationary point X^* ($p = X^* - X_0$).

This original approach has been generalized to solve a wider class of optimization problems featuring inequality constraints by using algorithms capable to identify and manage the set of active constraints.⁴ Such algorithms require to solve the quadratic problem many times as constraints are added and deleted from the active set. This naturally led to that iterative implementation of QP well known as sequential quadratic programming (SQP).

2. The BDH Program

BDH is a program which uses direct collocation to automatically convert an optimal control problem into a parameter optimization problem⁵ and then solves it using a SQP algorithm⁶. The user must provide an initial solution in an external file and write procedures to describe system dynamics, constraints and objective function in a file to be linked to the main program by the compiler. After convergence is obtained, the program halts reporting to file the optimal solution.

One main characteristic of BDH is that the integration scheme used for producing the continuity constraints is linear. This yields at each iteration a Hessian matrix of a particular form known as block diagonal (from which the name BDH, Block Diagonal Hessian). Therefore useful techniques which exploit matrix sparsity can be adopted⁷, making the optimization process very fast if compared to others.

3. Application and Testing

Three test problems that have been solved with BDH are presented in this section. They are chosen from Bryson's classical textbook on optimal control theory.⁸ Their known analytical solution served as the reference for testing BDH accuracy. The diversity of the problems helped to reveal limits and assets of the program with respect to different conditions.

* PhD student, Mombusho grantee, ** Professor

- Problem I: maximum velocity transfer

Given a point mass and a thrust vector of constant magnitude a acting on it, determine the direction the thrust must have to deliver the particle to a horizontal path of given altitude h , maximizing its final horizontal velocity $u(T)$. The final time T is given.

For setting this optimal control problem we can refer to Eq.1. The state vector $X=[x \ y \ u \ v]$ contains position and velocity of the particle. The control consists of the sole angle β . Objective function and dynamics constraints result:

$$F(X) = -u(T) \quad c(X) = \begin{bmatrix} \dot{x} - u \\ \dot{y} - v \\ \dot{u} - a \cos \beta \\ \dot{v} - a \sin \beta \end{bmatrix} = 0$$

The following boundary conditions:

$$x_0 = 0, \ y_0 = 0, \ u_0 = 0, \ v_0 = 0, \ t_0 = 0$$

$$y_f = h, \ v_f = 0, \ t_f = T$$

determine the optimal control law:

$$\tan \beta = \tan \beta_0 \left(1 - \frac{2t}{T} \right) \quad (2)$$

where the initial value β_0 is implicitly given by defining the three parameters a , h and T in:

$$\frac{4h}{aT^2} = \frac{1}{\sin \beta_0} - \log \frac{\sec \beta_0 + \tan \beta_0}{\sec \beta_0 - \tan \beta_0} / 2 \tan^2 \beta_0 \quad (3)$$

Comparison of numerical and analytical solutions

For the sake of a general principle, the initial guess for the control law must be as close as possible to the optimal (analytical) solution. In case the latter is completely unknown, a good starting point can be to use a linear guess. Let this be:

$$\beta = \beta_0 \left(1 - \frac{2t}{T} \right) \quad (4)$$

Instead of fixing the three left-hand parameters in Eq.3 and determine β_0 implicitly, we fix $\beta_0=45^\circ$ and solve for h (a and T are set equal to unity). Note that building the control law in this way not only produces a non-optimal initial guess but the system will generally not end at the prescribed final conditions.

The starting model consisted in an 11-point grid (57 variables). The resulting control profile (Fig.1a) adequately approximates the optimal curve, particularly within the interval $[0.2T, 0.8T]$. Near the boundaries the solution maintains its linear shape so that the boundary value β_0 , a main design factor of Eq.4, is not saved by the result. However, the equality constraints are all satisfied.

Looking at the trajectory (Fig.1b), the resulting solution approximates the optimal curve much better. The fact that numerical result and optimal reference match more with respect to the trajectory than to the control is due to the rough (linear) integration used by BDH and by the low number of nodes chosen for this case. Trajectory is generated by the control through integration and this introduces an error which depends

on the integration accuracy. On the other hand, the method used by BDH provides very fast solutions. The objective function value resulted to be $u(T)=0.876$ for a relative error of $e=5.57e-3$ ($u_{opt}=0.881$). This solution was calculated in a remarkable time of $t_{CPU}=0.22$ s using a 450 MHz Pentium II.

In order to evaluate BDH efficiency many tests were performed with an increasing number of nodes up to $N=151$. An indefinite increase in the number of variables must produce a stack overflow call. However, before this happened, other numerical problems were observed. The general trend in Fig.2 shows a decrease in relative error and an increase of computational time for a larger number of nodes. However, after a minimum error is reached performance worsens indicating an efficiency limit. In particular, trying with $N=151$ (757 variables) resulted in a calculation failure because of vector linear dependency. This kind of numerical problem is typical of ill-conditioning in the case of very similar numbers possibly generated by very fine time partitioning (large N).

Analysis of stability

Usually the optimal solution is not at hand and a guess must be tried. Even in the case of a simple linear law like Eq.4, two coefficients must still be chosen. To analyze the sensitivity of BDH results with respect to initial solution uncertainty, both the off-set β_0 and the inclination $d\beta/dt$ were varied independently, using a 31-point model for all the cases.

The results are depicted in Fig.3. As expected, any curve with constant inclination has a minimum relative error e at $\beta_0=45^\circ$, i.e. the value of the optimal solution. The point corresponding to the initial solution given by Eq.4 is indicated. Within the variation considered for β_0 and $d\beta/dt$, the error is always below $e=3.0e-3$ thus showing a good stability of BDH for this simple problem.

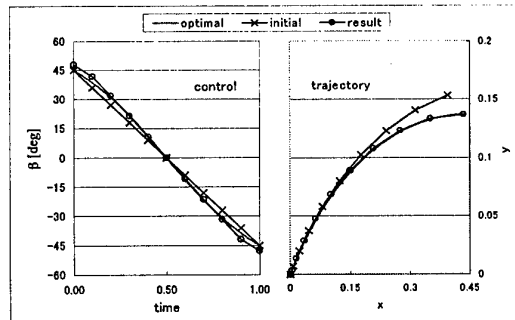


Figure 1a, 1b – Control curves and trajectories for Problem I (11 nodes)

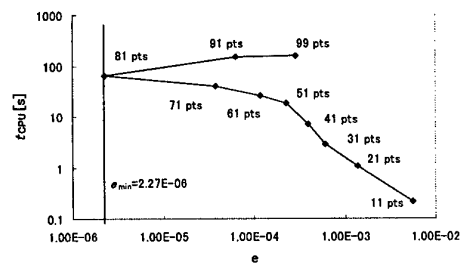


Figure 2 – Computational Time vs. Relative Error and number of nodes

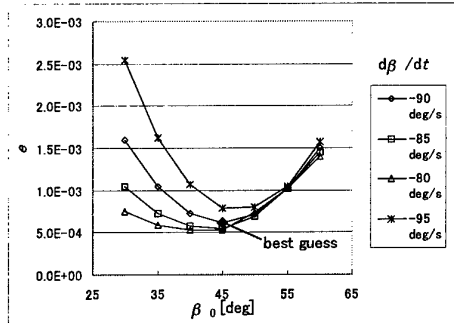


Figure 3 – Relative Error for different initial solutions

• Problem II: minimum time transfer

A ship travels with constant velocity V through a region of strong currents. These are oriented like the x axis and have an intensity which depends linearly on the y coordinate. Determine the route the ship must follow to travel between two given points A and B in the least time T .

The state variables $X=[x \ y]$ are the ship's coordinates. The control is the heading angle θ . Referring to Eq.1 we set:

$$F(X) = T \quad c(X) = \begin{bmatrix} \dot{x} - V \cos \theta - Vy \\ \dot{y} - V \sin \theta \end{bmatrix} = 0$$

with the boundary conditions:

$$x_0 = 3.66, \ y_0 = -1.86, \ t_0 = 0 \quad x_f = 0, \ y_f = 0$$

which allow the solution of an algebraic system with respect to the initial and final heading angles ($\theta_0=105^\circ$ and $\theta_f=240^\circ$). The analytical solution for the control law:

$$\tan \theta = \tan \theta_f + \frac{V(T-t)}{h}$$

can then be used to calculate the final (minimum) time, which results $T=5.46$ s for this case.

Best criterion for initial solution design

Preparatory tests indicated that using a limited number of points ($N=21$) and integrating the optimal control law of Eq.4 by a linear scheme along the sub-intervals does not generate a trajectory close to the optimal one. To avoid this, a much finer time partitioning and/or more accurate integration methods must be used. If this is not possible, the relation between control law and trajectory becomes obscure and it is important to know what criterion must be used for designing the initial solution. Here the two possible approaches were tried. In the first case a control law was derived from imposing a trajectory close to the optimal one. In the second case a control law was chosen near to the optimal control profile, even if the resulting trajectory largely diverged from the optimal one.

The results indicated the second method as the best one. Comparing the relative errors on the objective function value in the two cases showed an average $e \approx 1.0e-2$ for the first case vs. $e \approx 7.0e-4$ for the second case. Fig.4 shows an emblematic case where the initial trajectory is very far from the optimal one and the initial control profile is designed close enough to the optimal control profile by means of a linear interpolation. The results clearly converge to the optimal curves. The calculation time required was $t_{CPU}=10$ s and the relative error $e=6.4e-4$.

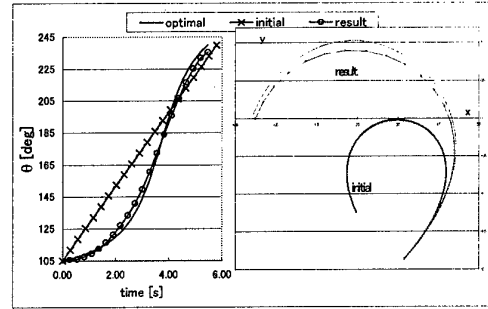


Figure 4a,4b – Control curves and trajectories for Problem II (21 nodes)

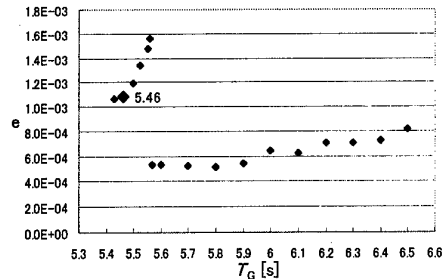


Figure 5 – Relative Error vs. Guessed Final Time

Providing feasible initial solutions

The objective function for the present problem is the final time T . Preparing the initial solution also requires to provide a guess T_G of the final time. The general rule would say that the closer the initial guess T_G and the optimal value T are, the more accurate the solution will be. Fig.5 shows results in contrast with this assumption. In the figure, which depicts the relative error versus T_G , the best of all guesses $T_G=T$ does not correspond to the least relative error. On the contrary, the best performances are to be obtained by $T_G > T$ (up to a certain limit). This can be interpreted with respect to feasibility, i.e. solution conformity with the constraints. Since the optimal solution is the best among all the feasible solutions, providing a non-optimal initial solution whose objective value is as good as the optimal ($T_G=T$) means to provide a non-feasible solution. This proves to be critical with respect to results quality. It is better to relax the initial solution demand on the objective value ($T_G > T$) and start the optimization process from inside the feasible region.

• Problem III: maximum enclosed area

An airplane in a constant wind field of velocity $u=0.2$ has a fixed velocity $V=1$ with respect to the air. Find the closed curve the airplane must fly to enclose the maximum area in a given time $T=1$. The x -axis is chosen in direction of the wind.

Using again the notation of Eq.1, we set $X=[x \ y]$ and:

$$F(X) = - \sum_{i=1}^n \frac{|x_i y_{i+1} - x_{i+1} y_i|}{2} \quad c(X) = \begin{bmatrix} \dot{x} - V \cos \theta + u \\ \dot{y} - V \sin \theta \end{bmatrix} = 0$$

where θ is the control variable. Given the boundary constraints:

$$x_0 = 0, \ y_0 = 1, \ t_0 = 0 \quad x_f = 0, \ y_f = 1, \ t_f = T$$

the analytical solution is an ellipse of eccentricity $e=u/V$, major axis $a=VT(1-e^2)^{1/2}$ perpendicular to the wind, minor axis $b=VT(1-e^2)$. The control law which generates the trajectory can be obtained by the equations of motion $c(X)=0$:

$$\theta = \tan^{-1} \left(\frac{\dot{y}}{\dot{x} - u} \right) \quad (4)$$

Dealing with an integral objective function

This problem differs from the previous two because the objective function is an integral value. BDH's linear integration scheme is thus expected to have a greater effect on solution accuracy here.

In Fig.6 different trajectories are depicted. In a first test the optimal control law itself was used on a 51-point model in order to evaluate the error introduced by the sole integration. Later, a linear initial solution joining the two boundary values of the optimal control was tried. As can be seen, none of the calculated trajectories follows the optimal curve. A better result was observed for the control curves, for which the error introduced by integration is smaller. Even for this critical conditions, the relative error on the objective function still gives a satisfactory result: $e=2.29e-3$ for the first case (discrete optimal) and $e=4.60e-3$ for the linear initial ($t_{CPU}=1.2$ min).

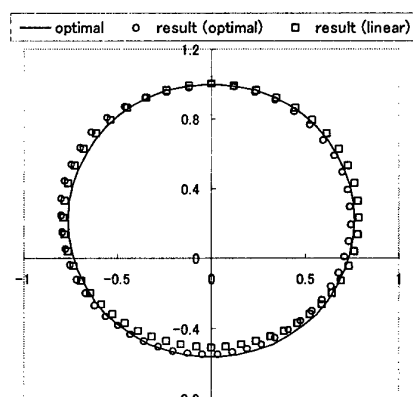


Figure 6 – Optimal and resulting trajectories for Problem III (51 nodes)

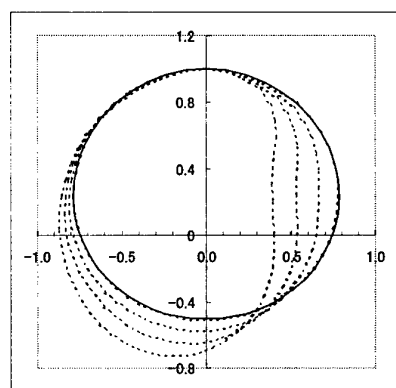


Figure 7 – Inequality constraints for Problem III (51 nodes)

Inequality constraints: "No-Fly Zones"

BDH is also capable to solve problems with inequality constraints. The present problem offers an interesting application of this capability in terms of "no-fly zones". In other words, the new objective is to maximize the area monitored by an aircraft in proximity of a border which must not be trespassed. As a simple case, the borders are defined as vertical lines. Fig.7 shows the results for different positions of the no-fly line. The inequality constraints are in all cases completely satisfied.

4. Conclusions and Developments

Three optimal control problems were solved using a SQP code (BDH) and compared with their known analytical solutions. The results showed a good approximation to the optimal value of the objective functions in all cases, often after very short computational time. Different time partitions were considered to test BDH efficiency. The sensitivity of the results with respect to initial solution uncertainty was also analyzed.

Many lessons were learned. Adopting few nodes ($N<20$) may be critical for BDH linear integration method, while very fine time partitioning ($N>100$) can produce ill-conditioning. Using initial solutions based on the control variable rather than on the trajectory (state variables) proved to be the right design criterion. Finally, it is recommendable to choose the initial solution from inside the feasible region.

The short computing time required by BDH makes it suitable for such tasks as parametric studies, conceptual vehicle design and optimal control problems. Currently the authors are applying it to solve re-entry trajectory optimization under aeroheating constraints. The latter is part of a major project aimed at the multidisciplinary design of a SSTO vehicle.

References

- [1] Hull, D. G., "Conversion of Optimal Control Problems into Parameter Optimization Problems", *Journal of Guidance, Control and Dynamics*, 20-1, 1997, pp.57-60.
- [2] Canon, M. D., Cullum, C. D., Polak E., *Theory of Optimal Control and Mathematical Programming*, McGraw-Hill, 1970.
- [3] Hargraves, C. R., Paris, S. W., "Direct Trajectory Optimization Using Nonlinear Programming and Collocation", *Journal of Guidance, Control and Dynamics*, 10-4, 1987, pp.338-342.
- [4] Goldfarb, D., Idnani, A., "A Numerically Stable Dual Method for Solving Strictly Convex Quadratic Problems", *Mathematical Programming* 27-1983, pp.1-33.
- [5] Tsuchiya, T., Suzuki S., "A Study on Simultaneous Design-Trajectory Optimization of Spaceplane", *JSME-OPID*, 1997
- [6] Fukushima, "A Successive Quadratic Programming Algorithm with Global and Superlinear Convergence Properties", *Mathematical Programming* 35-1986.
- [7] Betts, J. T., Huffman, W. P., "Application of Sparse Nonlinear Programming to Trajectory Optimization", *Journal of Guidance, Control and Dynamics*, 15-1, 1992, pp.198-206.
- [8] Bryson, A. E., Ho, Y., *Applied Optimal Control*, Blaisdell Publishing, 1969, pp. 59-63; 77-80.

CO-EVOLUTIONARY METHODS FOR TRAJECTORY OPTIMIZATION OF SPACE LAUNCH VEHICLES

Hyun-Wook Woo*, Woong-Rae Roh**, Youdan Kim*** and Min-Jea Tahk****

Department of Aerospace Engineering
Korea Advanced Institute of Science and Technology(KAIST)
373-1 Kusong-dong, Yuseong-gu, Taejeon, 305-701, Korea

Key Words: trajectory optimization

ABSTRACT

A co-evolutionary optimization method is applied to trajectory optimization in this paper. This method is based on the augmented Lagrangian formulation of constrained parameter optimization problems. By discretizing the control variable, a trajectory optimization problem can be transformed to a constrained parameter optimization problem and solved by using the co-evolution method. This work demonstrates that the co-evolution method is robust to the initialization of control parameters and provides accurate solutions.

1. INTRODUCTION

There have been lots of research works for finding solutions for optimal rocket trajectory problems. Numerical methods for solving trajectory optimization problems are classified into two methods, direct methods and indirect methods.

Indirect methods introduce the adjoint variables to augment the system governing equation, and explicitly employ the necessary conditions for optimality. The indirect methods usually seek the numerical solution of the multi-point boundary value problem, and these methods have the fast convergent characteristics in the neighborhood of the optimal solution. However, the indirect methods requires good initial guesses for the adjoint variables, and also the switching structure of the optimal solution should be known in advance to achieve the convergent optimal solution.

In the direct methods, the control variables and/or the state variables are represented by piecewise polynomials, and the discretized control and state variables at each time are considered as parameters for optimization. To satisfy the system governing equation, explicit numerical integration is performed using the discrete control time history. Or, the differential equation is converted, by using implicit integration schemes, to nonlinear constraint equations to be used in the optimization process. Then we have a nonlinear programming problem that can be solved by using a parameter optimization technique. The direct method is widely used to solve the

trajectory optimization problems since it does not require the adjoint variables, and the convergence radius of the direct methods is larger than that of the indirect methods. However, for the complicated multi-phase problems, the number of variables increases.

All of the above optimization methods require the gradient-based optimization tools to solve the multi-point boundary value problem or the nonlinear programming. The major drawbacks of gradient-based methods problem are due to the fact that the convergent solution heavily depends on the initial guesses for control history and/or adjoint variable history, and the solution might be the local optimal. To avoid these difficulties, several attempts are made to solve the trajectory optimization problems by other optimization techniques not using gradient information, for example, genetic algorithm, evolutionary algorithm, etc.

In this paper, a new method utilizing co-evolution approach is proposed to solve trajectory optimization problems[1]. The co-evolution method is first applied to min-max problems arising in the robust control design. And its application area has been extended to constrained optimization problems by using augmented Lagrangian formulation. The existing evolutionary algorithms for constrained problem are single-evolution methods and use penalty function method to deal with constraints. On the other hand, the new method is based on a game point of view and two players with opposite objectives evolve separately: one player is optimization parameters, and the other player is Lagrange multipliers. With this method, the optimal parameters satisfying constraints are efficiently found.

Since the direct method converts trajectory optimization problems to parameter optimization problem, the co-evolution method can be applied without difficulty. The performance of the new algorithm is demonstrated for a multi-stage rocket trajectory optimization problem in presence of a dynamic pressure constraint.

2.CO-EVOLUTIONARY AUGMENTED LAGRANGIAN METHODS

The co-evolution method used here is based on the method described in Refs.[1] and [2]. This method was originally developed to solve a saddle-point problem(or a zero-sum game) for which a payoff function $F = F(u, v)$ is to be minimized by u and maximized by v . If there exists a pair $(u^* \in U, v^* \in V)$ such that

$$\min_{u \in U} F(u, v^*) = \max_{v \in V} F(u^*, v) = F(u^*, v^*) = F^* \quad (1)$$

* Graduate Student, Department of Aerospace Engineering, Korea Advanced Institute of Science and Technology

** Graduate Student, Department of Aerospace Engineering, Seoul National University

***Associate Professor, Department of Aerospace Engineering, Seoul National University

****Associate Professor, Department of Aerospace Engineering, Korea Advanced Institute of Science and Technology

then the pair (u^*, v^*) is called a saddle-point solution. The saddle-point solution satisfies the pair of saddle-point inequalities:

$$F(u^*, v) \leq F(u^*, v^*) \leq F(u, v^*), \quad \forall u \in U, \forall v \in V \quad (2)$$

Although the variables u and v are assumed to be continuous, discretization of u and v leads to a static matrix game for which the best options of u and v can be determined by using security strategies. Since the matrix game is only an approximation of the zero-sum game, it gives an approximate solution of the exact saddle-point. To converge to the exact solution, we need an iterative procedure that can be successfully implemented by co-evolution.

The application of co-evolution for constrained optimization is straightforward. Using the augmented Lagrangian formulation, a constrained optimization problem can be transformed to a zero-sum game played by the parameter vector x and the multiplier (μ, λ) . If the primal problem has a solution, then it is always possible to formulate an augmented Lagrangian with at least one local saddle point. If the global saddle point is the only local saddle point, then it can be achieved by a properly designed co-evolution algorithm in most cases. In case of many local saddle points, the co-evolution process may converge to one of them, giving only a local minimum of the primal problem.

In this paper, the co-evolution method modified for constrained optimization will be referred to as co-evolutionary augmented Lagrangian method (CEALM).

3. NUMERICAL EXAMPLES

A. Maximum velocity transfer problem

As the first example of trajectory optimization using the co-evolution algorithm, we investigate the maximum velocity transfer problem to a given altitude at a fixed final time. This is an example taken from Ref. [3]. Here, the numerical solution from the co-evolution algorithm is compared with the exact solution. Consider a particle acted upon by a thrust acceleration of magnitude a . The equations of motion are

$$\begin{aligned} \dot{x} &= u \\ \dot{y} &= v \\ \dot{u} &= a \cos \beta \\ \dot{v} &= a \sin \beta \end{aligned} \quad (3)$$

where x, y are the inertial position coordinates, and the u, v are the velocity components of particle. The thrust direction angle β is the control variable.

The problem is to maximize the final horizontal velocity. Thus, we want to minimize the cost function

$$J = -u(t_f) \quad (4)$$

The initial conditions are $t_0 = 0$, $x(t_0) = 0$, $y(t_0) = 0$, $u(t_0) = 0$, $v(t_0) = 0$, and the final boundary conditions are $t_f = T$, $y(t_f) = h$, $v(t_f) = 0$. For constant-thrust acceleration, the exact solution is available and the optimal control law is a linear tangent law. We have taken $h = 100$, $T = 20$, and $a = 1.123972$. These parameter

values yields to a value of 75° for the initial control angle of the exact solution. The final states variables are determined as $x(t_f) = 122.1288$, $u(t_f) = 12.2129$.

To obtain a numerical solution by the co-evolution algorithm, the trajectory optimization problem is converted to a nonlinear programming problem of a finite number of parameters. The time interval from t_0 to t_f is divided into N elements and the control variable $\beta(t)$ is represented as a set of piecewise linear polynomial. The state equation is integrated by the explicit fourth-order Runge-Kutta algorithm.

The population sizes used for the co-evolution algorithm are $\mu = 10$ (parent population) and $\lambda = 50$ (offspring population). In Table I, the results for $N = 10$ and $N = 20$ are compared to the exact solutions to check the accuracy of the method. It can be easily seen that the co-evolution algorithm gives acceptable results for both cases. The numerical results for the control variable and all four state variables are shown in Fig. 1 to Fig. 5. Once again, these solutions are close to the exact optimal trajectories.

B. Maximum Final Velocity Problem (M3S-II)

The second example is similar to the first one except that the model is more realistic. In this example, the terminal velocity of M3S-II rocket constrained with terminal altitude and path angle, is optimized using the co-evolution method.

The launch vehicle is modeled as a point mass flying over a nonrotating, spherical Earth in the two dimensional plane. The states are mass m , distance from the center of Earth to the vehicle r , range angle ϕ , velocity V , flight path angle γ , and the control variable is the angle of attack α . Writing the equations of motion in dimensionless form gives [4]

$$\begin{aligned} \frac{dR}{d\tau} &= V \sin \gamma \\ \frac{d\phi}{d\tau} &= \frac{V \cos \gamma}{R} \\ \frac{d\gamma}{d\tau} &= \frac{1}{V} \left[\frac{A \sin(u - \gamma) + L}{M} + \left(\frac{V^2}{R} - \frac{1}{R^2} \right) \cos \gamma \right] \\ \frac{dV}{d\tau} &= \frac{A \cos(u - \gamma) - D}{M} - \frac{\sin \gamma}{R^2} \\ \frac{dM}{d\tau} &= -\frac{A_{vac}}{I_{sp}} \end{aligned} \quad (5)$$

where $R, V, M, \tau, A, A_{vac}, L, D$, and I_{sp} are dimensionless variable of $r, v, m, t, T, T_{vac}, l, d$, and i_{sp} . T_{vac} is the vacuum thrust, i_{sp} is the vacuum specific impulse, T is the thrust, d is the drag, and l is the lift.

The thrust is given by

$$T = T_{vac} - A_e p \quad (6)$$

where A_e is the exit area of the nozzles, p is the local atmospheric pressure.

The aerodynamic drag and lift are defined as the axial and normal force

$$\begin{aligned} d &= F_A \cos \alpha + F_N \sin \alpha \\ l &= -F_A \sin \alpha + F_N \cos \alpha \end{aligned} \quad (7)$$

$$F_A = qSC_a$$

$$F_N = qSC_{N_a}\alpha$$

where $q = 1/2\rho v^2$ is dynamic pressure, S is the aerodynamic reference area C_a is the axial force coefficient, C_{N_a} is the normal force coefficient.

1962 Standard Atmosphere is used for the atmospheric density and pressure model[5]. And the numerical values for the Earth model are $\mu_e = 3.986 \times 10^{14} m^3/sec^2$, $g = 9.81 m/sec^2$, $R_e = 6.378 \times 10^6 m$.

The constraints are specified as follows: 1) final altitude $\geq 600 km$, 2) final path angle ≤ 0 , 3) control input(angle of attack) should be bounded between $\pm 10^\circ$. Although original terminal constraints are equality constraints, it can be treated as inequality constraints in this problem

The parameters to be optimized are initial launch angle and discretized control input history. The time interval of the 2nd and 3rd stages are divided to produce N time intervals and α is represented by a set of piecewise linear polynomial. Since the 1st stage is a gravity turn mode, α is set as 0° . To prevent populations from diverging, the range of α for initial populations are limited to $\pm 1^\circ$.

The co-evolution algorithm with $\mu = 5$ and $\lambda = 25$ is applied up to 3000 generations. For 6 runs, the best costs and launch angles are in Table II , in which the solution obtained by the Sequential Quadratic Programming(SQP) method is also shown for comparison. Control input histories are shown in Fig.6. Computation results for trajectory, path angle, and velocity are shown in Fig.7, 8, and 9, respectively

4. CONCLUSIONS

In this paper, the CEALM is applied to trajectory optimization. This method uses a co-evolutionary algorithm based on the augmented Lagrangian formulation. With the new method, initial guess of optimization parameter is relatively easy. And the advantages of evolutionary algorithms regarding the local minimum problem are also effective. Numerical results compared with those of typical nonlinear programming methods show that the CEALM gives equivalent performance. With these advantages and performance, the proposed method seems to be practical and reliable. The long computation time remains to be solved.

REFERENCES

- [1] M.J. Tahk, "Co-evolution for engineering optimization problems: minimax design and constrained optimization," *JSASS Aircraft Symposium*, Yokosuka, Japan, Oct. 1998.
- [2] M.J. Tahk and B.C. Sun, "Co-evolutionary augmented Lagrangian methods for constrained optimization," to appear in *IEEE Transactions on Evolutionary Computation*.
- [3] Bryson, A. E., Jr., and Ho, Y.-C., *Applied Optimal Control*, Hemisphere Publishing, Washington, 1975.
- [4] Gilbert, E. G., Howe, R. M., Lu, P., and Vinh, N. X., "Optimal Aeroassisted Intercept Trajectories at Hyperbolic Speeds," *Journal of Guidance, Control, and Dynamics*, Vol. 14, No. 1, 1991, pp. 123-131.
- [5] Regan, F. J., and Anandakrishnan, S. M., *Dynamics of Atmospheric Re-Entry*, AIAA, 1993.

TABLE I
COMPARISON OF RESULTS

Number of Elements N	Number of Generation	Cost Function $-u(t_f)$	Initial Thrust angle $\beta_0(\text{deg})$
10	50,000	-12.2107	75.2071
20	100,000	-12.2123	75.0180
Exact	-	-12.2129	75.0000

TABLE II
BEST COSTS AND LAUNCH ANGLE

Method	Final Velocity(m/s)	Launch Angle(deg)
SQP	6807.438856	83.864039
CEALM1	6807.050136	83.864780
CEALM2	6807.047847	83.864562
CEALM3	6807.050507	83.864374
CEALM4	6807.050889	83.864328
CEALM5	6807.050136	83.864198
CEALM6	6807.050036	83.864253

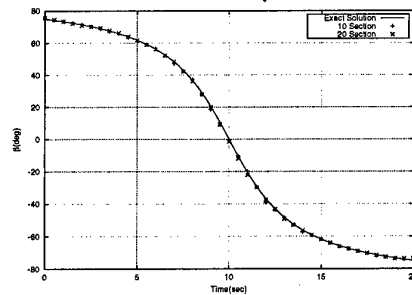


Fig. 1. Thrust angle β vs. time(Example A)

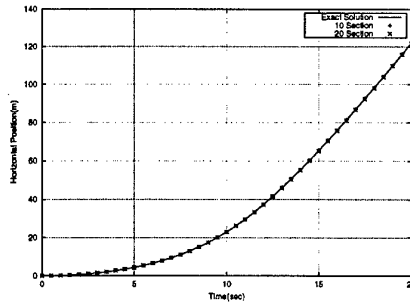


Fig. 2. Horizontal position x vs. time(Example A)

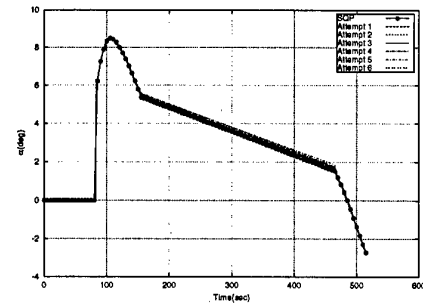


Fig. 6. Control History(Example B)

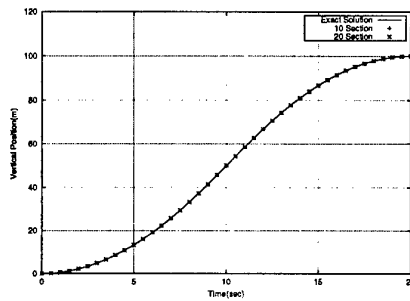


Fig. 3. Vertical position y vs. time(Example A)

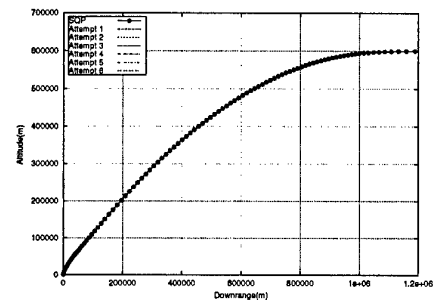


Fig. 7. Trajectory(Example B)

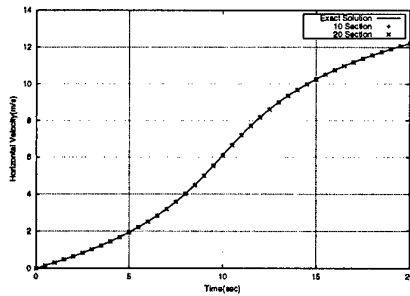


Fig. 4. Horizontal velocity u vs. time(Example A)

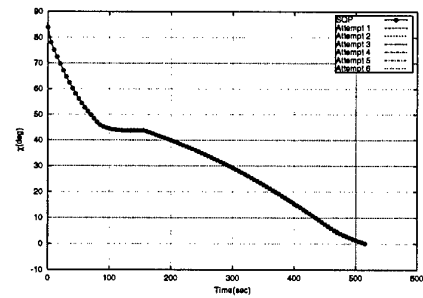


Fig. 8. Path Angle(Example B)

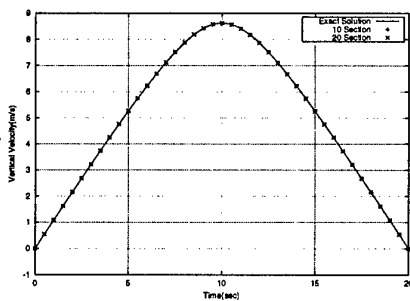


Fig. 5. Vertical velocity v vs. time(Example A)

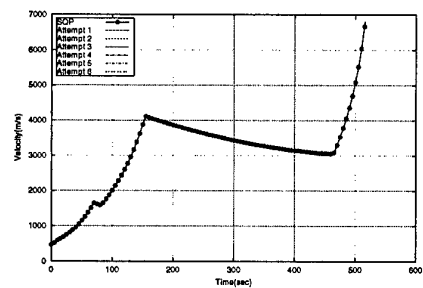


Fig. 9. Inertial Velocity(Example B)

HYPERVELOCITY TRAJECTORIES OF BALLISTIC ENTRY BY USING IMPROVED MATCHED ASYMPTOTIC EXPANSIONS

Zeal-Sain Kuo[†] and Yuan-Lung Yang*

Chung Cheng Institute of Technology
Tao-Yuan, Taiwan, 33509, R.O.C.

Key Words: Flight Dynamics, Hypervelocity Trajectory, Ballistic Entry, Matched Asymptotic Expansions

ABSTRACT

Explicit analytic solutions for a non-lifting vehicle entering the planetary atmosphere along a ballistic trajectory at near circular orbital speed are developed in closed form by using the improved matched asymptotic expansions. The closed-form solutions are presented incorporate gravitational and centrifugal terms with the aerodynamic term after matching process. In the improved technique, the second-order solutions are obtained by first considering the perturbations between the uniformly valid first-order solutions and the exact solutions. Then, the perturbation equations are integrated in the outer and inner regions, respectively, for a second-order matching. In this paper, we apply the improved technique to the atmospheric entry problems of hypervelocity ballistic motion. Analytical asymptotic solutions are obtained, and the solutions result in explicit form of expressions for the critical conditions at peak heating rate and maximum deceleration.

1. INTRODUCTION

A trajectory of interest for hypervelocity trans-atmospheric motion of entry vehicles is the ballistic entry trajectory. During the atmospheric passage, there are tremendous changes in speed, kinetic energy, dynamic pressure and heating rate. It is then of importance to have explicit analytical solutions for the motion of the entry vehicles, since the trajectories of the vehicles are desired. It has been pointed out that the fundamental equations of motion for atmospheric entry are not solvable analytically, but by restricting the equations to a specific region of application, approximate or asymptotic analytical solutions have been obtained. For example, for the case of ballistic entry at sufficiently large flight path angles, Gazley [1], Allen and Eggers [2] and Barbera [3] obtained the first-order solutions in which both the gravitational force and centrifugal force are neglected. For entry with a small lift-to-drag ratio and small initial angle, Chapman [4] and Yaroshevskii [5] developed several first-order theories based on totally different approaches. Their results were extended later by Brace [6], Longuski and Vinh [7] in which the limitations of Chapman's theory were removed, three-dimensional trajectories were studied, and high-order series solutions were obtained.

A powerful method for analyzing atmospheric entry problems governed by the dominant forces varying widely between two end-point regions is the method of matched asymptotic expansions (MAE). By using this method, some analytical solutions for atmospheric re-entry problems have been obtained, but they are restricted to the first-order solutions [8-9]. The classical method of MAE is generally applied to two-point-boundary value problems. When we apply the classical method to initial value problems, due to error propagation, the resulting accuracy usually depends on the physical problems. To go beyond the first-order solutions reported previously, in this paper we apply an improved MAE technique [10, 11] to the atmospheric entry problem: hypervelocity trajectories of ballistic motion. In the proposed technique, the second-order

solutions are obtained by first generating a set of equations for the small perturbations. Then, the equations of perturbations are integrated separately near the outer and inner boundaries to obtain the perturbed outer and inner expansion solutions, respectively, for a second-order matching. Moreover, the second-order solutions for ballistic entry were integrated via more rigorous procedures than those in the former paper [10] and the critical elements at the peak heating rate and the maximum deceleration are presented explicitly.

2. EQUATIONS OF MOTION FOR BALLISTIC ENTRY

We first consider a general case of planar entry trajectory into a non-rotating planetary atmosphere of an aerospace vehicle. Using the standard notation as shown in Fig. 1, we have the governing equations

$$\begin{aligned}\frac{dr}{dt} &= V \sin \gamma \\ \frac{d\theta}{dt} &= \frac{V \cos \gamma}{r} \\ \frac{dV}{dt} &= -\frac{\rho AC_D V^2}{2m} - g \sin \gamma \\ V \frac{d\gamma}{dt} &= \frac{\rho AC_L V^2}{2m} - \left(g - \frac{V^2}{r} \right) \cos \gamma\end{aligned}\quad (1)$$

We define the dimensionless variables $u = V^2/g_s r_s$, and $h = (r - r_s)/r_s$ for the speed and the altitude with subscript s for reference at sea level.

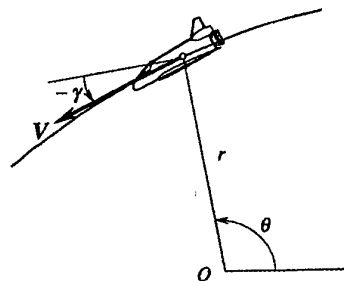


Figure 1 Trajectory Variables

Furthermore, we use a strictly exponential atmospheric model and Newtonian inverse-squared gravitational field as given in Ref. [10]. We have the dimensionless equations of motion

$$\begin{aligned}\frac{d\theta}{dh} &= \frac{1}{(1+h)\tan \gamma} \\ \frac{du}{dh} &= -\frac{2}{(1+h)^2} - \frac{B_D u e^{-h/\epsilon}}{\epsilon \sin \gamma} \\ \frac{d\gamma}{dh} &= \left\{ \frac{1}{(1+h)} - \frac{1}{u(1+h)^2} \right\} \frac{1}{\tan \gamma}\end{aligned}\quad (2)$$

In the equations, we have used a constant dimensionless coefficient as a physical parameter of the vehicle, which is defined as $B_D = \rho_s AC_{D_0}/m\beta$. The system (2) constitutes the

[†] Associate Professor, Department of Mechanical Engineering.

* Research Assistant, Department of Mechanical Engineering.

most appropriate dimensionless system of equations for analyzing ballistic entry.

3. FIRST-ORDER COMPOSITE SOLUTIONS

Outer Expansions (Keplerian Region)

At high altitude, in the equations of motion (2), $e^{-h/\varepsilon} \rightarrow 0$ and the aerodynamic force is negligible compared to the combined gravitational and centrifugal forces. Therefore, the outer expansions are obtained by repeated application of the outer limit, which is defined as the limit when $\varepsilon \rightarrow 0$ with the variable h and other dimensionless quantities held fixed. Assume the following expansion

$$x = x_o(h) + \varepsilon x_1(h) + \varepsilon^2 x_2(h) + \dots \quad (3)$$

By substituting into the system (11) and taking the outer limit, the first-order equations for the outer expansions are

$$\frac{du_o}{dh} = -\frac{2}{(1+h)^2}, \quad \frac{d\gamma_o}{dh} = \left\{ \frac{1}{(1+h)} - \frac{1}{u_o(1+h)^2} \right\} \frac{1}{\tan \gamma_o} \quad (4)$$

These are the equations for Keplerian motion with the outer solutions

$$u_o = \frac{2}{(1+h)} + C_1, \quad \cos \gamma_o = \frac{C_2}{\sqrt{C_1(1+h)^2 + 2(1+h)}} \quad (5)$$

where C_1 and C_2 are the two constants of integration.

Inner Expansions (Aerodynamic Predominant Region)

Near to the surface of the planet, the aerodynamic force is dominant. The inner expansions are obtained by repeated application of the inner limit, which is defined as the limit when $\varepsilon \rightarrow 0$ with the new altitude variable $\bar{h} = h/\varepsilon$ and the other dimensionless variables held fixed. We assume the following expansion

$$x = \bar{x}_o(\bar{h}) + \varepsilon \bar{x}_1(\bar{h}) + \varepsilon^2 \bar{x}_2(\bar{h}) + \dots \quad (6)$$

By substituting into the system (11) and taking the inner limit, the first-order equations for the inner expansions are

$$\frac{d\bar{u}_o}{d\bar{h}} = -\frac{B_D \bar{u}_o e^{-\bar{h}}}{\sin \bar{\gamma}_o}, \quad \text{and} \quad \frac{d\bar{\gamma}_o}{d\bar{h}} = 0 \quad (7)$$

This system can also be easily integrated to yield the inner solutions

$$\bar{u}_o = \bar{C}_1 e^{-\bar{h}}, \quad \text{and} \quad \bar{\gamma}_o = \bar{C}_2 \quad (8)$$

where \bar{C}_1 and \bar{C}_2 are the corresponding constants of integration. For simplicity of notation, we have defined

$$x = -\frac{B_D e^{-h/\varepsilon}}{\sin \bar{\gamma}_o} \quad (9)$$

First-order composite solutions

To have the solutions uniformly valid over both the outer and the inner regions, we construct the composite solutions by taking the sum of the outer and inner solutions and subtracting the parts they have in common. The basic matching principle for the first-order solutions is given as follows

$$x_c = x_o + \bar{x}_o - x_{oo} \quad (10)$$

where x_{oo} is the common limit,

$$x_{oo} = x_o(h \rightarrow 0) = \bar{x}_o(\bar{h} \rightarrow \infty) \quad (11)$$

We easily obtain the first-order composite solution

$$u_c = \frac{2}{1+h} + \bar{C}_1 e^{-\bar{h}} - 2, \quad \cos \gamma_c = \frac{C_2}{\sqrt{C_1(1+h)^2 + 2(1+h)}} \quad (12)$$

By using the matching condition (11), we have the relations between C_1 , C_2 and \bar{C}_1 , \bar{C}_2

$$2 + C_1 = \bar{C}_1, \quad \text{and} \quad \frac{C_2}{\sqrt{C_1 + 2}} = \cos \bar{C}_2 \quad (13)$$

4. SECOND-ORDER SOLUTIONS

Theoretically, we can proceed to derive the equations for outer expansions and inner expansions to a higher order in ε . But there is no assurance that the resulting equations are integrable except for the outer expansions. We shall construct the second-order solutions by considering the small discrepancies from the exact solutions. Let

$$u = u_c + z = u_o + \bar{u}_o - u_{oo} + z \quad (14)$$

$$\ln(\cos \gamma) = \ln(\cos \gamma_c) + q = \ln(\cos \gamma_o) + q$$

By substituting into the basic system (2) and using the equations for outer and inner expansions for simplification, we obtain the equations for the small perturbations z and q

$$\begin{aligned} \frac{dz}{dh} &= -\frac{B_D z e^{-h/\varepsilon}}{\varepsilon \sin \gamma} + \frac{2h}{(1+h)} \frac{B_D e^{-h/\varepsilon}}{\varepsilon \sin \bar{\gamma}_o} \\ \frac{dq}{dh} &= -\frac{1}{u_o(1+h)^2} + \frac{1}{u(1+h)^2} \end{aligned} \quad (15)$$

The initial conditions for z and q are $z(h_i) = 0$, and $q(h_i) = 0$, where the subscript i denotes the entry condition. Again we integrate the equations for the perturbations separately first in the outer region and then in the inner region. Rewrite the first equation of the perturbations (15) in terms of x , yields

$$\frac{dz}{dx} + z = \frac{2h}{1+h} \quad (16)$$

Upon integrating, we have the solution for the perturbation z

$$\begin{aligned} z &= e^{-x} \int \frac{2h}{1+h} e^x dx \\ &= 2h(-h + h^2 - \dots) + 2\varepsilon(-2h + 3h^2 - \dots) E_i(x) e^{-x} \\ &\quad + C_3 e^{-x} + O(\varepsilon^2) \\ &= \frac{2h}{1+h} + \frac{2\varepsilon}{(1+h)^2} E_i(x) e^{-x} + C_3 e^{-x} + O(\varepsilon^2) \end{aligned} \quad (17)$$

where C_3 is the constant of integration. The exponential-integral function is defined as

$$E_i(x) = \int_{-\infty}^x \frac{e^x}{x} dx \quad (18)$$

and is a tabulated function. It turns out that the improved composite solution for u is such that by combining the constants \bar{C}_1 and C_3 into a new constant C_3 , we have

$$u = \left[C_3 + \frac{2\varepsilon}{(1+h)^2} E_i(x) \right] e^{-x} + O(\varepsilon^2) \quad (19)$$

Compared with the former paper [10], the solution (19) is obtained by a totally different way with the same order of accuracy. It reveals that the simplification in the former paper is actually a higher-order approximation. To improve the composite solution q for the flight path angle, we now integrate the second equation of the Eq. (15) for q .

$$\begin{aligned} q &= \frac{1}{2} \ln u_o + \int \frac{dh}{u(1+h)^2} = \frac{1}{2} \ln u_o + \int \frac{e^x dh}{C_3(1+h)^2 + 2\varepsilon E_i(x)} \\ &= \frac{1}{2} \ln u_o - \frac{1}{2} \ln \left[1 + \frac{2\varepsilon}{C_3} E_i(x) \right] + \ln C_4 \end{aligned} \quad (20)$$

We then substitute the function $u(h)$ by its solution (19) to perform the quadrature. This gives with a very minor simplification, $1+h \approx 1$, in the integration the final solution

$$\cos \gamma = e^{\ln \cos \gamma_c + q} = \frac{C_4 \sqrt{u_o} \cos \gamma_c}{\sqrt{1 + \frac{2\varepsilon}{C_3} E_i(x)}} \quad (21)$$

By using the solutions for u_o and γ_o , we actually have with a new constant C_4 .

$$\cos \gamma = \frac{C_4}{(1+h) \sqrt{1 + \frac{2\varepsilon}{C_3} E_1(x)}} \quad (22)$$

The equations (19) and (22) constitute the second-order solutions for ballistic entry. The constants C_3 and C_4 are evaluated by satisfying the initial conditions of u_i and γ_i at $h = h_i$.

5. PEAK HEATING AND MAXIMUM DECELERATION DURING ENTRY

The study of aerodynamic heating is critically important to scientists and engineers involved in design of space vehicles and in planning flight missions. We use the solutions to analyze the average heating rates during entry as well as the deceleration. The time rate of average heat input per unit area is given by [12]

$$q_{av} = \frac{1}{4} C_F \rho V^3 \quad (23)$$

where the parameter C_F is the equivalent skin-friction coefficient assumed to be constant at a mean value for a specific vehicle. Using the dimensionless variables u and h , average heating rate per unit area can be expressed as

$$q_{av} = \frac{1}{4} C_F \rho_0 (g_s r_s)^{3/2} u^{3/2} e^{-h/\varepsilon} \quad (24)$$

Since the coefficient in the average heating rate of Eq. (24) represents the reference value at sea level, we can define a dimensionless average heating rate \bar{q}_{av} as the time rate of average heat input normalized by its maximum value during vertical entry, i.e., $\bar{q}_{av} = q_{av} / \max_{\gamma_i=90^\circ} (q_{av})$.

As an example, we selected $B_D = 638.47$, a typical value for ballistic vehicles, for the hypervelocity trans-atmospheric motion. Figure 2 presents the plots of the variations of the speed as function of the altitude for entry at nearly circular speed $u_i = 1.0$ (7900 m/s) with various entry angles γ_i . Figure 3 presents the variations of the flight path angle as function of the speed.

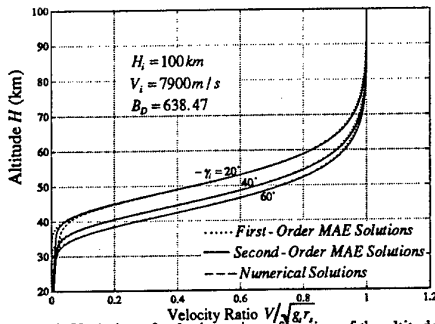


Figure 2 Variation of velocity ratio as function of the altitude for ballistic entry trajectory

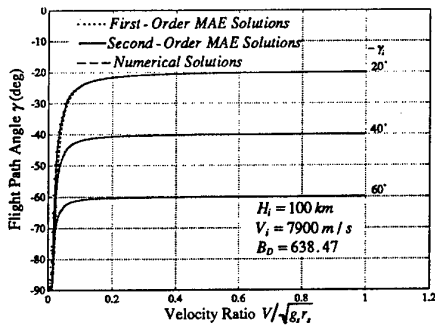


Figure 3 Variation of flight path angle as function of velocity ratio for ballistic entry trajectory

The dashed lines and the dotted lines represent the numerical solutions and the first-order MAE solutions, respectively. The solid lines represent the second-order MAE solutions. It is seen that the second-order solutions almost coincide with numerical solutions for the most part of the trajectory, and the flight path angle is nearly constant down to a low speed. Figures 4 and 5 show the variation of average heating rate \bar{q}_{av} as functions of velocity ratio and altitude, respectively, for various entry angles. To investigate the critical elements at peak heating rate, we maximize $q_{av}(h)$ with respect to h . Then, we have the relation at the point of peak heating rate, denoted by subscript *

$$\frac{2}{3} u_* = -\frac{B_D u_* e^{-h_*/\varepsilon}}{\sin \gamma_*} - \frac{2\varepsilon}{(1+h_*)^2} \quad (25)$$

The critical altitude, as given by the variable x is

$$x_* = \frac{\sin \gamma_*}{\sin \gamma_i} \left[\frac{2}{3} + \frac{2\varepsilon}{(1+h_*)^2 u_*} \right] \quad (26)$$

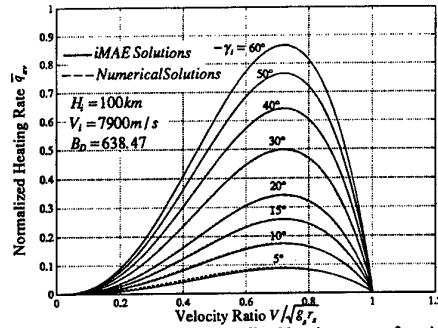


Figure 4 Variation of the normalized heating rate as functions of the speed for ballistic entry trajectory

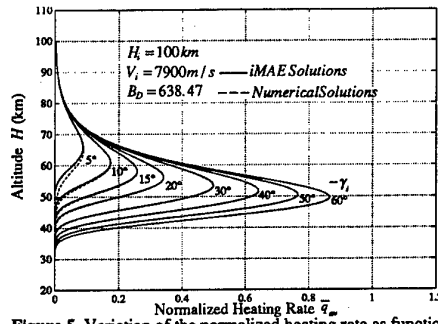


Figure 5 Variation of the normalized heating rate as function of the altitude for ballistic entry trajectory

Figure 6 presents the analytic solutions for peak heating rate (small circles) to compare with the pure numerical solutions (dashed line) in the upper half of the plot while the relative errors of the analytic solutions at peak heating rate are plotted in

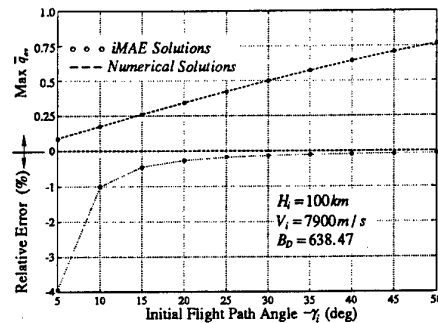


Figure 6 Maximum heating rate and its relative error as function of the entry angle in ballistic entry trajectory

the lower half. They show excellent agreement as compared with the numerical solutions, especially for moderate and large entry angles. The data in Table 1 reveal the numerical accuracy of the trajectory elements at the point of peak heating rate. In each box the upper value is the pure numerical solution while the lower value is computed with our iMAE solution.

Table 1 Comparison of the Trajectory Elements at the Peak Heating Rate for Various Entry Angles

$-\gamma_i$	5°	10°	20°	30°
h_*	0.0102245 0.0102162	0.0095393 0.0095342	0.0088065 0.0088047	0.0083881 0.0083873
$\sqrt{u_*}$	0.708008 0.695393	0.717564 0.713947	0.720125 0.719164	0.720732 0.720280
$-\gamma_*$	5.504485 5.551545	10.24054 10.28962	20.11412 20.14280	30.07124 30.09028
$(\bar{q}_{av})_{\max}$	0.090683 0.086624	0.175013 0.173181	0.342215 0.341297	0.499904 0.499238

The relative errors for trajectory elements at peak heating rate for various entry angles are exhibited in Fig. 7.

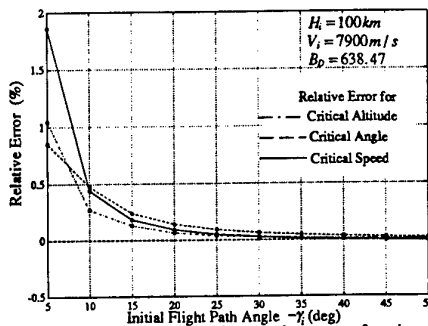


Figure 7 Relative errors of trajectory elements as function of the entry angle at maximum heating rate in ballistic entry trajectory

Now, let's consider the case of ballistic entry for deceleration due to the drag force evaluated according to $a/g_s = B_D u e^{-h/\epsilon} / 2\epsilon$. Table 2 presents the numerical comparison of the trajectory elements at the point of maximum deceleration for various entry angles.

Table 2 Comparison of the Trajectory Elements at the Maximum Deceleration for Various Entry Angles

$-\gamma_i$	5°	10°	20°	30°
h_*	0.0096913 0.0097033	0.0090658 0.0090654	0.0083485 0.0083500	0.0079340 0.0079354
$\sqrt{u_*}$	0.580598 0.559737	0.601986 0.596326	0.607680 0.606878	0.608854 0.609006
$-\gamma_*$	5.924900 6.066374	10.42902 10.49532	20.20269 20.23488	30.12684 30.14735
$(a/g_s)_{\max}$	15.78182 14.50861	29.78518 29.23728	57.89174 57.64989	84.46514 84.31512

Figure 8 plots the aerodynamic deceleration in g's as function of the velocity ratio for different initial entry angles.

6. CONCLUSIONS

In this paper, we apply the improved MAE technique to the atmospheric entry problems of hypervelocity ballistic motion. Analytical asymptotic solutions are obtained, and the solutions result in explicit form of expressions for the critical conditions at peak heating rate and maximum deceleration. Compared to the solutions obtained by numerical integration over a wide range of entry conditions, the second-order solutions obtained by this improved technique are very accurate. The critical elements at peak heating rate and maximum deceleration as well as their accuracy are evaluated. The iMAE solutions are very accurate when compared with the pure numerical solution of the equations of motion. Only for very small angles the desired

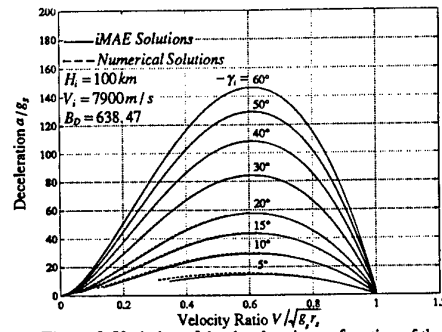


Figure 8 Variation of the deceleration as function of the speed for ballistic entry trajectory

accuracy cannot be realized. It has been pointed out that for this type of trajectory, all forces involved have the same order of magnitude, and this invalidates the basic foundation for applying the method of MAE. In conclusion, improved matched asymptotic solutions for hypervelocity trajectories of ballistic motion have been developed. The second-order solutions obtained by using the improved method apply to all phases of flight from the vacuum through the atmosphere with a high degree of accuracy. The comparison with numerical results clearly demonstrates the applicability and accuracy of the improved iMAE solutions.

ACKNOWLEDGMENTS

The authors are grateful to appreciate the funding from the Government since the research is partly supported by the National Science Council of the Republic of China under the project no. NSC88-2612-E014-001.

REFERENCES

- [1] Gazley, C., "Deceleration and Heating of a Body Entering a Planetary Atmosphere from Space," *The RAND Report* P-955, Feb. 1957.
- [2] Allen, H. J. and Eggers, A. J., Jr., "A Study of the Motion and Aerodynamic Heating of Ballistic Missiles Entering the Earth's Atmosphere at High Supersonic Speeds," NACA TR-1381, 1958.
- [3] Barbera, F. J., "Closed-Form Solution for Ballistic Vehicle Motion," *J. of Spac. and Rockets*, 18, 1, pp. 52-57, 1981.
- [4] Chapman, D. R., "An Approx. Analy. Method for Studying Entry into Planetary Atmospheres," NASA TR R-II, 1959.
- [5] Yaroshevskii, V. A., "The Approximate Calculation of Trajectories of Entry into the Atmosphere," Part I & II, Translated from *Kosmicheskie Issledovaniya*, 2, 4-5, 1964.
- [6] Brace, F. C., *An Improved Chapman Theory for Studying Entry into Planetary Atmosphere*, Ph.D. Dissertation, University of Michigan, MI, 1974.
- [7] Longuski, J. M., and Vinh, N. X., "Analytic Theory of Orbit Contraction and Ballistic Entry into Planetary Atmospheres," JPL Publication 80-58, Sept. 1980.
- [8] Shi, Y. Y., Pottsepp, L., and Eckstein, M. C., "A Matched Asymptotic Solution for Skipping Entry into Planetary Atmosphere," *ALAA Journal*, 9, 4, pp. 736-738, 1971.
- [9] Hough, M. E., "Ballistic Entry Motion, Including Gravity: Constant Drag Coefficient Case," *J. of Guid., Dyn. and Contr.*, 5, 6, pp. 553-557, 1982.
- [10] Vinh, N. X. and Kuo, Z.-S., "Improved Matched Asymptotic Solutions for Deceleration Control During Atmos. Entry," *ACTA Astronautica*, 40, 1, pp. 1-11, 1997.
- [11] Kuo, Z.-S. and Vinh, N. X., "Improved Matched Asymptotic Solutions for 3-D Atmospheric Skip Trajectories," *J. of Spac. and Roc.*, 34, 4, pp. 496-502, 1997.
- [12] Vinh, N. X., Busemann, A., and Culp, R. D., *Hypersonic and Planetary Entry Flight Mechanics*, University of Michigan Press, MI, U.S.A., 1980.

AN INTEGRATED METHOD FOR SHAPE AND FLIGHT TRAJECTORY OPTIMIZATION OF SPACEPLANE

Takeshi Tsuchiya* and Shinji Suzuki**

School of Engineering, the University of Tokyo
7-3-1 Hongo, Bunkyo-ku, Tokyo 113-8656, JAPAN

Key Words: Guidance and Control, Optimization Technique, Spaceplane

ABSTRACT

This paper presents a new parallel optimization method to solve large-scale design and control optimization problems and its applications. Generally, to obtain an accurate optimal solution, a large-scale problem has to be solved, and it takes much computing load and time. Therefore, the new method divides the problem into several sub-problems which can be solved in parallel. Firstly, this paper describes the way to decompose the problem and the fundamental algorithm to solve it. The important point of this study is how to deal with the conjunctive constraints among the sub-problems and define objective functions in each sub-problem. Finally, in this paper, the parallel optimization method is applied to a shape and flight trajectory optimization problem of spaceplane, and its optimal shape and ascent trajectory are estimated to demonstrate the effectiveness of the proposed parallel optimization method.

1. INTRODUCTION

In an aircraft design process, both design and control have to be simultaneously optimized to obtain an extremely high performance. Simultaneous design and control optimization, however, is difficult, because the both are in different technical fields and a large number of variables have to be analyzed and optimized. For a conventional aircraft, a configuration and geometrical parameters of the aircraft are optimized for assumed flight patterns, and, after the aircraft has been designed, flight paths or trajectories are optimized precisely. However, an advanced aircraft, e.g. spaceplane, is required to have severe missions and simultaneous optimization is an important problem. For the large-scale design and control optimization problem, there is an idea that one problem is divided into some small-scale sub-problems, which can be optimized in parallel.

Parallel optimization methods have been studied to solve practical problems for structure and shape designs. The reason is that number of variables for practical design analysis is huge and cost of computers with capacity to optimize the variables is very high. In addition, aircraft designs are difficult so that many technical fields of fluid, engine, structure, control and so on are in a jumble. Therefore multidisciplinary design has been fundamentally performed, by which these different fields are adjusted and each field is analyzed and optimized independently for itself.

Many studies for large-scale mathematical programming problems begun with Dantzig-Wolfe decomposition algorithm¹⁾ for linear programming reported in 1960. For nonlinear programming problem, two methods called model coordination method and goal coordination method which are reviewed by

Kirsch²⁾ has been well accepted. In addition, a hybrid method³⁾ combining these two methods has been studied in recent years. However, these decomposition algorithms have not been widely applied. Recently Dr. Sobieski in NASA Langley Research Center has proposed numerical methods for more practical multidisciplinary optimization problems. According to the new method called Collaborative Optimization⁴⁾, optimized variables are shared with variables depending on only each sub-system (field or discipline) and global variables depending on more than two sub-systems. An optimization problem for global variables is defined on upper level than sub-problems optimizing sub-systems, and the global level optimization and the sub-system optimization is repeated alternately. In each sub-system optimization, the global variables are optimized to coincide with the values given by the global level optimization. Consequently, after some iterations, the collaborative points of the global variables satisfying all sub-problems are obtained. Sobieski and his fellows strive to apply the proposed method to aircraft designs⁴⁾. While it is more practical than the conventional ones and can refine the nominal design certainly, there are no guarantees that the obtained solution is a global optimal value.

Based on past achievements, this study aims to develop the decomposition algorithm which can be used for practical large-scale design problem. In this paper, as an example of the large-scale optimization problem, the body and wing shape and ascent trajectory optimization problems for a future space transportation vehicle, spaceplane, is introduced.

2. PARALLEL OPTIMIZATION METHOD

In this section, let us one optimized large-scale system composed of three subsystems. The following description covers the case where there are more subsystems. First, an optimized variable is grouped into three parts.

$$\mathbf{x} = (\mathbf{x}_1^T, \mathbf{x}_2^T, \mathbf{x}_3^T)^T \quad (1)$$

Equality and Inequality constraints are divided, too, and an optimization problem is defined as

$$\text{minimize } f(\mathbf{x}_1, \mathbf{x}_2, \mathbf{x}_3) \quad (2a)$$

$$\text{subject to } \mathbf{g}_E(\mathbf{x}) = \begin{bmatrix} g_{E1}(\mathbf{x}_1) \\ g_{E2}(\mathbf{x}_2) \\ g_{E3}(\mathbf{x}_3) \end{bmatrix} = \mathbf{0} \quad (2b)$$

$$\mathbf{g}_I(\mathbf{x}) = \begin{bmatrix} g_{I1}(\mathbf{x}_1) \\ g_{I2}(\mathbf{x}_2) \\ g_{I3}(\mathbf{x}_3) \end{bmatrix} \leq \mathbf{0} \quad (2c)$$

* Graduate Student, Department of Aeronautics and Astronautics

** Professor, Department of Aeronautics and Astronautics

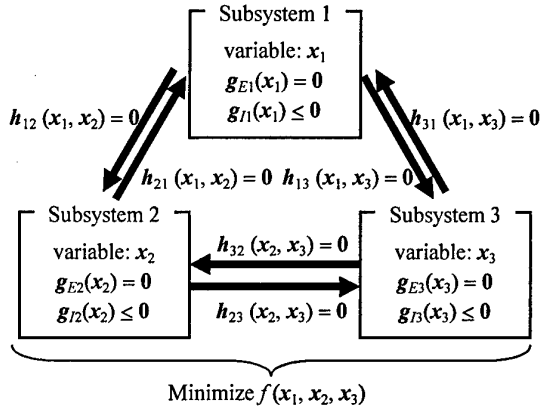


Fig. 1 Three subsystems and their conjunctions

$$h(x) \equiv \begin{bmatrix} h_{12}(x_1, x_2) \\ h_{21}(x_1, x_2) \\ h_{13}(x_1, x_3) \\ h_{31}(x_1, x_3) \\ h_{23}(x_2, x_3) \\ h_{32}(x_2, x_3) \end{bmatrix} = 0 \quad (2d)$$

where an equality constraint h_{ij} and $h_{ij} = 0$ is respectively called a conjunctive function and a conjunctive condition which connects two subsystems i and j . The distinction of two conjunctive functions h_{ij} and h_{ji} with reverse subscripts is clarified later.

Let us arrange an optimization problem in subsystem i .

$$\text{variable: } x_i \quad (3a)$$

$$\text{minimize } f(x_1, x_2, x_3) \quad (3b)$$

$$\text{subject to } g_{Ei}(x_i) = 0 \quad (3c)$$

$$g_{Ii}(x_i) \leq 0 \quad (3d)$$

$$h_{ji}(x_j, x_i) = 0 \quad (j=1, 2, 3 \text{ and } i \neq j) \quad (3e)$$

It is impossible to solve the sub-problem i with regard to x_i independently, because the conjunctive function h_{ji} is also a function of x_j . Therefore, the crucial point of the study is how to deal with the conjunctive conditions and how to define the sub-problems in order to attain highly independent level and to get superior and steady convergent characteristics. In addition, though the original large-scale optimization problem certainly has an objective function, the optimization problems of the divided subsystem often have no objective, because the objective function f doesn't necessarily contain three variables, x_1 , x_2 and x_3 .

The following defines an optimization sub-problem i of the subsystem i proposed in this paper.

$$\text{variable: } x_i \quad (4a)$$

$$\text{minimize } f(x_1, x_2, x_3) + \sum_{j=1(i \neq j)}^3 v_{ij}^T h_{ij}(x_i, x_j) \quad (4b)$$

$$\text{subject to } g_{Ei}(x_i) = 0 \quad (4c)$$

$$g_{Ii}(x_i) \leq 0 \quad (4d)$$

$$h_{ji}(x_j, x_i) = 0 \quad (j=1, 2, 3 \text{ and } i \neq j) \quad (4e)$$

where v_{ij} is a Lagrange multiplier for the conjunctive condition

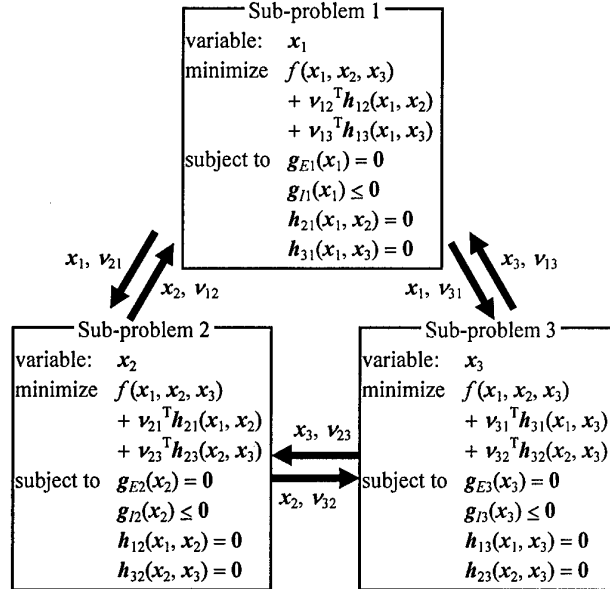


Fig. 2 Three sub-problems and their data exchanges

$h_{ij}(x_i, x_j) = 0$. Note that the optimized variables in the sub-problem i are x_i and v_{ij} , and the others are dealt with as constants. One characteristic of the proposed definition is to use the Lagrange multiplier to add the conjunctive functions to the objective function. The proposed sub-problems surely have the objective.

A fundamental algorithm to solve the sub-problems is summarized as follows:

- (1) Determine proper initial solutions of all the variables x_i and Lagrange multipliers v_{ij} , and substitute them.
- (2) Solve all sub-problems in parallel with optimization methods by which not only the variables but also the Lagrange multipliers can be computed, e.g. a sequential quadratic programming (SQP) method⁵.
- (3) Exchange the obtained variables and multipliers among the sub-problems as shown in Fig. 2, and return to (2).

3. SPACEPLANE DESIGN STUDY

In this section, a simultaneous shape and ascent trajectory optimization problem for a spaceplane is defined and solved to show effectiveness of the proposed parallel optimization method. Figure 3 gives three technical fields, body design field, aerodynamic analysis field and trajectory planning field, of spaceplane design study in this paper, and an objective is to maximize payload weight. Therefore, a large-scale optimization problem is divided into three sub-problems assigned to the technical fields. These fields are not independent but bound to exchange their results. Every field contains some variables of body shape, wing shape, performance and aerodynamic coefficients, whose variables must become same values in an optimal solution. So conjunctive conditions that same variables in different fields are equal are defined. The following describe outlines on these fields.

3.1 Body Design

The spaceplane shape model adopted in this paper is illustrated in Fig. 2. Takeoff Weight is 300 ton and the simple body is composed of an elliptical cylinder body, a tangent ogive

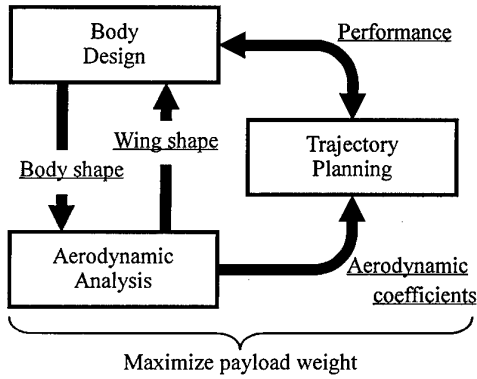


Fig. 3 Three technical fields

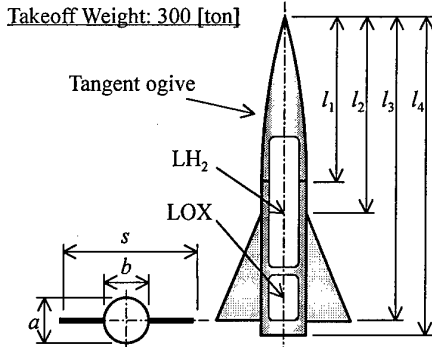


Fig. 4 Spaceplane model

nose and a delta wing. The design variables in this field are body length except for wing size l_1 , l_4 , a (≥ 6 m) and b (≥ 6 m), and performance variables, viz. maximum dynamic pressure q_{\max} (≤ 100 kPa), and maximum load factor n_{\max} (≤ 4 G). Note that the tank volume of fuel compounded from liquid hydrogen (LH₂) and liquid oxygen (LOX) must be less than 70 % of the total body volume.

In this field, a maximized objective function, payload weight, besides the objective set up from the conjunctive conditions as described above, is defined. According to WAATS⁶⁾ program, structural weight W_{STR} can be estimated from the body and wing size. Considering the fuel weight W_{fuel} obtained in the trajectory planning fields together, payload weight W_{payload} is defined as

$$W_{\text{payload}} = 300 - W_{\text{STR}} - W_{\text{fuel}} \quad [\text{ton}] \quad (5)$$

3.2 Aerodynamic Analysis

The aerodynamic characteristics of the model are analytically computed by CRSFLW method in Ref. 7 and 8. Five sampling points are selected from low speed to hypersonic speed, where aerodynamic parameters related to lift coefficient and drag coefficient are calculated. Three variables, l_2 , l_3 and s ($\geq b$), representing the wing size are decided in this field. The aerodynamic coefficients are used to compute trajectories in the following field and the wing size is needed to estimate the structural weight in the body design field.

3.3 Trajectory Planning

The spaceplane takes off, rises and is accelerated by ATR (to Mach 6), SCR (switched from ATR and useable to Mach 12) and ROC (useable with ATR and SCR at the same time). Then,

after the engine is cut-off above 90 km, it zooms up to 400 km with no thrust in an elliptical orbit. Finally, it is put into a 400 km circular orbit at the apogee in the elliptical orbit.

State variables are altitude h , velocity v , flight-path angle γ and weight m . A control variable is defined as the angle of attack α . Motion equations⁸⁾ of the spaceplane are expressed as

$$\frac{dh}{dt} = v \sin \gamma \quad (6a)$$

$$\frac{dv}{dt} = \frac{(T_{\text{ATR}} + T_{\text{SCR}} + T_{\text{ROC}}) \cos \alpha - D}{m} - \frac{\mu \sin \gamma}{r^2} \quad (6b)$$

$$\frac{d\gamma}{dt} = \frac{(T_{\text{ATR}} + T_{\text{SCR}} + T_{\text{ROC}}) \sin \alpha + L}{mv} + \left(\frac{v}{r} - \frac{\mu}{vr^2} \right) \cos \gamma \quad (6c)$$

$$\frac{dm}{dt} = - \left(\frac{T_{\text{ATR}}}{I_{\text{SPATR}}} + \frac{T_{\text{SCR}}}{I_{\text{SPSCR}}} + \frac{T_{\text{ROC}}}{I_{\text{SPROC}}} \right) \frac{1}{g_0} \quad (6d)$$

where μ is the gravity constant, g_0 is the gravity acceleration at the ground level, and D and L are the lift and drag respectively, which are computed by the aerodynamic coefficients obtained in the above field. T_{ATR} , T_{SCR} and T_{ROC} are the thrust of air-turboramjet (ATR) engine, scramjet (SCR) engine and rocket (ROC) engine, I_{SPATR} , I_{SPSCR} and I_{SPROC} are specific impulse of each engine, which are represented in Ref. 8.

Initial conditions at time $t=0$ are specified as

$$h(0) = 0 \quad [\text{km}] \quad (7a)$$

$$\gamma(0) = 0 \quad [\text{deg}] \quad (7b)$$

$$m(0) = 300 \times 10^3 \quad [\text{kg}] \quad (7c)$$

$$L \cos \alpha + (T - D) \sin \alpha \geq m(0) g_0 \quad (7d)$$

$$v(0) \leq 150 \quad [\text{m/sec}] \quad (7e)$$

Terminal conditions at the engine cut-off time $t=t_f$ is expressed as

$$h(t_f) \geq 90 \quad [\text{km}] \quad (8a)$$

$$\gamma(t_f) \geq 0 \quad [\text{deg}] \quad (8b)$$

and the apogee altitude computed by the terminal states, $h(t_f)$, $\gamma(t_f)$ and $v(t_f)$, needs to be 400 km.

In addition, the following path constraints are defined.

$$h \geq 0 \quad [\text{km}] \quad (9a)$$

$$q \leq q_{\max} \quad (9b)$$

$$\alpha \leq 20 \quad [\text{deg}] \quad (9c)$$

$$n \leq n_{\max} \quad (9d)$$

where q is dynamic pressure and n is load factor.

It should be noted that the motion equations change discontinuously since the operating engines are switched according to the flight conditions. Therefore the trajectory planning field is subdivided into four stages, that is, ATR, SCR, SCR+ROC and ROC stage, which provide four sub-problems.

The optimization problem in this field is what is called an optimal control problem that deals with dynamic variables depending on time. In this paper, according to a BDH method⁸⁾, time, variables and constraints are discretized to 200 elements, and the optimal control problem is transformed into nonlinear programming with static variables. The BDH method is one of numerical methods for the optimal control problem. Moreover,

the advantage is that it is easy to deal with various constraints, such as differential equations and inequality constraints, and that the variables quickly converge to solutions.

This field decides intake area of ATR engine and SCR engine, S_{ATR} and S_{SCR} , thrust of ROC engine T_{ROC} , and the fuel amount consumed until arriving at the circular orbit, by which the tank volume is computed in the body design field.

3.4 Numerical Results

The numerical solutions are shown in Fig. 5–7 and Table 1. The maximized payload weight is negative value, -13.75 ton, and the spaceplane cannot reach the orbit even without the payload. It is general that the weight estimation by present technological level indicates the negative payload weight. It means that the weight reduction more than 5 % is required to realize it.

Figure 5 and table 1 show the optimized wing area and the intake area of ATR are very small, and the intake area of SCR is 0 m², which means that SCR is unnecessary in this calculation. It can be considered that the wing area and ATR are respectively the limit size in order to take off and fly the vehicle against the aerodynamic drag, and that the volume of LH₂ is reduced because SCR isn't used.

4. CONCLUSIONS

First, this article proposed the new parallel optimization method for a large-scale system design with a huge number of variables and constraint conditions. This method divides the problem into some small optimization sub-problems based on subsystems constituting the system, which are solved in parallel.

Second, a shape and ascent trajectory optimization problem for spaceplane was studied by this method. Consequently, obtained numerical solutions indicate useful design data of a spaceplane.

REFERENCE

1. Lasdon, L. S., "Optimization Theory for Large Systems", The Macmillan Company, 1970.
2. Kirsch, U., "Optimum Structural Design", McGraw-Hill, 1981.
3. Suzuki, K. and Ohtsubo, H. "The Constraints between Subsystems in the Distributed Structural Optimization", Proceedings of the Conference on Computational Engineering and Science, 2-2, pp. 613-616, 1997.
4. Braun, R. D., Moore, A. A. and Kroo, I. M. "Collaborative Approach to Launch Vehicle Design", J. Spacecraft and Rockets, 34-4, pp. 478-486, 1997.
5. Ibaragi, H. and Fukushima, M. "FORTRAN77 Optimization Programming", Iwanami Shoten, 1991, (in Japanese).
6. Glatt, G. R., "WAATS-A Computer Program for Weights Analysis of Advanced Transportation Systems", NASA CR-2420, 1974.
7. Mendenhall, M. R., Goodwin, F. K., Dillenius, M. F. E. and Kline, D. M. "Computer Program for Calculating the Static Longitudinal Aerodynamic Characteristics of Wing-Body-Tail Configurations", NASA CR-2474, 1975.
8. Tsuchiya, T. and Suzuki, S. "A Study on the Numerical Method for Simultaneous Optimization for Spaceplane Design and its Flight Trajectory", J. the Japan Society for Aeronautical and Space Sciences, 46-533, pp. 346-353, 1998.

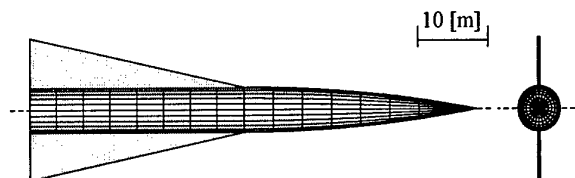


Fig. 5 Optimal shape

Table 1 Characteristics of optimal spaceplane

Characteristics		Optimal values
Body length	l_4 [m]	63.48
Body height	a [m]	6.00
Body width	b [m]	6.36
Wing span	s [m]	10.02
Intake area of ATR	S_{ATR} [m ²]	12.59
Intake area of SCR	S_{SCR} [m ²]	0.00
Thrust of ROC	T_{ROC} [ton]	226.6
Max. thrust	T_{max} [ton]	226.6
Max. dynamic pressure	q_{max} [kPa]	100.0
Max. load factor	n_{max} [G]	3.82
Payload weight	$W_{payload}$ [ton]	-13.75

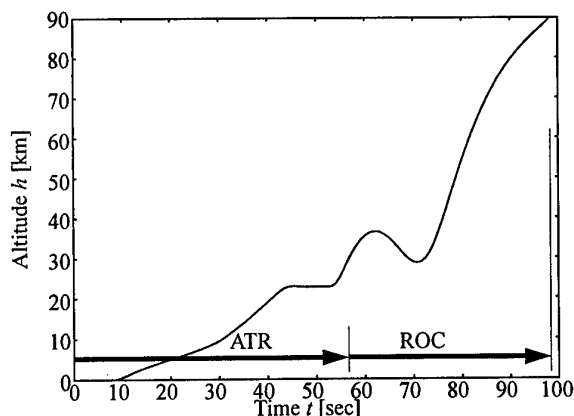


Fig. 6 Time history of altitude

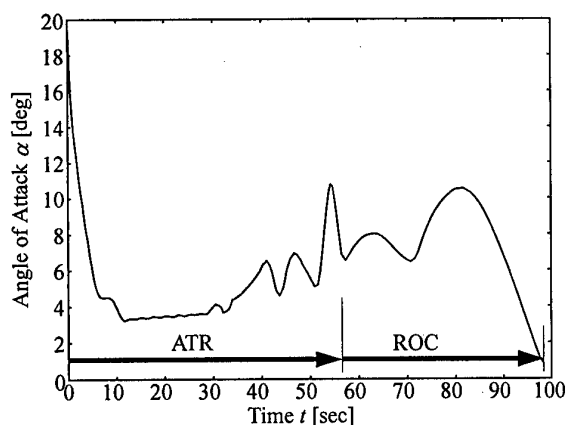


Fig. 7 Time history of angle of attack

Orbital Maneuvering of Reusable Launch Vehicle through Tether

K. D. Kumar* and Y. Miyazawa†

Flight Division, National Aerospace Laboratory, Osawa 6-13-1, Tokyo, Japan 181 0015

Key Words: Reusable Launch Vehicle, Orbital Maneuver, Tether

Abstract

The advent of communication satellites in polar orbits of 600-1200 km altitude and the development of international space station (ISS) at 400 km altitude and 51.6° inclination have put an urgent need for low cost access to such orbits. The paper presents the payload deployment to such lower earth orbits by reusable launch vehicle (RLV) through tether. This also makes the reentry of RLV possible without orbit maneuvering system (OMS). The approximate rules for maximum altitude change of RLV and payload after release are obtained. The numerical performance results for a typical spacecraft, Hope-X are presented. It is found that the use of tether for RLV is very promising.

1. INTRODUCTION

The advent of communication satellites in polar orbits of 600-1200 km altitude and the development of international space station (ISS) at 400 km altitude and 51.6° inclination have put an urgent need for low cost access to such orbits. The use of space tether¹⁻⁴ can make this goal achievable. It can perform simultaneously the tasks of reducing the altitude of reusable launch vehicle (RLV) after payload release so that it can return to earth as well as increasing payload altitude to reach desired higher orbit. Here, we study orbital maneuvering of a typical spacecraft, H-II Orbiting Plane Experiment (Hope-X) through tether.

The Lagrangian formulation procedure is adopted for obtaining the governing ordinary differential equations of motion for the constrained system. Subsequently, an approximate rule for maximum altitude change of RLV/payload after release is obtained. Finally, for a detailed assessment of the proposed concept, the set of exact governing equations of motion is numerically integrated.

2. FORMULATION OF THE PROBLEM

We consider a system model comprising of two point masses,

*Science & Technology Agency Fellow, Guidance and Control Laboratory

†Head, Guidance and Control Laboratory

RLV and payload connected through a tether in a keplerian orbit executing three-dimensional librational motion (Fig. 1). The RLV and the payload have masses m_1 and m_2 , respectively. The tethers made of a light material like Kevlar, has a mass ρ_t per unit length. The coordinate frame $E-X_1Y_1Z_1$ represents an inertial frame with origin at earth's mass center, E. The Y_1Z_1 plane is the equatorial plane and the X_1 -axis is towards the north pole. The Y_1 -axis is along the line of intersection of the orbital and equatorial planes i.e., along the line of nodes, and towards the ascending node; the Z_1 -axis completes the right-hand triad. The $E-XYZ$ frame is another inertial frame, with its origin at E. The Y -axis coincides with Y_1 -axis, X -axis is along the orbit normal, while the Z -axis completes the right-hand triad. The YZ plane is the orbital plane. The $E-XYZ$ frame can be obtained from $E-X_1Y_1Z_1$ frame by rotation through an angle i_0 (orbit inclination) about the line of nodes. The $E-X_2Y_2Z_2$ frame is a non-inertial geocentric frame such that the Y_2Z_2 plane coincides with the orbital plane and the Y_2 -axis points towards the center of mass of the tethered satellites system S, from E, while X_2 -axis is along the orbit normal. The $S-x_0y_0z_0$ frame is a rotating coordinate frame or orbital reference frame such that y_0 -axis points away from the earth along the local vertical, x_0 -axis is normal to the orbital plane and the z_0 -axis is along the local horizontal so as to complete the right hand triad. This frame is obtained from $X_2Y_2Z_2$ frame by translation from E to S. For the variable vector length \bar{L} joining the two satellite mass centers S_1 and S_2 , the angle β denotes rotation about the axis normal to the orbital plane and is referred as in-plane swing or pitch angle while the angle η represents its out-of-plane swing or roll angle. The resulting coordinate frame associated with this vector is denoted by $S-x_1y_1z_1$. This frame is obtained from $S-x_0y_0z_0$ frame by first β rotation about the x_0 -axis; that transforms $S-x_0y_0z_0$ axes to $S-x_1y_1z_1$ axes and this is followed by η rotation about z_1 -axis. The instantaneous center of mass of the system is defined by radial distance R and true anomaly θ . The position vectors of masses m_1 and m_2 are denoted by \bar{r}_1 and \bar{r}_2 , respectively. The system under consideration has the following generalized coordinates :

Orbital radius of the center of mass 'S' of the system : R

Latitude argument of 'S' : θ

vector \bar{L} : length L , β and η

and tether strains : ϵ_i

Applying the Lagrangian formulation approach, we obtain the following governing nonlinear, coupled ordinary differential equations of motion :

$$\begin{aligned}\ddot{R} &= \dot{\theta}^2 R - \mu/R^2 + (3/2)(\mu/R^2)(M_e/M)(L/R)^2(1-3\cos^2\beta\cos^2\eta) \\ \ddot{\theta} &= -2(\dot{R}/R)\dot{\theta} - (3/2)(\mu/R^3)(M_e/M)(L/R)^2\sin 2\beta\cos^2\eta \\ \ddot{\beta} &= 2(\dot{R}/R)\dot{\theta} - (\dot{\theta} + \dot{\beta})\{(2+\mu_c)(\dot{L}/L) - 2\dot{\eta}\tan\eta\} \\ &\quad - (3/2)(\mu/R^3)\{\sin 2\beta - (M_e/M)(L/R)^2\sin 2\beta\cos^2\eta\} \\ \ddot{\eta} &= -(2+\mu_c)(\dot{L}/L)\dot{\eta} - (1/2)(\dot{\theta} + \dot{\beta})^2\sin 2\eta \\ &\quad - (3/2)(\mu/R^3)\cos^2\beta\sin 2\eta \\ \ddot{L} &= \{(\dot{\theta} + \dot{\beta})^2\cos^2\eta + \dot{\eta}^2 - (\mu/R^3)(1-3\cos^2\beta\cos^2\eta)\}L - \mu_c(L/2) \\ &\quad \cdot [3(\dot{L}/L)^2 + (\dot{\theta} + \dot{\beta})^2\cos^2\eta + \dot{\eta}^2 \\ &\quad - (\mu/R^3)(1-3\cos^2\beta\cos^2\eta)] - \lambda/M_e\end{aligned}\quad (1)$$

where,

M_e =equivalent system mass= $(1/M)(m_1+m_2/2)(m_2+m_1/2)-m_1/6$;
 M =total system mass= $m_1+m_2+m_1$; $m_1=\rho_1 L$;
 $\mu_c=(L/M_e)(dM_e/dL)=(m_1/3)[(m_2+m_1/2)-2(m_1+m_2/2)]/M_e$
 $\lambda=EA\epsilon_i U(\epsilon_i)$; $\epsilon_i=L/L_0-1$; $U(\epsilon_i)=1$ if $\epsilon_i \geq 0$; 0 if $\epsilon_i < 0$,
 L_0 =unstretched tether length

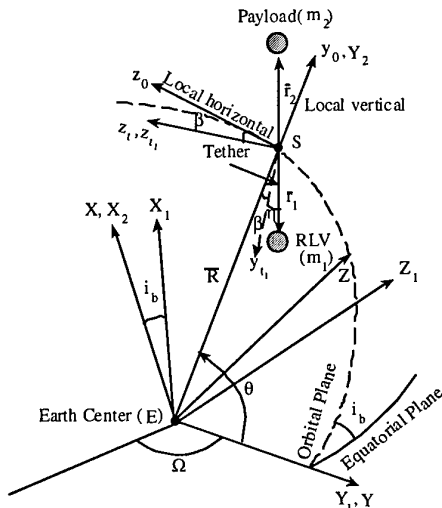


Fig. 1 Geometry of proposed system model.

2. POSITION AND VELOCITY OF RLV/PAYLOAD AT RELEASE POINT

The position and velocity of RLV and payload at the instant of release are expressed as,

$$R_i = [R^2 + r_i^2 + 2Rr_i\cos\beta\cos\eta]^{1/2}, \quad i=1,2$$

$$\begin{aligned}V_i &= [\dot{R}^2 + R^2\dot{\theta}^2 + r_i^2\dot{\eta}^2 + r_i^2(\dot{\theta} + \dot{\beta})^2\cos^2\eta - 2\dot{R}r_i\{\dot{\eta}\cos\beta\sin\eta \\ &\quad + (\dot{\theta} + \dot{\beta})\sin\beta\cos\eta\} + 2Rr_i\dot{\theta}\{-\dot{\eta}\sin\beta\sin\eta \\ &\quad + (\dot{\theta} + \dot{\beta})\cos\beta\cos\eta\}]^{1/2}, \quad i=1,2\end{aligned}\quad (2)$$

where, $r_1 = -(m_2+m_1/2)/M$; $r_2 = (m_1+m_2/2)/M$

Here, it is assumed that reel-in/reel-out operations have ended prior to the tether being cut, i.e., $\dot{r}_i=0$.

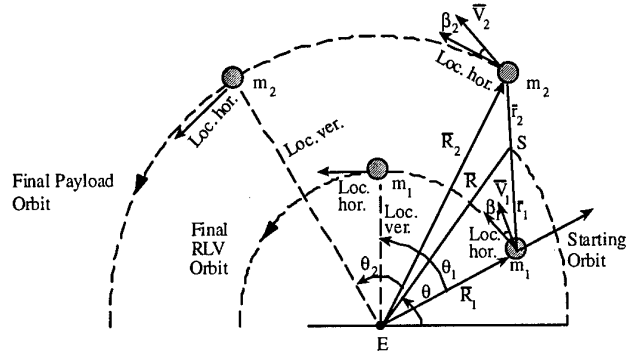


Fig. 2 Position and velocity of the RLV/payload at the release point.

4. ORBITAL ELEMENTS OF RLV/PAYLOAD AFTER RELEASE

The semimajor axis and eccentricity of the orbit of RLV/payload after its release can be written as,

$$\begin{aligned}a_i &= R_i / \{2 - R_i V_i^2 / \mu\} \\ e_i &= [\{(R_i V_i^2 / \mu) - 1\}^2 \cos^2\beta_i + \sin^2\beta_i]^{1/2}\end{aligned}\quad (3)$$

where, β_i , the angle between the velocity \bar{V}_i of mass m_i and the local horizontal (Fig.2), is given by,

$$\begin{aligned}\beta_i &= \pi/2 - \cos^{-1}\{|\bar{R}_i \cdot \bar{V}_i| / R_i V_i\}, \quad \bar{R}_i \cdot \bar{V}_i \geq 0 \\ \beta_i &= -\pi/2 + \cos^{-1}\{|\bar{R}_i \cdot \bar{V}_i| / R_i V_i\}, \quad \bar{R}_i \cdot \bar{V}_i < 0\end{aligned}\quad (4)$$

The decrease in perigee height of RLV and the gain in apogee height of payload are given by

$$\begin{aligned}\Delta R_{p1} &= R_p - R_{p1} = R_p - a_1(1 - e_1) \\ \Delta R_{a2} &= R_{a2} - R_a = a_2(1 + e_2) - R_a\end{aligned}\quad (5)$$

where, R_p and R_a are perigee and apogee heights of the starting orbit, respectively.

In the presence of out-of-plane librations, the plane of the released RLV/payload differs from that of the starting orbital plane, i.e., Y-Z plane. The inclination of the new orbit to the starting orbit, i_{bi} , is given as follows :

$$\tan i_{bi} = (h_{yi}^2 + h_{zi}^2)^{1/2} / h_{xi}, \quad i=1,2\quad (6)$$

where, $h_{xi} = Y_i V_{zi} - Z_i V_{yi}$; $h_{yi} = Z_i V_{xi} - X_i V_{zi}$; $h_{zi} = X_i V_{yi} - Y_i V_{xi}$

5. APPROXIMATE MAXIMUM ALTITUDE CHANGE OF RLV/PAYLOAD AFTER RELEASE

In order to obtain maximum decrease in perigee of RLV and maximum increase in apogee of payload, \bar{R}_i and \bar{V}_i must be perpendicular, i.e., $\beta_i = \pi/2$.

$$\bar{R}_i \cdot \bar{V}_i = 0, \quad i=1,2 \quad (7)$$

$$\text{or, } \dot{R} \{1+(r_i/R)\cos\beta\cos\eta\}/r_i - \dot{\beta} \sin\beta\cos\eta + \dot{\eta} \cos\beta\sin\eta = 0 \quad (8)$$

$$\text{or, } \dot{R} \{1+(r_1/R)\cos\beta\cos\eta\}/r_1 = \dot{R} \{1+(r_2/R)\cos\beta\cos\eta\}/r_2 \quad (9)$$

$$\text{or, } \dot{R} (r_2 - r_1)/(r_1 r_2) = 0$$

Since $r_1 \neq r_2$, $\dot{R} = 0$ (10)

Substituting this in Eq. (8) and for simplicity ignoring out-of-plane librations, we get $\beta=0$ i.e., the release of RLV/payload must take place when the tether is aligned with the local vertical during librations.

From Eqs. (2) the position and velocity of RLV/payload at release point can be written as

$$R_i = R + r_i$$

$$V_i = [R^2 \dot{\theta}^2 + r_i^2 (\dot{\theta} + \dot{\beta})^2 + 2Rr_i \dot{\theta} (\dot{\theta} + \dot{\beta})]^{1/2} \quad (11)$$

Considering RLV/payload is released at an angle θ measured from the reference line (Fig. 1), we obtain the following relations:

$$R \dot{\theta} = a\omega_n (1 + e\cos\theta)/(1 - e^2)^{1/2}$$

$$\dot{\theta} + \dot{\beta} = \omega_n [(1 + e\cos\theta)^2/(1 - e^2)^{3/2} + \delta] \quad (12)$$

where, a, e = semi-major axis and eccentricity of the starting orbit; δ = ratio of pitch rate to the mean orbital rate ω_n ; $\omega_n = (\mu/a^3)^{1/2}$; μ = gravitational constant.

Using these relations in Eqs. (11), we get

$$V_i^2 = \{\omega_n^2 a^2/(1 - e^2)\} [(1 + e\cos\theta)^2 + \{\hat{r}_i/(1 - e^2)^2\} \{(1 + e\cos\theta)^2 + \delta(1 - e^2)^{3/2}\} \times \{\hat{r}_i\{(1 + e\cos\theta)^2 + \delta(1 - e^2)^{3/2}\} + 2(1 + e\cos\theta)\}] \quad (13)$$

where, $\hat{r}_i = r_i/a$

Since $r_i \ll R$, this implies $r_i \ll 1$. Taking this into consideration, the above equation simplifies to

$$V_i^2 = \{\omega_n^2 a^2/(1 - e^2)\} [(1 + e\cos\theta)^2 + \{2\hat{r}_i(1 + e\cos\theta)/(1 - e^2)^2\} \times \{(1 + e\cos\theta)^2 + \delta(1 - e^2)^{3/2}\}] \quad (14)$$

Substituting this in Eqs. (3), the perigee and apogee heights of RLV and payload are expressed as

$$R_{p1} = a(1 + e\cos\theta) + r_1 \{7 + 4\delta + 4(5 + \delta)e\cos\theta\}$$

$$R_{a2} = a(1 + e\cos\theta) + r_2 \{7 + 4\delta + 4(5 + \delta)e\cos\theta\} \quad (15)$$

For minimum R_{p1} and maximum R_{a2} ,

$$\partial R_{p1}/\partial\theta = 0; \quad \partial R_{a2}/\partial\theta = 0$$

$$\text{or, } \sin\theta = 0, \quad \theta = k\pi, \quad k=0,1,\dots,n$$

Thus, the minimum R_{p1} and the maximum R_{a2} occur at $\theta = \pi, 3\pi, 5\pi, \dots$ and $\theta = 2\pi, 4\pi, 6\pi, \dots$ respectively and are written as

$$(R_{p1})_{\min} = a(1 - e) + r_1 \{7 + 4\delta - 4(5 + \delta)e\}$$

$$(R_{a2})_{\max} = a(1 + e) + r_2 \{7 + 4\delta + 4(5 + \delta)e\} \quad (16)$$

The maximum decrease in perigee height of RLV and the maximum gain in apogee height of payload are given as follows:

$$(\Delta R_{p1})_{\max} = -r_1 \{7 + 4\delta(1 - e) - 20e\}$$

$$(\Delta R_{a2})_{\max} = r_2 \{7 + 4\delta(1 + e) + 20e\} \quad (17)$$

6. RESULTS AND DISCUSSION

With a view to assess the efficacy of the proposed concept, the detailed system response is numerically simulated using Eqs. (1). We assumed the following numerical data: $m_1 = 14000$ kg; $\rho_t = 1$ kg/km; EA = tether modulus of rigidity = 10^4 Newton; L_0 = initial tether length = 10 m; Starting Perigee of (RLV + Payload) Orbit = 6628 km; R_E = earth radius = 6378 km. The system is assumed to enter the starting orbit with the following initial conditions:

$$\dot{L} = \dot{\beta} = \dot{\eta} = \dot{\eta} = 0$$

The tether is deployed using swing release as given below:

$$L_0 = L_{\infty} \exp[C(t - t_0)] \quad (18)$$

where, $C = 0.0008$ for $L_0 < 100$ km and $C = 0.0007$ for $L_0 \geq 100$ km are taken.

The RLV/payload is released on a forward swing when the libration angle is instantaneously zero. By varying the predeployment true anomaly (Ψ_0), the forward swing zero libration is caused to occur nearly simultaneously with perigee passage, yielding maximum increase in altitude of payload. However, when the forward swing zero libration is caused to occur nearly simultaneously with apogee passage, the maximum decrease in altitude of RLV occurs. Here, we are considering later situation. Figures 3 and 4 show the position of RLV/payload and length L along with inplane swing angle, β , respectively, for cases of 4000 kg of payload mass deployed at 400 km altitude and 2000 kg of payload deployed at 800 km altitude. The results for different cases are summarised in Table 1. The RLV/payload

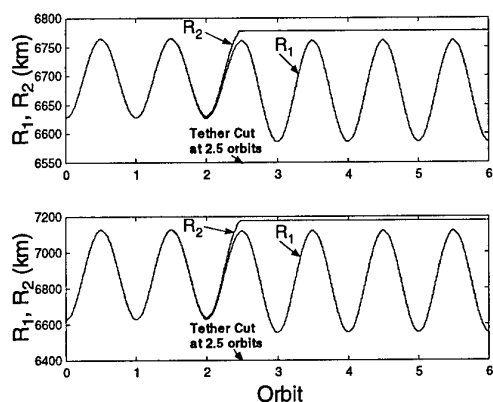


Fig 3. Showing the positions of RLV and payload during the TSS mission : (a) $m_2=4000$ kg, payload deployed at 400 km, (b) $m_2=2000$ kg, payload deployed at 800 km.

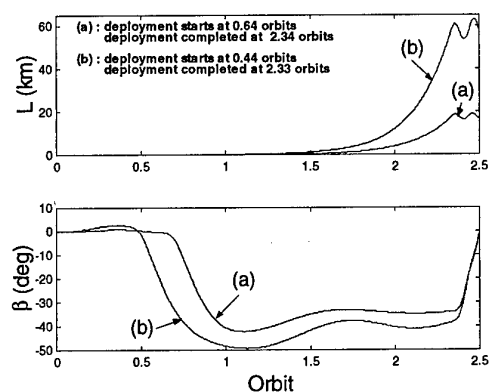


Fig 4. Showing the length L and inplane swing angle, β as effected by payload deployment : (a) $m_2=4000$ kg, payload deployed at 400 km, (b) $m_2=2000$ kg, payload deployed at 800 km.

is released at 2.5 orbits. It is important to note that the maximum decrease in perigee height of RLV as stated by Eq. (17) matches with the simulation results within maximum error of 50 meter.

Table 1. RLV/payload altitude after its release.

Payload Mass (m_2) (kg)	Tether Length (km)	Eccentricity of Starting RLV +Payload Orbit	Payload Deployed At Altitude (km) Circular Orbit	RLV Placed At Altitude (km)
1000	15.3	0.0101	400	239
	52.9	0.0365	800	212
	103.5	0.0599	1200	185
2000	15.8	0.0102	400	229
	55.2	0.0363	800	175
	105.9	0.0598	1200	125
4000	17.2	0.0102	400	208
	62.2	0.0356	800	101
	106.0	0.0606	1200	6

7. CONCLUSIONS

Here, we investigated the orbital maneuvering of RLV through tether. The numerical performance results for Hope-X are presented. The exact numerical integration of the governing nonlinear equations of motion establishes the feasibility of the concept. It is found that the payload boasting to lower earth orbits of 400-1200 km altitude along with the reentry of RLV without OMS is feasible. The concept proposed may be particularly attractive for future space missions involving RLV.

REFERENCES

1. Bekey, I., "Tethering a New Technique for Payload Deployment," Aerospace America, pp.36-42, March 1997.
2. Colombo, G., Martinez-Sanchez, M., and Arnold, D., "Use of Tethers for Payload Orbit Transfer," Smithsonian Astrophysical Observatory, NAS 8-33691, Cambridge, MA, March 1982.
3. Kyroudis, G. A., and Conway, B. A., "Advantages of Tether Release of Satellites from Elliptic Orbits," Journal of Guidance, Control and Dynamics, Vol. 11, No. 5, pp. 441-448, 1988.
4. Kumar, K., Kumar, R. and Misra, A. K., "Effects of Deployment Rates and Librations on Tethered Payload Raising," Journal of Guidance, Control and Dynamics, Vol. 15, No. 5, pp. 1230-1235, 1992.

A Study of the Swimming Path of the Penguin

Masanori Harada *, Shinichiro Itoh **, Nobuaki Arai*** and Yasuhiko Naito****

*** National Defense Academy, 1-10-20 Hashirimizu, Yokosuka, Kanagawa, 239-8686, Japan

** Kyoto University Graduate School of Informatics Biosphere Informatics, Kyoto University Kyoto 606-8501, Japan

**** National Institute of Polar Research 9-10, Kaga 1-chome, Itabashi-ku, Tokyo 173-8515, Japan

Key words : Flight Dynamics, Guidance and Control, Penguin

Abstract

In this paper, the swimming path of the penguin is analyzed by means of optimal control theory to compare it with observed swimming data. Equations include the effect of added mass, which has to consider when the mass of the fluid has the same order of body mass such as the paraglider analyzation. In the analysis, one must consider the state variable inequality constraint for both the velocity and depth of the penguin. Numerical results are presented to compare with or without the added mass case and observed data.

1. Introduction

Penguins are well known that dive into the sea very deeply when they required catching foods. Even small size of penguins can have been dived into 150-200m. National Institute of Polar Research has been observed those penguin's diving data. But, sea birds such as penguins have large difference between their theoretical oxygen consumption and dynamic motions. The purpose of our study is to investigate characteristic of the penguin's vertical motion from optimal control theory that often used in optimization of aircraft trajectories.

* Research Associate, Department of Mechanical Engineering

** Lecturer, Department of Mechanical Engineering

*** Associate Professor, Department of Social Informatics

**** Professor, Behavioral Ecology Group

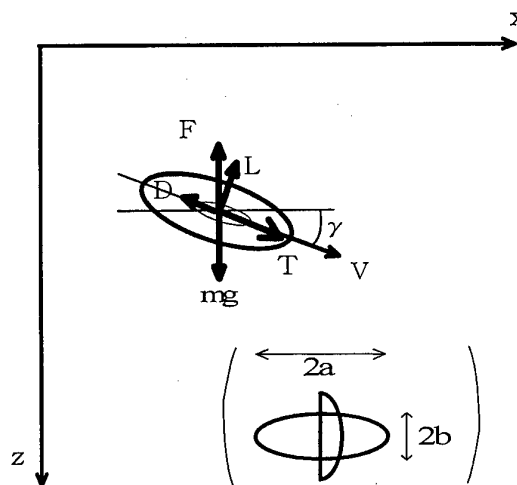


Fig.1 Axis for vertical motion of the penguin

2. Formulation of the penguin motion

2.1 Equations of motion

Equations of motion for the penguin are define as Eq.(1)-(4) from Fig.1 for simple mass point model. Equations are including added mass term, which can not neglected the effect of relative moving fluid mass surrounding body.

$$(m + A_{11}) \frac{dV}{dt} = T - \frac{1}{2} \rho_s V^2 S (C_{D0} + KC_L^2) - m_s g \sin \gamma \quad (1)$$

$$(m + A_{33}) V \frac{d\gamma}{dt} = \frac{1}{2} \rho_s V^2 S C_L - m_s g \cos \gamma \quad (2)$$

$$\frac{dx}{dt} = V \cos \gamma \quad (3)$$

$$\frac{dz}{dt} = -V \sin \gamma \quad (4)$$

here

Added mass are define as Eq.(5) and (6).

$$A_{11} = k_1 \left(\frac{4}{3} \rho_s \pi a b^2 \right) \quad (5)$$

$$A_{33} = k_2 \left(\frac{4}{3} \rho_s \pi a b^2 \right) \quad (6)$$

AR_e : Aspect ratio, C_L : Lift coefficient, C_{D0} :Zero lift drag coefficient, C_T :Thrust coefficient, a :Ellipse body length, b : Ellipse body radius, g :Gravitational acceleration, k : Induced drag coefficient, k_1, k_2 :Added mass coefficient, L : Breathing capacity, m : Penguin mass, m_f :Mass from floating, m_s :Total mass, S :Wing area, t :Time, T :Thrust, V :Velocity, z :Depth, γ :Path angle, ρ_p :Penguin density, ρ_s :Sea density

2.2 Optimization method

In order to solve optimal trajectory of the swimming of the penguin modified GA (genetic algorithm) for optimal control problem is used here. This optimization method defines time history of control variables as directly referred to chromosome values. For an example:

Chromosome $\Rightarrow \{0.5, 0.3, 0.3, 0.4, 0.2, 0.6, 0.8, 0.9, 1.0\}$

Control variable $\Rightarrow u[0]=0.5, u[1]=0.3, \dots, u[8]=1.0$

Since control variables are defined then iteration sequence as bellow start to find optimal control variables set.

- Make control variables set from chromosomes
- Solve differential equations
- Solve performance index
- Sort all chromosome by index value
- Crossover chromosome by better index value
- Substitute chromosome
- Mutate chromosome
- Restart from a. until convergent condition is occurred

Initial conditions of the problem can use for differential equations. Inequality constraints of control variables are constrained by max/min of chromosome's variables. Final conditions and state variables inequality constraint are stated into performance index by penalty function method.

3. Numerical simulations

Initial conditions:

$$V_0 = 1.0[m/s], \quad \gamma_0 = -20[\text{deg}], \quad x_0 = z_0 = 0[m]$$

Final conditions:

$$\gamma_f = 0[\text{deg}], \quad z_f = 0[m]$$

Constraints:

$$0 \leq C_T \leq 0.2, \quad -0.5 \leq C_L \leq 0.5 \quad (7)$$

$$V \leq 4.0[m/s], \quad z \geq 0[m] \quad (8)$$

Performance index

$$I = \int_0^t \{ (V - 2.5)^2 + (z - 15)^2 \} dt \quad (9)$$

Eq.(9) is defined that fishes for the penguin are swimming around 15[m] depth of the sea and the penguin's mean velocity of swimming is 2.5[m/s]. At the calculation of without added mass case, let $A_{11} = A_{33} = 0$ in Eq.(1) and (2).

National Institute of Polar Research observes swimming data of the penguin 97GA4715: 5934-5980. Fig.2 shows result of without added mass case. All variables have oscillational characteristic that it explains result is close to unstable solution and very sensitive to variation of control variables at assuming parameter values. Fig.3 shows result of added mass case. It is similar to observe data of the penguin and equations are more stable then without added mass case. Each case shows that velocity is increasing when the penguin is floating to the sea level. It is very interesting that constraints of state variables both velocity and depth must be considered in same time.

4. Conclusions

The optimal swimming path of the penguin is solved by the optimal control method. Numerical results that are compared with observe data is explaining the formulation of penguin's motion are required the added mass theory.

REFERRNCES

- 1) Azuma A.: Aeronautics(I), Shoukabo.
- 2) Takae Y., et al.: Proceedings of the 35th Aircraft Symposium, JSASS,1997,pp.569-572.

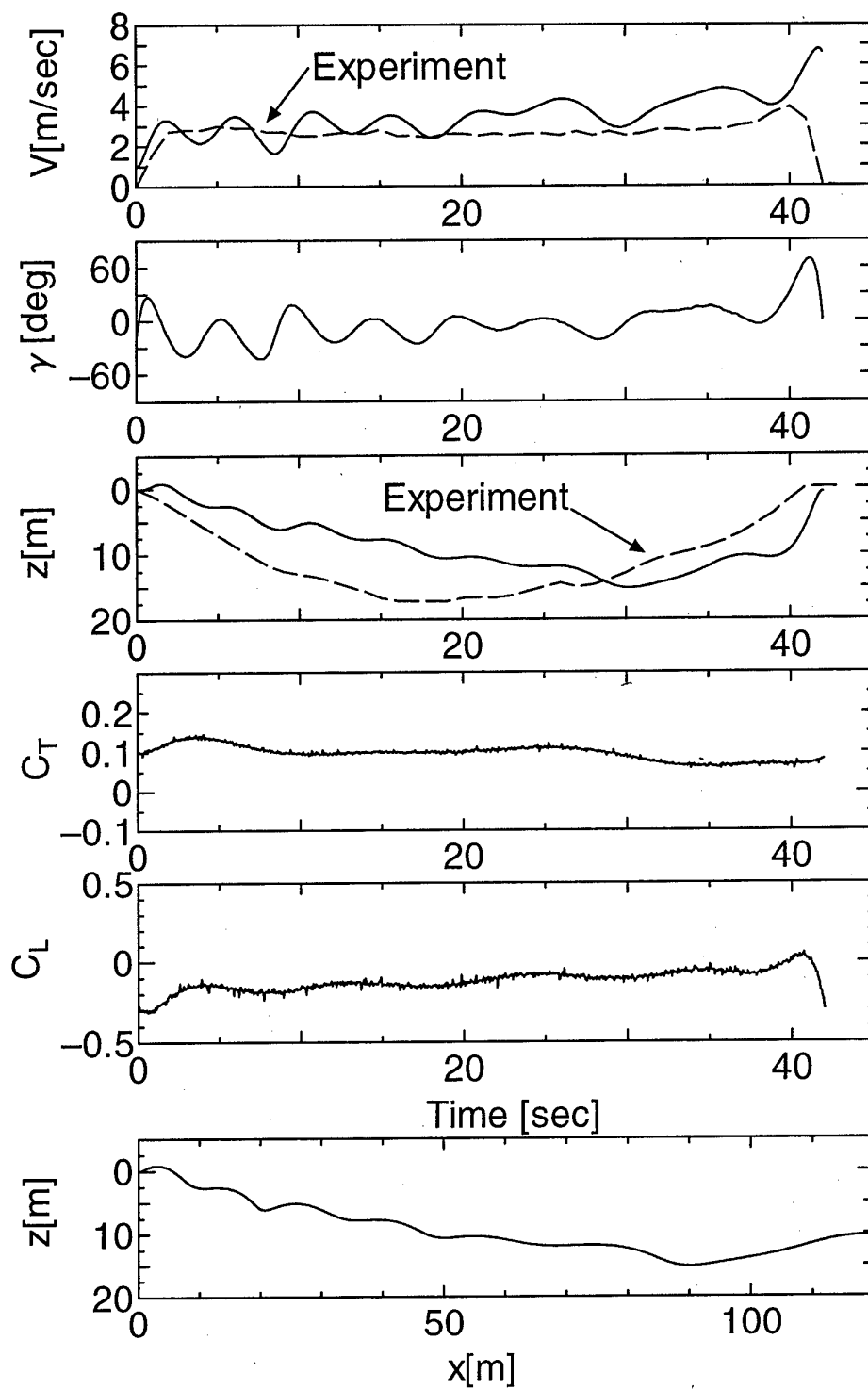


Fig. 2 Numerical solution for without added mass case

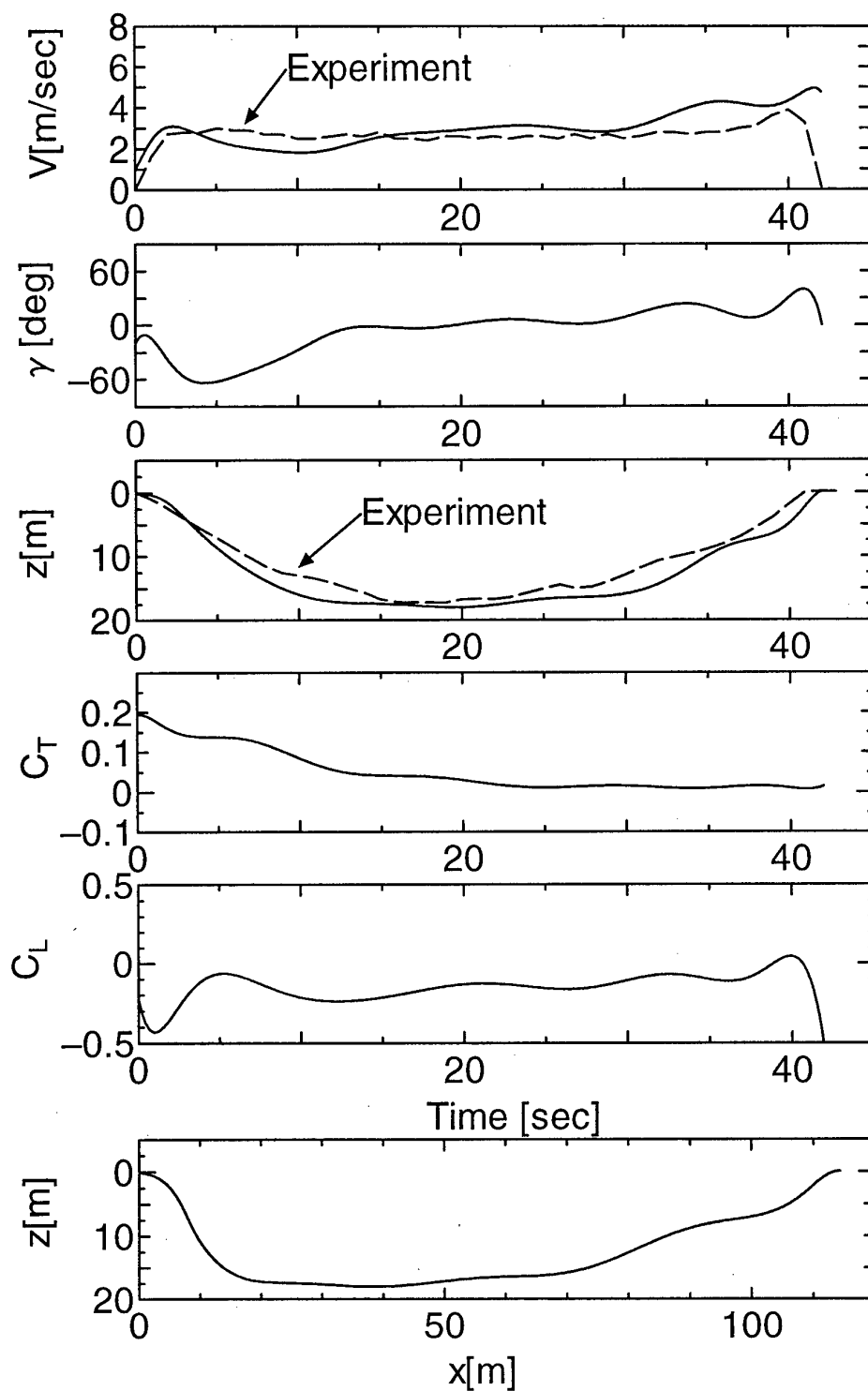


Fig. 3 Numerical solution for added mass case